CRANFIELD UNIVERSITY

Cinzia Taccoli

# Experimental and Computational Analysis of Purge Systems for Radiation Pyrometers

School of Engineering

PhD Thesis

# Cranfield University

School of Engineering
Department of Power and Propulsion

PhD Thesis
Academic Year 2010-2011

Cinzia Taccoli

# Experimental and Computational Analysis of Purge Systems for Radiation Pyrometers

Supervisor: Dr João Alexandre Amaral Teixeira

July 2011

This thesis is submitted in partial fulfilment of the requirements for the Degree of
Doctor of Philosophy

*To my grandparents*
*Oreste and Elena*
*Forever in my heart*

*"If you're going through hell keep going"*

Winston Churchill

# Abstract

Maximizing the turbine entry temperature (TET) is fundamental to increase engine efficiency and reducing fuel consumption. Nonetheless, safety and reliability requirements have to be fulfilled. The life of gas turbine blades is strictly connected to their temperature through the creep deformation process. For this reason temperature monitoring is an essential requirement. Commonly this is achieved by means of devices such as thermocouples which are placed in the bulk flow.

The usefulness of these devices as the means of supplying turbine blade temperature information is limited given their slow response time and the fact that the blade temperature is inferred from that of the surrounding gas rather than measured directly. This in turn means that critical blades parts (e.g., trailing edge) or the presence of hot spots are not identified in a discrete manner. These drawbacks can be addressed by using instead a radiation pyrometer, which is characterized by a fast response time, high accuracy, and by being contactless.

The pyrometer optical front-end is a lens which collects the radiation emitted by a spot on the turbine blades. However, since the lens is exposed to the harsh engine environment, contaminants entrapped by the turbine flow can therefore be easily deposited on the lens thus filtering the radiation and resulting in an under-estimation of the actual blade temperature.

The fouling of the lens is generally tackled by using a purge air system that employs air bled from the compressor to divert those particles whose trajectory is directed towards the lens.

Currently the employment of optical pyrometry is often confined to military applications due to the fact that their turbine entry temperatures are higher than in

civil applications. Besides, the maintenance schedule established for military engines is far more frequent than what is practiced in airline engines. Therefore, the design of current purge air systems reflects these facts. Before optical pyrometers can be commonly used for civil applications more research is required since some of the fundamentals of the fouling mechanisms remain to be clarified. This is then the knowledge gap the present research sought to fill. Its aim was to conduct a comprehensive investigation of the phenomena that underpins the lens fouling process in order to provide a set of guidelines for optimising the design of purge air systems.

The initial part of the research was dedicated to the study of the purge flow inside a given pyrometer configuration. The scope was to identify the main flow structure that determines the fouling process and at the same time to validate the results obtained via computational fluid dynamics (CFD) analyses conducted in a second phase of the research. Given the reduced dimensions of the pyrometer purge system, it was not possible to gain the appropriate optical access to take flow measurements. Consequently, a large scaled experiment was performed, employing the Particle Image Velocimetry (PIV) technique for the acquisition of experimental data of the flow field. The distortion of the image and light reflection introduced by the presence of curved glass surfaces was investigated by means of a feasibility experiment. The experimental study highlighted the presence of a large recirculation zone that can trap contaminants and direct them towards the pyrometer lens. The experimental data were in agreement with computational fluid dynamics results obtained by using two different turbulence models.

In a second instance, attention was focused on the particle deposition as seen from a fluid dynamics perspective. A computational fluid dynamics analysis aimed at reproducing the flow field of an existing pyrometer purge system enabled the identification of those features that can significantly impact on the lens fouling process. It was found that the geometry of the air curtain configuration plays a fundamental role. However, given the high speeds involved, the main force governing the contaminants deposition is the drag. Additionally, particles with high inertia hit the purge tube wall and then bounce towards the pyrometer lens, while contaminants with low inertia can be trapped by a large recirculation zone and subsequently directed towards the lens.

In a third phase of the research, the impacts between the contaminant particles and the lens were investigated through a finite element analysis (FEA) aimed at identifying the most important factors that contribute to the lens fouling process. Particles moving at low speed can be deposited on the lens by means of electrostatic and Van der Waals forces. Conversely, particles with very high velocity can be deposited on the lens through the same mechanisms involved in the cold spraying process, which is a technique commonly used for coating deposition.

A local melting can occur at the interface between the lens and the contaminants due to the high stresses created by the asperities and high sliding velocity of the particles. As a result, while large particles bounce back, debris remains bonded to the lens surface.

Last but not least, the findings of the several steps of the present research have been brought together in order to produce guidelines to be followed by engineers engaged in the redesign of more efficient pyrometer purge systems.

# Acknowledgements

# Contents

# Nomenclature

| | |
|---|---|
| ALE | Arbitrary Lagrangian Eulerian |
| CCD | Charged Coupled Device |
| CFD | Computational Fluid Dynamics |
| DNS | Direct Numerical Simulation |
| DRW | Discrete Random Walk |
| DSAP | Dual Spectral Area Pyrometer |
| FAR | Fuel Air Ratio |
| FEA | Finite Element Analysis |
| FFT | Fast Fourier Transform |
| HP | High Pressure (turbine) |
| JKR | Johnson-Kendall-Roberts model of elastic contact |
| LES | Large Eddy Simulation |
| LDA | Laser Doppler Anemometry |
| PEEQ | Equivalent Plastic strain rate |
| PIV | Particle Image Velocimetry |
| PPR | Purge Pressure Ratio |
| PZT | Lead zirconate titanate |
| RANS | Reynolds Averaged Navier Stokes |
| RMS | Root Mean Square |
| RNG | Re-Normalization Group |
| SDP | Super Deep Penetration |
| SEM | Scanning Electron Microscope |
| SFC | Specific fuel consumption |
| SHG | Second Harmonic Generator |
| SPIV | Stereoscopic Particle Image Velocimetry |
| SST | Shear Stress Transport |
| TBC | Thermal Barrier Coating |
| TEM | Transmission Electron Microscope |
| TET | Turbine Entry Temperature |
| | |
| $\alpha^*$ | Cameras mounting angle |
| $\alpha_\varepsilon$ | $\varepsilon$ inverse Prandtl number |
| $\alpha_k$ | $k$ inverse Prandtl number |
| $\alpha_1,\ \alpha_2,\ \alpha_3$ | Angle between the absolute velocity vector and the engine axis at stator inlet, rotor inlet and rotor outlet respectively |
| $\beta$ | Purge flow angle – Patent US 4306835 |
| $\beta_1,\ \beta_2,\ \beta_3$ | Angle between the relative velocity vector and the engine axis at stator inlet, rotor inlet and rotor outlet respectively |
| $\delta_{ij}$ | Kronecker Symbol |
| $\varepsilon$ | Turbulent Dissipation rate |
| $\dot{\varepsilon}_0$ | Reference Strain Rate |
| $\varepsilon_\lambda$ | Body Emittance |
| $\bar{\varepsilon}_{pl}$ | Effective Plastic strain rate |

| | |
|---|---|
| $\phi_{12}$ | Interaction parameter |
| $\gamma_1$ | Surface tension of body 1 |
| $\gamma_2$ | Surface tension of body 2 |
| $\gamma_{12}$ | Interfacial tension |
| $\lambda$ | Wavelength |
| $\mu$ | Dynamic viscosity |
| $\mu_{eff}$ | Effective viscosity |
| $\mu_f$ | Fluid viscosity |
| $\mu_g$ | Gas dynamic viscosity |
| $\mu_t$ | Turbulent Viscosity |
| $v^*$ | Poisson Ratio |
| $v$ | Kinematic Viscosity |
| $v_f$ | Radiation frequency |
| $\rho_f$ | Fluid density |
| $\rho_p$ | Particle Density |
| $\sigma$ | Stefan-Boltzmann constant |
| $\tau_c$ | Eddy crossing time |
| $\tau_{\Lambda L}$ | Lagrangian time scale |
| $\tau$ | Time |
| $\tau_{mE}$ | Eulerian time scale |
| $\tau_\lambda$ | Eddy Time scale |
| $\theta$ | Actual temperature |
| $\hat{\theta}$ | Non dimensional temperature |
| $\theta_{melt}$ | Melt temperature |
| $\theta_{transition}$ | Transition temperature |
| $\omega$ | Specific Dissipation |
| $\omega_a$ | Combined surface energy between the sphere and the substrate |
| $\zeta$ | Random generated value considering a Gaussian distribution |
| $\Delta E$ | Energy difference between two atomic energy levels |
| $\Delta x, \Delta x_1, \Delta x_2$ | Displacement along the x-axis: Total, of the first camera, of the second camera |
| $\Delta y, \Delta y_1, \Delta y_2$ | Displacement along the y-axis: Total, of the first camera, of the second camera |
| $\Delta z, \Delta z_1, \Delta z_2$ | Displacement along the z-axis: Total, of the first camera, of the second camera |
| $\Delta t$ | Time interval |
| $\Delta t^*$ | Impact Characteristic Time Scale |
| $\Delta T$ | Temperature Gradient |
| $\Lambda$ | Eddy length scale |
| $\psi$ | Angle between the pyrometer and the engine axis |
| $\Theta_{p,ij}$ | Particle diffusivity |
| $A$ | Material parameter-Johnson Cook model |

| | |
|---|---|
| $B$ | Material parameter-Johnson Cook model |
| $A_n$ | Turbine annulus area |
| $C$ | Correlation strength |
| $C_A$ | Adhesion Damping Coefficient |
| $C^*$ | Material parameter–Johnson Cook Model |
| $C_d$ | Drag Coefficient |
| $C_H$ | Dynamic Damping Coefficient |
| $C_\mu$ | Turbulent Constant |
| $C_{1\varepsilon}$ | RNG $k$-$\varepsilon$ constant |
| $C_{2\varepsilon}$ | RNG $k$-$\varepsilon$ constant |
| $C_\mu$ | RNG $k$-$\varepsilon$ constant |
| $D_{inner}$ | Inner turbine annulus diameter |
| $D_{mean}$ | Mean turbine annulus diameter |
| $D_{outer}$ | Outer turbine annulus diameter |
| $D_\omega$ | Cross Diffusion |
| $E$ | Elastic Modulus |
| $Ec$ | Eckert number |
| $E_f$ | Second band total emission (for DSAP technique) |
| $E_{fb}$ | Second band blade emission (for DSAP technique) |
| $E_{fr}$ | Second band reflected emission (for DSAP technique) |
| $E_u$ | First band total emission (for DSAP technique) |
| $E_{ub}$ | First band blade emission (for DSAP technique) |
| $E_{ur}$ | First band reflected emission (for DSAP technique) |
| $E_1$ | Atomic energy at level 1 |
| $E_2$ | Atomic energy at level 2 |
| $F_A$ | Adhesion Force |
| $F_{AD}$ | Adhesion Damping Force |
| $F_{body}$ | Body forces |
| $F_{Brownian}$ | Brownian motion force |
| $F_{coll}$ | Collision forces |
| $F_{drag}$ | Drag force |
| $F_H$ | Hertzian Force |
| $F_{HD}$ | Dynamic Damping force |
| $F_{AD}$ | Adhesion Damping Force |
| $F_{history}$ | History force |
| $F_{lift}$ | Lift force |
| $Fr$ | Froude Number |
| $F_{surf}$ | Surface forces |
| $F_{thermophoresis}$ | Thermophoresis Force |
| $F_{virtualMass}$ | Virtual Mass force |
| $F_1, F_2$ | Surface free energy of body 1 and body 2 respectively |
| $F_{12}$ | Interfacial free energy |
| $G_b.$ | Generation of $k$ (RNG $k$-$\varepsilon$) model due to mean buoyancy |

| | |
|---|---|
| $G_k$ | Generation of $k$ (RNG $k$-$\varepsilon$) model due to mean velocity gradient |
| $\widetilde{G}_k$ | Generation of $k$ (SST $k$-$\omega$) model |
| $G_\omega$ | Generation of $\omega$ ($k$-$\omega$) model |
| $I$ | Radiation Intensity |
| $I_a$ | Radiation intensity Emitted by a non-blackbody |
| $I_b$ | Radiation intensity Emitted by a blackbody |
| $I_1$ | Image intensity of the interrogation window – first exposure |
| $I_2$ | Image intensity of the interrogation window – second exposure |
| $I_{1avg}$ | Average Image intensity of the interrogation window – first exposure |
| $I_{2avg}$ | Average Image intensity of the interrogation window – second exposure |
| $K$ | Effective material stiffness |
| $L$ | Macroscopic Length scale |
| $Mn$ | Mach Number |
| $M$ | Material parameter, Johnson Cook model |
| $M1, M2, M3$ | Mirror 1, 2, 3 respectively |
| $N$ | Material parameter Johnson Cook model |
| $Nd:Yag$ | Neodymium-Doped Yttrium Aluminium Garnet |
| $N_p$ | Number of particles |
| $P*$ | Gaussian distribution |
| $P$ | Beam combining polarizer |
| $P1$ | First lens focal point – Patent US 4657385 |
| $P2$ | Second lens focal point – Patent US 4657385 |
| $Pr$ | Prandtl number |
| $Re$ | Reynolds Number |
| $R_g$ | Gas constant |
| $Re_p$ | Particle Reynolds Number |
| $Ru$ | Ruark Number |
| $R_\varepsilon$ | RNG k-ε additional term taking in account high strain rates |
| $St$ | Stokes number |
| $St_{turb}$ | Turbulent Stokes Number |
| $Sh$ | Strouhal Number |
| $T$ | Temperature |
| $T_g$ | Gas temperature |
| $U$ | Turbine speed |
| $V_{m\text{-}m}$ | Average root mean square of the molecules speed |
| $Y_k$ | Dissipation of $k$ Fluctuating dilation contribution |
| $Y_\omega$ | Dissipation of $\omega$ |

| | |
|---|---|
| $a$ | contact radius |
| $a_{eq}$ | Contact radius at Equilibrium condition |
| $A^*$ | Speed of Sound |
| $C$ | Speed of light |
| $c_\mu$ | Eddy length scale constant |
| $c_p$ | Specific heat |
| $c_\tau$ | Eddy time scale constant |
| $C_1, c_2, c_3$ | Flow velocity at stator inlet, rotor inlet, rotor exit respectively |
| $c_\forall$ | virtual mass coefficient |
| $D$ | Particle diameter |
| $d_{crit}$ | Particle critical diameter |
| $Dx$ | Displacement along x |
| $dy$ | Displacement along y |
| $F^*$ | Camera lens aperture number |
| $F$ | Stokesian correction factor |
| $F_0$ | Intensity of the ring force |
| $G$ | Gravitational acceleration |
| $H$ | Planck's constant |
| $I$ | Integral power intensity |
| $K^*$ | Boltzmann's constant |
| $K$ | Turbulent kinetic energy |
| $K_1$ | Particle Stiffness |
| $K_2$ | Substrate Stiffness |
| $K_1$ | Particle Stiffness |
| $k_t$ | Thermal Conductivity |
| $L$ | Characteristic length |
| $l_{m-m}$ | Average free mean path |
| $M$ | Microsphere Mass |
| $m_p$ | Particle mass |
| $N^*$ | Interrogation window size |
| $N$ | Mass centre displacement |
| $\dot{n}$ | Microsphere velocity |
| $\ddot{n}$ | Microsphere acceleration |
| $P$ | pressure |
| $R$ | Microsphere radius |
| $T$ | Time |
| $t_{stop}$ | Particle Stopping Time |
| $T^*$ | Characteristic Time |
| $u_D$ | Macroscopic characteristic velocity |
| $u_{@p}$ | Velocity of the fluid extrapolated at the particle centre mass |
| $U$ | Component of velocity along the x axis, absolute value |
| $\bar{u}$ | Component of velocity along the x axis, steady mean value |

| | |
|---|---|
| $u'$ | Component of velocity along the x-axis, fluctuating value |
| $V$ | velocity |
| $v'$ | Fluctuating velocity component along the y-axis |
| $\hat{v}$ | Particle average velocity |
| $v_f$ | Fluid Velocity |
| $v_p$ | Particle Velocity |
| $v_r$ | Particle Rebound Velocity |
| $v_0$ | Particle Initial Velocity |
| $x^*$ | Particle Characteristic Length |
| $x_p$ | Particle Position |
| $x_p'$ | Deviation from the path |
| $W$ | Particle relative velocity |
| $w'$ | Fluctuating velocity component along the z-axis |
| $w_0$ | Initial relative velocity |
| $w_1,\ w_2$ | Flow relative velocity at stator inlet and rotor inlet respectively |
| $\forall_p$ | Volume occupied by the particle |
| $\langle q \rangle$ | Ensemble average path |
| $\langle x_{p,i}' x_{p,j}' \rangle$ | Particle mean path |

# List of Figures

# List of Tables

# Chapter 1
# Introduction

## 1.1 Project Overview

The efficiency of a gas turbine engine depends on the maximum temperature achievable in the Brayton cycle. As a result, the combustion temperature has to be maximized while at the same time engine safety and reliability have to be assured. When a material is exposed for an extended period of time at high temperatures the failure point can be achieved even if the maximum stress applied is lower than the yield stress. This mechanism, known as creep, can be subdivided in three different phases, Figure 1.1. In the primary stage the deformation quickly increases with time, to then significantly slow down during the second phase with the material deforming at almost constant speed. In the final stage the deformation increases exponentially and the material will quickly reach the rupture point (Betten (2005)).
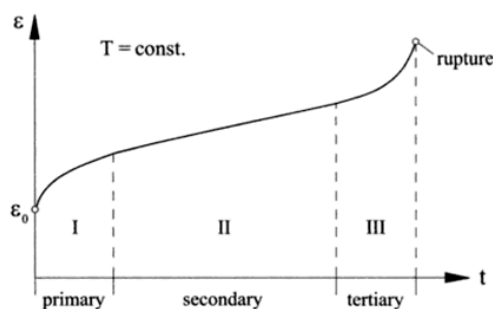


**Figure 1.1**: *Typical creep curve (Betten (2005)).*

It is important to notice that the material creep life quickly diminishes with the operational temperature. Therefore, the monitoring of the blade is a crucial task in avoiding early engine failures.

When used to monitor blade temperatures, conventional sensors, such as embedded thermocouples, have several drawbacks, summarised by Koeschel et al. (1986) and Sellers et al. (1989) in:

- Short life.
- Increase in blade local stresses due to the presence of wires.
- Impossibility of monitoring critical zones of the blade. Since the capability of a thermocouple to take temperature measurements depends on the local wall thickness of the blades, thin walls cannot be instrumented (i.e. trailing edge). Therefore, even considering an optimum use of thermocouples, only a few local measurements are achievable. Consequently, often no temperature data can be obtained in some critical zones of the blades.
- Low time response.

The use of a non-contact system overcomes the thermocouples disadvantages. A radiation pyrometer collects the energy emitted by a spot situated on the blade and, exploiting thermodynamic laws correlates, this radiation with the blade temperature.
The radiation is collected by a lens, that it is the only part of the optical system exposed to the engine environment, and then sent to a detector. The signal is subsequently processed and in the end analyzed providing the user with temperature read out, Figure 1.2.
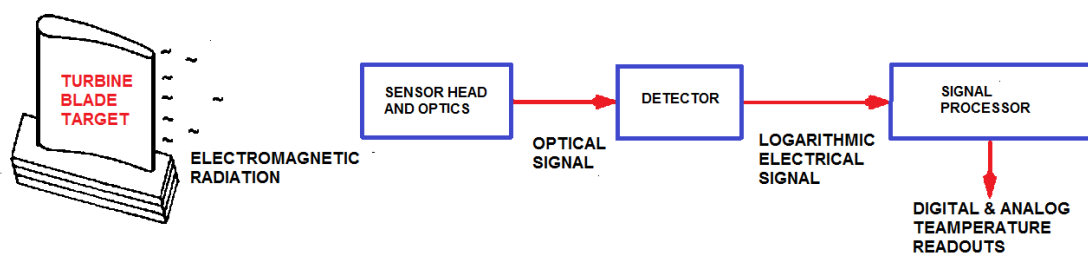


**Figure 1.2:** *Radiation Pyrometer components (Rohy et Compton (1973)).*

The pyrometer functioning could be jeopardized by the harsh gas turbine environment and hence this device is installed in the engine casing, as sketched in Figure1.3.
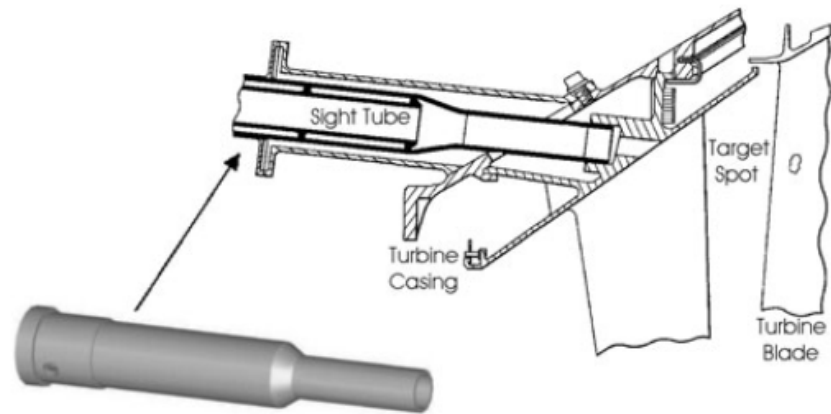
**Figure 1.3:** *Optical pyrometer installation (Kerr (2002a)).*

Data collected by radiation pyrometers have repeatedly prevented serious engine failures and can be used to set engine operating conditions based on the turbine entry temperature (TET) as a function of blade peak temperature (Sellers et al. (1989)).

In Figure 1.4 it is possible to observe a typical blade temperature monitoring map created by data collected by an optical pyrometer. When a blade is operating in overheated conditions this regular map pattern will show a spike in temperature.
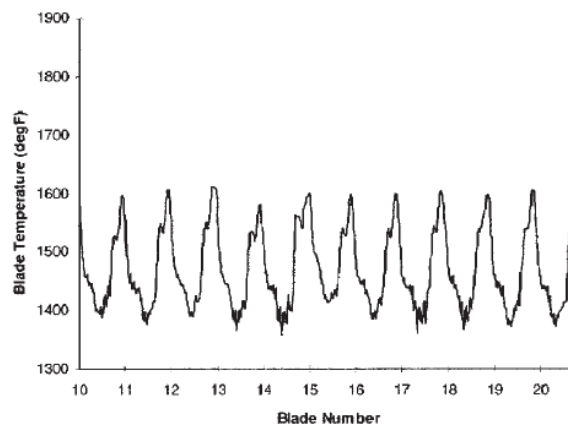


**Figure 1.4:** *Blade Temperature monitoring map (Kerr (2002a)).*

The accuracy of the pyrometer relies upon the assumption that the radiation, emitted by the turbine blades, is received without being previously masked or filtered. Nevertheless, the engine flow is laden with contaminants, like sands or metal particles, which could easily be deposited on the lens thus generating significant temperature reading errors. In order to address the fouling of the lens, the radiation pyrometer is equipped with a purge air system which uses relatively clean air, available in the engine, to keep the lens free from deposits. Over the years different

purge system configurations have been developed, nonetheless all of them belong to one of the following categories: air scrubbing, air curtains and still tube purge systems, Figure 1.5, (Kerr et Ivey (2002b)). In the air scrubbing arrangement, Figure 1.5a the air is directed over the lens to both discharge contaminants and to actively remove particles that could have been previously gravitationally deposited when the engines are shut down. Nevertheless, this configuration is efficient only if the purge air is sufficiently clean. In reality, the purge air is drawn from the compressor, and therefore it can be one of the main sources of contaminants. Consequently, in the second and in the third purge air systems categories, the contact between the lens and the purge air is avoided. This can be achieved by means of an air curtain, formed by positioning the air purge inlets forward of the lens, Figure 1.5b or through the insertion of a still tube, Figure 1.5c both aimed at creating a zone of still air in front of the lens.



(a)                                          (b)

(c)
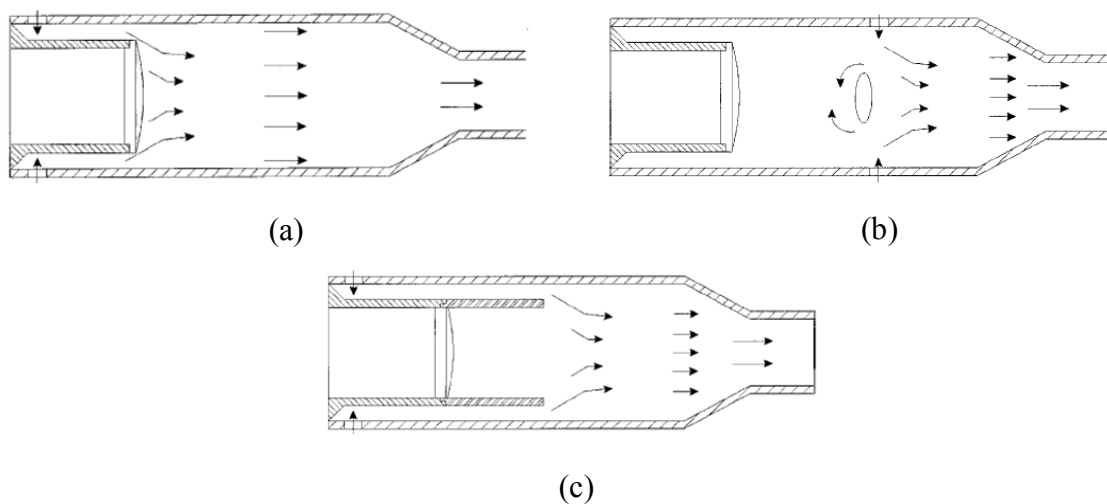
**Figure 1.5:** *Pyrometer purge system configurations (Kerr et Ivey (2002b)); (a) Air scrubbing (b) Air curtain (c) Still tube.*

Despite the many existing purge pyrometer designs, the lens fouling rate is nowadays still significant and consequently radiation pyrometers are mainly installed in military engines. In fact the high cost of maintenance, where the pyrometer is dissembled for cleaning procedures, makes the pyrometer installation frequently prohibitive for civil applications, hence leading to the use of less efficient devices.

A first step in designing a more efficient purge pyrometer system relies upon a deep understanding of the mechanisms involved in the lens fouling process. The only qualitative and quantitative study regarding the contaminants deposition on the lens can be found in Kerr (2002a). The author used computational fluid dynamics (CFD) to investigate the purge flow field and to predict the amount of contaminants deposition. Nevertheless, his study did not analyze in details the mechanism involved in the lens fouling.

## 1.2 Research Aim

The aim of the present research project is the clarification of the physical aspects behind the fouling of pyrometer lenses. This would allow the designer to exploit the findings of this research to produce an optimized purge system configuration.

The research aim is achieved through the following objectives:

- Survey of the current state of the art;

- Identification of the main features of the purge air flow;

- Identification of the contaminants deposition mechanisms;

- Analysis of the impacts of the system contaminants/lens for different velocities and temperatures;

- Delineation of a methodology to design a more efficient purge system configuration.

The objectives have been achieved through the implementation of the project methodology reported in the next paragraph.

## 1.3 Project Methodology

In order to gain a complete insight into the phenomenon of lens fouling phenomenon, three different techniques have been used.

They are:

- Numerical, using Computational Fluid Dynamics (CFD). This study was aimed at the analysis of the main features of a given purge air flow and at the contaminants trajectory and consequent deposition on the lens ;
- Numerical, using Finite Element Analysis (FEA). The main objective of this step was the analysis of the lens/contaminants impacts;
- Experimental, using the Stereoscopic Particle Image Velocimetry technique (SPIV). This analysis was targeted at evaluating the quality of CFD in predicting the main purge air flow characteristics.

Theoretical derivation using state of the art literature and information collected through the three previously listed techniques have been integrated to delineate the guidelines to be followed in order to optimize the pyrometer purge air configuration.

Figure 1.6 summarises the methodology used in the present research.
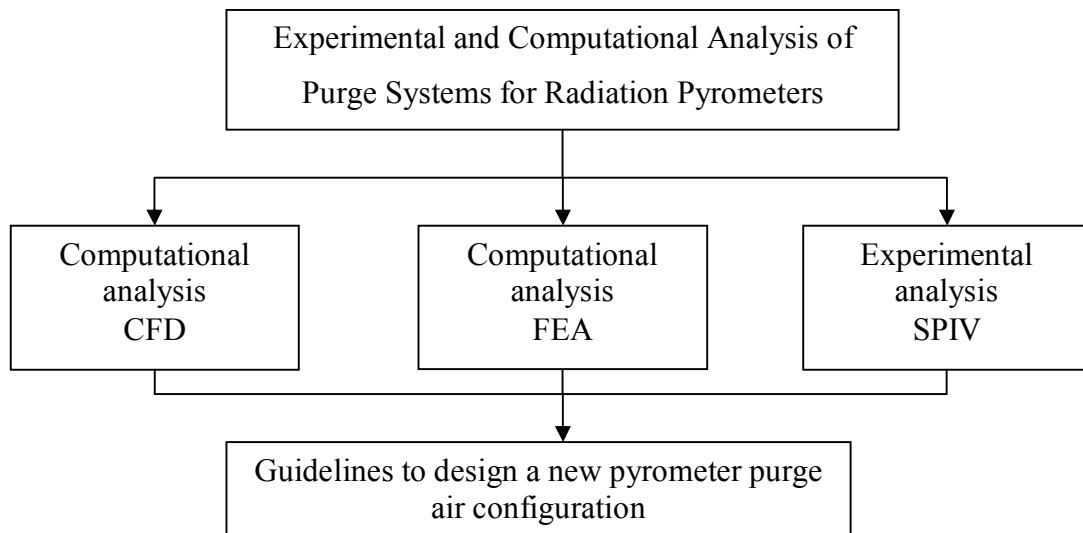


**Figure 1.6:** *Research methodology.*

## 1.4 Thesis Outline

The understanding of the principle of the pyrometer functioning is the first step in the delineation of the research problem area and it is reported in Chapter 2, together with a description of the currently available designs of the pyrometer purge air system. Furthermore, in this Chapter the work of Kerr (2002a) and its conclusions are summarised.

Chapter Three describes the experimental work which is primarily aimed at identifying the main flow features of the purge flow field and at evaluating CFD prediction capabilities. Subsequently the research is conducted investigating the particles deposition mechanisms by means of a CFD analysis using the multiphase theory principles. This is described in Chapter Four. The lens/contaminants collisions have then been studied by a FEA analysis reported in Chapter Five. All the research findings are discussed in Chapter six hence providing the guidelines to follow in designing a new pyrometer purge air configuration.

## 1.5 Conclusions

Radiation pyrometers could successfully substitute traditional devices in monitoring the blade temperatures (even if thermocouples will be continued to be used to take turbine gas temperature measurements). Nevertheless, their optical front-end, represented by the lens used to collect the radiation, is exposed to the harsh engine environment. The signal received by the lens can therefore easily be filtered by eventual contaminants deposited on the lens. Therefore, one of the pyrometer crucial components is represented by the purge system. The main idea at the base of its design, is the use of high speed clean air to discharge eventual contaminants, previously entrapped by the turbine flow, directed towards the lens. Nevertheless, the only available air in the engine has to be drawn from the compressor and consequently it contains small particles, like sand or engine erosion products. In open literature, the study conducted by Kerr was aimed at investigating quantitatively the contaminants deposition. Nevertheless, a clear explanation of the mechanisms involved in the lens fouling is not present and therefore nowadays there is not enough information available in the scientific world to re-design a more efficient purge

pyrometer system. Consequently this work is aimed at gaining at deeper understanding of the lens fouling process.

The project sponsor, Meggitt UK Ltd.has become involved in the project to further improve its understanding of the pyrometer purge system functioning.

# Chapter 2
# Literature Review

In this Chapter the problem area is delineated throughout a comprehensive literature review, which has been conducted as follows:

- Firstly, the pyrometer operational principles have been investigated, thus highlighting the necessity of designing an efficient purge pyrometer system.
- The state-of-the-art purge system configurations were subsequently analyzed, including also a detailed description of the existing patents.
- Kerr's study (2002a) is reported at the end of this Chapter. This is the only work available in the open literature where the contaminants deposition has been investigated both qualitatively and quantitatively.

The knowledge gaps that will be addressed in the next Chapters are summarized in the conclusions of the present literature survey.

## 2.1 Pyrometer Operational Principles

The pyrometer design is based upon the physical property of materials known as thermal agitation. The molecules and the atoms of any substance at a temperature above absolute zero vibrate and, as a consequence, emit energy in the form of electromagnetic waves. The rate of energy radiated per unit area increases with

temperature. On the strength of this principle, pyrometers are optical devices that allow the estimation of any body temperature by quantifying the energy radiated by it.

### 2.1.1 Fundamental Equations

In order to correlate the energy emitted by a specific body and its temperature it is necessary to introduce the following concept of a blackbody as: a perfect absorber that emits in each part of the spectrum the maximum energy obtainable per unit time from any radiator of equal area, depending only on the temperature value.

Consequently, a blackbody is also a perfect radiator. In fact, if all the energy is absorbed, neither reflected or transmitted, and if the body is in a thermal equilibrium state, then it has to emit the same amount of energy absorbed, otherwise its temperature would rise above, or fall below, that of the environment.

It is evident that in nature a perfect blackbody does not exist: it is possible to find only partial absorbers that, accordingly to their physical and thermal characteristics, reflect or transmit (or both) a part of the incident radiant energy and hence emit a fraction (called emittance) of that of a complete absorber. Emittance $\varepsilon_\lambda$ is defined as:

$$\varepsilon_\lambda = \frac{I_a(\lambda,T)}{I_B(\lambda,T)} \leq 1 \qquad (2.1)$$

Where $I_a$ and $I_b$ are the radiation intensities emitted by a non-blackbody and by a blackbody respectively, at a certain wavelength $\lambda$ and for a certain temperature $T$.

It is worth noting that usually the emittance does not depend only on temperature, composition, size, shape and surface condition of the body under consideration, but also on the band of wavelengths for which the fraction applies. A graybody is a body for which the emittance does not vary with the wavelength (Harrison (1960)).

The power intensity of the energy radiated by a blackbody is expressed by Planck's law as:

$$I(\lambda,T) = \frac{2\pi c^2 h}{\lambda^5 (e^{(hc/k^*\lambda T)} - 1)} \qquad (2.2)$$

Where $I$ is the power intensity, $h$ is the Planck's constant, $c$ is the speed of light and $k^*$ is the Boltzmann's constant.

If the pyrometer collects the body radiation at one specific wavelength then the body temperature can be calculated through Equation 2.2.

Otherwise, if the pyrometer receives a certain range of wavelengths then the Equation 2.2) should be integrated in that range. In detail, Stefan-Boltzmann's law (Equation 2.3) is used to calculate the power intensity $i$, when the pyrometer collects the entire wavelength spectrum:

$$i(T) = \int_\lambda I(\lambda,T)d\lambda = \sigma T^4 \qquad (2.3)$$

Where $\sigma$ is the Stefan-Boltzmann constant. For a non-blackbody the (2.2) and (2.3) equations should be corrected introducing the body emittance $\varepsilon_\lambda$, thus obtaining the following formulas:

$$I(\lambda,T) = \varepsilon_\lambda \frac{2\pi c^2 h}{\lambda^5 (e^{(hc/k^*\lambda T)} - 1)} \qquad (2.4)$$

$$i(T) = \int_\lambda \varepsilon_\lambda I(\lambda,T)d\lambda = \varepsilon_\lambda \sigma T^4 \qquad (2.5)$$

In this work, the pyrometer under consideration is installed inside the engine casing and receives infrared radiation from a target spot situated on a turbine blade surface. This spot has a typical diameter ranging from one to ten millimetres (Koeschel et al. (1986)). Furthermore, the turbine blades are generally safely approximated as grey bodies.

### 2.1.2 Pyrometer Design

The key elements in a pyrometer are:

- Optical system;
- Detector;
- Signal processor;
- Data acquisition system.
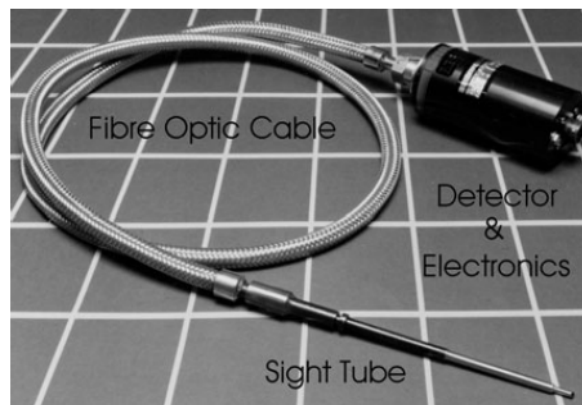


**Figure 2.1:** *Optical pyrometer components (Kerr et Ivey (2004a)).*

The optical system focuses the incoming radiation through a sapphire lens and subsequently sends it to a detector. The design of the lens is therefore a trade off between the structural requirement of standing high values of stress and temperature and the necessity of a good level of signal/noise ratio. The former requires that the penetration through the engine casing is as small as possible while the latter is necessary to obtain a good resolution of the temperature profiles. In theory to obtain a good level of signal/noise ratio the lens of the optical system should be as large as possible in order to collect the maximum energy from the target (Atkinson et Strange (1987)).

Furthermore, designing an optical system implies also the design of a deviation mirror, of a cooling mean for the probe along with its support, and of an air purge system to avoid fouling of the lens (Atkinson et Strange (1987)).

The detector/amplifier, being an electronic unit, is placed far from the harsh environment of the turbine where high temperatures and vibrations could jeopardize its correct functioning.

If it is assumed that the analogical to digital signal conversion is made without errors then the detector/amplifier unit establishes the accuracy of the pyrometer.

The detector design main requirements can be summarised in (Koeschel et al. (1986)):

- Maximum signal to noise ratio at the photo current conversion;
- Fast time response;
- Small linear and non linear distortions;
- Sufficient slew rate in order to exclude transient inter-modulations at high signal dynamics.

Usually, when the pyrometer is used to analyse the blade temperature then the detector is a silicon diode. In fact, this is fast enough to detect the temperature profile of the individual blades of the rotor and its spectral response is in a region where there is no interference caused by the constituents of the hot gas stream. Furthermore, its spectral response produces a voltage output that approximates to a tenth power function of temperature thus reducing the sensitivity of the measured output to eventual changes in the surface emittance.

The detector signal output is then pre-amplified, compressed and linearised by the high speed electronic equipments of the conditioning system, and finally sent to the data acquisition system that displays a readable temperature output, provided in terms of an average, average peak and maximum peak signal.

The average signal represents the arithmetic average of the rotor blades temperatures while the maximum peak signal is the temperature of the hottest blade. The average peak signal is used only when the pyrometer is focusing through the rotor blades, i.e. when this signal quantifies the radiation emitted by the alternating sequence of blades and background. In this situation the average temperature has no meaning and the average peak corresponds to the blade metal temperature.

### 2.1.3  Pyrometer Installation

The amount of radiation detected by the pyrometer depends on its field of view; thus a wrong positioning of the pyrometer in the turbine casing can eventually jeopardise the temperature reading accuracy.

A first guideline for the pyrometer installation can be found in Kirby's work (1986), where it is stated that to obtain accurate temperature measurements the pyrometer has to focus on the blades suction surface.

This observation agrees with Atkinson's et Strange's (1987) and Douglas's (1980) studies, which observed a maximum error of 50-100 K when the pyrometer collects radiation emitted by a spot situated on the first stage blade pressure surface. Even considering the worst case scenario when the pyrometer is focusing on the blade suction surface, the amount of radiation interference received is 1/30 of that detected when focusing on the blade pressure surface. This is due to the fact that the combustor flame radiation reflected by the suction surface is diluted in intensity by the view factor between this surface and the pressure surface of the adjacent blades (Kirby (1986)).

Obviously, the quantitative outcomes of these studies are dependent on the geometry of the turbine under study; nevertheless they have a general qualitative value. Therefore, if the temperature monitoring of the blade pressure surface is of interest, then it is necessary to introduce flame radiation correction methods (2.1.4.1).

### 2.1.4  Source of Reading Error

The main reading error sources can be summarized in:

- Reflected Radiation;
- Variation in Emittance;
- Non luminous gases;
- Lens fouling.

A brief description of these errors can be found in the following paragraphs.

### 2.1.4.1 Reflected Radiation

In modern aircraft engines characterised by short combustion chambers, high turbine inlet temperature and pressure, and by fuels with high flame luminosities, the reflected energy from the blade of the first stage can amount to 75% of that received by the pyrometer (Atkinson et Strange (1987), Kerr (2002a)), Figure2.2. This makes the pyrometer positioning in the turbine casing an important issue to be tackled (Section 2.3).
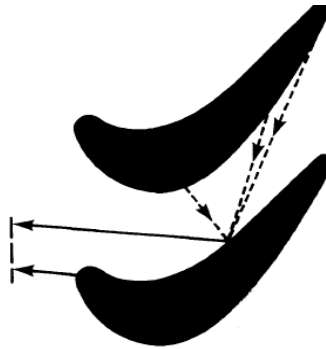


**Figure 2.2**: *Reflected radiation can amount to 75% of the radiation received by the pyrometer (Kerr et Ivey (2002b)).*

There are three main sources of reflected radiation (Kerr et Ivey (2002b)):

- Nozzle guide vanes;
- Combustor;
- Adjacent blades.

The combustor fireball produces most of the radiation present in the engine; this emission can be reflected by various blades towards the pyrometer. This phenomenon is particularly important when Thermal Barrier Coatings (TBCs) are used. In fact, even if TBC are more effective in protecting turbine blades from the aggressive gas

turbine environment than oxidized metals, they also have a higher reflectance and at elevated temperature they become transparent or translucent.

Nevertheless, when the reflected radiation is 50% or less of the pyrometer signal then the temperature reading can be corrected employing the Dual Spectral Area Pyrometer technique (DSAP). The DSAP is an algorithm for which it is possible to subtract the reflected component from the total radiative signal simply by measuring the energy emitted by the turbine blades in two different wavelength bands (Suarez et Przirembel (1990)).

This approach can be successful, even if it has to be assured that the magnitude of the reflected component does not overwhelm the blade surface emission. It is possible to obtain the spectral measurement of the reflection component using an additional spectral band, therefore using three signals in conjunction with an iterative algorithm to calculate and update the spectral ratio of the reflected component. Sufficient processing time would be available since the rate of change of the reflected component ratio is several times slower than the blade passing frequency.

In detail Suarez-Gonzalez (1987) states that the total output signal for the first band $E_u$ is the sum of the blade emission $E_{ub}$ and the reflected component $E_{ur}$ namely:

$$E_u = E_{ub} + E_{ur} \qquad (2.6)$$

Similarly the total output signal for the second band is:

$$E_f = E_{fb} + E_{fr} \qquad (2.7)$$

Where the total output signal for the second band $E_f$ is the sum of the blade emission $E_{fb}$ and the reflected component $E_{fr}$.

Combining these two signals a correction function can be found:

$$E_u - ( E_{ur} / E_{fr} )E_f = E_{ub} - (E_{ur}/E_{fr} )E_{fb} \qquad (2.8)$$

In Equation 2.8 the pyrometer input signal (left hand side), containing reflection and target emission terms, is related to terms linked only with the emission of the blade surface (right hand side). In this way it is possible to obtain a reflection-corrected blade temperature.

Nevertheless, Assadi et Strange (1987) asserts that the DSAP is valid only under the following hypotheses:

• The temperature of the source of the reflected energy is significantly higher than the temperature of the blade surface;

• The source of the reflected radiation and all reflecting surfaces are grey in nature;

• Only one source of reflected energy has an apparent temperature significantly higher than the surface temperature being measured (therefore in the presence of thermal barrier coating the DSAP is not valid);

• The reflection source temperature is constant with time.

### 2.1.4.2 Variation in Emittance

The correct pyrometer temperature reading relies on the knowledge of the target spot emittance. Therefore, any fluctuation in this value can introduce errors and jeopardise the correct operation of the pyrometer.

When the blades are made of super alloys, phenomena like erosion and oxidation can modify the emittance value. This change can be relevant as reported in Kerr's et Ivey's work (2002b) where it is stated that a high nickel alloy blade emittance can pass from an initial value of 0.7 at the beginning of its life to a final one in the range of 0.8-0.9. This value does not change indefinitely and a stable condition is reached when the oxide layer is thick enough to be opaque. Therefore, for a fully oxidised blade the assumption of grey body is sufficiently correct (Beynon (1981)).

Additional difficulties arise when thermal barrier coatings are used. In the first place, a new algorithm has to be implemented in order to identify the metal temperature knowing that of its coating. In fact, the main aim of the temperature reading is the condition monitoring not of the TBC but of the super alloy, the structural material carrying the load.

Furthermore, the thermal barrier coatings are transparent or translucent in the wavelengths suitable for pyrometer applications while they have high emittance in a band (8 -12 μm) where the pyrometer response is probably too low to be of any use (Atkinson et Strange (1988)). In fact low emittance is a synonym for low radiation level that can be easily masked by the reflected radiation (Section 2.1.4.1).

A different approach to tackling this issue can be found in De Lucia and Lanfranchi (1994) work where the authors developed a computer code able to calculate accurately and continuously the apparent emittance of the object under examination.

### 2.1.4.3 Non Luminous Gases

The turbine gas flow is a source of temperature errors, absorbing part of the radiation emitted by the blade or containing combustion products that cause a considerable number of emissions, reflections and scattering phenomena.

The unique characteristic of gas radiation allows the elimination of this kind of error. In fact, unlike the radiation of a solid or a liquid, which is distributed continuously with wavelength, the emission of a gas is essentially discontinuous and consists of a few narrow bands concentrated in specific wavelength intervals scattered over the infrared spectrum. Consequently, the solution to overcoming the measurement errors introduced by the non-luminous gases is to restrict the work wavelength range of the pyrometer to spectral regions, known as windows, in which the combustion products do not absorb or emit any radiation.

### 2.1.4.4 Lens Fouling

Fouling of the pyrometer lens is one of the major issues that have hindered pyrometer installation on civil engines. Contaminants deposited on the lens absorb part of the incoming radiation resulting in an under-estimated temperature reading. This can allow engine operation over the blade thermal resistance point, causing premature blades failures.

There are two main different sources of contaminants:

- Gas turbine. In this case particles such as soot, sand or metal can, under the influence of turbulence and unsteadiness, deviate from their main path-line and enter inside the sight tube of the pyrometer;

- Purge flow. In order to discourage gas turbine particles reaching the lens a purge system is installed around the pyrometer sight tube and high velocity flow is discharged into the turbine. The ideal solution would use clean dry nitrogen flow directed at high speed over the lens. Unfortunately, in an aero-engine, nitrogen gas is not available and therefore air drawn from the compressor is used instead. This arrangement complicates the design of the air purge system because compressor bleed air contains impurities which can contribute to lens contamination (Hayden et al. (1988)).

A first attempt to identify the contaminants composition and source can be found in Hayden et al. The authors categorise the particles in three different groups depending on their state of nucleation, accumulation or coarse mode:

- Particles in the nucleation mode (0.0005-0.1$\mu$m) are formed from the condensation of hot vapours during the combustion processes and from the nucleation of atmospheric species. They are usually too small to adversely affect the cleanliness of the lens;

- Particles in the accumulation mode (0.1-2.5$\mu$m) are formed by the coagulation of the particles in the nucleation mode and from the condensation of vapours

onto existing particles, causing them to grow into this size range. Usually, they are a considerable amount of the mass in a typical aerosol. Particles in the accumulation mode are the most difficult to remove in any aerosol system including a purge air system;

- Particles in the coarse mode (2.5-100μm) are usually ingested by the engine and come from the surrounding atmosphere, i.e. wind blown and volcanic dust and plant particles.

Therefore, the main conclusion of Hayden et al. is that most part of the particles has a natural source. In fact, it is sufficient to consider that the major components of the atmosphere are sulphate, ammonium, nitrate ions, lead and carbon containing material including soot and condensed organic matter; while the coarse fraction consists mainly of crystal material such as Fe, Ca and Si. The number or mass concentration of atmospheric aerosols depends largely on the altitude and the proximity to natural and man-made sources.

In addition to atmospheric aerosols, combustion aerosols from turbine engine exhaust may be ingested by the compressor while an aircraft is following another on the ground or when an engine is idling.

## 2.2 Pyrometer Purge System

The design of the pyrometer purge system plays a crucial role in guaranteeing a correct functioning of the device itself: contaminants deposited on the optics filter absorb the radiation emitted by the blade, masking the real metal temperature. In this way, temperatures exceeding the thermal resistance of the blade surface are permitted, thus jeopardising the turbine life (Sellers et al. (1989)).

### 2.2.1 Pyrometer Purge System Configurations

Different purge air systems have been developed over the last decades in the attempt to design a more efficient pyrometer and enable its use in civil aircraft engines.

Common features can be found in all configurations: the pyrometer is a result of the integration of a sight tube that holds the lens, and of a sleeve tube that surrounds the sight tube and has one or more openings into which the purge flow enters. In addition, usually the sleeve tube includes cylindrical and conical sections in order to produce a region that accelerates the purge air flow, discharging it at high speed into the turbine main flow (Hayden et al. (1988)).

The pyrometer is then installed in the turbine casing in a position sufficiently distant from the turbine flow and focusing on the blades through a passageway that goes from the exit of the pyrometer housing to the gas turbine stream.

Even if there are many configurations of the purge air system, all of them can be classified into three main categories: air scrubbing, air curtain and still tube (Kerr et Ivey (2002c)), shown in Figure 2.3.

(a)                                                           (b)

(c)
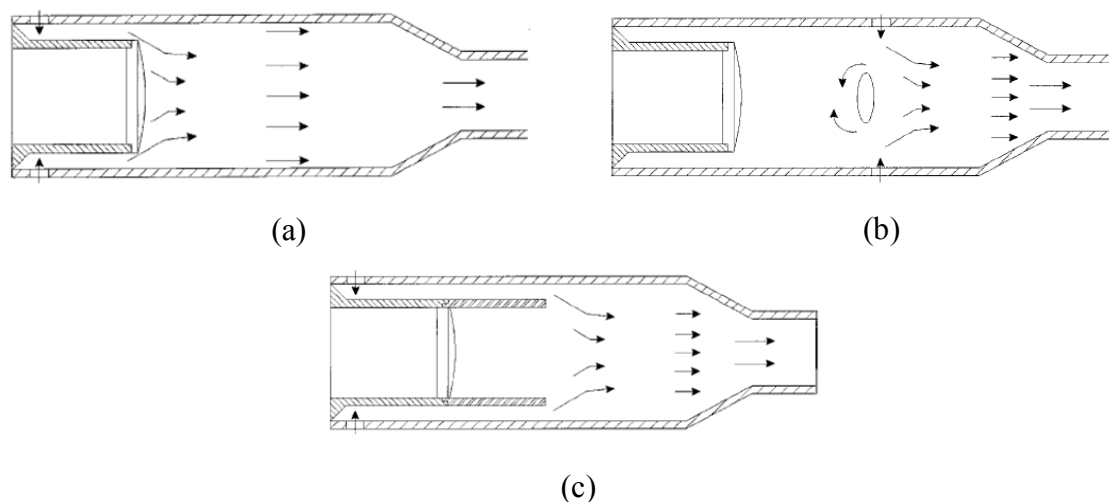
*Figure 2.3: Pyrometer purge air configurations (a) Air scrubbing) (b) Air curtain (c) still tube (Kerr et Ivey (2002c))*

### 2.2.1.1 Air Scrubbing Category

In the air scrubbing arrangement (Figure 2.3a) the compressor air is directed at high velocity over the lens thus removing ignition phase deposits produced during the engine start up, and preventing the contact between the contaminants contained in the turbine main flow and the lens (Berenblut et Masom (1982)).

In the air scrubbing system the main advantages can be summarised as (Hayden et al.(1988)):

- Continuous lens scrubbing during engine operation and start up;
- Removal of large particles which often settle on the optical lens surface by gravity when the sensor is installed in the lower quadrant of the engine.

While the disadvantages can be summed up as:

- Increment of the deposition likelihood of contaminants trapped in the compressor air due to their proximity to the lens;
- Impossibility of removing the submicron and large sticky particles deposited on the lens.

### 2.2.1.2 Air Curtain and Still Tube Categories

The air curtain system and the still tube configurations (Figure 2.3b-c) were developed in order to reduce the likelihood of having particles trapped in the purge flow deposited on the lens.

The basic concept behind these configurations is that the flow, instead of being directed towards the lens, is separated from it through a zone of still air. This is achieved either by adding to the purge flow system a still tube aimed at isolating the lens from any flow (Figure 2.3c) or by introducing the purge flow in a forward position with respect to the lens (Figure 2.3b). Even if the still tube configuration can be considered as a variant of the air curtain systems, in the present research it is treated as a different category due to the fact that their corresponding efficiencies are considerably different.

For the air curtain configuration the effectiveness of preventing particles entrapped in the turbine stream from reaching the pyrometer lens is the same for the air scrubbing one. Nevertheless, in this configuration the main advantage is the non-contact purge

air/lens. This reduces the possibility of lens contamination from compressor air supply particles (Hayden et al. (1988)).

The main drawbacks can be summed up as:

- Accumulation of contaminants in the dead air zone formed between the air curtain and the lens;
- Absence of a mechanism for removing contaminants apart from maintenance cleaning procedures;
- Particles deposition on the lens during engine idling operations without the possibility of removing these contaminants by air scrubbing action;
- Turbine gas penetration into the air curtain due to air stream instabilities with consequent contaminants entering the still air zone.

Using a computational code, Swithenbank (1986) found out that even if the jet flow protects the lens fairly well there is a large recirculation zone in front of the lens centre and an annular recirculation zone downstream of the purge slot. This recirculation zone in front of the lens centre is generally in the order of one fifth of the lens diameter, thus involving a remarkable increase in the probability of particles being deposited in this region.

A more efficient configuration can be achieved if the air curtain is obtained by the addition of a still tube (Kerr et Ivey (2002c)), as shown in Figure 2.3c, which can significantly reduce the intensity of the recirculation zone (Figure 2.4).



(a)                                                          (b)
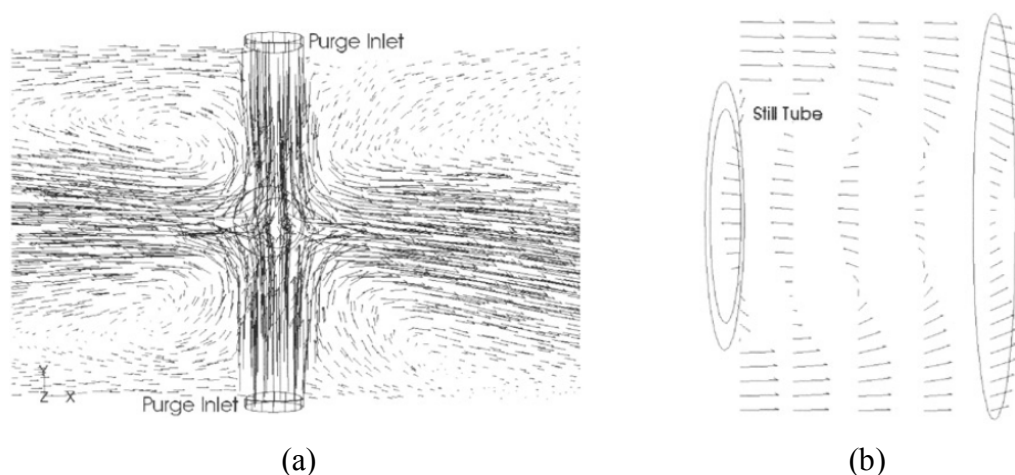
**Figure 2.4:** *Recirculation zone (a)Air curtain (b) Still tube. From Kerr et Ivey (2002c)*

During the 80s and 90s many patents aimed at maintaining clean the pyrometers lens have been registered ant they are described in the next section. Nevertheless, these configurations have proven to be unsuccessful in keeping the lens free from deposits long enough to allow the pyrometer installation on civil aircraft.

## 2.2.2 Patents

The pyrometer lens has to be maintained free from deposits in order to guarantee a correct reading of the blades temperature; to fulfil this requirement different purge air systems have been developed in the last decades and are described here.

In the past, the attention was focused separately on two different phenomena. Initially, it was only considered possible that the lens contamination was due to the action of particles present in the gas turbine that eventually were deviating from their main path going towards the pyrometer lens.

Only later it was understood that a second phenomenon can be predominant: most of the particles can be sourced directly from the purge system air drawn from the compressor flow. Consequently, nowadays it is necessary to use a purge air flow that both discourages the gas turbine particles to enter inside the pyrometer sight path and avoids the contact between the purge air and the lens.

A brief description of the most interesting patents found in literature follows:

### 2.2.2.1 Fluid Screens and Deflection System (Patent US 4306835 – Hurley (1981))

In this invention the attention is focused only on the particles carried by the gas turbine flow; the purge air drawn from the compressor is considered quite clean and therefore it is used to create a protective air curtain.

The fluid screens produced are two: the former is situated in front of the lens while the latter is at the exit of the sight tube.

The first air curtain is obtained forcing the air to pass through apertures in the sight tube nearby the lens; the axis of the holes forms an acute angle with the axis of the sight tube, developing a flow inclined ($\beta$ in Figure 2.5) at 50°-60° in respect to the longitudinal axis.

The portion of the flow that is not passing over the lens, flows in a channel, situated between the engine casing and the sight tube, and creates a second fluid screen exiting in proximity to a deflection system which is obtained extending a side of the sight tube inside the gas turbine flow, as reported in Figure 2.5.

The lip of the sight tube entering inside the turbine flow will deflect the hot gases reducing the likelihood that particles trapped in the gas turbine stream will be directed towards the lens.

(a)

(b)                                                (c)
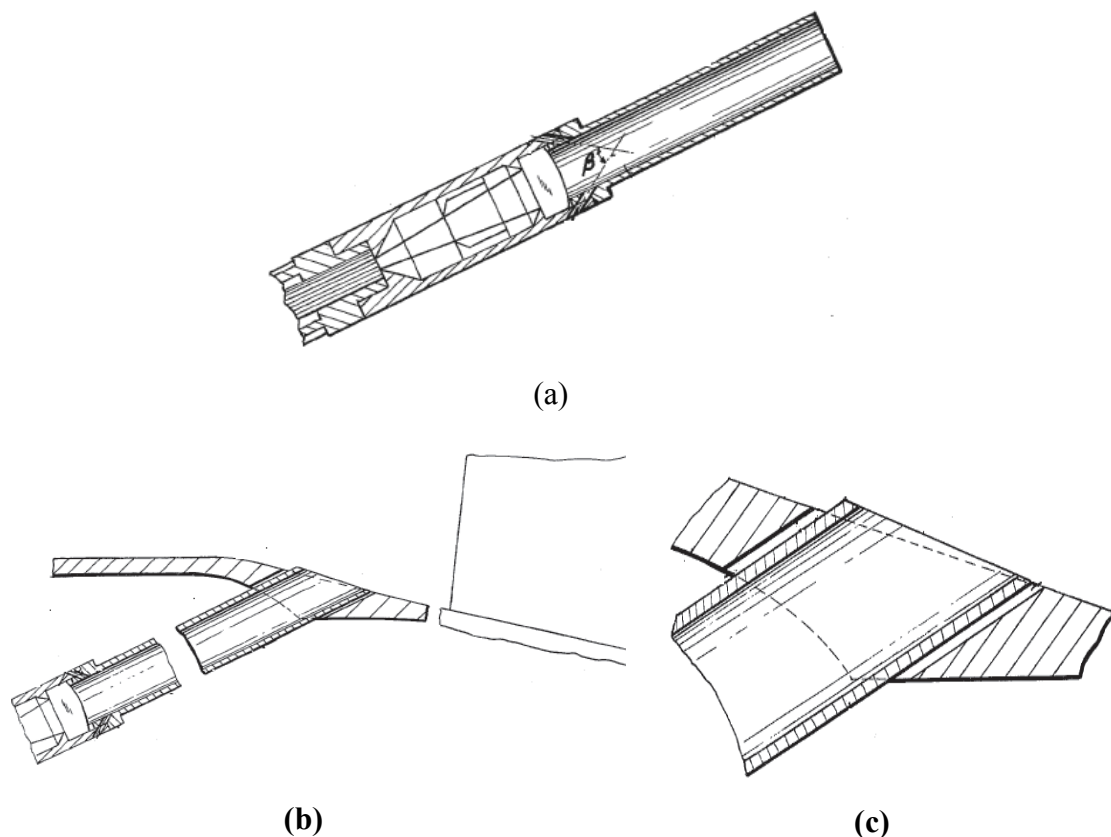
**Figure 2.5:** *(a) First fluid screen  (b) Second fluid screen created by extending the sight tube into the gas turbine flow (c) Detail showing the lip of the sight tube entering inside the turbine flow. From  Hurley (1981)*

## 2.2.2.2  Still Tube (Patent US 4650318 – Pointer et Masom (1987b))

If particles from the compressor are considered one of the main causes for the lens fouling, it is consequently necessary to avoid the contact between the purge air flow (that it is still important to discourage the gas turbine flow to enter inside the pyrometer) and the lens.

For this reason, in this patent, the lens is situated in the rear part of a still tube where, in theory, there is no flow. In reality, it was demonstrated that a recirculation zone, which develops at the still-tube outlet, can bring particles towards the lens.

In Figure 2.6 the dashed lines represent the compressor air that feeds the six holes, which are situated in the second part of the still tube.

The authors state that this expedient can ensure a positive flow from the rear area of the still tube towards the front: through a cross-section area reduction it is inducted in the forward part a pressure lower than that of the rear of the sight tube (where the diameter is larger), sweeping in this way gas away from the still tube.
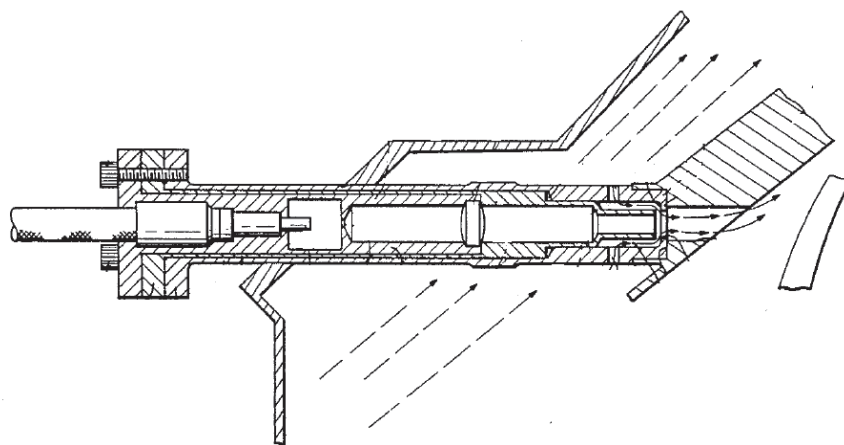


**Figure 2.6:** *Still tube configuration. From  Pointer et Masom (1987b)*

### 2.2.2.3 Three Lenses System (Patent US 4657385 – Pointer et Masom (1987a))

In this patent an alternative method is described of guaranteeing the correct reading of the blade temperature: while a purge air system is still present, a certain level of contaminants deposition is accepted. Essentially, thanks to a system composed of three lenses (Figure 2.7), it is possible to detect the level of contamination of the lens, and therefore to correct the temperature reading of the pyrometer.



(a)



(b)
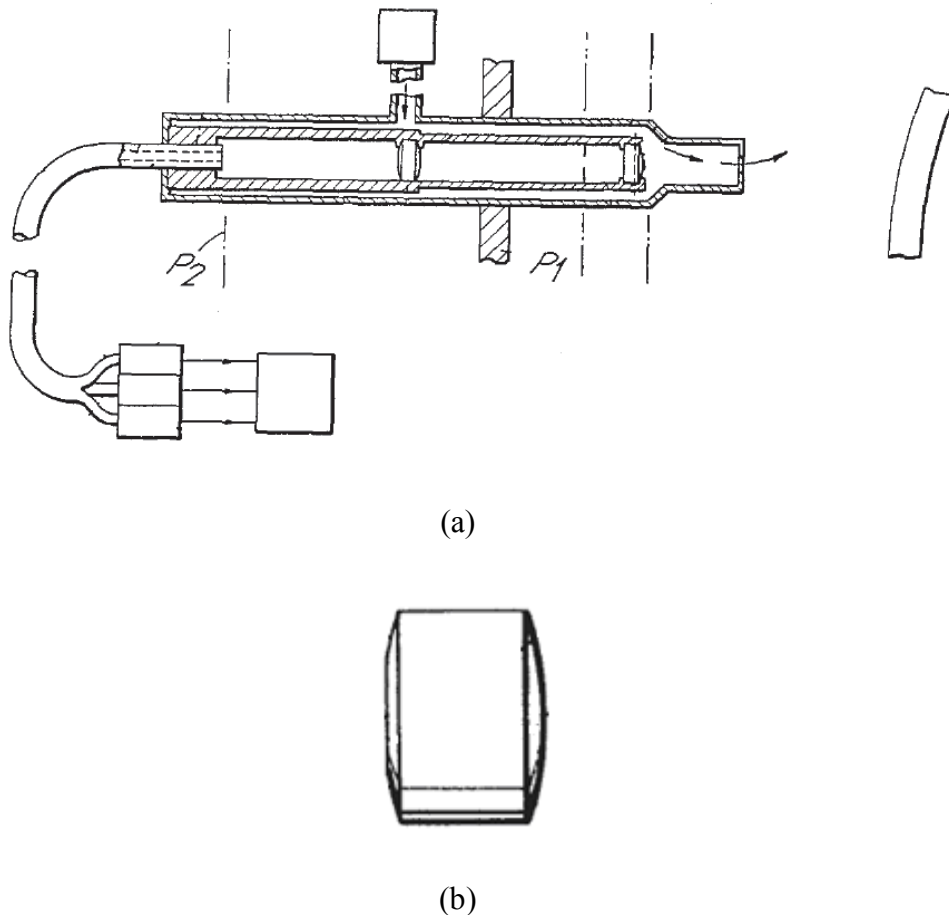
**Figure 2.7:** *(a) Still tube integrated with a three lenses system (b) Rear lenses assembly. From Pointer et Masom(1987a)*

The first lens is situated at the end of the sight tube and its focal plane is indicated in Figure 2.7 as P1.

Towards the back of P1 there is an assembly, formed by two surfaces acting as two lenses, as shown in Figure 2.7b. The front surface of the assembly is curved while the rear one has a central flat transverse region surrounded by a curved zone. Light passing through the flat central region will only be subjected to the converging effect of the front surface, while light passing through the outer annular region will experience an additional converging effect as a result of the curvature of the outer region.

The geometry of the system of three lenses, just described,  is such that the first lens and the outer region of the rear lens assembly forms an image of the blades, respectively at the plane P1 and P2, while the outer region of the central part of the rear lens forms an image of the first lens.

At the rear end of the lens tube, there is located the forward end of the fibre-optic cable. The cable has three fibre bundles, each of them receiving different information, as described in detail below.

To the front surface of the forward lens is secured a circular disc mask, which has a size such that its image, formed by the central region of the rear lens assembly, has approximately the same diameter as the central fibre bundle. In this way the image of the transparent part of the forward lens is focused solely on the outer fibre bundles.

A second mask is mounted in the first image plane P1. The mask has an annular form, with a central aperture characterized by a diameter which is such that, when visualised on the second image plane P2, the aperture has substantially the same size as the central bundle.

The use of these two masks ensures that the radiation from the sharp image of the blade is supplied only to the central bundle.

The radiation from the image of the front surface of the lens is supplied only to the two outer bundles, each bundle viewing half the forward lens surface.

The radiation passing trough the fouled lens produces different signals in the two outer bundles and by comparison of these two outputs the amount of the lens fouling can be estimated, and therefore it is possible to correct the temperature reading of the central bundle.

### 2.2.2.4 Swirling Purge Air Flow With Mask (Patent US 4738528 - Craft (1988))

In this design the purge air for cleaning the lens surface is introduced along the outer periphery of the lens. This results in swirling or vortex air that, directed spirally towards the lens, actively remove particles. The purge flow is considered appropriate for this purpose, and therefore clean.

The main drawback of this invention is that the flow, while it swirls toward the centre of the lens, becomes completely axial, and consequently develops a stagnation zone that can be the origin of particles deposition.

In detail, it is possible to distinguish two different zones on the lens: the first one, adjacent to the stagnation zone, in which the lens is coated by the contaminant particles, and a second one, near to the former, which is completely clean (Figure 2.8a). In order to avoid reading errors of the blades temperature, a mask blockage is used on the centre of the lens, blocking all the radiation passing through this zone (Figure 2.8b).

It is worthwhile noticing that while the mask mean and the contamination layer can block the same amount of radiation, the contamination layer also creates unwanted differential attenuation in various parts of the spectrum.

From Craft's estimations, the use of a mask does not jeopardise the efficiency of the pyrometer, in fact:

- A mask with a diameter equal to two tenths of the lens diameter blocks only 4% of the light flux;

- A mask with a diameter equal to three tenths of the lens diameter blocks only 10% of the light flux.



(a)

(b)                                    (c)
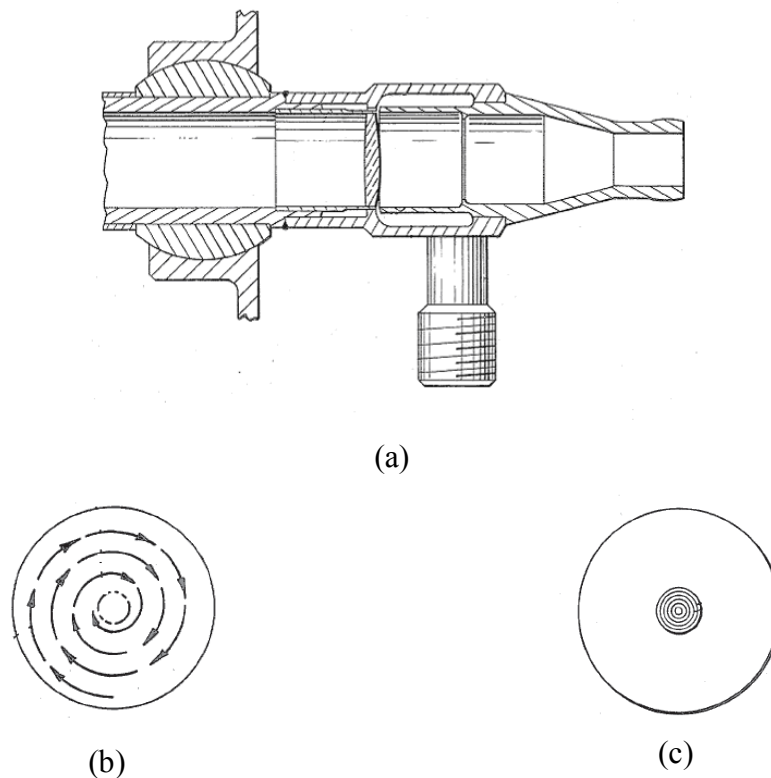
**Figure 2.8:** *(a) Swirling purge air configuration (b) Swirling flow in front of the lens with a stagnation zone in the middle (c) Mask. From Craft (1988)*

### 2.2.2.5  Filter, Swirling Flow and Deflection System (Patent US 4934137 – Mackay (1990))

The peculiarity of this patent is the employment of a combination of different arrangements in order to prevent the deposition of particles on the lens surface. The innovation is introduced by the creation of a swirling flow, used to avoid the formation of a centrally converging jet within that portion of the plenum between the lens and the aperture.

In fact, the presence of a converging flow would create areas of relatively stagnant air in which particulates could accumulate.

The purging air passes through a filter that separates the particles with a diameter equal or greater then two microns, before flowing along the external surface of the sight tube, where circumferentially, a swirl component (made up of an alternate series of crenels and merlons) is installed, as reported in Figure 2.9.

A converging section is situated just before the lens and acts as a ramp (approximately parallel to the lens) that accelerates the swirling flow, ensuring an effective scrubbing action.

The last expedient is the creation of a surface, obtained by rounding the rim of the inward-facing surface of the shroud, as reported in Figure 2.10, able to deflect contaminants present in the gas turbine flow that otherwise might enter into the sight tube.
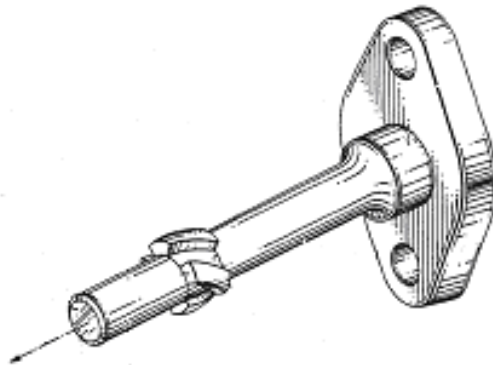
**Figure 2.9:** *Swirling device composed by merlons. From Mackay (1990)*

(a)

(b)
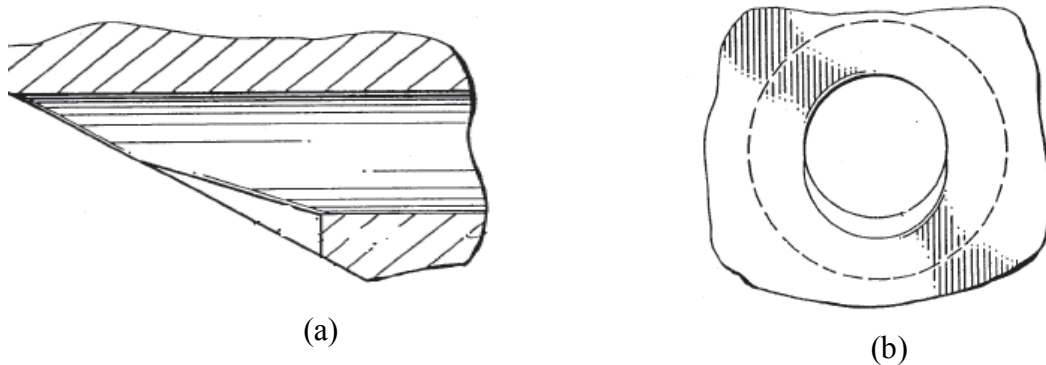
**Figure 2.10:** *(a) Deflection system, side view (b) Deflection system, front view. From Mackay (1990)*

### 2.2.2.6 Inertial Separation Mean and Symmetric Scrubbing Flow
### (Patent US 4786188 – Myhre et Miller (1988))

In this patent the scrubbing action of the purge flow is considered a mandatory requirement and, to use a clean flow, parts of the contaminants are removed from the air drawn from the compressor. The scrubbing action is obtained forcing the flow to pass through openings symmetrically distributed around the lens (Figure 2.11).
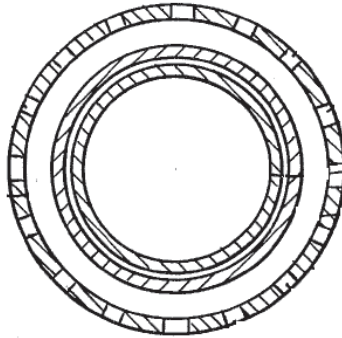


**Figure 2.11:** *Symmetrical openings. From Myhre et Miller (1988)*
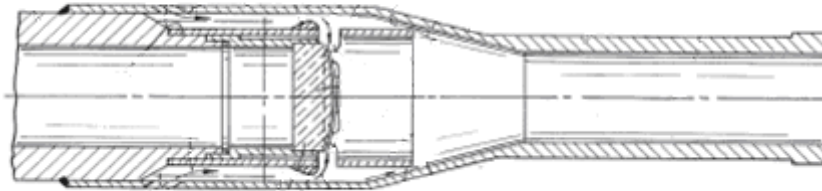


**Figure 2.12:** *Abrupt deviation imposed to the flow to cause separation. From Myhre et Miller (1988)*

The cleaning action is performed by exploiting the inertia law; in Figure 2.12 it is possible to note the abrupt change of direction imposed to the flow. The heavier particles, such as those larger than a few microns, are not able to follow the change of direction and therefore they are separated from the main flow.

The partially cleaned flow scrubs the lens and should be able to re-entrain eventual contaminants deposited on the surface.

Myhre et Miller state that sub micron particles are removed with difficulty if they are already deposited, anyway this does not jeopardise the operation because very small particles don't have enough inertia momentum to penetrate the boundary layer and reach the lens surface.

### 2.2.2.7 Inertial Separation Mean and Asymmetric Scrubbing Flow I (Patent US 4836689 - O'Brien et Myhre (1989))

In this invention an inertial separation is combined with an asymmetrical flow, respectively, to clean the purge air flow and to avoid the presence of stagnation zones in front of the lens, where particles can be deposited, Figure 2.13.
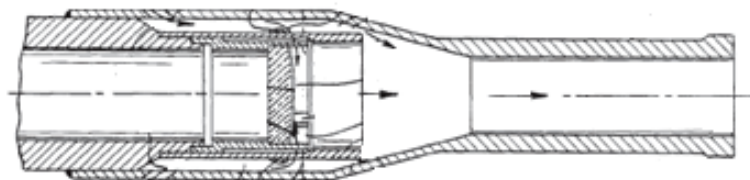


**Figure 2.13:** *Inertial separation configuration. From O'Brien et Myhre (1989)*

In the patent US 4786188 (Figure 2.11) the openings are uniformly distributed in space, and as a result the flows are balanced and when they merge (in correspondence with the centre of the lens) a central stagnation region is created.

In this patent the inertial separation expedient is the same as that reported in the patent US 4786188, with the difference that in this design there is a non-uniform disposition of the openings (obtained by inserting disrupting bars) to guarantee asymmetrical flows (Figure 2.14). In this way, the scrubbing action is not jeopardised, since in front of the lens the flow is shifting and turbulent rather than stagnant.

**Figure 2.14:** *Asymmetrical distribution of the openings. From O'Brien et Myhre (1989)*

A further asymmetry can be obtained by using openings with different diameters thus ensuring the presence of flows with different velocities.

### 2.2.2.8 Inertial Separation Mean and Asymmetric Scrubbing Flow II (Patent US 5146244 – Myhre et al. (1992))

With this invention slight modifications are performed in the Patents US 4836689, where the recirculation zones were still present, with bubbles formed on the adjacent lens and on the side of the disrupting bars where particles will tend to accumulate. The inertial separation is still present and the idea of having an asymmetrical scrubbing flow is not abandoned, but the obstructions are eliminated as being recognised as the cause of dead air zones. A helical surface, such as a spring, obtained by machining or deforming the surface, is circumferentially deployed around the sight tube, obstructing only in part the flow passage (Figure 2.15).

The air, passing in the external part of the sight tube, creates:

- An axial flow around the outside of the helix;
- A helical flow due to the passage of the air inside the coils of the spring.

Thanks to the flow structure just described, in which the flow has a tangential velocity component, stagnation zones on the lens surface are only momentary, their position shifts continuously in the time, thus eliminating any dead spots or other low speed flow areas that cause the accumulation of particles .

In a second variant of the invention the spring is not present and the end surface of the tube in front of the lens is inclined with respect to the axis of the sight tube. In this way the slot or gap created, in which the flow has to pass, is wider at the top and narrower at the bottom. This configuration causes an asymmetric flow that will tend to shift laterally across the lens (Figure 2.16 ).
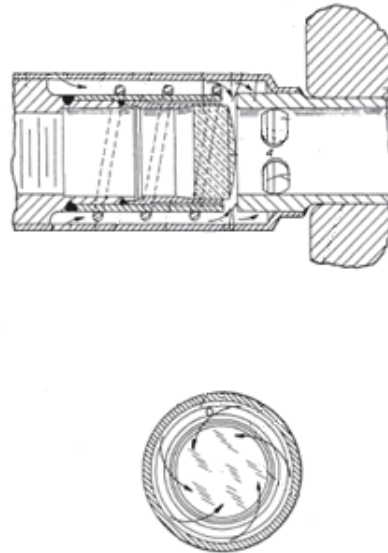
**Figure 2.15:** *Inertial separation system. Asymmetrical flow created by means of a spring. From Myhre et al. (1992)*
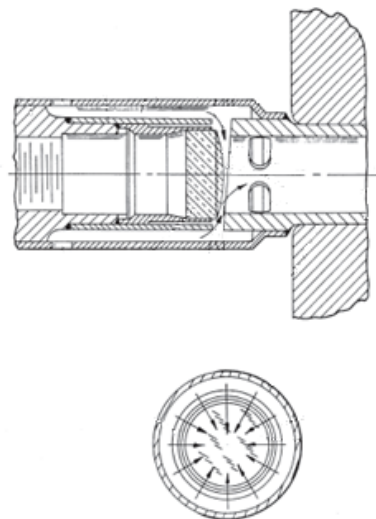
**Figure 2.16:** *Inertial separation system.  Asymmetrical flow created by means of gaps of different size positioned  at the top and at the bottom of the lens. From Myhre (1992)*

### 2.2.2.9 Spiralling Flow (Patent US 4784491 – Penney et Lund (1988))

The main feature of this design is the presence of a swirling flow aimed at diverting incoming particles toward the channel walls, which are for this reason grooved (Figure 2.17).

A window mount, situated in front of the lens, has four equally spaced peripheral openings to allow the passage of air to a gas nozzle, which has in the upper part four equally spaced tangential slots exiting into a central tapered tube. The gas nozzle is held against the lower surface of a window which encloses the tangential gas channels (Figure 2.17). A spiral motion is imparted to the gas as it flows at high velocity through these tangential channels, swirling down the central exhaust into the sight tube.

The wall of the sight tube has relatively deep grooves, preferably screw threads, pitched in the direction of the gas motion as it swirls toward the opening. Moving particles, smoke and debris, such as are generated by an industrial process, are turned toward the grooved wall and prevented from depositing on the optics (in the central area), maintaining good light transmission.



(a)                          (b)
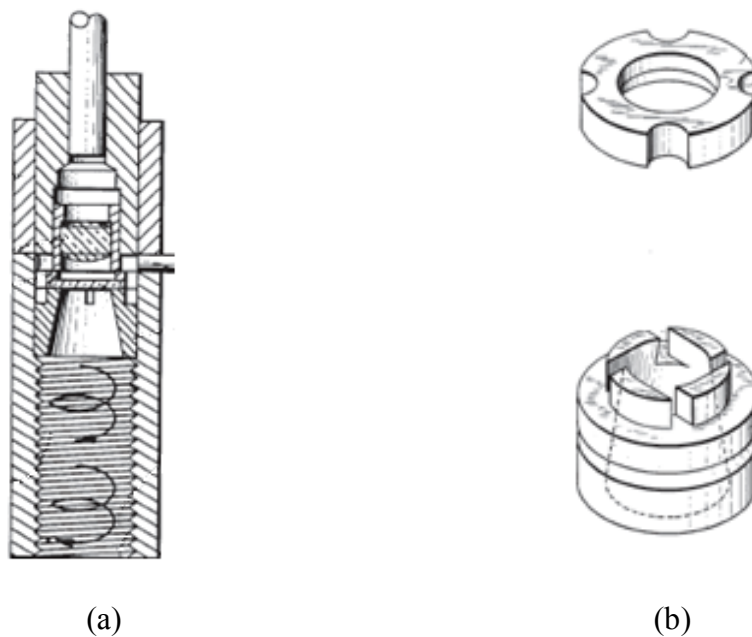
**Figure 2.17:** *(a) Spiraling flow system with grooved walls (b) Mount and nozzle. From Penney et Lund (1988)*

### 2.2.2.10    Still Tube With a Reducing Swirl System I  (Patent US 5599105 – Ridley et Fearnehough (1997))

In this patent for the first time a still tube has been introduced. Its presence is aimed in avoiding contact between the lens and the purge flow while the configuration should prevent the formation of a recirculation zone at the outlet of the still tube.

At least two axially spaced chambers are positioned about the purge tube, each pair of chambers being linked by a respective restrictive opening such that a difference in pressure exists between the adjacent chambers in use.



(a)                                                              (b)
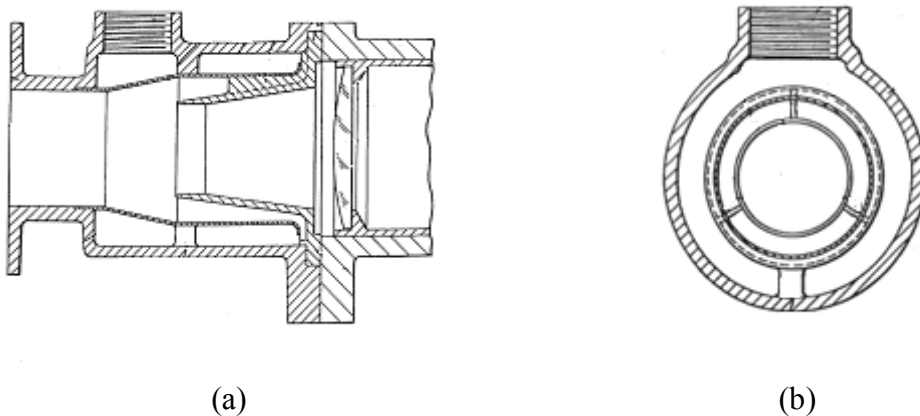
**Figure 2.18:** *(a) Reducing swirl system. Side view - Patent US 5599105 (b) Reducing swirl system. Front view. From Ridley et Fearnehough (1997)*

The upstream chamber is connected to the source of the purge air while the downstream chamber feeds the air in the purge tube. This configuration originates a swirling flow, around the purge tube, characterized by a non uniform velocity distribution.

To attenuate this flow field a swirl reducing system is utilized (Figure 2.18), and is composed of:

•        Vanes, that extend more than halfway along the length of the still tube, allowing a final straightening of the flow, and removing swirls;

•        Tapering of the still tube;

•        A sharp lip installed at the end of the still tube.

### 2.2.2.11    Still Tube With a Reducing Swirl System II  (Patent US 5421652 – Kast et Prasad (1995))

The principle at the base of this invention is the same as the Patent US 5599105 (the use of a still tube with a reducing swirl system) but in this case the swirl reducing system is obtained through the installation of a pair of diffusers positioned midway along the sight tube and at its tip (Figure 2.19).
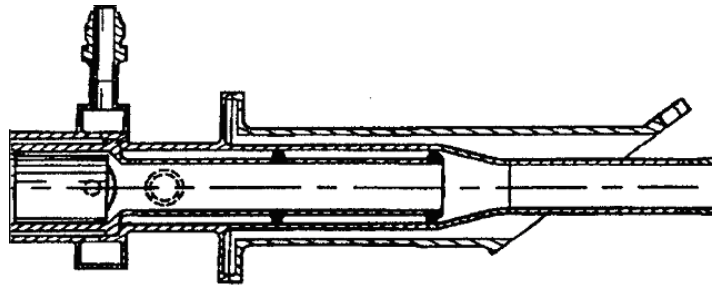
**Figure 2.19:** *Reducing swirl system obtained by the utilise of diffusers. From Kast (1995)*

## 2.3 Kerr's Analysis

A first insight regarding the flow physic regulating the flow streaming along the pyrometer purge system can be found in Kerr (2002a). Through a numerical simulation the author analyses the curtain purge air system mounted in the civil aero-engine GE90 of the Boeing 777.

The pyrometer under study employs the still tube configuration.
The purge tube is circular in shape and has only one inlet in which the purge air flow is fed. Subsequently, the purge flow swirls around the annular spacing between the purge sleeve and the still tube with the development of a non-uniform velocity field (Figure 2.20).

An air straightening component is installed around the still tube (Figure 2.20) and it is made up of a pair of diffuser rings: one positioned midway along the sight tube and the other at its tip. The diffuser ring is essentially a perforated plate forming a partial

blockage in the flow cross-section, creating higher backpressure, which tends to even out flow asymmetries.

For the purge air system under investigation, the diffuser rings consist of eight fins, with each ring blocking approximately 50% of the flow cross-section.



(a)                                          (b)
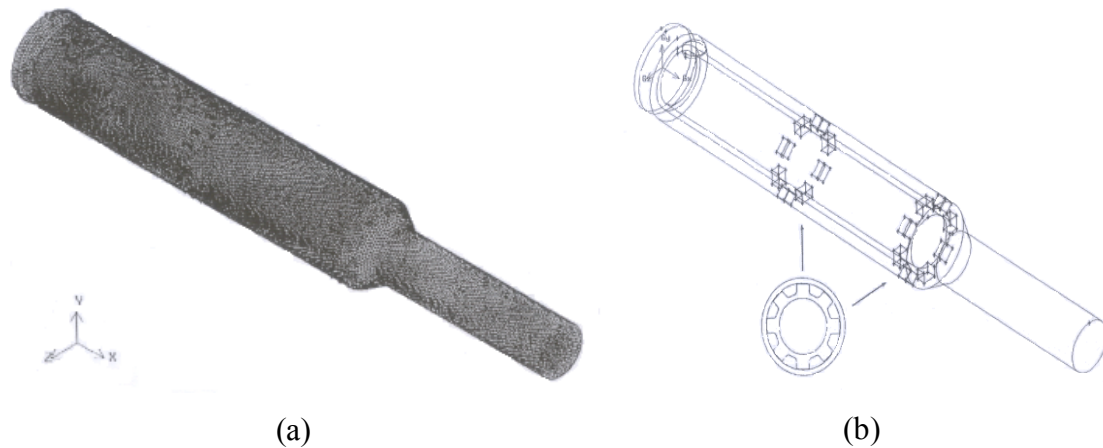
**Figure 2.20:** *Model of the GE90 pyrometer (b) GE90 pyrometer, diffuser rings (Kerr (2002a)).*

The purge air of the pyrometer installed in the Turbo-Union RB199 aero-engine which powers the Tornado aircraft is described in another of Kerr's et Ivey's work (2003), Figure 2.21. Also in this case the air curtain is created by means of a still tube. However the configuration is more compact in order to comply with the stricter military engine requirements.

The purge air is fed from a plenum surrounding the purge sleeve through two rows of six inlets.



(a)                                          (b)
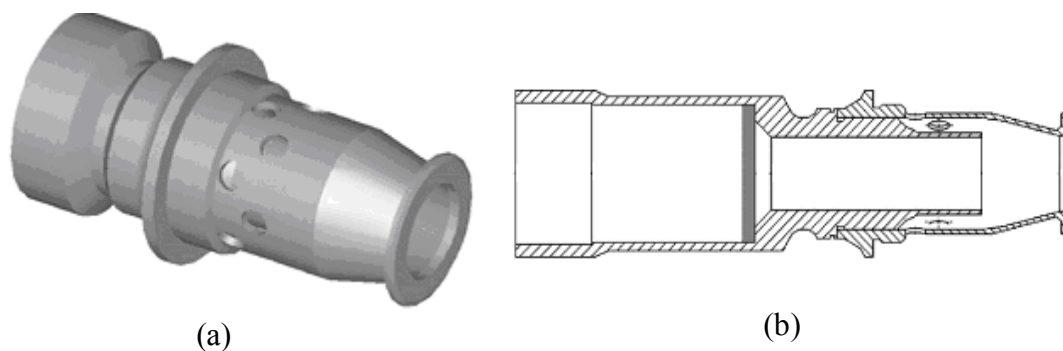
**Figure 2.21:** *(a) RB199 pyrometer model (b) RB199 pyrometer model (Kerr et Ivey (2003)).*

Despite the different configurations of the GE90 and the RB199 purge flow system the velocity flow field main feature is the same: a recirculation zone situated in front of the still tube (Figure 2.22) can transport particles trapped in the purge air flow towards the lens.

From the CFD analysis of these two pyrometers Kerr (2002a) states that the main parameter governing the contaminants deposition is the Purge Pressure Ratio (PPR) defined as:

$$Purge\ \Pr essure\ Ratio = \frac{\Pr essure\ at\ purge\ inlet}{\Pr essure\ at\ purge\ outlet} \qquad (2.9)$$

In order to decrease the percentage of particles that can reach the lens the PPR has to be as high as possible. In fact, the higher the PPR is, the higher the capacity of the purge air system to redirect big particles that are coming from the turbine and that are penetrating the sight tube.

Additionally, considering the recirculation zone forming in front of the still tube, a higher PPR means that the small particles coming from the compressor will not be captured by the swirl, avoiding therefore further particle deposition on the lens. It has to be noted that Kerr and Ivey (2002d) reached the conclusion that the swirling flow forming at the mouth of the still tube is the main flow main characteristic in the particle deposition mechanism.



(a)                                                              (b)
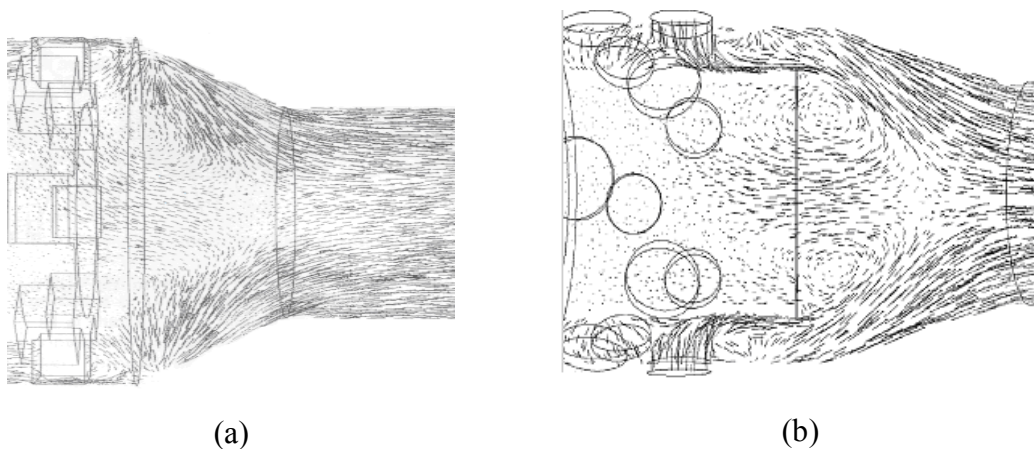
**Figure 2.22**: (a) Recirculation zone at the GE90 pyrometer outlet, Kerr et Ivey (2004b) (b) Recirculation zone at the RB199 pyrometer outlet, Kerr et Ivey (2003).

### 2.3.1  Analysis for the GE90

Kerr's computational fluid dynamic conclusions are (Figure 2.23):

- The level of deposition of contaminants coming from the purge airflow reach a constant and maximum value for particles having a diameter smaller than 0.05 $\mu$m: 6.25% at cruise speed and 5.35% at maximum thrust;

- The level of deposition of particles coming from the purge airflow and with a diameter in the transition region (0.05-1.5 $\mu$m) decrease increasing the diameter. The shape of the curve seems to follow a sigmoid curve (S shape). In detail, particles with a diameter greater than 1.5 $\mu$m have a negligible effect on lens fouling since such particles have a high momentum and therefore do not swirl around the core of the still tube ;

- The level of deposition is negligible for particles coming from the turbine and with a diameter less than 100$\mu$m and an initial velocity less than 100m/s at cruise speed These contaminants are completely redirected back out of the pyrometer sight tube;

- The turbine deposition curve shows a transition region regarding particles with the particles' ability to reach the lens increasing with the diameter;

- All the turbine contaminants with a diameter and an initial velocity over a specified value have a high degree of momentum thanks to which they can penetrate the purge air flow and impact on the lens (Figure 2.23).
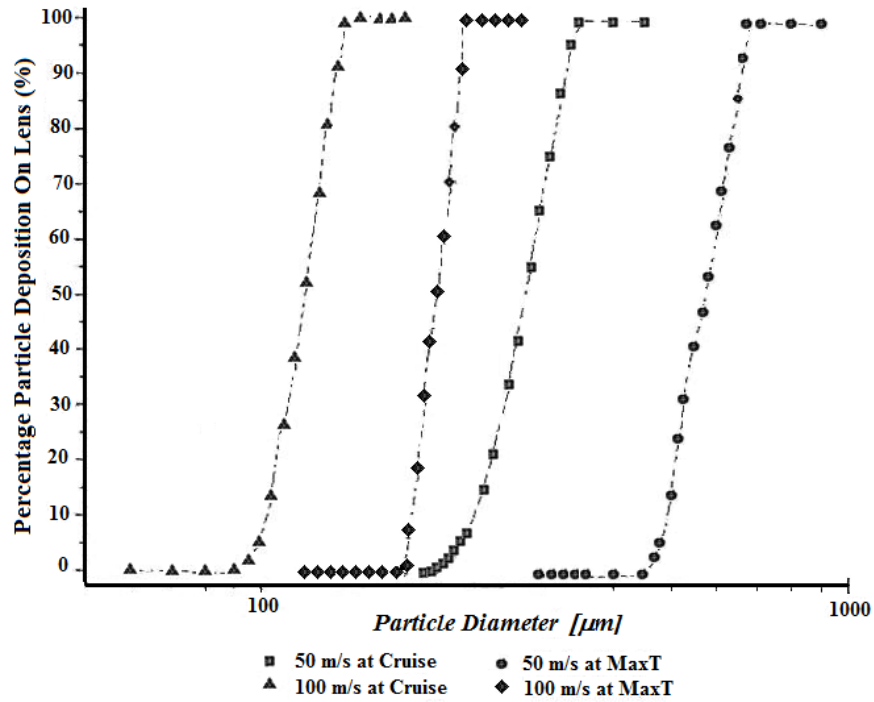
(a)
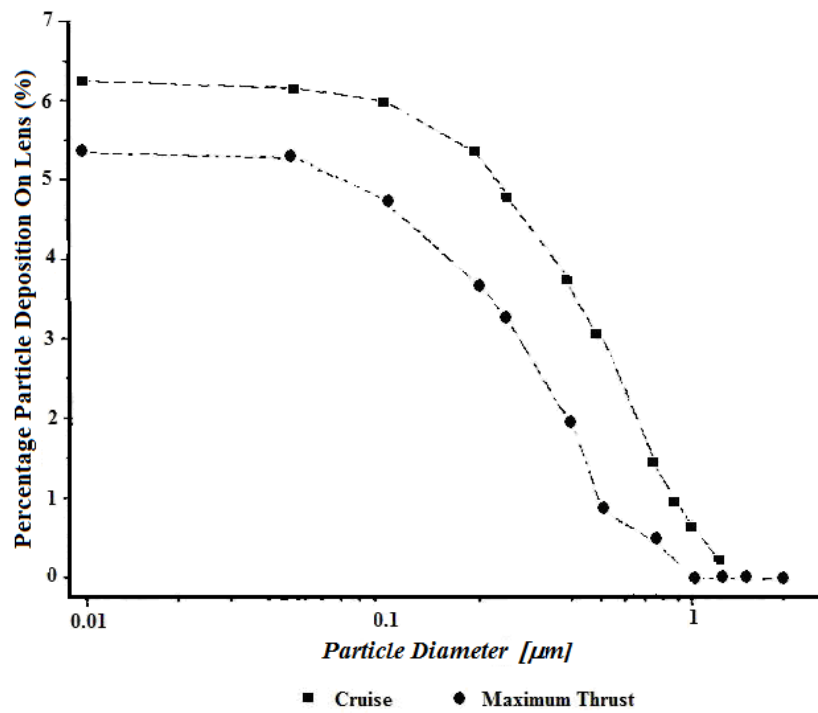


(b)

**Figure 2.23:** *(a) Level of deposition of contaminants escaped from the gas turbine flow (GE90 pyrometer) (b) Level of deposition of contaminants contained in the purge air (GE90 pyrometer).*

### 2.3.2 Analysis for the RB199

The qualitative conclusions reached by Kerr et Ivey (2003) for the RB199 pyrometer are the same as reported for the GE90 pyrometer. Nevertheless, a quantitative analysis shows that the level of deposition is higher for the military pyrometer, probably due to the shorter length of its still tube.

In detail, the constant level of deposition of contaminants trapped in the compressor air is approximately 10.5% at cruise and 8.5% at maximum thrust for particles having a diameter smaller than 0.1 μm (Figure 2.24b).

Particles coming from the turbine, with an initial velocity of 50 m/s and a diameter of 300μm have enough inertia to completely penetrate the purge air system and impact on the lens (Figure 2.24b).
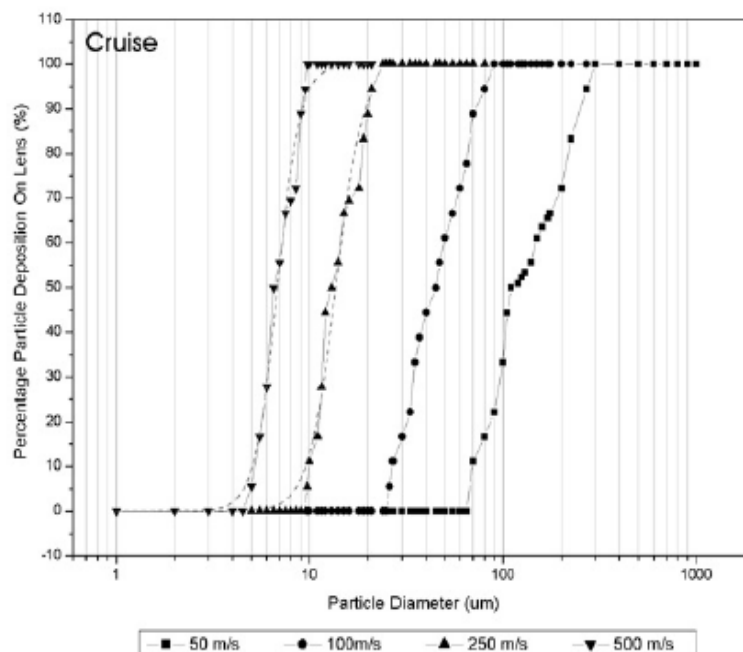


(a)
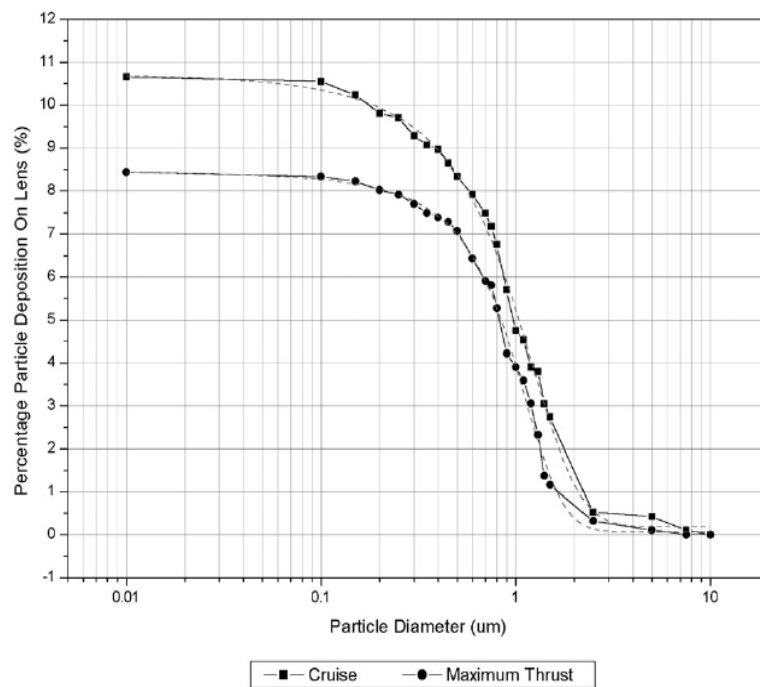
(b)

**Figure 2.24:** *(a) Level of deposition of contaminants escaped from the gas turbine flow (RB199 pyrometer) (b) Level of deposition of contaminants contained in the purge air ( RB199 pyrometer).*

## 2.4 Conclusions

In civil aircraft the monitoring of blade temperature is largely performed by means of traditional devices such as thermocouples. Nevertheless, the presence of drawbacks, like the impossibility of taking measurements in critical spots, has made the designer look for alternative solutions. The pyrometer is a contactless optical device characterised by a reading fast response, which would allow overcoming the disadvantages of traditional devices. Nonetheless, its employment requires keeping the lens free from contaminants deposits. Many patents have been registered during the 80's and 90's seeking to tackle this problem. However, these configurations have been not successful in keeping the lens clean for a time slot long enough to not involve prohibitive maintenance costs. Previous efforts were aimed at evaluating the level of deposition of contaminants of two purge pyrometers configurations that are nowadays employed in two different engines. It reached the conclusion that the pressure ratio between the pyrometer purge system inlet and outlet is the main

parameter governing the deposition of contaminants. Nevertheless, the mechanisms involved in the deposition are still unclear and therefore in the next Sections a detailed analysis of the purge flow and of the contaminants depositions phenomena are examined.

# Chapter 3
# Experimental Study

## 3.1 Introduction

A deep understanding of the physics governing the purge air flow relies upon the validity of the CFD results presented in Chapter 4 that are the base of the general theoretical principles controlling the contaminants deposition phenomenon. Consequently, the experimental study presented in this work seeks to provide validation of the CFD predictions of the pyrometer purge system main flow structures.

Given the reduced dimensions of the pyrometer purge system, it is not possible to gain the appropriate optical access to take flow measurements. One expedient to deal with this problem is by scaling up the pyrometer purge system and having relevant objects of the model geometry in glass. Nevertheless, in this case it is necessary to ensure an effective use of suitable optical techniques through curved glass surfaces. In fact, this configuration introduces high levels of reflections and distortions that could jeopardize the experiment outcome.

Consequently, in order to tackle the reflections issue the experimental work presented in this research has been subdivided into two different steps:

- A feasibility study experiment;
- A large scale model of the pyrometer purge system.

This Chapter is divided into three main sections. The first part describes both the particle image velocimetry (PIV) principles and the main features in common between the two experiments listed above. The second and the third part describe the main inherent characteristics of the preliminary and large scale experiments, respectively.

## 3.2 PIV principles and common features of the two experiments

LaVision PIV system and DaVis software have been used for both experiments. The PIV principles and the main features in common between the two experiments are described in the next paragraphs.

### 3.2.1 Two Dimensional PIV

The optical technique known as Particle Image Velocimetry (PIV) has been selected in this work as the adequate optical method to experimentally analyze the flow field of the pyrometer purge air system. The PIV technique has the significant advantage, over Laser Doppler Anemometry (LDA) and other probe methods, to perform measurements of the flow velocity field over a plane section rather than in a single point. A basic PIV configuration is illustrated in Figure 3. 1.
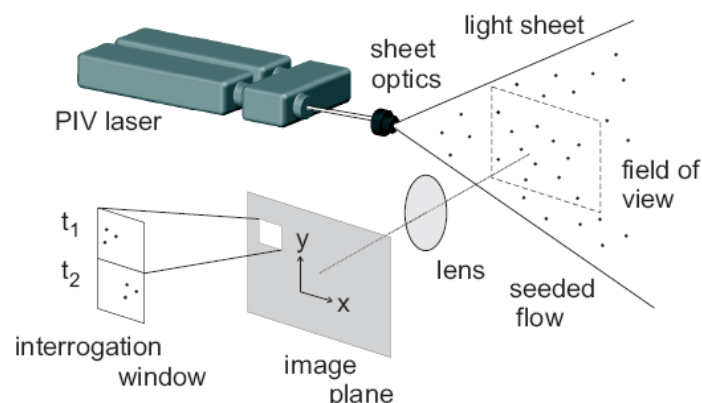


**Figure 3. 1:** *PIV Configuration (DaVis 7.2 Software Manual (2009a)).*

A laser beam is converted into a planar sheet of light while one or more cameras are positioned in a specific frame to acquire images of the illuminated plane section. At

least two images are recorded, separated by an appropriate time interval. The PIV recordings are then divided into small subareas, called interrogation windows, in which it is assumed that all the particles have the same velocity. In other words, it is hypothesized that, during the time interval between the two recorded images, all the particles within the same interrogation window have moved of the same displacement. The evaluation of this displacement together with the knowledge of the time interval allows computing the velocity vector corresponding to every subarea.

Each interrogation cell contains a certain number of pixels, and a value representative of the intensity of received light is associated to each pixel. An appropriate light intensity threshold establishes whether a particle is present in that pixel. Therefore, to guarantee the correct utilization of the PIV system, the particles density has to be sufficiently low to distinguish each particle in the images. However, at the same time the particle density has to be sufficiently high to guarantee that a significant number of particles can be found in each interrogation cell.

The cross-correlation method (Figure 3.2) is usually utilized to evaluate the particle displacement: two images of the interrogation cells, obtained at two different times, are compared using an adequate algorithm, which associates each pixel of the first image with a pixel of the second image. The peak of the cross-correlation method is obtained when the average particle displacement is identified. Therefore, this method is successful only if the system parameters have been selected in a way that the same particles are recorded in the two instants, in the same interrogation cell.
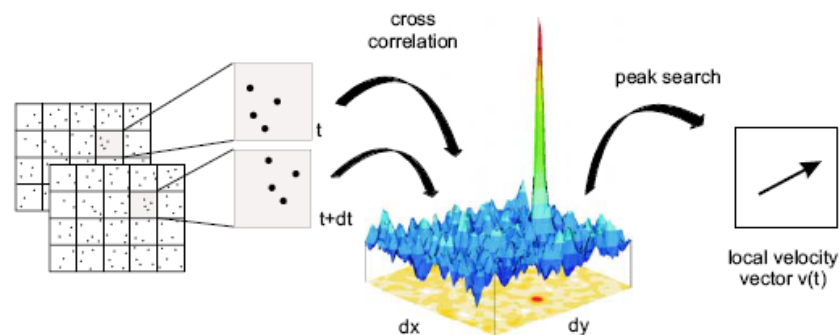


**Figure 3.2:** *Cross correlation (DaVis 7.2 Software Manual (2009a)).*

Once the displacement is obtained, a velocity vector is displayed in the centre of each cell, in a manner similar to the vector plots in computational fluid dynamics simulation (Tavoularis (2005))

### 3.2.2 Stereoscopic PIV

The classic PIV is a two dimensional technique. Therefore, considerable errors, that can not be adequately evaluated, generally affect the results deriving from the analysis of flows that are substantially three dimensional, even if the measurement plane is placed in the direction of the main flow.

In order to address this issue, it is necessary to use the stereoscopic PIV configuration (SPIV) which allows the measurement of all three velocity components. In this case, it is required to use at least two cameras, placed symmetrically with respect to the light sheet normal, and with their lenses inclined at an angle $\alpha^*$ with respect to the sheet plane.

Each camera measures the particles displacement perpendicular to its viewing direction. In this way, two different projections of the velocity are obtained and, as a result, the resultant velocity vector can be derived (Figure 3.3)
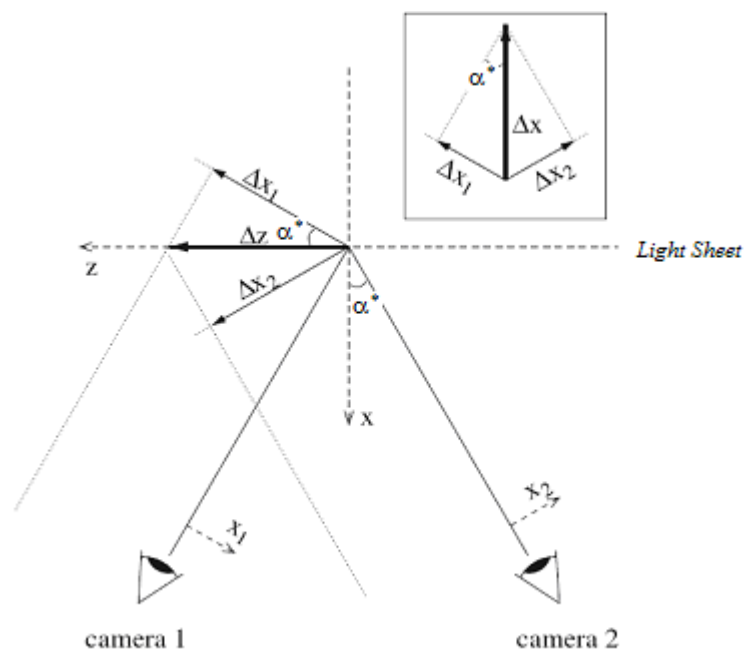


**Figure 3.3:** *Stereoscopic PIV principle.*

Considering Figure 3.3 the reconstruction formulas for the 3D displacement vector ($\Delta$x, $\Delta$y, $\Delta$z) are:

$$\Delta x = \frac{\Delta x_1 - \Delta x_2}{2 \sin \alpha^*} \qquad (3.1)$$

$$\Delta y = \frac{\Delta y_1 + \Delta y_2}{2} \qquad (3.2)$$

$$\Delta z = \frac{-\Delta x_1 - \Delta x_2}{2 \cos \alpha^*} \qquad (3.3)$$

In the arrangement described above the cameras do not focus the whole measurement plane, but instead an inclined one, unless the Scheimpflug condition is verified. According to the Scheimpflug criterion, the image, the lens and the object planes for each camera have to intersect in a common point, as shown in Figure 3.4.
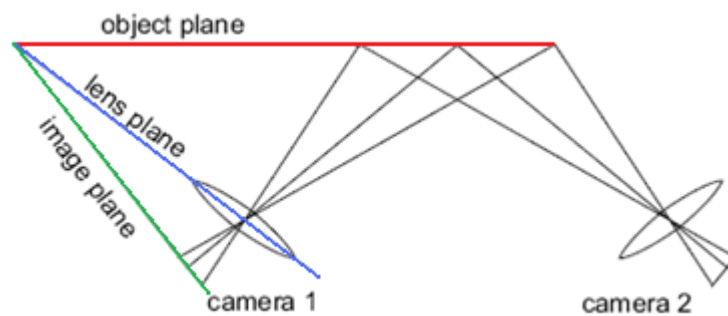


**Figure 3.4:** *Scheimpflug condition .*

Unfortunately, this arrangement has the side effect of introducing a strong perspective distortion: the factor of magnification is no longer constant across the complete field of view and needs additional calibration, which is generally referred to as dewarping.

The steps that need to be undertaken during a SPIV velocity field measurement are sketched in Figure 3.5 (Magand (2009)) and will be explained in the next paragraphs.
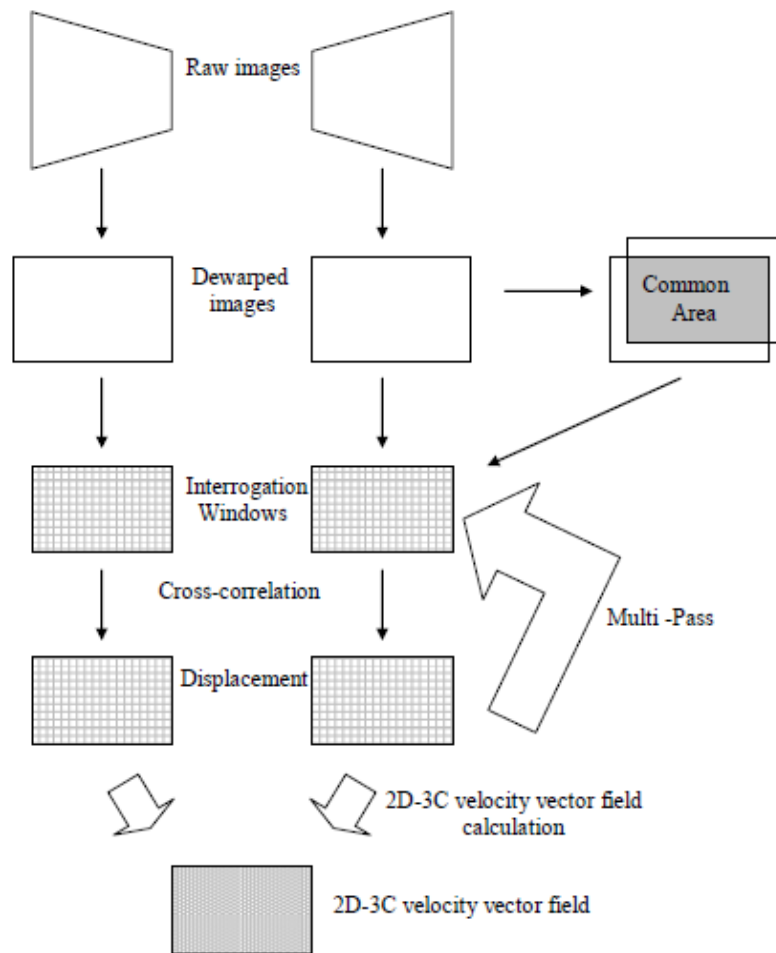
**Figure 3.5:** *SPIV velocity field measurements (Magand (2009)).*

### 3.2.2.1 Dewarping

In the analysis of 3D images the first step consists in the examination of the 2D vector fields of the particle displacements observed by each camera. However, in this way the 2D vector fields obtained are distorted due to the inclination of the cameras with respect to the measurement plane. Therefore, it is crucial to map the images plane into the measurement plane. For this purpose, a calibration plate, marked by an array of crosses or dots at known positions has to be utilized and positioned into the measurement plane.

Two different methods can be utilised to effectively dewarp the images:

- Camera pinhole model. With this mathematical model the relative position cameras-measurement plane is estimated. Consequently, the model correlates the image on the camera chip with the real world objects. The main advantage of this configuration is that the calibration plate can occupy just a portion of the field of view as the pinhole fit method can extrapolate the correlation;

- Polynomial function. A mapping function which correlates the image planes with the measurement plane. Prasad (2000) states that the mapping functions can be approximated, with sufficient accuracy, with a second-order polynomial function.

Generally, the pinhole model is not effective when radial distortions are added, as by focusing through a non-planar glass window. Additionally, in this case also the second-order polynomial function involves large errors. Consequently, in the present work for both experiments a third-order polynomial function has been used. Doorne et Westerweel (2006) have demonstrated that the use of this polynomial is reasonably accurate when radial distortions are present.

### 3.2.2.2 Images Acquisition and Analysis

A misregistration is a common error performed during the dewarping algorithm: errors in the mapping procedure can produce a difference of the dewarped images of the two cameras. In order to minimize this error, Wieneke (2005) suggests to cross-correlate several PIV images and then to utilize the averaged value. Doorne et Westerweel (2006) identify 400 as the minimum number of images to obtain a reliable representation of the cross-correlation function.

Two main approaches for the stereo cross correlation are offered by DaVis Software.

The first is the standard FFT (Fast Fourier Transform) based algorithm where the correlation strength $C$ is given by:

$$C(dx,dy) = \sum_{x=0,y=0}^{x<n^*,y<n^*} I_1(x,y) I_2(x+dx,y+dy), -\frac{n^*}{2} < dx,dy < -\frac{n^*}{2} \quad (3.4)$$

where $I_1$ and $I_2$ are the image intensities of the interrogation windows in the first and second exposures images from camera 1 (or camera 2), $n^*$ is the size of the interrogation window, $dx$ and $dy$ are the displacements along $x$ and $y$. Nevertheless, with this approach, the correlation function is biased towards higher intensities if the background and signal intensities are variable. This effect can be minimized normalizing the equation 3.4 by means of the average intensities. In this case the correlation strength $C$ is expressed as:

$$C(dx,dy) = \frac{\sum_{x=0,y=0}^{x<n^*,y<n^*}\left(I_1(x,y)-I_{1avg}(x,y)\right)\left(I_2(x+dx,y+dy)-I_{2avg}(x+dx,y+dy)\right)}{RMS\left(I_1(x,y)-I_{1avg}(x,y)\right)RMS\left(I_2(x+dx,y+dy)-I_{2avg}(x+dx,y+dy)\right)} \quad (3.5)$$

Where $I_{1avg}$ and $I_{2avg}$ are the average intensities of the interrogation windows.

It has to be noted that the standard deviation of the first interrogation window is constant, while for the latter it depends on the displacements $dx$ and $dy$. In this way, either the variation in the background intensity or in the signal density can be offset.

In the post-processing phase, in order to increase the resolution of the velocity field the interrogation windows can be overlapped. The first step of this procedure consists in a first evaluation of the velocity vector field using the largest interrogation window size that has been previously appropriately chosen by the user. Overlapping is not used in this phase. This first estimation is then used in a second evaluation of the flow field and it will work as a reference. The interrogation window size is now half of the one used in the first step, and its position is shifted in a way aimed at ensuring the correlation between the same particles in the two images, Figure 3.6
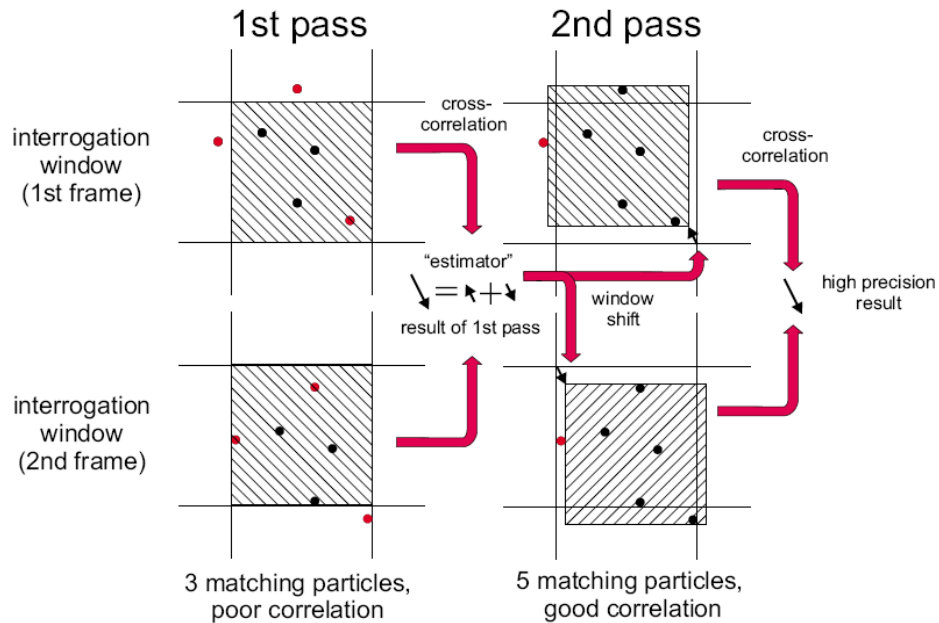
**Figure 3.6:** *Multi pass method*

### 3.2.3   PIV Equipment

The PIV equipment main components are:

- Nd:Yag Laser;
- Cameras and Optics;
- Seeding system;f

A brief description of each element can be found in the following sections.

#### 3.2.3.1  Nd:Yag Laser

The PIV equipment utilized in the present research includes a Nd:Yag Laser (Quanta Ray PIV-400-10) set in a double pulse mode configuration. This laser consists of three major components:

- A neodymium-doped yttrium aluminum garnet (laser material);
- A pump source;
- An oscillator.

Generally, atoms can change their energy status by absorbing or emitting a photon whose energy expressed by Planck's law (3.6) is equal to the energy difference between two energy levels ($\Delta E$).

$$\Delta E = h\nu_f \quad (3.6)$$

Where $h$ is Planck's constant and $\nu_f$ is the radiation frequency.

If an atom has only two energy levels with a energy level difference equal to $\Delta E$, then it can pass from one to another in three different ways (Raffel et al. (2007)), as shown in Figure 3.7:

- Absorption. The atom, after having absorbed an impinging photon whose energy content is exactly equal to $\Delta E$, passes from the lower energy level $E_1$ to the higher energy level $E_2$;
- Spontaneous emission. In this case an atom that is already in an excited status with an energy level $E_2$ drops spontaneously to the energy level $E_1$ emitting a photon with an energy equal to $\Delta E$;
- Stimulated emission. This phenomenon is at the base of laser physics. If an electron already in an excited status $E_2$ is impinged upon by a photon with energy equal to $\Delta E$ it will be forced to pass to the lower energy level $E_1$ while it will emit the incident photon plus a second one in phase with the former.
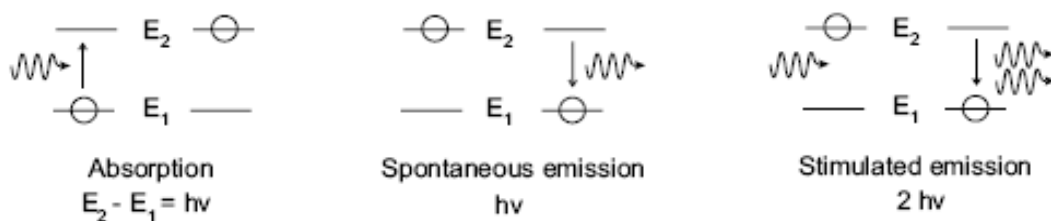


**Figure 3.7:** *Three different interaction electromagnetic wave / laser material (Raffel et al. (2007)).*

Consequently, in a laser system, optical pumping is a necessary mechanism that forces the so called population density inversion phenomenon for which the number of electrons at the energy level $E_2$ is greater than the number of electrons at lower energy level $E_1$. Nevertheless, density population inversion is impossible if the laser material has only two energy levels. In this case, in fact, when the material is pumped until it reaches the state for which the number of electrons at energy level $E_1$ equals the number of electrons at energy level $E_2$, the likelihood to have absorption or emission is exactly the same. If the material has three energy levels, then, more than half of the atoms need to be excited in order to have stimulated emissions. Consequently, in order to have an efficient laser system the laser material needs to have four different energy levels for which the lower level used is $E_2$ and not the basic level $E_1$, as it is for a neodymium-doped yttrium aluminum garnet, Figure 3.8.
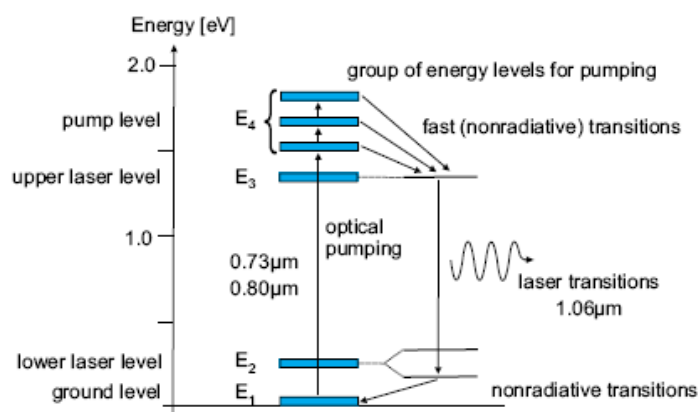


**Figure 3.8:** *Interaction between the laser garnet and the electromagnetic wave (DaVis FlowMaster Hardware 7.2 (2009b)).*

Once inversion of the population is obtained spontaneous emission starts and this excites other atoms: the stimulated emission is augmented and takes the form of a chain reaction.

In order to amplify the radiation in a preferred direction the laser rod has a cylindrical shape: in this case the amplification occurs along the longest dimension.
Furthermore, in order to have an exponential augmentation of the radiation the laser rod is positioned between two mirrors, thus forming an oscillator and forcing the light to pass again and again in the laser medium until a stationary state is reached.

The resonance conditions are controlled and then appropriately changed using a Q-Switch (giant pulse formation) to release all the energy created and stored in the laser rod in a pulse of infrared right at 1064nm and with duration of 8ns.

The final output is then obtained using a second harmonic generator that converts the infrared light at 1064nm to green light at 532nm.

A typical configuration of a Nd:Yag PIV laser is sketched in Figure 3.9, where two laser rods are used, each of them creating the impulse light for just one of the PIV image frames taken.
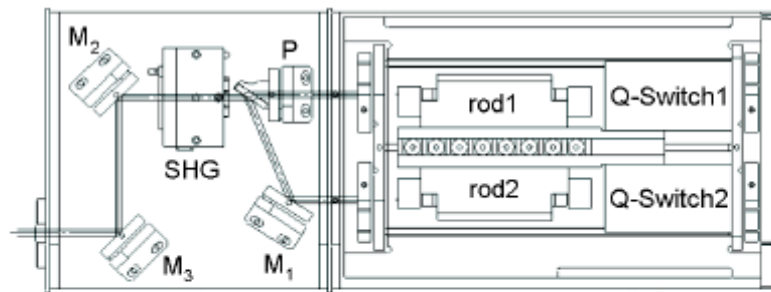


**Figure 3.9:** *Laser Nd:Yag dual oscillator, rod1 rod2: laser garnets, M1,M2,M3 mirrors, P:beam combining polarizer, SHG:second harmonic generator (DaVis FlowMaster Hardware 7.2 (2009b)).*

### 3.2.3.2  Cameras and Optics

In order to analyze the 3D structures of the flow, for both the preliminary and the large scale experiment the PIV stereoscopic configuration has been used (Section 3.2.2). The cameras have been installed in a frame that held them at 45° respect to the vertical axi (z-axis) (Figure 3.10a).

The frame was mounted on a TSI 3-axis traverse system (Figure 3.10b) that was operated under computer control in order to accurately position the cameras along the three axes $x,y,z$.
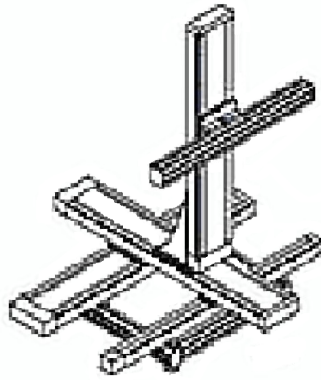
(a)         (b)

**Figure 3.10:** *Cameras mounted on a traverse system at 45° respect to the z axis. Configuration used for both experiments (a) Schematic view (b) Camera installation.*

A fused silica positive cylindrical lens and a glass positive spherical lens have been used to produce a laser sheet with an average thickness of 1mm.

The images have been recorded using two La Vision Flow Master cameras with Nikon 50 mm focal length multi-element lenses mounted on the camera head.

For both experiments the cameras were focusing on the same side of the laser sheet. Consequently the light intensity scattered towards the two cameras is different. As a result two different camera lenses aperture have been used: $f^*/1.4$ for the former and $f^*/1.2$ for the latter

It is important to notice that when the cameras take the first image of the double frame, the CCD (Charge Coupled Device) time exposure depends only on the time required to take the image and it is in the range of microseconds. Dissimilarly, when the second frame is acquired the time exposure is affected strongly by the time required by the PIV system to read the first exposure. As a result, the second exposure time is in the order of hundred of milliseconds, which may result in the cameras collecting also any unwanted background light. In order to address this issue, a 532nm band-pass filter has been installed in front of the cameras lenses.

The necessary synchronization among the two laser impulses, the cameras exposures and readouts out is sketched in Figure 3.11.
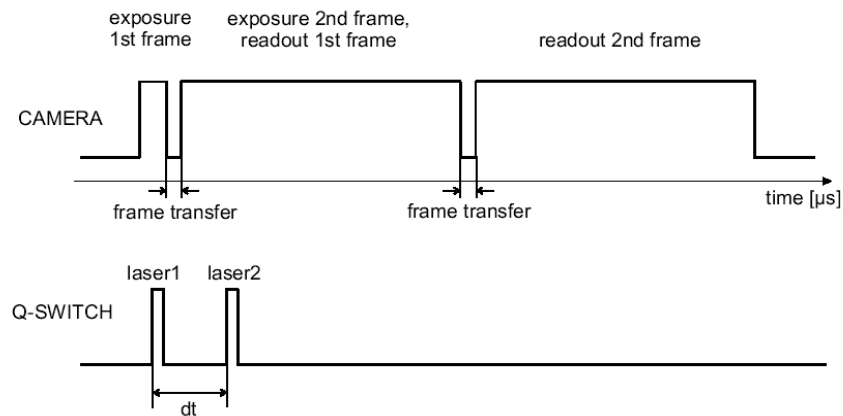
**Figure 3.11:** *PIV time synchronization between cameras exposure, frame transfers, readouts and Laser openings.*

### 3.2.3.3 Seeder

Generally, the quality of PIV measurements depends upon two main parameters:

- $\Delta t$, i.e. the time interval between two images frames. This parameter is characteristic of the flow velocity field in exam;
- Seeding intensity.

It is important to remember here, as stated in Section 3.2.4, that in order to guarantee a correct utilization of the PIV system, the particles density has to be sufficiently low to distinguish each particle in the images. However, at the same time the particle density has to be sufficiently high to guarantee that a significant number of particles can be found in each interrogation cell.

Consequently, in order to successfully use the PIV technique it is important to control and finely adjust the seeding intensity. Therefore, in this work it has been used a liquid seeder made up of four Laskin nozzles that can be switched on or off, Figure 3.12.

Pressurized air passes through the Laskin nozzles, which operating at sonic condition create air bubbles into the seeding liquid. However, these bubbles, thanks to the action of shear stresses, trap liquid particles that are then released as the bubbles reach the free surface. In order to avoid the presence of big seeding particles an impactor plate is inserted inside the seeder forcing the liquid particles to pass through the small gap between the seeder walls and the impactor plate. Additionally, the seeding density could be lowered using a dilution jet, Figure 3.12.

The seeding material chosen has been the mineral oil "Shell Ondina" for both experiments: it fulfills the requirements of being non-toxic, cheap and to scatter enough light towards the cameras.



(a)

(b)
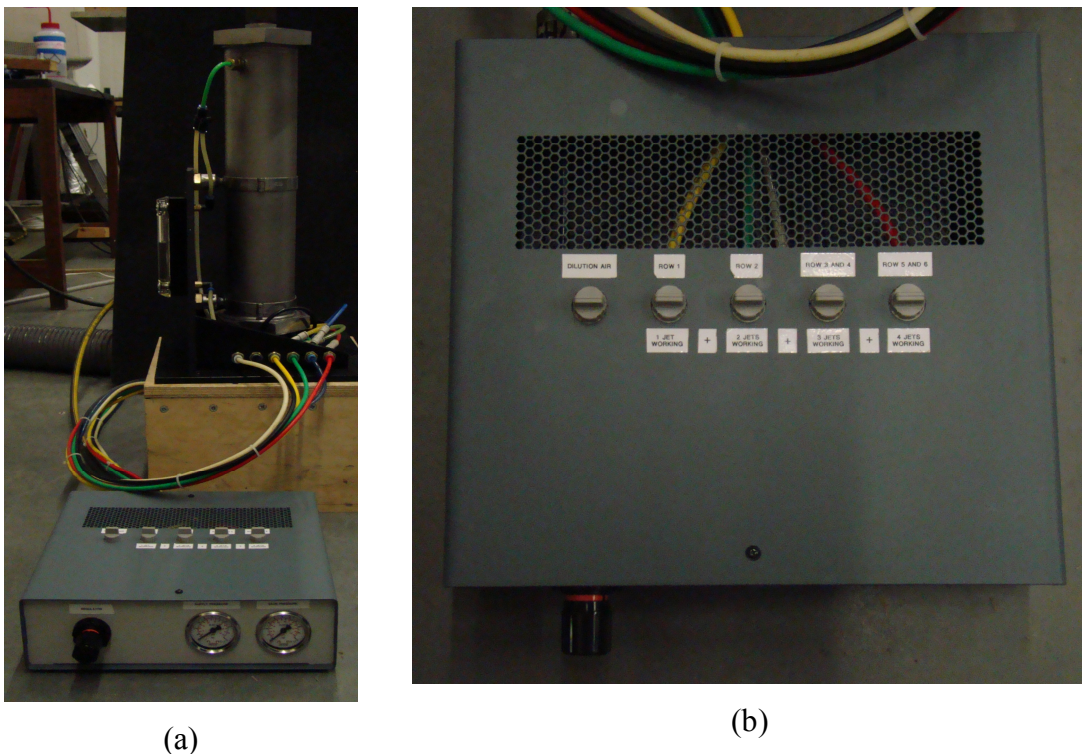
**Figure 3.12:** *Seeder with adjustable seeding density used in the present work.*

## 3.3 Preliminary Experiment

The large scale model implies the use of non-flat glass surfaces introducing high levels of distortions and reflections that can jeopardize the experiment outcome.

Consequently, a feasibility study was conducted by means of a preliminary experiment. This consisted in the observation, through curved glass surfaces, of the vortex structures created by a fluid streaming around a solid steel cube. The main objectives of this preliminary experiment can be summarised in:

- Evaluation of the amount of the reflection deriving from the curved glass surfaces;
- Evaluation of methods to attenuate the reflection (i.e. anti-reflecting painting placed in different zones of the glass tube);
- Evaluation of PIV measurements quality deterioration when non-flat glass surfaces are used.

The study was performed considering the following three different setups,: in open air, with one glass tube inserted , with two glass tubes inserted.. In order to decrease the reflection issue, laser grade borosilicate glass tubes were used due to their optical properties. These three steps (Figure 3.13) were necessary to evaluate the deterioration of the quality of PIV measurements.



(a)

(b)

(c)
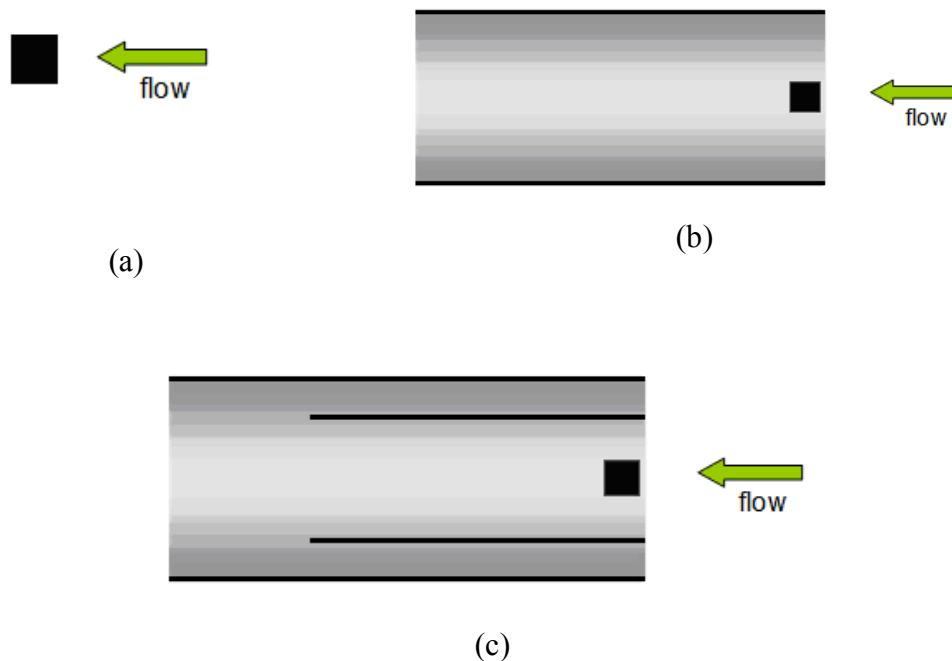
**Figure 3.13:** *Preliminary Experiment Steps, (a) In open air (b) In a glass tube (c) In two glass tubes.*

### 3.3.1 Dewarping

As discussed in Section 3.2.2.1 the first step is the dewarping of the SPIV images. For this reason a calibration plate with crosses of 2mm diameter and separation of 5mm (Figure 3.14) was inserted in the measurement plane (downstream area with respect to the cube). The calibration plate was installed on a multistage holder and positioned in three different parallel positions with a displacement of 0.5 mm. For each position one image per camera was taken. The set of six images was used both to correct the off axis viewing and to calculate the off plane component of the velocity. In Figure3.14 the calibration plate as identified by the camera 1 (Figure 3.14a) and by the camera 2 (Figure 3.14b) is sketched, the red squares are the crosses identified by the software. In Figure 3.14b-c the strong perspective distortion introduced by mounting the cameras at 45° respect to the vertical axis is evident. Once the crosses position seen by each camera is identified, the two images are combined together and the dewarping procedure is applied thus producing the final image of the calibration plate, Figure 3.14c. This last image is the one used when post-processing the PIV images in order to correlate the position of the seeding particles seen by the cameras with their real position in space. In order to not jeopardize the accuracy of the velocity measurements the polynomial mapping procedure was preferred over the pin-hole dewarping method. As explained in Section 3.2.2.1, if a third-order polynomial equation is used as calibration method even in presence of radial distortions, the measurement accuracy is still acceptable (Doorne et Westerweel (2006) ).

The calibration procedure was repeated in the same way for the three different experiment steps described in 3.3, being the image distortion level dependent on the number of curved surfaces positioned between the camera and the measurement plane.

(a)

(b)

(c)
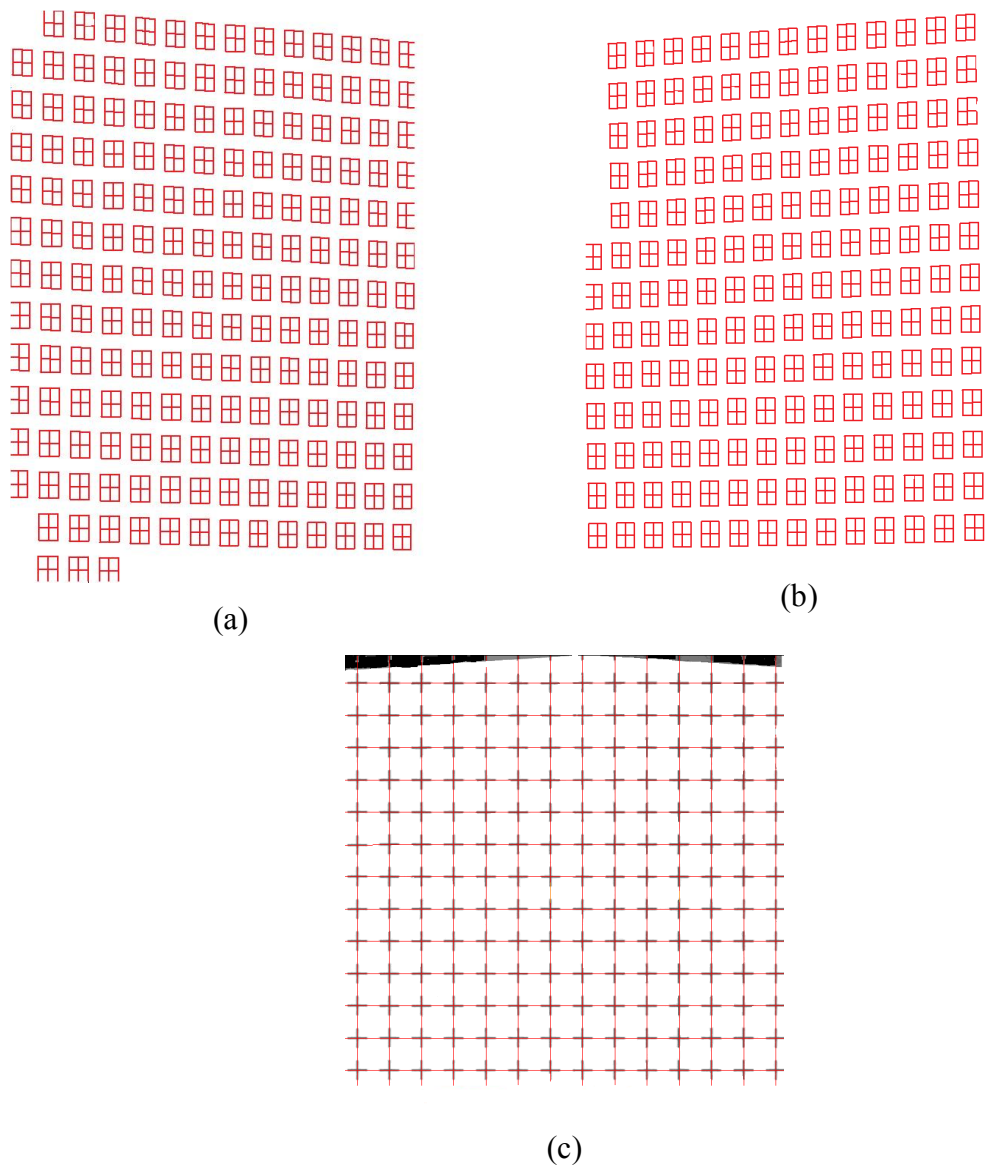
**Figure 3.14:** *Dewarping. Crosses identified by camera 1 (a) and camera 2 (b) where each red square represents a cross. (c): Dewarped image*

The root mean square of the dewarping function for the three experimental setups are reported in Table 3.1.

It is evident from this table that the root mean square (RMS) increases as more curved glass surfaces are interposed between the cameras and the flow. Nevertheless, this calibration results are a first suggestion that even if the PIV measurements quality decreases the deterioration of the measurement is not such as to jeopardize the

experiment outcome. In fact, as reported by Davis Software 7.2 user's guide a RMS up to 0.8 pixels is still considered acceptable.

| | RMS No glass tube | RMS One Glass Tube | RMS Two Glass Tubes |
|---|---|---|---|
| **Camera 1** | 0.232 | 0.378 | 0.500 |
| **Camera 2** | 0.239 | 0.385 | 0.512 |

**Table 3.1:** *RMS of the dewarping function for the three experimental configurations.*

### 3.3.2 Reflection Issue

Two different laser sheet configurations were used to examine the level of reflections generated by the presence of the glass tubes walls. In the first configuration, the laser sheet was passing through the lateral surface of the glass tube, as illustrated in Figure 3.15

(a)



(b)
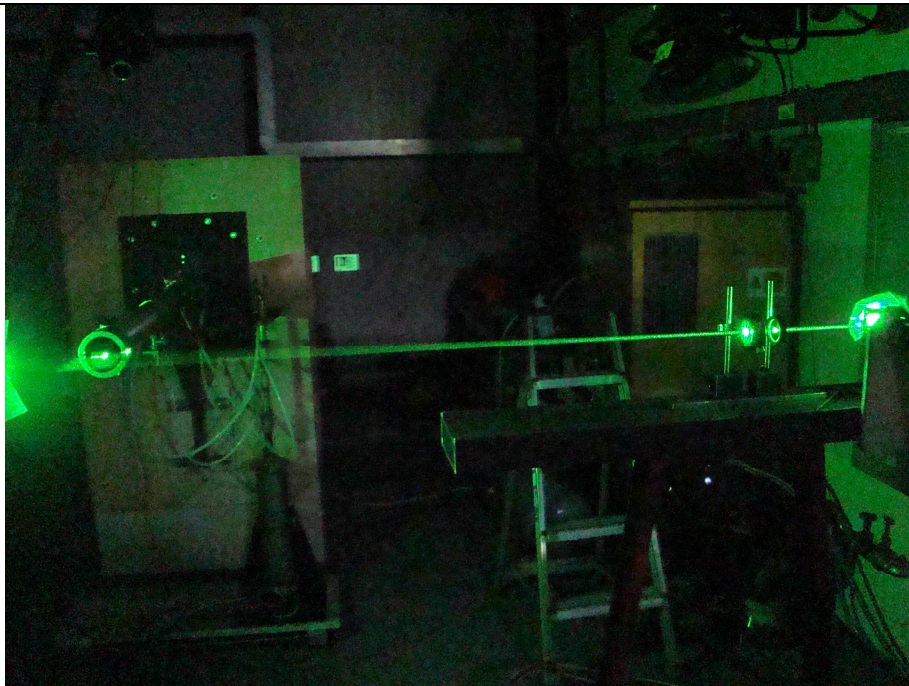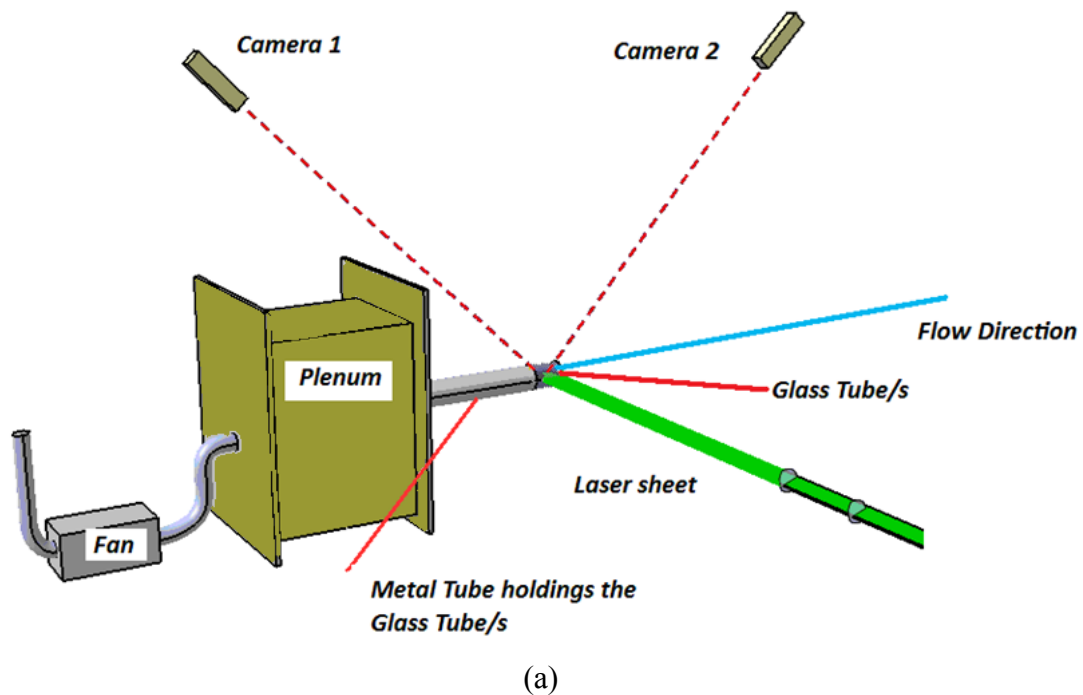
**Figure 3.15:** *First configuration of the experiment (a) Scheme of the test rig (b) Picture taken during one of the runs of the experiment.*

In this arrangement the cameras had full visibility of the area downstream of the cube. Nonetheless, the level of reflections was high and the reflected signal covered the useful signal in the zone of interest. As it is possible to observe in Figure 3.16-17,21 the level of scattered light is given by the different colors, with dark blue meaning

almost no scattered light and with white representing the maximum level of scattered light. In Figure 3.16-17,21the edge of the cube is clearly visible in dark blue. Each particle of the seeding scatters light when hit by the laser sheet. As long as the seeding particles can be distinguished one from the other it is possible to successfully process the images. Nevertheless, from Figure 3.16-17,21it is possible to see that the light due to reflection coming from the glass or from the cube surface creates white strips on the image that mask the seeding particles present in that area. In these zones it is not possible to process the signal and consequently no velocity measurement can be taken.
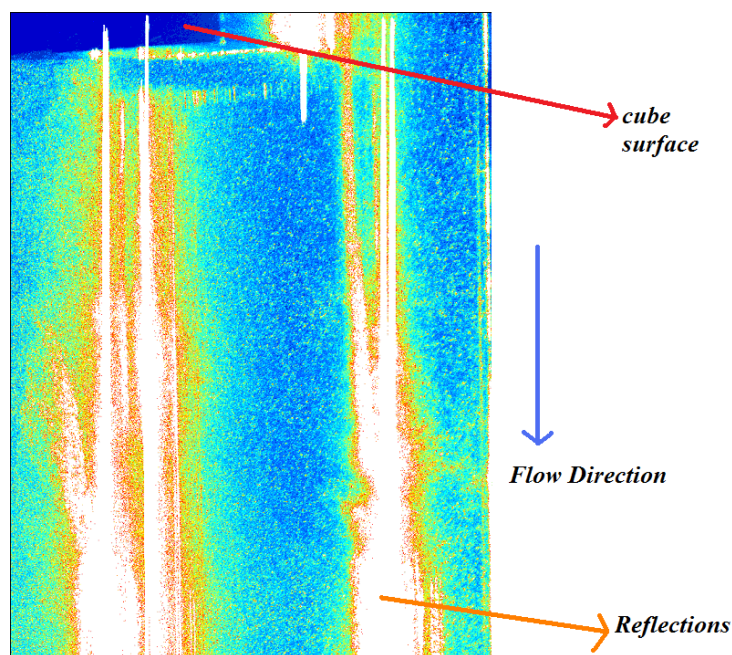


**Figure 3.16:** *Reflections.*

In order to decrease the amount of reflection a black paint was used in different parts of the glass surface. It was found that the reflections were shifted but their intensity was not lowered, Figure 3.17
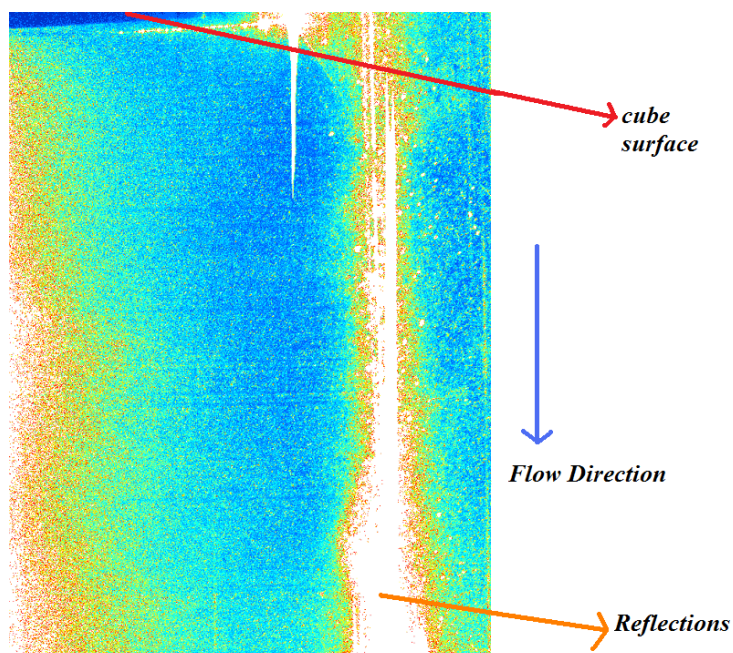
**Figure 3.17:** *Reflections, glass surface partially painted in black.*

Therefore, the idea of using Rhodamine 6G to paint the glass surface was examined. Rhodamine 6G absorbs energy at 532nm and emits most of this energy shifted in the range of 555 to 585 nm with a maximum at 566 nm. In Figure 3.18 the spectra of emission and absorption of Rhodamine 6G are reported. The two signals can be separated equipping the cameras with a filter that blocks the fluorescent signal (and therefore the reflections from the glass surface) and let most of the original signal pass through. Nevertheless, using Rhodamine 6G laser grade did not give the expected results, apart from being highly toxic and expensive. Consequently, an alternative set-up of the experiment was examined.
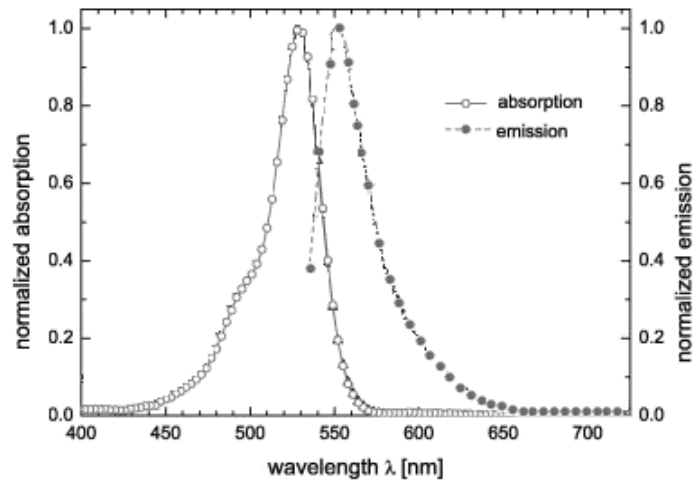
**Figure 3.18:** *(a) Absorption spectrum of Rhodamine 6G (b) Emission spectrum of Rhodamine 6G (Trenkmann et al. (2012)*

In this second configuration (Figure 3.19), the laser sheet was inserted from one end of the glass tube and the cameras were moved of 90° around the vertical axis (Figure 3.20a). It was found that a lower level of reflection was created by the laser impacting on the cube surface.
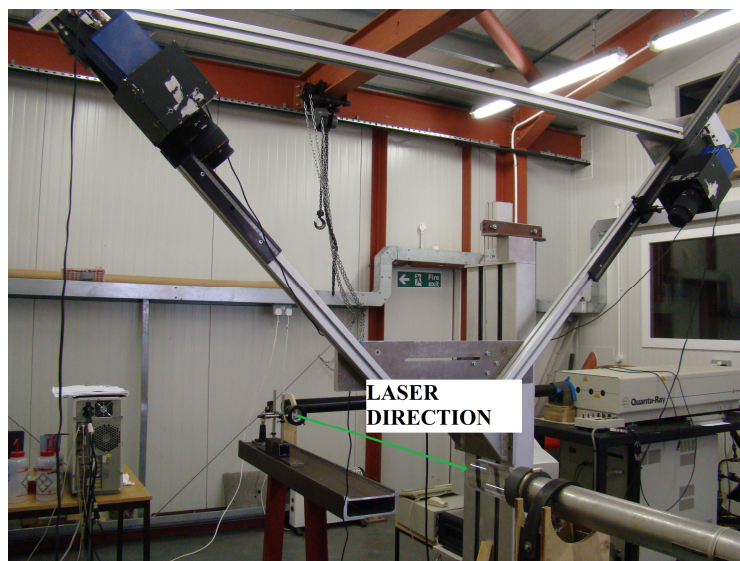


**Figure 3.19:** *Second configuration of the experiment.*

A part of the useful signal was covered by reflections, making the observation of the entire recirculation zone impossible. However this did not compromise the quality of the remaining data. In Figure 3.20b the area interested by the reflections is sketched.
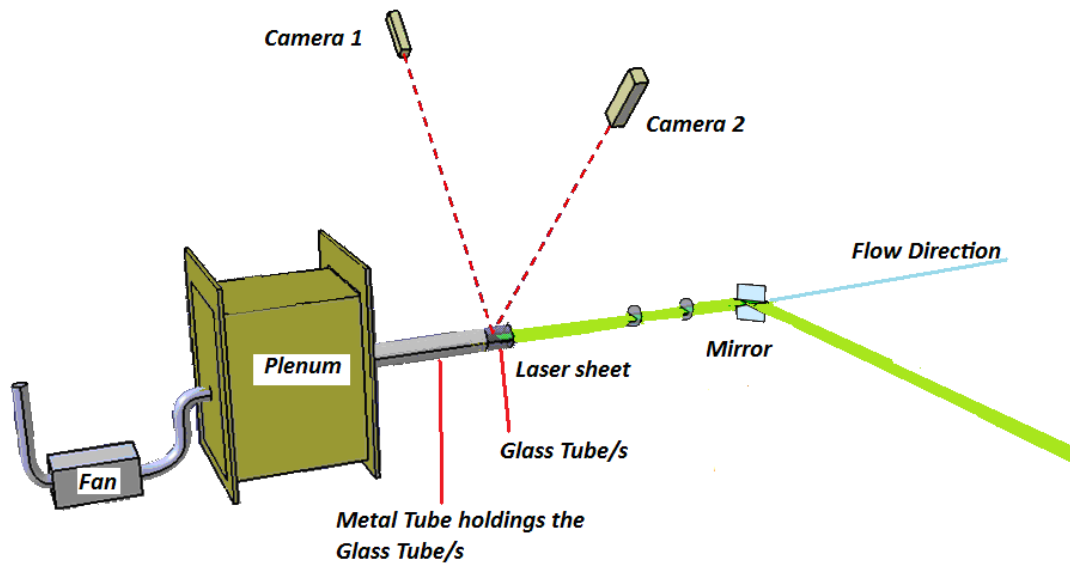
(a)
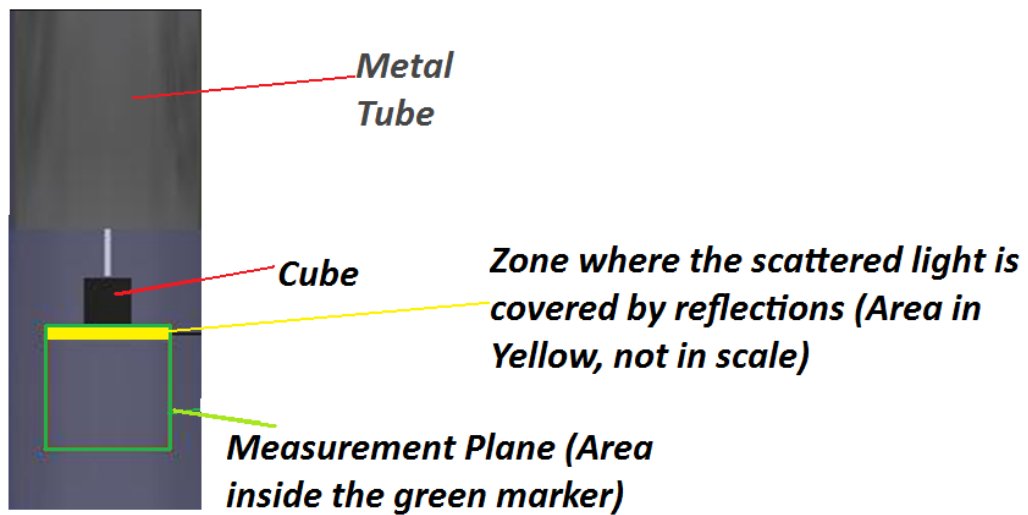


(b)

**Figure 3.20:** *(a) Laser sheet direction (b) Zone of interest, in black the zone covered by reflection is reported.*

The reflection levels created by the laser impacting the cube for each one of the experimental setups taken into consideration are reported in Figure 3.21.

(a)

(b)

(c)
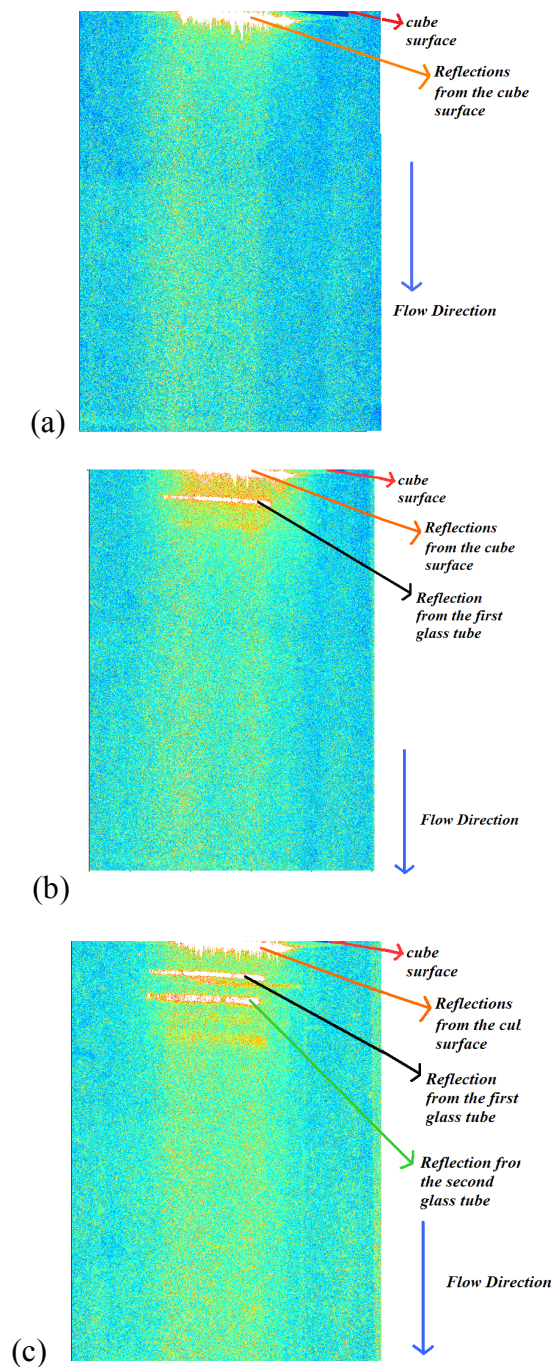
**Figure 3.21:** *Reflections level for the second configuration of the experiment (a) No glass tube present (b) One glass tube (c) Two glass tubes.*

### 3.3.3 Experimental Results

In order to minimize the mis-registration error (Doorne et Westerweel (2006)) five hundred images have been taken and averaged. The images have been processed using the standard FFT cross-correlation with an overlap of 50%. The multi-pass algorithm has been used considering an initial window of 256x256 pixels and a final window of 32x32 pixels.. The PIV results are reported in Figure 3.22.
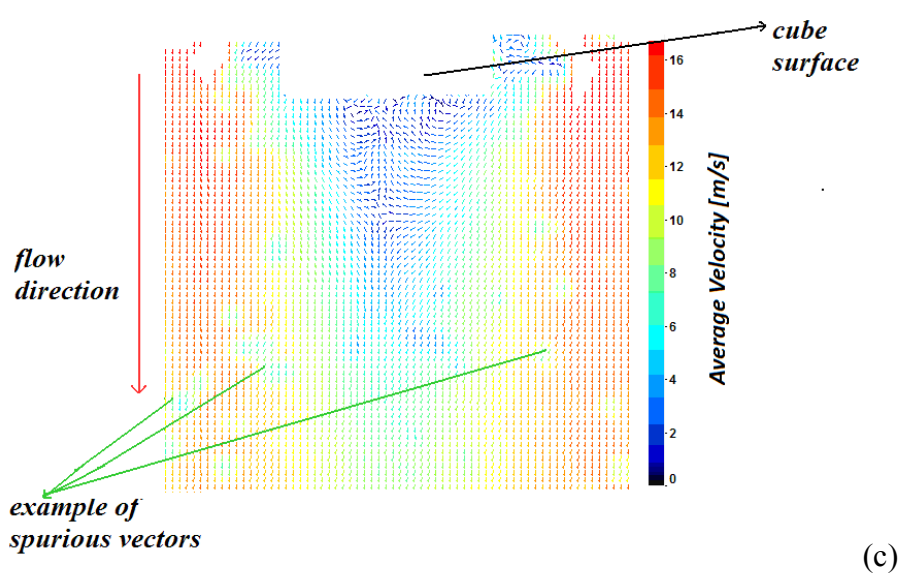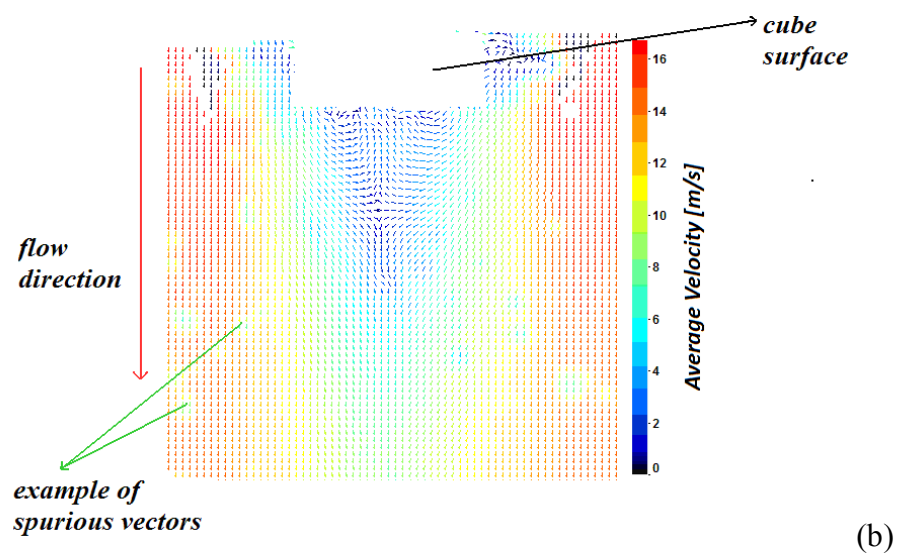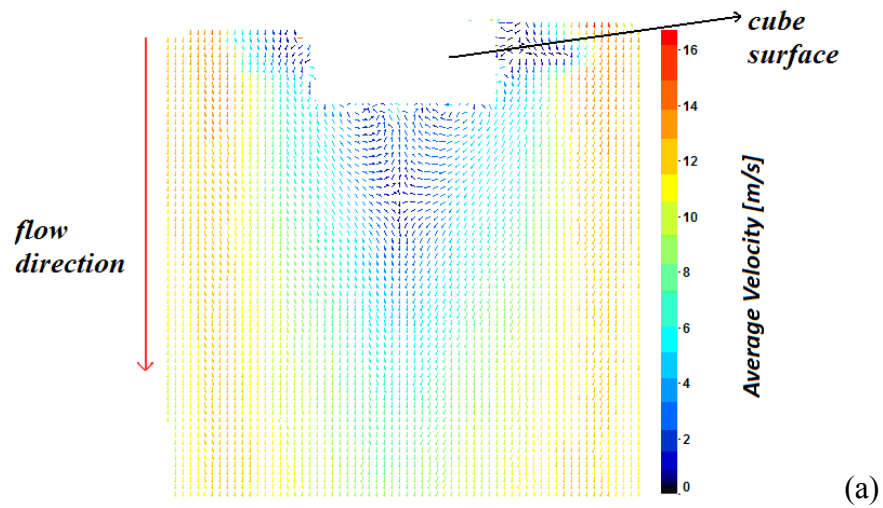
**Figure 3.22:** *PIV velocity field with: (a) No Glass Tube (b) One glass tube (c)Two glass tubes.*

The mean velocity turns out to be lower when no glass tubes are used. This is due to two reasons. Firstly, when the cube is inserted in the glass tube, the latter is mounted inside the metal tube that is used to channel the flow. Therefore the cross section is that of the glass tube (Figure 3.23b) Consequently, in the configuration in which the cube is in open air the cross section of the flow is given by the radius of the metallic tube (Figure 3.23a). Secondly, the flow is discharged in open air and therefore it is not limited by the presence of the glass tube.
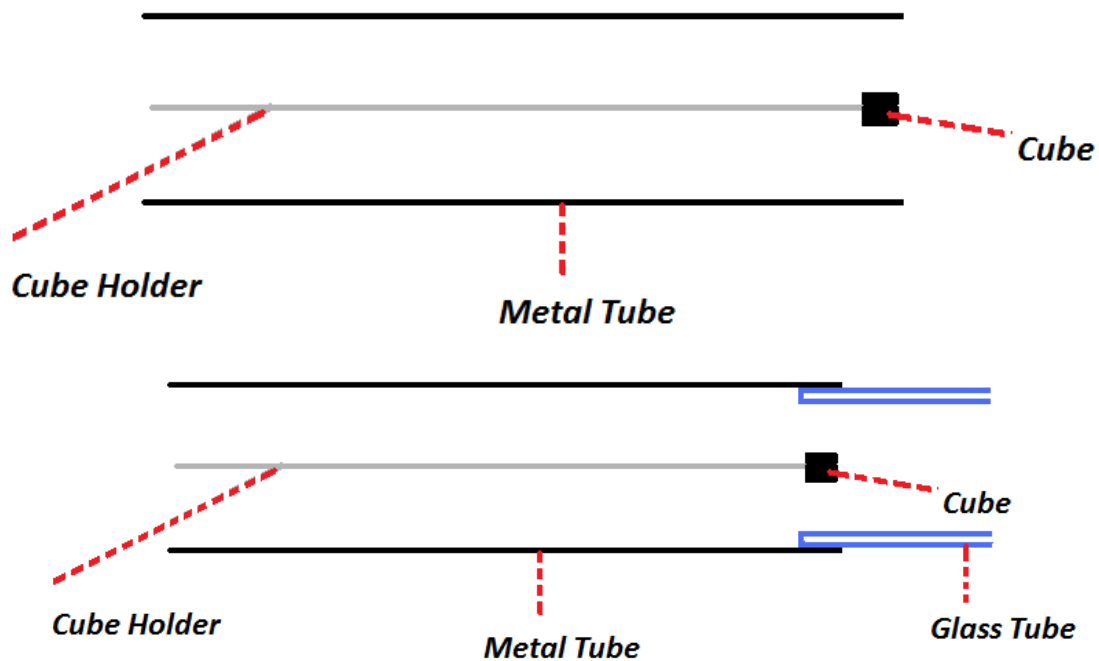


**Figure 3.23:** *Experiment configurations (a) No Glass Tube, the flow is discharged in open air (b) With glass tube*

As it is possible to observe in Figure 3.22, the use of glass tubes introduces many spurious vectors during the velocity field calculation. It has been found that even small defects of the glass tubes, like presence of scratches, small stones, knots, airlines in the glass surface, or not perfect circularity/straightness of the tubes add further measurement errors. When two glasses are used instead of one the recirculation zone appeared to be less symmetrical and additional spurious vectors are present.

Therefore, from this first analysis it is evident that the employment of non-flat glass surfaces causes a deterioration of the PIV analysis measurements. Nevertheless, the small differences between the two velocity fields, obtained with one or two glass

tubes, suggests that the use of curved surfaces doesn't detriment the quality of the experimental analysis to an extent such that the experiment should not be performed. Nonetheless, in order to better asses the PIV measurement quality a CFD analysis of the experiment can be found in the next Section 3.3.4.

### 3.3.4 Experimental Results and CFD Data

In this section a CFD analysis of the experimental setup has been performed in order to assess the deterioration of the PIV data. The use of CFD is necessary as the velocity fields with and without glass tubes are not directly comparable.

A structured mesh of two millions nodes has been created using GAMBIT 2.3 mesh generator and the flow field has been investigated using FLUENT v6.4.

The k-ε RNG turbulence model has been used (see the CFD Section 4 for details about this model). No other turbulence models have been analyzed as the purpose of this study is not CFD validation but rather the evaluation of the quality deterioration in PIV measurements when non-flat glass surfaces are used. A pressure based solver was used. A second order solution obtained. The cube side length is 2.5 cm, the glass diameter in which the cube was inserted 3.7 cm radius and a thickness of 0.15 cm. the mass flow at the inlet at ambient temperature was 0.068 Kg/s. The results are reported in Figure 3.24.



(a)                                             (b)
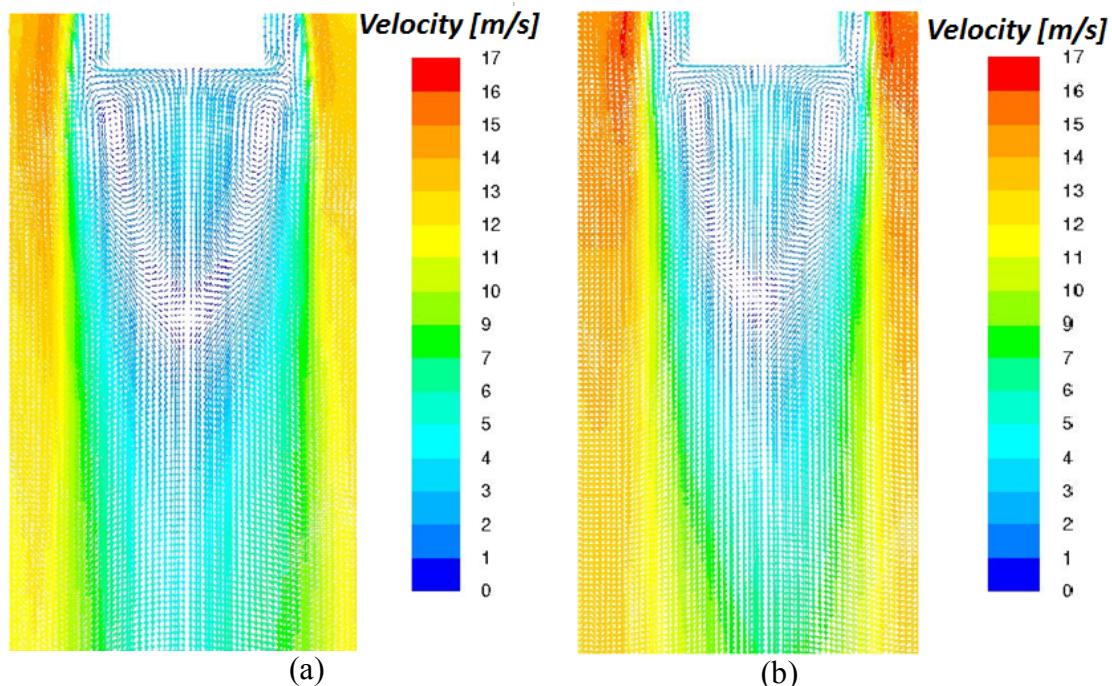
**Figure 3.24:** *CFD results with: (a) no glass tube; (b) glass tubes.*

The CFD data confirmed that the average velocity is lower in the case where the cube is in open air.

The main outcome of the comparison between the CFD and experimental data is that the numerical data seems to over-predict the length of the wake behind the cube.

This observation is confirmed by the direct comparison of the quantitative data taken in different stations. The stations used are reported in Figure 3.25 (at 1, 1.3, 1.7 cm from the cube for Station 1, 2 , 3 respectively).
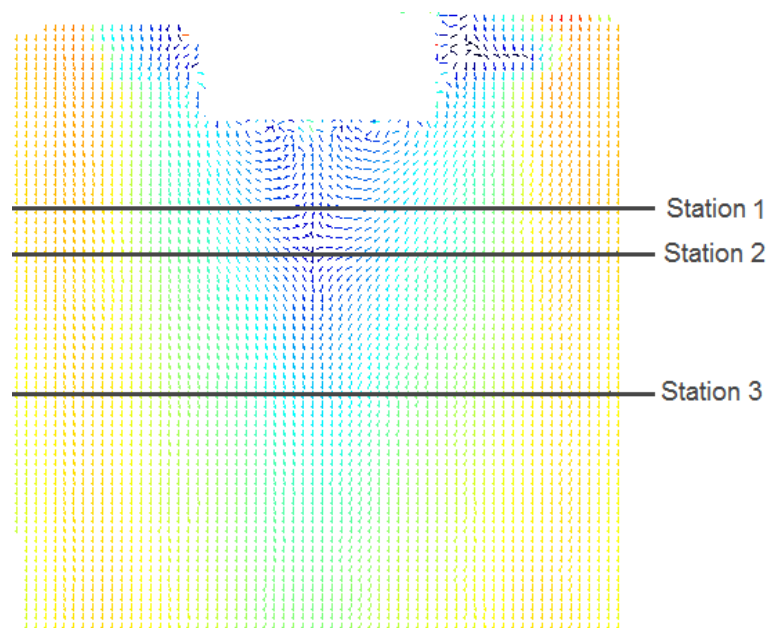


**Figure 3.25:** *Stations position.*

The results for the case where the cube is in open air are reported in Figure 3.26, whereas the cases with one and two glass tubes are reported in Figure 3.27.
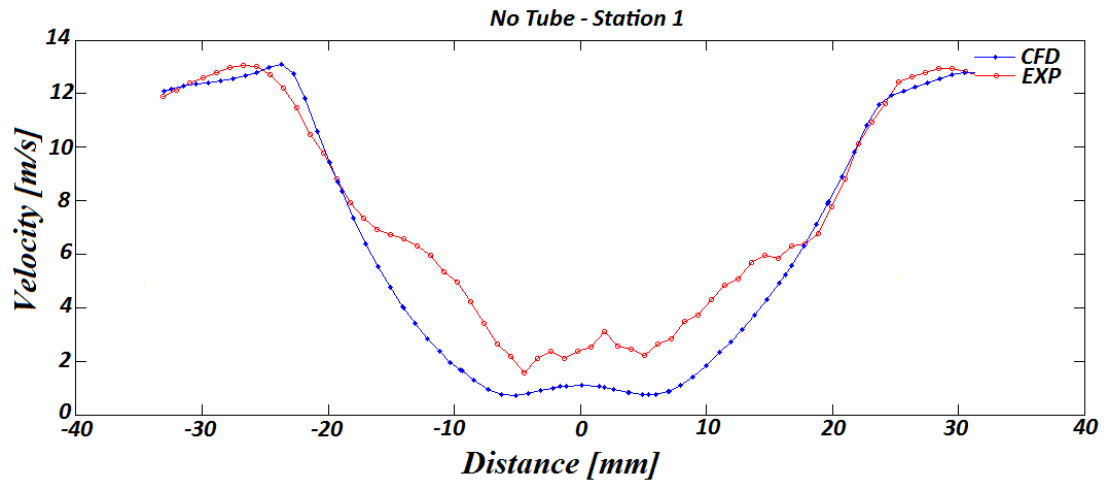
(a)
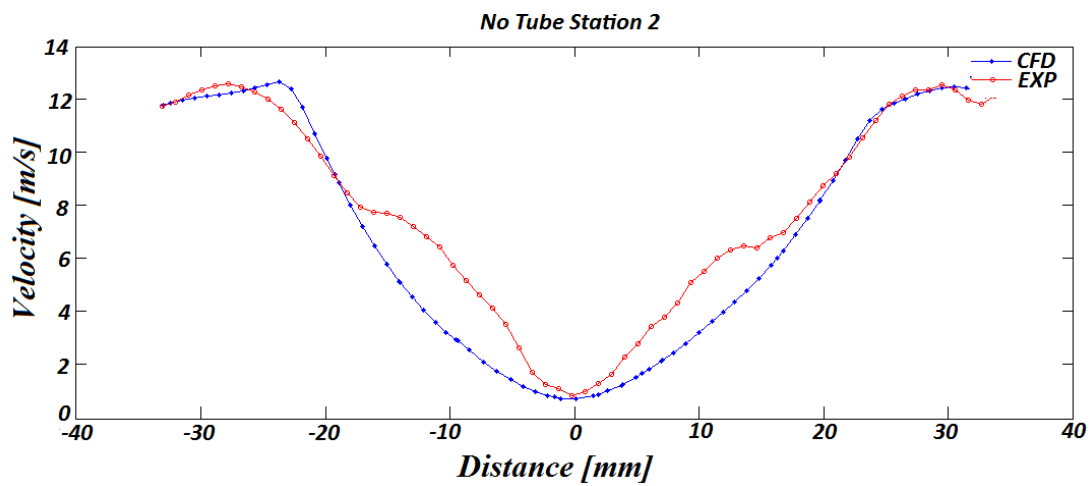


(b)
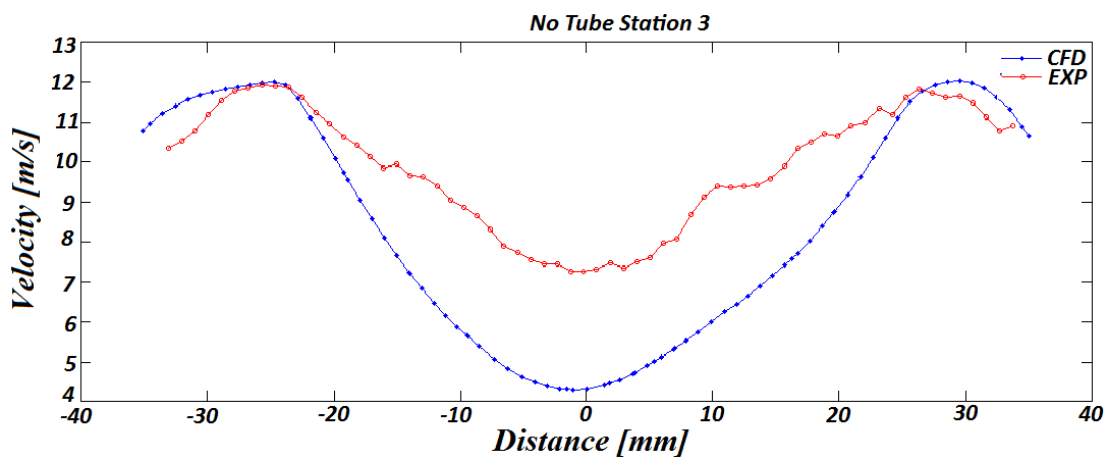


(c)

**Figure 3.26:** *Comparison between CFD and PIV data when the cube is in open air. In red are the experimental results while in blue the numerical ones for: (a) Station 1 (b) Station 2 (c) Station 3.*

(a)



(b)



(c)
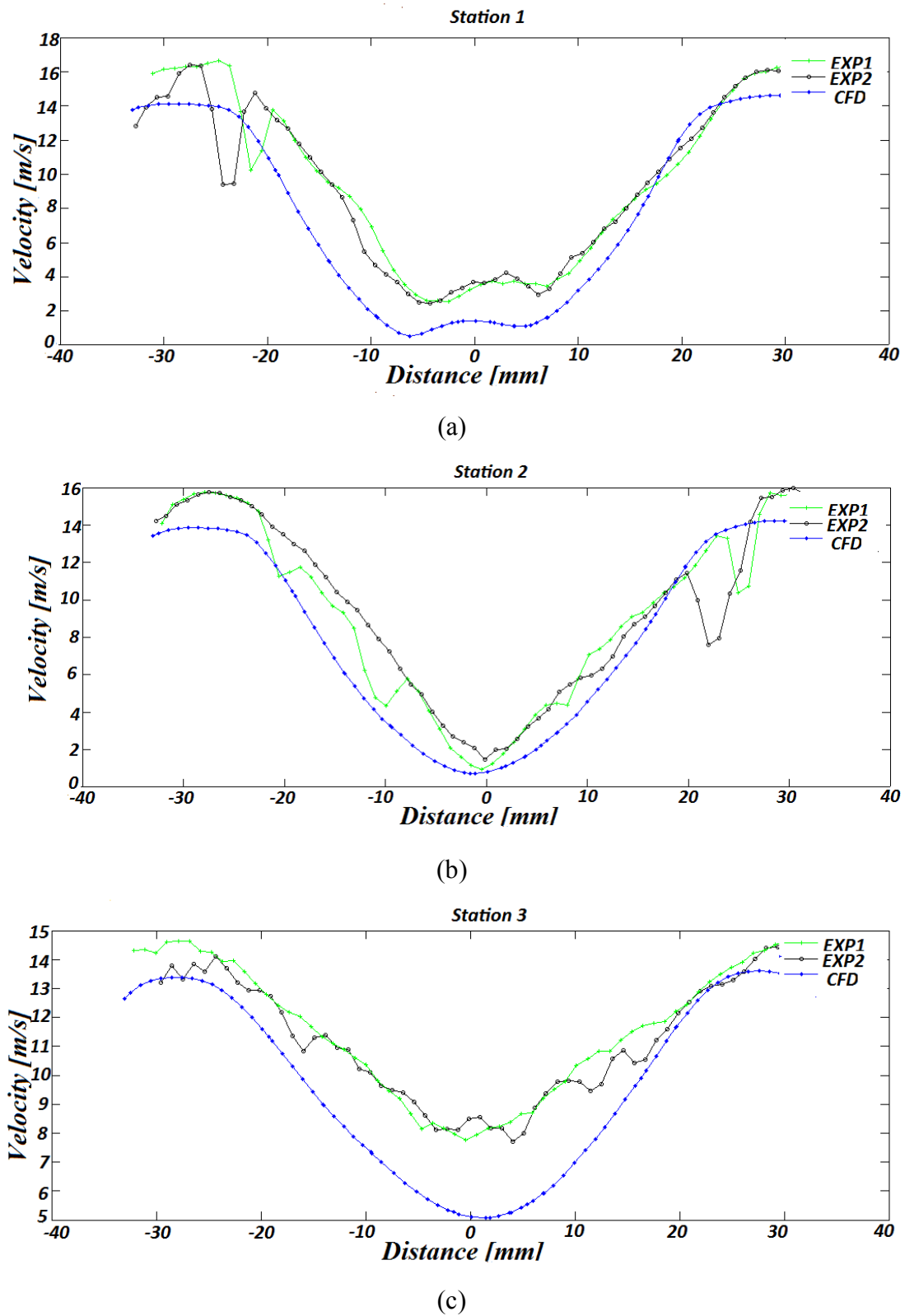
**Figure 3.27:** *Comparison between CFD and PIV data when the cube is in one or two glass tubes. In green are the experimental results with one tube, in black the*

76

*experimental results with two glass tubes and in blue the numerical results for: (a) Station 1 (b) Station 2 (c) Station 3.*

Some level of asymmetry can be observed in the CFD results. This is due to the previously described difficulties in obtained a converged numerical solution. As it is clear from Figure 3.26c and Figure 3.27c the length of wake behind the cube is higher in the case of the CFD analysis. This is shown by lower values of the velocity in the wake region of the flow field predicted by the numerical results in station 3. Nevertheless, this phenomenon occurs both for the configuration in which the cube is in open air and inside the glass tubes. Consequently, it is clear that this disagreement between numerical and experimental analyses is not due to errors introduced by the presence of non-flat glass surfaces. This disagreement can be due to an over-prediction of the size of the recirculation area of the numerical analysis. Furthermore, it has to be noticed that the size of the PIV area of measurement has not been optimized. Focusing on a large area means that the velocity vectors are averaged and therefore the PIV accuracy is reduced and the recirculation area size can in this way be wrongly estimated.

From Figure 3.27 it is possible to compare the PIV data acquired with one or two non-flat glass surfaces. At Station1 more spurious vectors are present when two glass tubes are used, nevertheless the opposite happens at Station 2. This is likely to be due to the complex interactions of the reflected light with the relative position of glass surfaces irregularities. Consequently the only presence of spurious vectors does not suggest that the quality of the signal is any worse when two glass tubes are used instead of one. Nevertheless, it has to be noted that from the dewarping procedures that the PIV measurements where two glass tubes were used are affect by a higher uncertainty.

In conclusion, it is evident that new registration errors are introduced when glass tubes are employed. Nonetheless, the analysis of the acquired data from the different experimental configurations, shows that the PIV measurements are still representative of the flow field.

## 3.4 Large Scale Experiment

The identification of the main physic phenomena involved in the lens fouling process is the first fundamental step in successfully designing a more efficient purge system configuration. In the present work, the test case described in the next paragraph has been used for CFD, FEA and experimental analyses.

### 3.4.1 Test Case Description

The test case taken into consideration is a purge air system with an air curtain configuration obtained through the installation of a still tube. The pyrometer under study is currently installed in a military aircraft engine.

It is important to remember that the still tube configuration should:

• Avoid the contact between the purge air (that it is drawn from the compressor and therefore contains contaminants ingested by the engine) and the lens;

• Generate a high-speed flow in order to prevent that particles contained in the gas turbine flow could deviate from their path and reach the pyrometer lens.

The pyrometer purge air system is obtained through three concentric tubes: namely the housing, the purge and the still tube (Figure 3.28).

The housing tube is installed in the turbine casing and it should protect the pyrometer from the high structural stresses created by the harsh turbine environment. The air coming from the compressor enters through a single aperture positioned at the bottom of the housing tube and then streams inside six small equally spaced holes positioned on the purge tube.
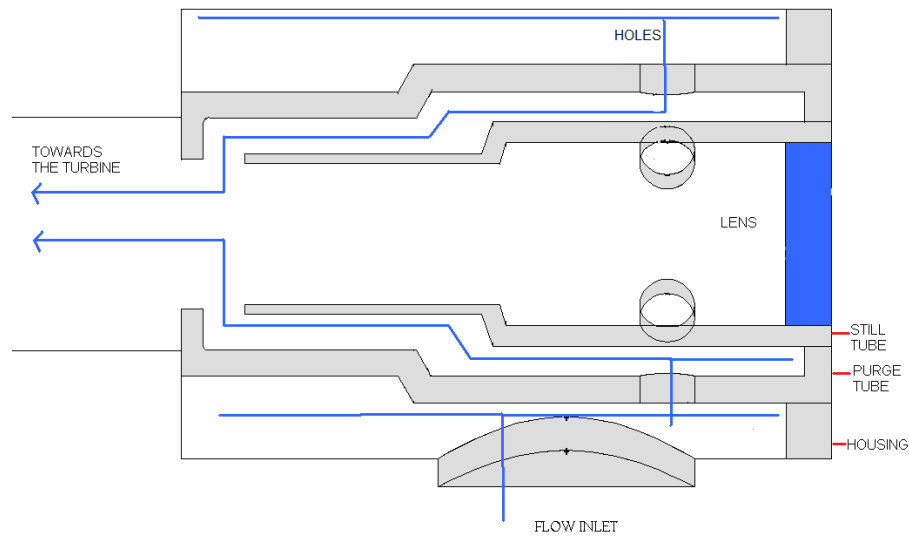
**Figure 3.28:** *Pyrometer purge system.*

It has to be considered that, since the air is fed through only one hole in the purge housing, the resultant flow will be circumferentially non-uniform. Nevertheless, the six holes on the purge tube operate as a perforated plate reducing the main non-homogeneity features of the flow.

The purge tube consists of circular and conic sections that create converging zones that accelerate the flow towards the exit. A convergent section is also present inside the still tube thus helping to create a fluid-dynamic stability: the flow is essentially still, but if there is a small increase of pressure at the outlet of the still tube, with a consequent flow directed towards the lens, the divergent section will decelerate that flow. This produces a consequent increase in the inner pressure (before the convergent part) which discourages flow migration into the tube.

The gap between the end of the still and the purge accelerates the flow coming from the purge tube and thus generating a high velocity zone that decreases the likelihood of contaminants moving towards the lens.

The pyrometer is then focusing on a spot on the turbine blade through a further tube passing through the turbine casing.

79

### 3.4.2 Similarity Theory

The similarity between two different fluid dynamic fields is verified when is also verified the equality among the dimensionless groups necessary and sufficient to describe completely the phenomenon in exam.

The dynamic similarity ensures that the ratios between specific forces are the same for the real and scaled models, thus allowing the study of a fluid dynamic phenomenon using a different scale.

This kind of similarity is the most complete and it involves geometric (the model conserves the same shape of the real scale system) and kinematics similarity (fluid streamlines similar).

Nonetheless, it is not possible to obtain the equality among all the dimensionless groups (and often among some of them); therefore it is important to choose that fundamental non dimensional numbers that can guarantee a complete description of the phenomenon under study.

The most popular non dimensional groups, by which the non dimensional conservation laws are formulated, are the following:

$$Mn = \frac{v}{a} \qquad \text{Mach Number} \qquad (3.7)$$

$$Re = \frac{vl}{v} \qquad \text{Reynolds Number} \qquad (3.8)$$

$$Sh = \frac{l}{vt^*} \qquad \text{Strouhal Number} \qquad (3.9)$$

$$Ru = \frac{\rho_f v^2}{p} \qquad \text{Ruark Number} \qquad (3.10)$$

$$Fr = \frac{v}{(gl)^{\frac{1}{2}}} \qquad \text{Froude Number} \qquad (3.11)$$

$$Pr = \frac{\mu c_p}{k_t} \qquad \text{Prandtl Number} \qquad (3.12)$$

$$Ec = \frac{v^2}{c_p \Delta T} \qquad \text{Eckert Number} \qquad (3.13)$$

Where $v$ is the velocity, $a^*$ the speed of sound, $v$ the kinematic viscosity, $l$ the characteristic length, $t^*$ the characteristic time, $\rho_f$ the fluid density, $p$ the pressure, $g$ the gravitational acceleration, $\mu$ the dynamic viscosity, $c_p$ the specific heat, $k_t$ the thermal conductivity, and $\Delta T$ the temperature gradient. Each group gives an evaluation of a different ratio: the Mach number is the ratio between the inertia and elastic forces, the Reynolds number between the inertia and viscous forces, the Strouhal number between convective time (forces) and the local characteristic time of the phenomenon, the Ruark number between dynamic pressure and the static pressure, the square Froude number between the inertia forces and gravitational forces, the Eckert number between two characteristic temperatures, while the Prandtl number depends only on the features of the fluid .

In the present work the test case implies high speed, temperatures and pressures; therefore it is necessary to decide which non dimensional group is important for the flow field under investigation as it is impossible to fulfill the equality for all the non-dimensional groups. A trade off was reached scaling the test case by a factor of ten while choosing the boundary condition in such a way to conserve the order of the Reynolds number in proximity of the exit of the still tube. In this way the same level of turbulence for both cases is ensured. Among all the possible Reynolds numbers that can be defined inside the purge air system, the one that has been chosen preserves the main features of the flow in proximity of the still tube and, consequently, the governing phenomena of the contaminants deposition. The geometric similarity is, in this way, fulfilled even if small geometric details were modified for the scaled case due to construction requirements of the test rig (i.e. transition joints, Section 3.4.3). This decision of conserving the Reynolds number instead of any other non dimensional numbers was based on the fact that the deposition of heavy particles (that are of interest in this work) is mainly controlled by drag force and turbulence (see Chapter 4). The geometric features of the purge air system are of fundamental importance for the drag force, which is mainly governed by the relative speed between the contaminants and the flow field. Another important factor that can influence the particles motion is represented by the turbulent structures. In fact, the interaction of particles with turbulent eddies can enhance the particle dispersion.

However, it will be shown in Chapter 4 that the drag force is in reality the only force controlling the contaminants deposition.

### 3.4.3   Test Rig

As it was shown in Section 3.3 the use of non-flat glass surfaces introduces high levels of distortion and reflection. Thanks to the preliminary experiment it has been seen that the RMS of the calibration function increases as more curved surfaces are used. Therefore, in order to limit the deterioration of PIV measurements, both the purge and the still tube have been scaled up and made in glass, while the housing tube has been replaced by a wooden box (Figure 3.29). The transitions joints connecting the cylindrical pyrometer parts have been made in plastic to ease the test rig construction and the still tube was hold in position thanks to the installation of additional plastic fins (Figure 3.29b). In order to decrease the reflection issue,  laser grade borosilicate glass tubes were used due to their optical properties.

Air has been fed to the box (Figure 3.29d) through an aperture positioned at the bottom of the box, where a honeycomb panel straightener has also been inserted in order to homogenize the flow. At the top of the box two glass windows allowed optical access to the cameras.

A further glass tube was installed outside the box in order to simulate the elongated tube of the test case pyrometer that passes through the turbine case.
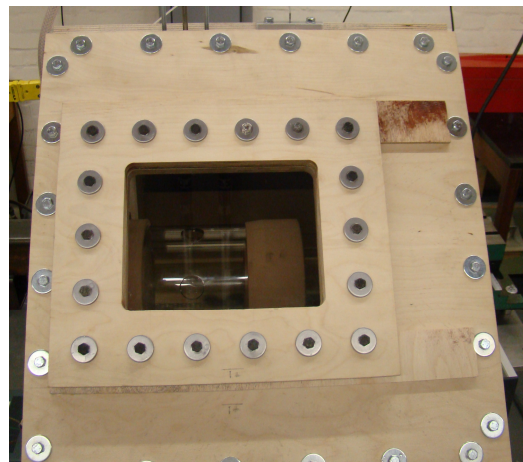
Figure 3.29: (a) Purge tube; (b) Still tube; (c) Assembly: purge/still tube system; (d) Housing box. The glass windows allow the two cameras to take pictures of the purge flow.

As described for the preliminary experiment, Section 3.3, the cameras were mounted on a traverse system in order to finely adjust their positioning along the *x,y,z* axes (Figure 3.30)

A Scheimplug angle of 7° was used.

(a)                                                            (b)
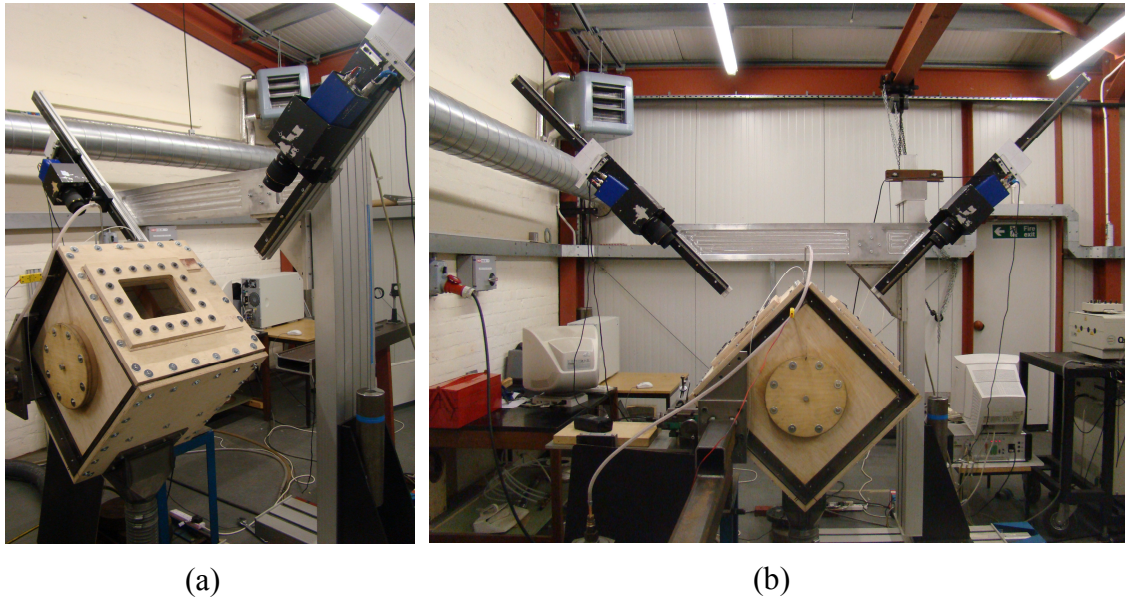
**Figure 3.30:** *Test Rig and Cameras positioning on the traverse system.*

The calibration plate was installed on a multistage holder and positioned in three different parallel positions with a displacement of 0.5 mm to each other. For each position one image per camera was taken. The set of six images was used both to correct the off axis viewing and to calculate the off plane component of the velocity.

Two main measurement planes have been chosen, one inside the still tube and one in the external elongated tube as reported in Figure 3.31.
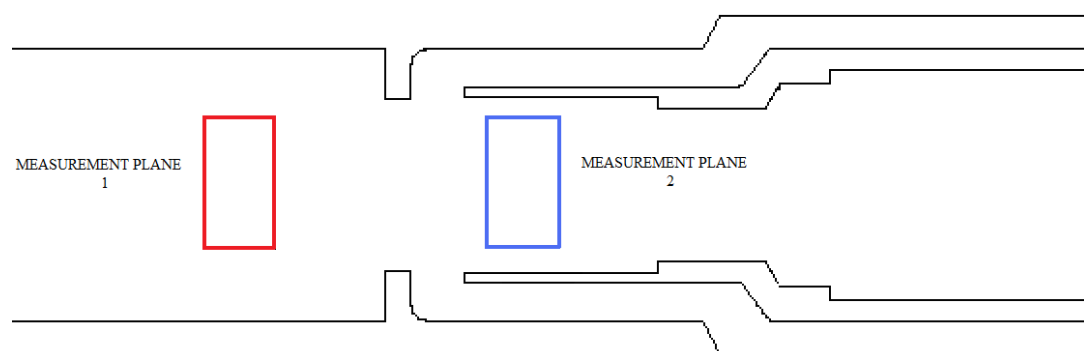


**Figure 3.31:** *Measurement planes.*

### 3.4.4   Experimental Results

In order to minimize the misregistration error (Doorne et Westerweel (2006)) one thousand images have been taken and averaged. The images have been processed via

a normalized cross-correlation with an overlap of 50%. The multipass algorithm has been used starting from an initial window 128x128 and finishing with to a final window 16x16.

The PIV results are reported in Figure 3.32 and Figure 3.33 for the measurement plane 1 and 2, respectively.
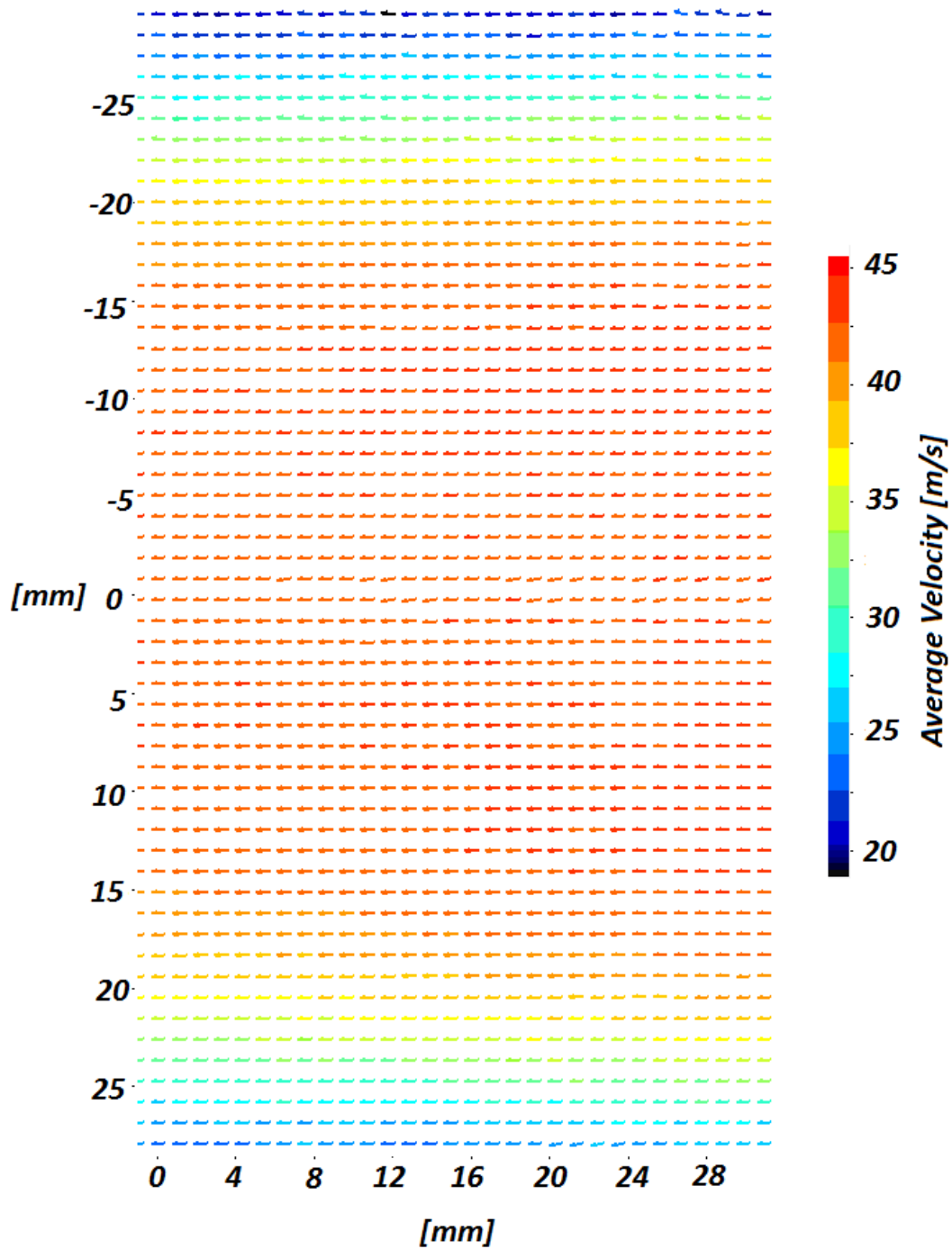


**Figure 3.32:** *PIV velocity field / measurement plane 1.*

85
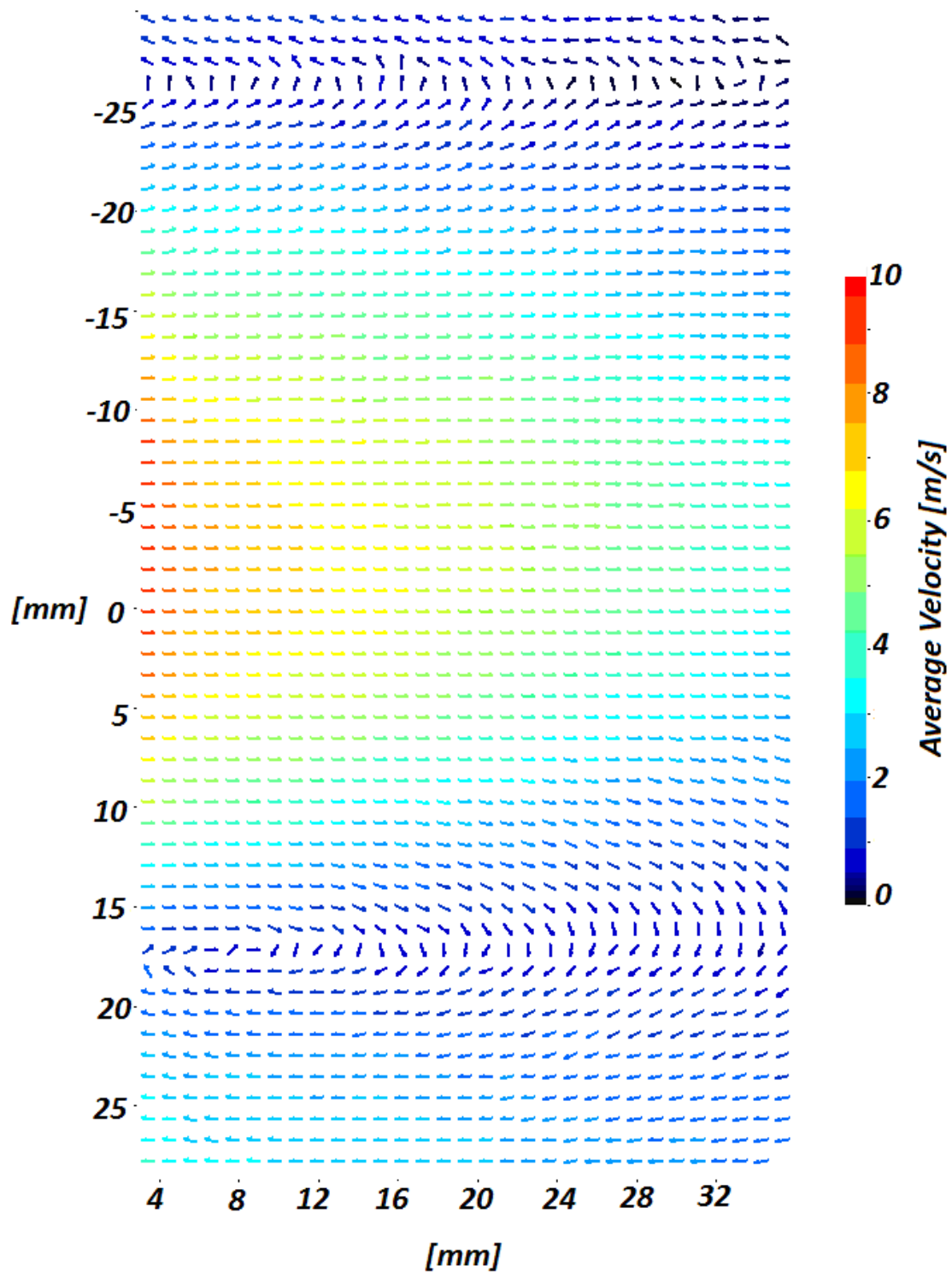
**Figure 3.33:** *PIV velocity field / measurement plane 2.*

The experiment results highlighted the presence of a recirculation zone in front of the still tube. This flow feature is the main drawback of an air curtain purge air system configuration using a still tube as it can trap eventual contaminants present in the purge air leading them towards the lens.

### 3.4.5 CFD Modeling of the Experiment

In order to judge the capability of CFD analysis to predict the main features of the purge pyrometer flow, FLUENT v12.1 has been used to modeling the large scale experiment.

An unstructured tetrahedral mesh with two million nodes for a total of ten million elements has been created utilizing GAMBIT 2.4 mesh generator.

The CFD model included the box while the tube at the exit of the purge pyrometer system has been elongated in order to apply the boundary condition of pressure outlet at the exit. This configuration is not an exact replica of the experimental setup (the pyrometer should discharge in a room). Nonetheless, it is a reasonable trade off between computational expenses and modeling of the real case.

Two different turbulence models have been analyzed: the k-ε realizable and the k-ω SST (see the CFD Section 4 for details about these models).

A detail of the computed velocity fields are reported in Figure 3.33 and Figure 3.34.
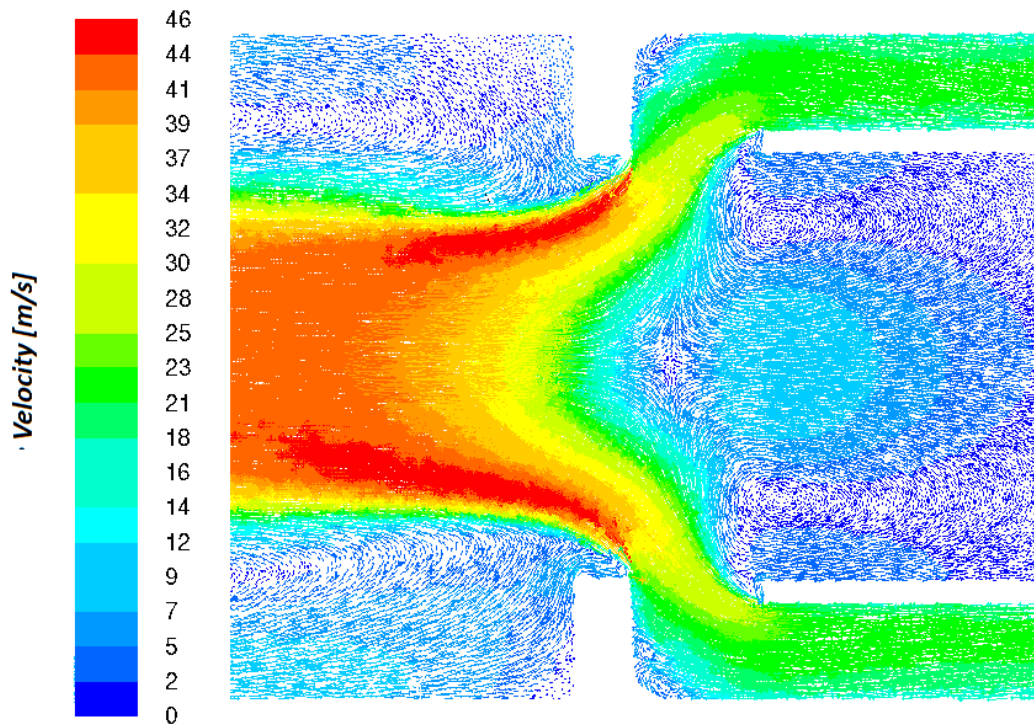
**Figure 3.34:** *k-ε realizable average velocity field.*
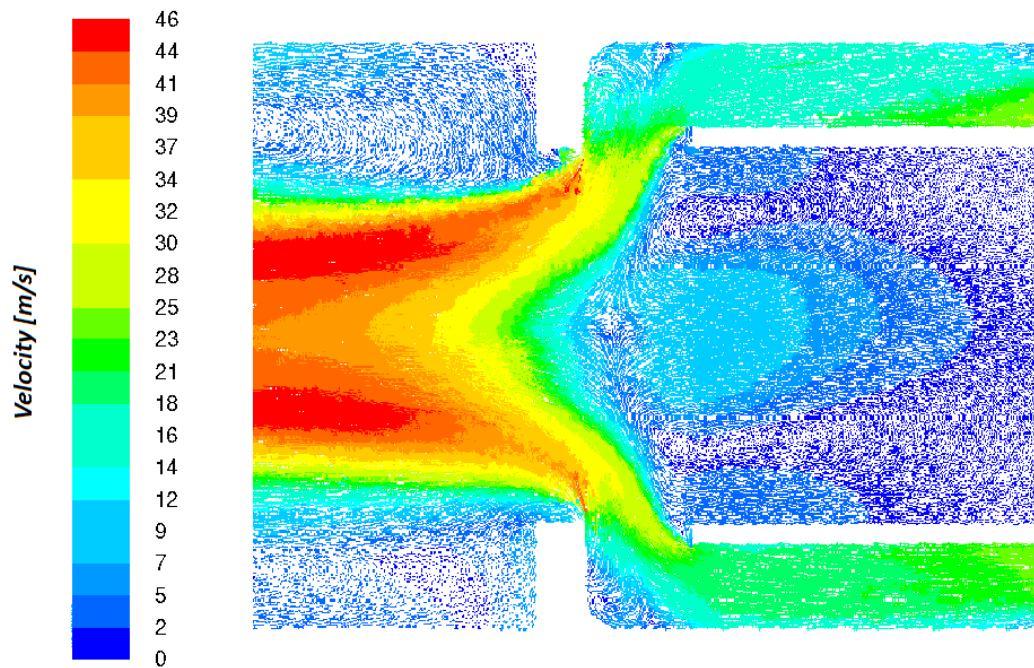


**Figure 3.35:** *k-w SST average velocity field.*

It is remarkable that while the k-ε realizable steady state solution reached convergence easily the k-ω SST started to oscillate after two thousand iterations.

From the experimental results of the single images taken in different time instants, it is clear that the flow is highly unsteady (Figure 3.36). The recirculation zone changes rapidly its position, and this phenomenon can actually affect the contaminants deposition level on the pyrometer lens. Furthermore, it is likely that this unsteadiness jeopardizes the convergence of the k-ω SST model.
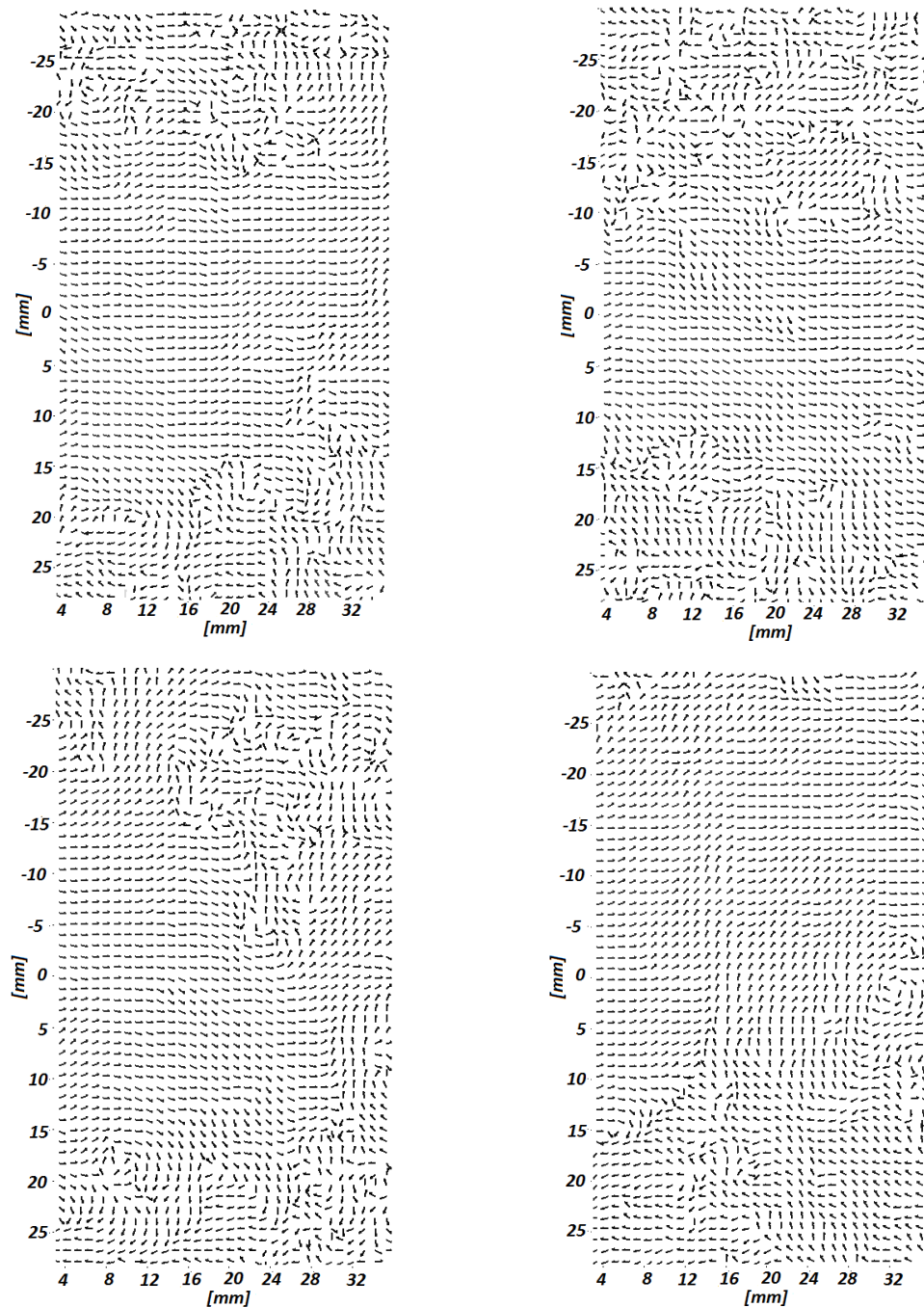


**Figure 3.36:** *Recirculation zone in different time instants (PIV results)*

As a consequence, unsteady simulations were run. Their time average velocity fields are reported in Figure 3.34, 3.35. In this case the k-ω SST model reached convergence and its averaged flow field results are reasonable. Nevertheless, a more detailed analysis of the experimental and CFD data was performed with the aim of judging the quality of the results.

The stations used for the direct comparison between the PIV and CFD results are sketched in Figure 3.37.
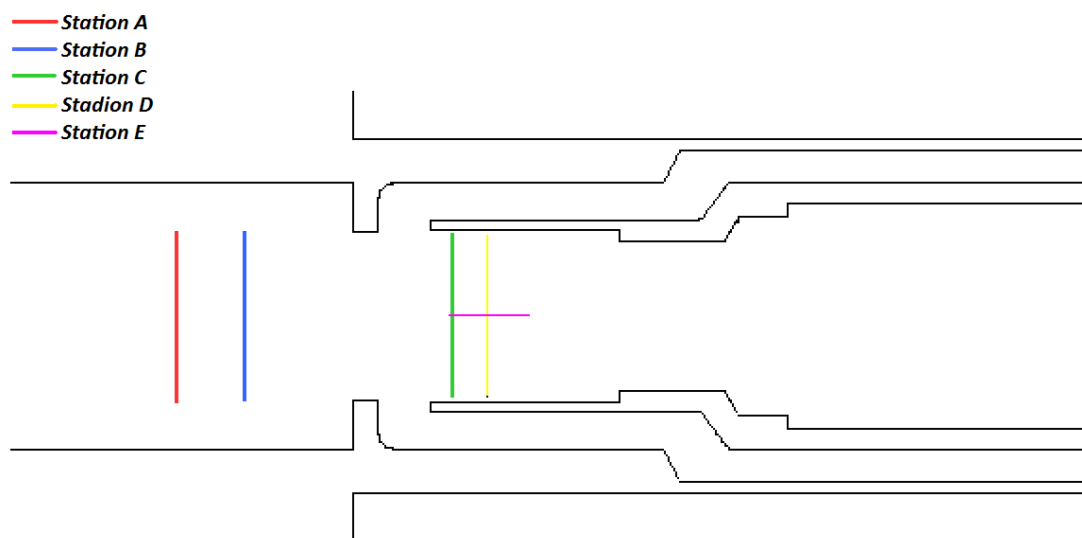


**Figure 3.37:** *Position of the stations used for direct comparison of CFD/experimental results.*

The results for station A and B are reported in Figure 3.38 and 3.39 (velocity fields)
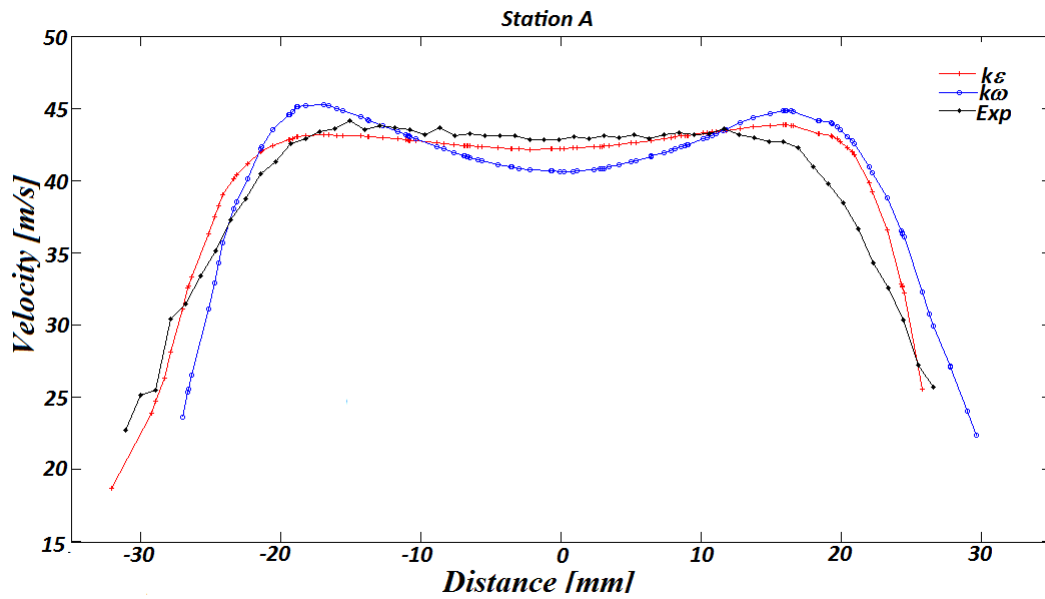
**Figure 3.38:** *Comparison of CFD/experimental results, station A.*
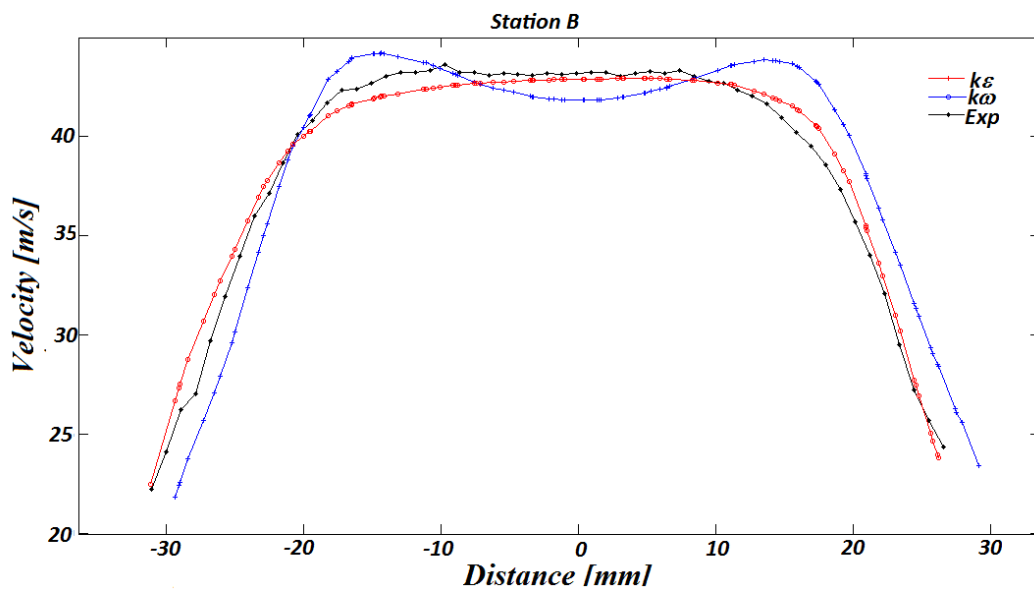


**Figure 3.39:** *Comparison of CFD/experimental results station B.*

Station A and B are in the measurement plane 1, that is in the tube outside the pyrometer purge system, where the flow reaches its maximum velocity. In this case the experimental data and the k-ε realizable model give similar results while the k-ω SST over-predicts the velocity values.

The data analysis in the recirculation zone is depicted in Figure 3.40-42.
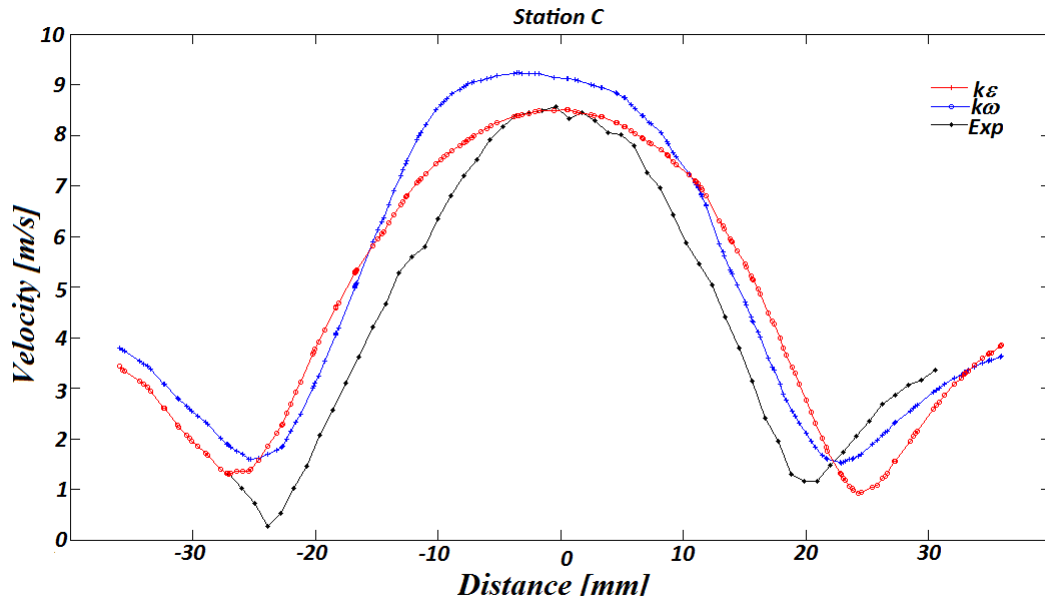
**Figure 3.40:** *Comparison of CFD/experimental results – Recirculation Zone.*
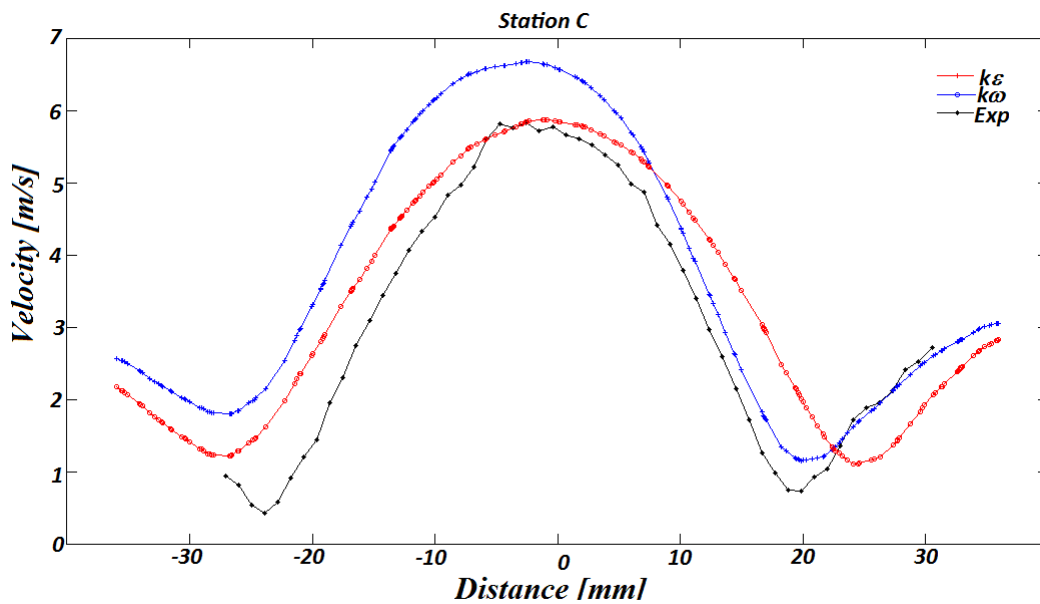


**Figure 3.41:** *Comparison of CFD/experimental results- Recirculation Zone.*
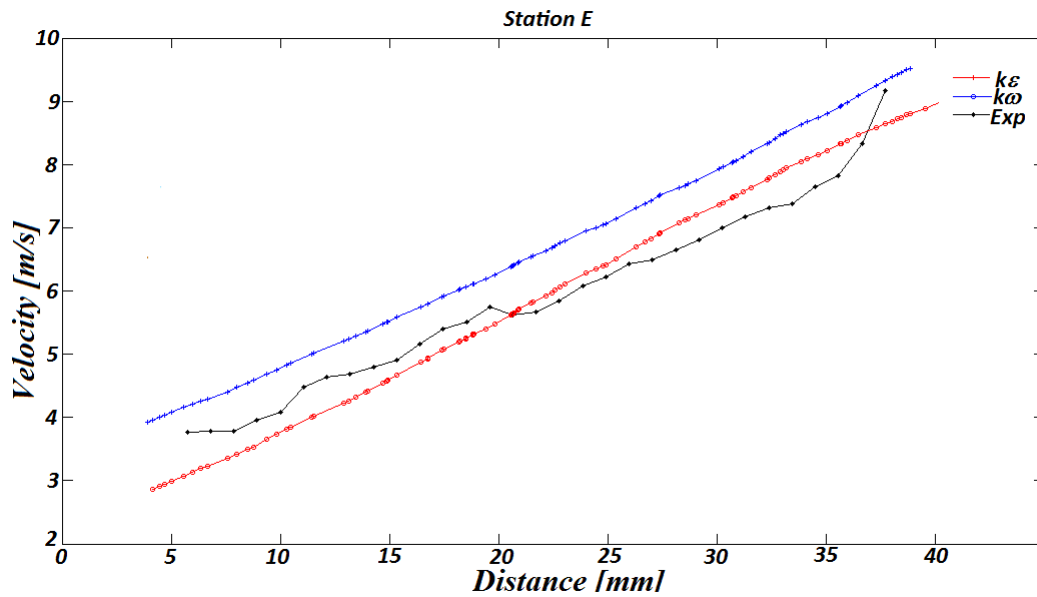
**Figure 3.42:** *Comparison of CFD/experimental results – Recirculation zone, central line.*

Both turbulence models predict higher velocities than the experimental analysis for the recirculation zone. Nevertheless, the over-prediction of the k-ω SST model is remarkably higher than that of the k-ε realizable model. Furthermore, the CFD predicted sizes of the vortexes in the recirculation zone is higher than that measured by PIV system. As for the preliminary experiment, it has to be remembered that the PIV identify just one vector for each interrogation window. Consequently this can decrease the measurements accuracy. From Figure 3.40-42 errors in the PIV output can be clearly observed in the form of asymmetry of the data. The k-ω SST model over-prediction of the average velocities values is due to an under-prediction of the dissipation of energy due to turbulence phenomena.

### 3.4.6   Conclusions

In this chapter the experimental work conducted in this research has been presented. The selected optical technique has been the Stereoscopic PIV as it allows 3D measurements of the velocity field over a plane rather than in a point. The introduction of non-flat glass surfaces introduces high level of optical distortions while reflections are generally created every time the laser sheet impacts on a surface. These reflections are augmented and multiplied as more curved glass surfaces are introduced.

The recirculation zone highlighted by the large scale experiment has been predicted both by the k-ε realizable and the k-ω SST models. Nevertheless, the k-ω SST model showed more convergence problems for the steady state solution while by over-predicting the average velocities values, due probably to an under-prediction of the dissipation of energy due to turbulence phenomena. However, both models gave feasible results and will be used in Chapter 4 to evaluate the flow in the test case pyrometer purge flow.

# Chapter 4

# Numerical Investigation of Particles Deposition Phenomena

A first insight into the flow physics of the pyrometer purge air system provided in the work of Kerr (2002a). The level of contaminants deposition on the lens has been predicted by the author via several computational fluid dynamics (CFD) analyses and described by plotting the percentage of deposited particles versus the particle diameter. Nevertheless, a number of aspects of the lens fouling process still need to be clarified. In detail, the evaluation of results is not supported by a description of the physics mechanism involved, so that their generalization is not straightforward.

The CFD analysis performed in this work is focussed on understanding the physical phenomena that bring the contaminants towards the purge pyrometer lens. The delineation of these physical processes is the first fundamental step in successfully designing a more efficient purge system configuration.

In order to tackle the problem described above, a real case regarding a pyrometer purge system installed in a well known military engine is analysed in this Chapter. This scenario was chosen as the details for a correct setting of the simulation were kindly provided by the sponsor of the present research Meggitt UK Ltd.

The computational fluid dynamic study is aimed at the particle dispersion analysis.

The CFD conclusions are then used as the baseline to explain the results of a finite element model of the contaminants/lens impacts developed in Chapter 5.

## 4.1 Contaminants Physics

The mixture made up by the contaminants and the purge flow is only one of the many examples of multiphase flows, which were for the first time analysed by Soo in 1965, and since then widely studied, as they play an important role in many natural phenomena and industrial applications. While a detailed dissertation about multiphase flows can be found in Sommerfeld (1997), Crowe et al. (1998), Soo (1990), a general theory capable of describing them is still incomplete, mostly for the lack of experiments that could validate numerical and theoretical models (Poelma (2004)).

The physics of multiphase flow depends upon many variables, among which particle shape, size and density play a fundamental role.

A first categorization of the multiphase flows can be achieved by analysing the level of mutual interaction between the contaminants and the main phase. Four main groups can therefore be identified based on the degree of coupling between the two phases:

**- One-way coupling**. In this case the mixture is regarded as dilute: the main phase regulates the particles motion, while the contaminants influence on the fluid phase is negligible (Loth (2010)). Nevertheless, the particles may be able or not to follow all the fluid motions and therefore a clustering effect can be noticed (Eaton et Fessler (1994)). Hence, when the one-way coupling assumption can be made, the numerical analysis of the multiphase physics can be simplified. The fact that the secondary phase does not affect the continuous one indicates that the particles motion can be resolved "a posteriori", after having analysed and solved the main flow field. Elghobashi (1994) states that the threshold over which the assumption of one way coupling ends corresponds to a volume loading of $10^6$, while a lower threshold can be found set at $10^5$ as in Elghobashi et Trusdell (1993);

- **Two-way coupling**. The particles affect the flow motion and vice versa. One of the mean features of this interaction is the capability of the particles to either augment or decrease the turbulence level, mainly depending upon the relative velocity between the two phases (Loth (2000)). Due to the nature of this category only a coupled treatment for the two phases is possible. For this group, many authors set a particle volume loading lying between $10^2$ and $10^5$. Nevertheless, in the scientific community disagreement exists regarding which parameter should be used to identify this category;

- **Three way coupling**. When this regime exists, the contaminants interact with each other, although there is not direct contact between the particles. In fact, the particles can affect the motion of other particles by modifying the surrounding flow field (through aerodynamic forces and the eventual presence of wakes);

- **Four-way coupling**: The particles interact directly through relative collisions. This can happen only if the contaminants volume concentration is higher than 10% (Loth (2010)).

In this work, it has been chosen to consider the contaminants/purge flow system included into the one-way coupling category. This assumption has been based on the hypothesis that an aircraft engine in standard operating condition ingests a limited contaminants amount. Therefore, the present analysis is limited to a maximum contaminants volume load of $10^5$ (Elghobashi et Truesdell (1994)).

Furthermore, it is important to stress that all the considerations carried out in the present Chapter are valid only if the main phase can be approximated as a continuum with respect to the dispersed one. It can be found in Loth (2000) that this condition is verified only if the free mean path of the fluid is negligible when compared to the particle size. The average free mean path for a gas expressed by the distance $l_{m-m}$ between two gas molecules $m$ and $m$ is given by the following formula:

$$l_{m-m} = \frac{2\mu_g}{\rho_f V_{m-m}} \qquad (4.1)$$

Where $\mu_g$ and $\rho_f$ are respectively the dynamic viscosity and the density of the fluid, while $V_{m\text{-}m}$ is the average root mean square of the molecules speed.

Considering the ideal gas law, $V_{m\text{-}m}$ is given by:

$$V_{m-m} = \sqrt{\frac{8}{\pi} R_g T_g} \quad (4.2)$$

With $R_g$ the gas constant ant $T_g$ its temperature.

## 4.2 Eulerian and Lagrangian Approaches

As summarized by Dehbi (2008), in order to study particles dispersion two different particle tracking approaches can be followed: the Eulerian and the Lagrangian method.

In the Eulerian approach the dispersed phase is handled in the same way of the flow phase, therefore as a continuum controlled by its own set of conservation laws. This approach is usually applied for dense flows in which the interaction level can be regarded as part of the four way coupling category.

In spite of its efficiency (Zhang et Prosperetti (1994)) the Eulerian method has the main drawback of being characterized by the complexity arising from the necessity of delineating accurately the exchange rates between the two phases and of defining appropriate closure laws (Drew (1983)). A simplified Eulerian approach is known as the mixture fraction method (Baxter (1989)) and it can be used when the secondary phase can be safely approximated as a scalar. This simplification of the problem can be applied only if the dynamic and the thermodynamic transport rates between the main and the secondary phase are considered to be sufficiently fast (Faeth (1983)). Therefore, when this assumption is valid the dispersed phase has the same temperature and velocity of the main phase in each point of the domain. This hypothesis allows to avoid considering two different phases in the domain. Instead, the flow field can be completely described by one single phase having the properties

of a local mixture described by the local concentration of the dispersed phase. Nevertheless, this approach is not of interest in the pyrometer purge flow analysis as it implies considering only that contaminants with an inertia such that they act as a flow tracers. Furthermore, with the complete Eulerian approach, modelling eventual reflections or erosion phenomena at the domain boundaries is not straightforward. In despite of all these complications, a successful application of the Eulerian approach can be found in Mostafa's et Elghobashi's work (1985).

The Lagrangian method is applicable only when the particle volume load is less than 10% of the total volume and therefore only if the relative interaction between particles is negligible. This approach can accurately predict the dispersion of particles by resolving firstly the flow field (considered as a continuum) and then calculating the trajectory of an appropriate number of injected particles (considered as a dispersed phase) (Maxey (1987)). The trajectory of the single particles (described as moving points with their own velocities and properties) is then obtained by estimating the effect of the forces acting on each particle (i.e. drag, gravity, lift, thermophoretic force) through Newton's second law. Consequently, the Lagrangian approach is computationally expensive, because it necessitates a simultaneous tracking of a large number of particles until stationary statistics is reached (Loth (2010)).

As stated before, in the present work the system given by the purge flow and the contaminants is treated as a one way coupling system and therefore the Lagrangian approach has been used.

As a consequence, the analysis has been conducted through two main steps, resolving firstly the main flow field and then using these results as a baseline for the particles injection.

## 4.3 Main Flow Phase – Domain Definition

The installation of the pyrometer inside the turbine casing is a critical aspect in ensuring a correct reading of the turbine blades temperature: it can enhance or decrease the reflections amount (as explained in Section 2.1.4.1) and it can affect the efficiency of the purge air system. In fact, a change in the pyrometer installation configuration implies a modification of the relative angle between the turbine flow

and the optical device, thus easing or slowing down the penetration of gas turbine contaminants into the pyrometer sight tube.

In order to minimise the likelihood of the lens collecting the reflection of the radiant energy emitted by the combustion fireball, the pyrometer is usually located after the first stage of the high-pressure turbine where it takes temperature measurements of a specific spot on the blade suction surface (Figure4.1a).

In the engine under study, the pyrometer is installed at the pitch angle and at the yaw angle, with respect to the axis of rotation sketched in Figure4.1a, 4.1b (the values are not here reported for confidentiality reasons). The analysis of the velocity triangles (Section 4.2.2) shows why this configuration reduces the likelihood that particles carried by the gas turbine flow could reach the pyrometer sight tube.



(a)



(b)                                    (c)
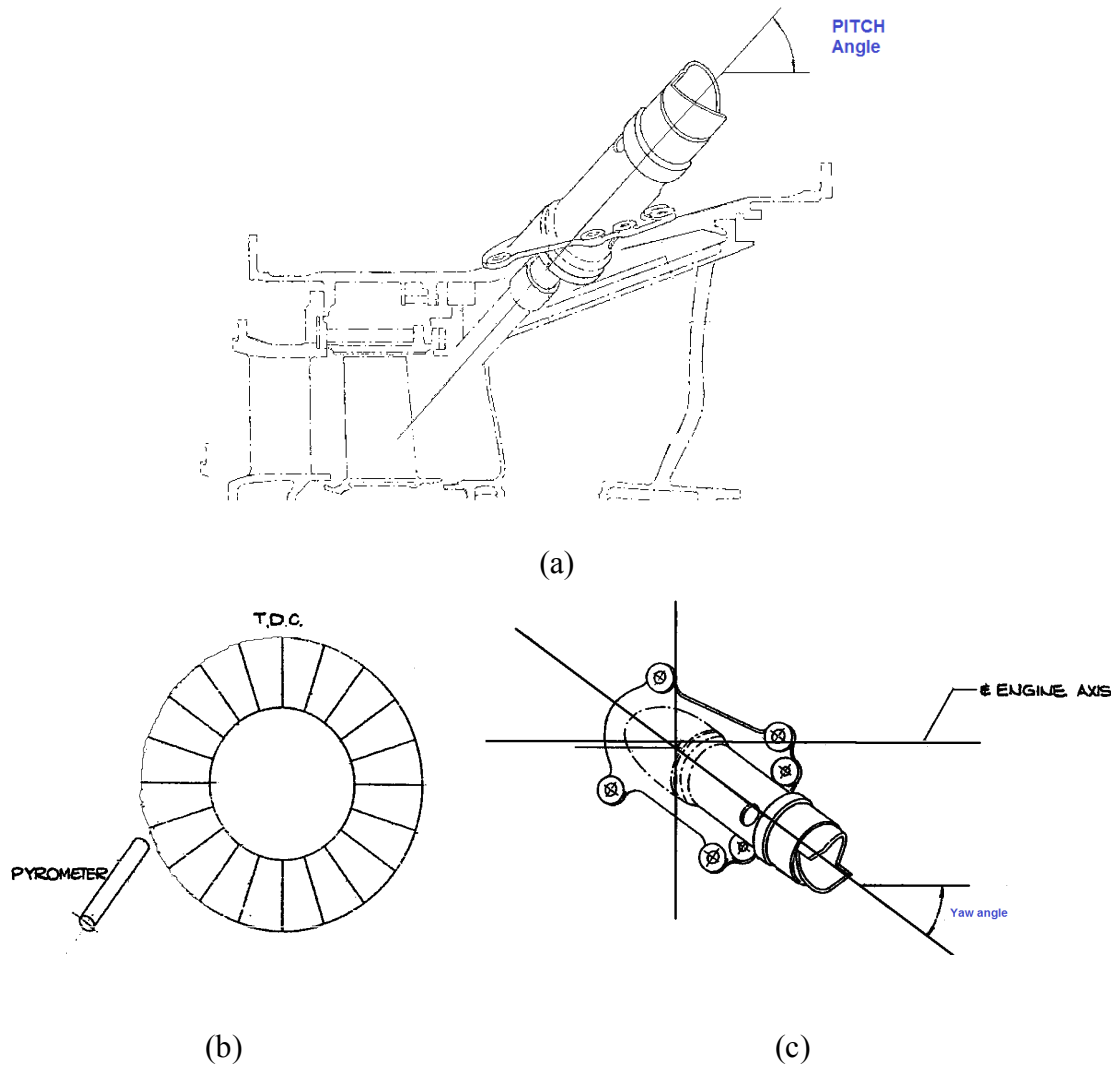
**Figure 4.1**: *(a) Pyrometer installation – Pitch angle (b) Installation of the pyrometer, prospective view(c) Installation of the pyrometer – Yaw angle.*

The purge air system type is characterised by an air curtain configuration obtained via a still tube, as described in Section 2.2.1.2.

A description of the pyrometer purge air system is not provided here as it can be found in Chapter 3, where the large scale model experiment design has been based on the same purge pyrometer configuration under investigation.

The CFD model comprises the pyrometer, the tube passing through the casing (here referred to as the elongated tube) and a section of the turbine annulus, which has been extended in order to ensure a fully developed flow at the pressure outlet boundary. The turbine-casing arc that has been reproduced is large because the sides of the section have been modelled as periodic boundaries: the flow conditions on one side have to be the same of the other one. Nevertheless, this is a reliable assumption only if the boundaries are far from the flow disturbances generated by the presence of the pyrometer purge system.

## 4.4 Main flow phase  - Flow Boundary Conditions

In order to define the boundary conditions of the CFD model and to describe the working scenario of the purge pyrometer system it is necessary to obtain data of the engine in which the pyrometer is installed.

In the present research, the pyrometer under investigation is installed in a military aircraft. Since detailed information of the engine is not available from its manufacturers for confidentiality issues, it has been necessary to obtain an approximation of the required data by means of a simulation program.
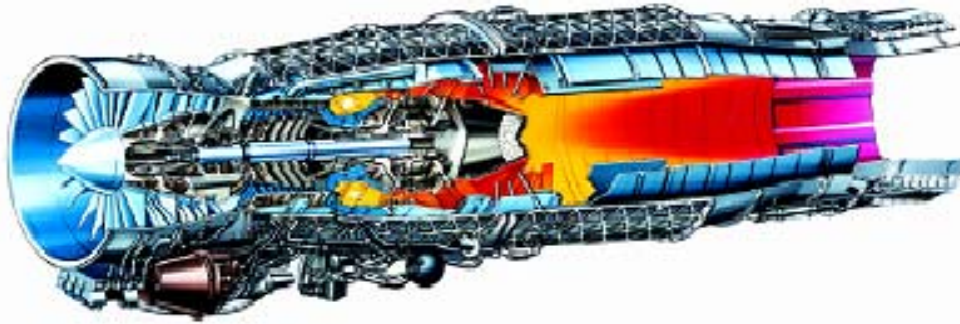
**Figure 4.2:** *Cross section of the engine under study.*

Shown in Figure 4.2 is a cross section of the engine. Table 4.1 provides the details of some of the engine specifications, which are of a public domain and available on internet.

| Engine Specification | |
|---|---|
| Length [m] | ≈ 4.0 |
| Diameter [m] | ≈ 0.85 |
| Dry thrust [kN] | > 60 |
| With reheat [kN] | > 90 |
| Bypass ratio | 0.4:1 |
| Total pressure ratio | 25:1 |
| Fan ratio | 4.2:1 |
| Air mass flow [kg/s] | 77 |
| SFC dry [g/kN,s] | 23 |
| SFC reheat [g/kN,s] | 49 |

**Table 4.1:** *Engine specification.*

The engine under study is an advanced design based on a fully modular augmented twin-spool low bypass layout.

The air entering the engine is compressed firstly by a three stage low-pressure fan and then by a five stage high-pressure compressor. Throughout the three-stage fan, it is possible to achieve a pressure ratio of a 4.2:1 and, if the take off condition is considered, an air mass flow of about 75/77 kg/s.

It is also well worth noting that the overall pressure ratio obtained through eight stages is 25:1.

The air, after being compressed, enters an annular combustor where high temperatures are achieved (up to 1800 K) for ensuring high engine performance.

Nevertheless, the high temperature at the outlet of the combustor requires particular precautions to be applied at the entrance of the high-pressure turbine, since the maximum temperature can exceed the melting point of the blades. For this reason, the blades of the engine are protected against the high temperatures by using air cooling channels, which however adversely affect the achievable air combustion temperature and consequently the engine efficiency. Thermal barrier coatings are not used, thus avoiding the emissivity issue (Section 2.4.2) that could jeopardise the correct pyrometer functioning.

### 4.4.1   Model of The Engine -Turbomatch Analysis

A model of the engine under study is mandatory in order to deduce where the purge air is drawn from.

The code Turbomatch, developed by the School of Engineering at Cranfield University, provides a means for predicting the performance of the gas turbine engine under study. It is a FORTRAN based code. It exploits thermodynamic cycle principles, and the conservations laws to simulate the design, off-design and deteriorated function points for different operating conditions (Ntantis (2008))

To define the boundary conditions of the problem it is necessary to extract information on the purge air supply (determined by the air coming from the compressor) and on the flow in proximity of the purge air discharge point onto the turbine main flow path (determined by the conditions after the first stage of the HP turbine). The scheme of the Turbomatch model used is sketched in Figure 4.3.
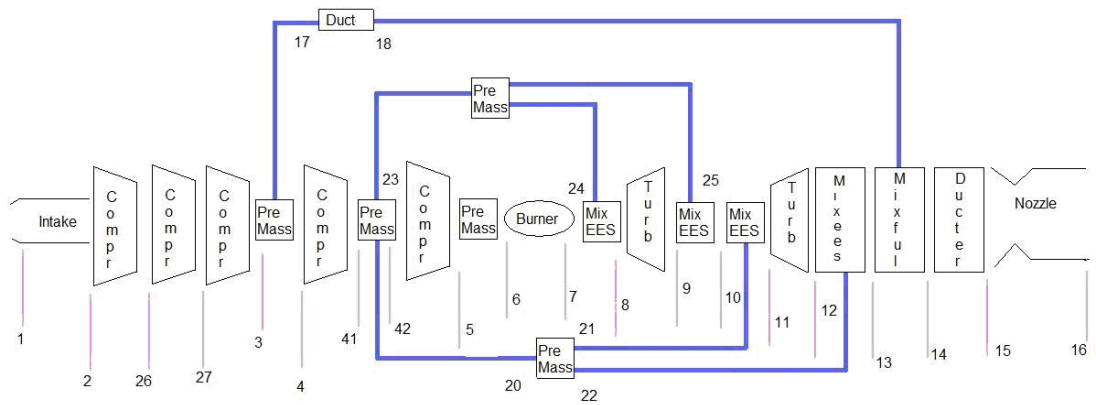
**Figure 4.3:** *Turbomatch scheme of the engine under examination.*

The results of the simulation during the cruise phase at Mach 1.2 and at an altitude of 11000 m are reported in Table 4.2.

| Station | F.A.R. Fuel/Air ratio | Mass Flow [kg/s] | Pstatic [Atm] | Ptotal [Atm] | Tstatic [K] | Ttotal [K] |
|---|---|---|---|---|---|---|
| 1 | 0.00000 | 41.800 | 0.22330 | 0.54178 | 216.65 | 279.26 |
| 2 | 0.00000 | 41.800 | ****** | 0.53636 | ****** | 279.26 |
| 3 | 0.00000 | 41.800 | ****** | 2.25955 | ****** | 452.19 |
| 4 | 0.00000 | 25.385 | ****** | 2.25955 | ****** | 452.19 |
| 5 | 0.00000 | 24.184 | ****** | 13.95774 | ****** | 807.96 |
| 6 | 0.00000 | 21.765 | ****** | 13.95774 | ****** | 807.96 |
| 7 | 0.03105 | 22.441 | ****** | 13.27499 | ****** | 1800.00 |
| 8 | 0.02881 | 24.134 | ****** | 13.27499 | ****** | 1736.96 |
| 9 | 0.02881 | 24.134 | ****** | 4.87649 | ****** | 1434.34 |
| 10 | 0.02794 | 24.859 | ****** | 4.87649 | ****** | 1417.59 |
| 11 | 0.02786 | 24.935 | ****** | 4.87649 | ****** | 1415.35 |
| 12 | 0.02786 | 24.935 | ****** | 1.94416 | ****** | 1180.56 |
| 13 | 0.02765 | 25.113 | 1.85360 | 1.94416 | 1163.76 | 1176.83 |
| 14 | 0.01654 | 41.528 | 1.85147 | 1.98508 | 894.37 | 910.04 |
| 15 | 0.01654 | 41.528 | ****** | 1.88583 | ****** | 910.04 |
| 16 | 0.01654 | 41.528 | 0.54258 | 1.88583 | 661.42 | 910.04 |
| 17 | 0.00000 | 16.415 | ****** | 2.25955 | ****** | 452.19 |
| 18 | 0.00000 | 16.415 | 1.85415 | 2.14657 | 433.92 | 452.19 |
| 19 | 0.00000 | 0.000 | ****** | 0.00000 | ****** | 0.00 |
| 20 | 0.00000 | 0.254 | ****** | 5.35254 | ****** | 601.16 |
| 21 | 0.00000 | 0.076 | ****** | 5.35254 | ****** | 601.16 |
| 22 | 0.00000 | 0.178 | ****** | 5.35254 | ****** | 601.16 |
| 23 | 0.00000 | 2.418 | ****** | 13.95774 | ****** | 807.96 |
| 24 | 0.00000 | 1.693 | ****** | 13.95774 | ****** | 807.96 |
| 25 | 0.00000 | 0.726 | ****** | 13.95774 | ****** | 807.96 |
| 41 | 0.00000 | 25.385 | ****** | 5.35254 | ****** | 601.16 |
| 42 | 0.00000 | 24.184 | ****** | 5.35254 | ****** | 601.16 |

**Table 4.2:** *Turbomatch data at cruise condition Mach=1.2 altitude=11000m With ** *data not available*

Examining the output of Turbomatch, it is possible to deduce that the purge air is drawn from the compressor. In fact, it is possible to exclude the duct (stations 17/18 in Figure 4.3) as a source of the purge air, since in this case the inlet pressure of the purge air system would be below the outlet pressure, corresponding to the conditions downstream of the HP turbine rotor.

Therefore, during the first stage of the research the final boundary conditions for the pyrometer model were therefore chosen by assuming that the purge air is bled from an intermediate compressor stage and imposing a 1.6 pressure with the turbine pressure values. In a second phase of the research, these values were then adjusted to the data coming directly from the manufacturer but are not reported here for being categorised as classified.

### 4.4.2 HP Turbine Velocity Triangles

Useful information can be found in the work of Zilli (2004), who used some sketches of the engine from the literature to deduce some fundamental geometric features. Thanks to an iterative process, initialized with the dimensions taken directly from the drawings in Jane's Information Group (2003), he refined the engine geometry by means the guidelines and limitations available for the real engine.

The annulus area dimensions of the HP turbine are assumed to be:

$$D_{inner} = 0.464 \ [m]$$
$$D_{outer} = 0.560 \ [m]$$
$$D_{mean} = 0.512 \ [m]$$
$$A_n = 0.0772 \ [m^2]$$

The hub to tip ratio is 0.825. The annulus dimensions have been subjected to a slight modification in order to accommodate the boundary conditions fixed by Turbomatch

for the simulation of the engine. Considering the velocity triangles, sketched in Figure 4.5, the results obtained are reported in the Table 4.3.
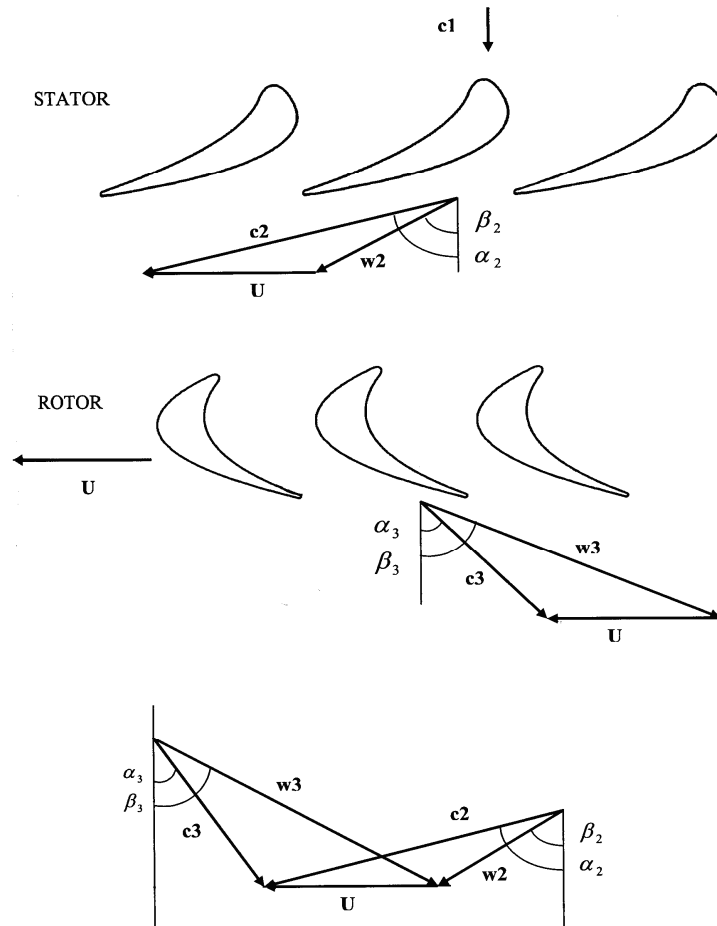


**Figure 4.4:** *Velocity triangles.*

| Position | $\alpha_3$ [deg] | $c_3$ [m/s] |
|----------|------------------|-------------|
| Hub | 52.19 | 572.88 |
| 25% | 50.78 | 555.46 |
| 50% | 49.43 | 539.98 |
| 75% | 48.19 | 526.17 |
| Tip | 46.88 | 513.78 |

**Table 4.3**: *Kinematics turbine flow field*

All the calculations were performed by using an iterative process in order to accomplish the conservation laws regulating the flow.

Ultimately, to obtain the final angle between the pyrometer and the flow inside the turbine, the angles of the velocity triangles and of the installation of the pyrometer have to be combined. It has to be stressed that the direction of rotation of the rotor blades in Figure4.5 corresponds to the British design practice whereby the engine rotates in a clockwise direction when looking downstream.

It is therefore clear that the two angles $\alpha_3$ and $\psi$ in Figure4.5 and Figure 4.6, respectively, are to be added.
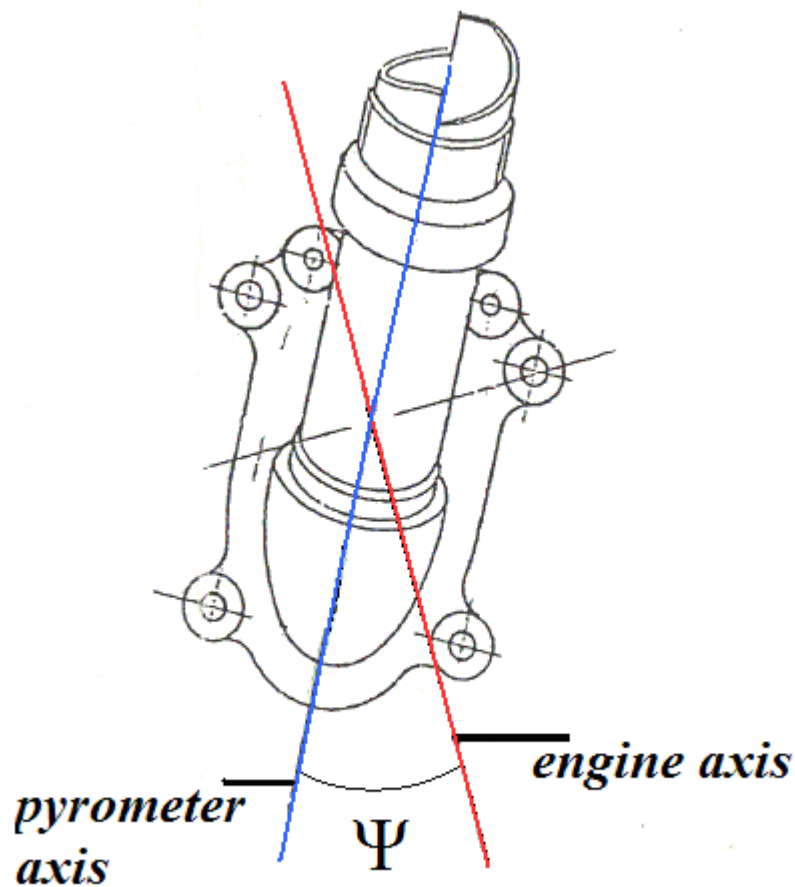


**Figure 4.5:** *Installation of the pyrometer.*

Therefore, based on this work, it can be concluded that the relative angle between direction of the flow downstream of the first HP turbine rotor and the pyrometer axis is comprised in a range between 80° to 90°. In general, for the pyrometer installation this value is highly recommended because it prevents the flow from being directed towards the lens.

### 4.4.3  Fluent Modelling

The geometry of the pyrometer was decomposed in a different set of sub-volumes to create, where possible, a structured mesh in order to improve the quality of the numerical simulation.

GAMBIT was used to generate the mesh. Nevertheless, due to the complexity of the flow developing inside the purge system, some refinements were needed and performed in FLUENT in order to obtain a convergent solution. The final mesh was made of 12 million nodes and a grid independency study was not possible as a further refinement of this mesh was computationally too expensive.

In the latest FLUENT version 12.1, the pressure and the density based solvers were reformulated, and both adapted to solve a wide range of flows, in contrast with their capabilities in the previous FLUENT versions. Both methods solve the velocity field from the momentum equations. However, while the density-based approach obtains the density and the pressure fields from the continuity equation and the equation of state, the pressure-based method solves a pressure (or a pressure correction) equation obtained from a manipulation of the continuity and momentum equations (FLUENT (2009)).

A high resolution of the flow field can be obtained by combining the pressure-based solver with a coupled approach. This method is preferable to the segregated algorithm, which solves the momentum equation and pressure correction equations separately, which determines a slow convergence. The coupled algorithm, instead, solves the momentum and pressure-based continuity equations together, thus improving both convergence velocity and accuracy (FLUENT (2009)).

The turbulence was simulated through different turbulence models and the relative results were compared.

### 4.4.3.1 Turbulence Formulation

The turbulence flow can be thought as made up of eddies of different sizes, each characterised by a length scale, a time scale and a velocity scale. The biggest vortices, characterized by an integral length scale, break up in smaller vortices that then undergo the same process. This process is known as energy cascade, where energy is transferred from the bigger to the smaller eddy. This process continues until the eddy characteristic length is so small that the viscosity of the fluid can effectively dissipate the kinetic energy into internal energy. In fact, at this point, velocity gradients are so high that the viscous stresses, that are proportional to them, dissipate the energy of the flow and therefore no turbulent structures smaller than this (known as Kolmogorov's scale) can exist.

When the particle is immersed in a turbulent flow it interacts with the whole range of eddies. Therefore, this implies that, in order to correctly estimate the particle motion, each eddy should be correctly simulated. This can be achieved through Direct Numerical Simulation (DNS), in which the turbulent field is completely solved without recurring to filtering or empirical modelling. Nevertheless, as it is shown in the paper of Piomelli (1997) the computational grid should be in the order of the $Re^4$. This implies that nowadays DNS can be used only to solve very simple flow fields.

Therefore, time dependent solutions of the Navier-Stokes equations are often unfeasible when complex geometries and high Reynolds numbers are involved. Common approaches to address this issue are known as:

- Reynolds Averaging;
- Filtering.

### 4.4.3.2 Reynold Averaging Navier Stokes Equations

In a turbulent flow the inertia forces are significantly higher than the viscous forces. Despite the deterministic nature of the Navier-Stokes equations, a statistic approach is

necessary when modelling turbulence, because it is demonstrated that very small variations on the initial boundary conditions can lead to substantial different results.

The flow field variables are decomposed in a steady mean value and a fluctuating one, i.e. for the component along the x axis the velocity $u$ is:

$$u(t) = \bar{u} + u'(t) \qquad (4.3)$$

Where $\bar{u}$ is the average value and $u'(t)$ is the fluctuating one. A detailed discussion about the Reynolds Averaged Navier-Stokes (RANS) models can be found in the work of Vandromme (1997). Here, only the main features of these models are summarised.

The scalar fluid variables, decomposed into the mean (ensemble-averaged or time-averaged) and fluctuating components, are substituted into the exact instantaneous Navier-Stokes equations and then time averaged. In the resultant equations, new terms appear, representing the turbulent contribution to the momentum transport. The momentum conservation law becomes:

$$\frac{\partial}{\partial t}\left(\rho_f u_i\right) + \frac{\partial}{\partial x_j}\left(\rho_f u_i u_j\right) = -\frac{\partial p}{\partial x_i} + \frac{\partial}{\partial x_j}\left[\mu\left(\frac{\partial u_i}{\partial x_j} + \frac{\partial u_j}{\partial x_i} - \frac{2}{3}\delta_{ij}\frac{\partial u_l}{\partial x_l}\right)\right] + \frac{\partial}{\partial x_j}\left(-\rho_f \overline{u_i' u_j'}\right) (4.4)$$

Where $\left(-\rho_f \overline{u_i' u_j'}\right)$ is the Reynolds stress tensor.

The introduction of this new unknown means that there is a closure problem to be tackled because the equation system to be solved is now under-constrained. The most common way to deal with the closure problem is to use the Bousinnesq hypothesis for which the Reynolds stresses can be expressed in terms of the velocity gradient through a new flow property called turbulent viscosity, $\mu_t$. In detail, the Bousinnesq hypothesis is formulated as:

$$-\rho_f \overline{u_i' u_j'} = \mu_t\left(\frac{\partial u_i}{\partial x_j} + \frac{\partial u_j}{\partial x_i}\right) - \frac{2}{3}\left(\rho_f k + \mu_t \frac{\partial u_k}{\partial x_k}\right)\delta_{ij} \qquad (4.5)$$

Where $k$ is the turbulent kinetic energy defined as:

$$k = \frac{1}{2}\left( \overline{\left(u_1^{'}\right)^2} + \overline{\left(u_2^{'}\right)^2} + \overline{\left(u_3^{'}\right)^2} \right) \quad (4.6)$$

It has to be noted that Bousinnesq formulation considers the turbulent viscosity as a scalar quantity and this is not strictly true.

The RANS models are usually differentiated on the number of equations used to close the problem. Being the aim of this work the analysis of the contaminants dispersion, the models that are not capable of giving information on the eddy time and length scales are not discussed here (zero and one equation models).

### 4.4.3.3 RANS k-ε

This is a two-equation semi-empirical method that requires the introduction of two further equations to overcome the closure issue. The two main turbulent variables are the kinetic energy $k$ and the turbulent dissipation rate $\varepsilon$. The model transport equation for $k$ is derived from the exact equation, while the model transport equation for $\varepsilon$ has been based on physical considerations. The turbulent viscosity is defined as:

$$(4.7)$$

The constant $C_\mu$ of this model derives from experimental analyses and in the standard k-ε its value is set to 0.09 (FLUENT (2009))

Three different models are available in FLUENT:

- Standard. It is valid only for fully developed turbulent flows.
- Re-Normalization Group (RNG). Improved version of the k-ε model that takes in account for low Reynolds number effects and the consequences of swirls on turbulence. Therefore it is more accurate and reliable than the standard method.
- Realizable model. It satisfies mathematical constraints on the Reynolds stresses, whereas neither the standard nor the RNG are realizable. The

realizable model provides a better prediction of the boundary layer under strong adverse pressure gradients, separation, and recirculation conditions.

Being the flow field inside the pyrometer purge system characterized by both high and low speeds, the RNG model was utilized in the present analysis as it takes in account the effect of low Reynolds number. The k and $\varepsilon$ equations are expressed as:

$$\frac{\partial}{\partial t}(\rho_f k) + \frac{\partial}{\partial x_i}(\rho_f k u_i) = \frac{\partial}{\partial x_j}(\alpha_k \mu_{eff} \frac{\partial k}{\delta x_j}) - \rho_f \overline{u_i' u_j'} \frac{\delta u_j}{\partial x_i} + G_k + G_b - \rho_f \varepsilon - Y_M$$

(4.8)

$$\frac{\partial}{\partial t}(\rho_f \varepsilon) + \frac{\partial}{\partial x_i}(\rho_f \varepsilon u_i) = \frac{\partial}{\partial x_j}(\alpha_k \mu_{eff} \frac{\partial \varepsilon}{\delta x_j}) + C_{1\varepsilon} \frac{\varepsilon}{k}(G_k + C_{3\varepsilon} G_b) - C_{2\varepsilon} \rho_f \frac{\varepsilon^2}{k} - R_\varepsilon$$

(4.9)

The generation of $k$ due to mean velocity gradient is represented by $G_k$ while that due to buoyancy by $G_b$. $Y_M$ is the contribution of the fluctuating dilatation in compressible turbulence to the overall dissipation rate, $\alpha_\varepsilon$ and $\alpha_k$ are the inverse effective Prandtl numbers. $C_{1\varepsilon}$, $C_{2\varepsilon}$, and $C_\mu$ are constants while $\mu_{eff}$ is the effective viscosity. $R_\varepsilon$ is the terms that allow the RNG k-$\varepsilon$ model to quickly response to high strain rate. For a detailed description and derivation of the terms in Eq. 4.8 and 4.9 please refer to FLUENT(2009)

### 4.4.3.4 RANS k-ω

This is a two-equation empirical model developed by Wilcox (1993) to take into account the effects of low Reynolds numbers, compressibility, and shear flow spreading. The two main field variables are the turbulent kinetic energy $k$ and the specific dissipation $\omega$. Since its first formulation, this method has been modified to increase its accuracy.

In detail one of the most important developments is the model introduced by Menter (1993), that combines the $k$-$\omega$ and the $k$-$\varepsilon$ models by using one or the other method in

the zone of the domain where they perform best: standard $k$-$\omega$ in the inner region of the boundary layer, and a high-Reynolds-number version of $k$-$\varepsilon$ in the outer part of the boundary layer. This RANS model is called shear-stress transport (SST) $k$-$\omega$ and includes also a modified turbulent viscosity formulation to account for the transport effects of the principal turbulent shear stresses. The $k$-$\omega$ equations are expressed as it follows:

$$\frac{\partial}{\partial t}(\rho_f k) + \frac{\partial}{\partial x_i}(\rho_f k u_i) = \frac{\partial}{\partial x_j}\left(\Gamma_k \frac{\partial k}{\partial x_j}\right) + \widetilde{G}_k - Y_k \qquad (4.10)$$

$$\frac{\partial}{\partial t}(\rho_f \omega) + \frac{\partial}{\partial x_i}(\rho_f \omega u_i) = \frac{\partial}{\partial x_j}\left(\Gamma_\omega \frac{\partial \omega}{\partial x_j}\right) + G_\omega - Y_\omega + D_\omega \qquad (4.11)$$

Where $Y_k$ and $Y_\omega$ represents the dissipation terms of k and $\omega$ respectively. The generation of k and $\omega$ are given by terms $\widetilde{G}_k$ and $G_\omega$ and the cross diffusion term is represented in Eq.4.11 by $D_\omega$. For a detailed description of these terms please refer to FLUENT (2009).

### 4.4.3.5 Large Eddy Simulation

Large Eddy Simulation (LES) formulation is based on a different conceptual approach, known as filtering, in order to tackle the issue of turbulence modelling. As the name of this method suggests, the turbulent structures of the flow are filtered through the mesh, and therefore only the eddies that are equal or larger than the size of the grid are simulated. Smaller vortices behaviour is then deduced through a theoretical model.

This expedient is justified by the Kolmogorov's turbulence theory (Pope (2000)). Kolmogorov's stated that the characteristics of the smallest turbulent scales are universal and therefore similar for every turbulent flow, independently from the boundary condition of the case under investigation. This is the reason why modelling the small vortices instead of directly simulating them is a reasonable assumption.

The filtering process adds new unknown terms, thus new equations have to be introduced in order to have a closed system of equations.

### 4.4.3.6 Main Phase Flow Field

The flow field behaviour was simulated applying the ideal-gas law for compressible flows, while the kinetic-energy theory was used to compute the other air properties in order to take into consideration the different features of the two flows of the problem under study: the main flow in the turbine and the purge air flow that is drawn from the compressor

The pressure based solver was chosen to reduce computational efforts because of the high number of mesh nodes at hand. The second order discretization scheme was used for the RANS models (Section 4.4.3.2) while for the LES model (Section 4.4.3.5) the central differencing scheme was used as it improves accuracy. For the LES simulation, the PISO (Pressure Implicit with Splitting of Operators) algorithm with skeweness correction was used to improve the convergence.

The velocity field resolved by means of the different turbulence models are reported in Figure 4.6-9.

The subgrid-scale stresses resulting from filtering are unknown and they have to be modelled. The LES Kinetic-Energy Transport sub-grid model was used. This model takes its name from the fact that it takes in account of the transport of subgrid-sccale turbulence kinectic energy. For more details please refer to Fluent (2009). It has to be noted that in the present work the LES simulation was not optimised as it was not the main aim of the research. It is advised to consider running an optimised LES study in a future phase of the research (see Section 6).

The main flow field characteristics are the same of those described for the large scale model in Chapter 3. The flow accelerates quickly after having entered the housing inlet with a negligible velocity and then it leaves the purge tube at almost sonic

conditions. The pyrometer purge system has been designed in order to produce elevated velocities aimed at discouraging contaminants entrapped by the turbine flow from entering the elongated tube and successively reaching the lens. The recirculation flow structure appearing at the inlet of the still tube is as expected. These vortices are thought to be one of the drawbacks of the air curtain configuration as they can trap the contaminants potentially leading them towards the lens. Furthermore, the flow inside the still tube tends to move helicoidally towards the lens, as described by Kerr (2002a). It is important here to notice that, since the flow accelerates quickly while leaving the purge tube, the zone in front of the still tube is characterized by high velocities. This characteristic of the flow is important for being one of the main factors controlling the purge contaminants deposition, as it will be shown in Section 4.5.6.
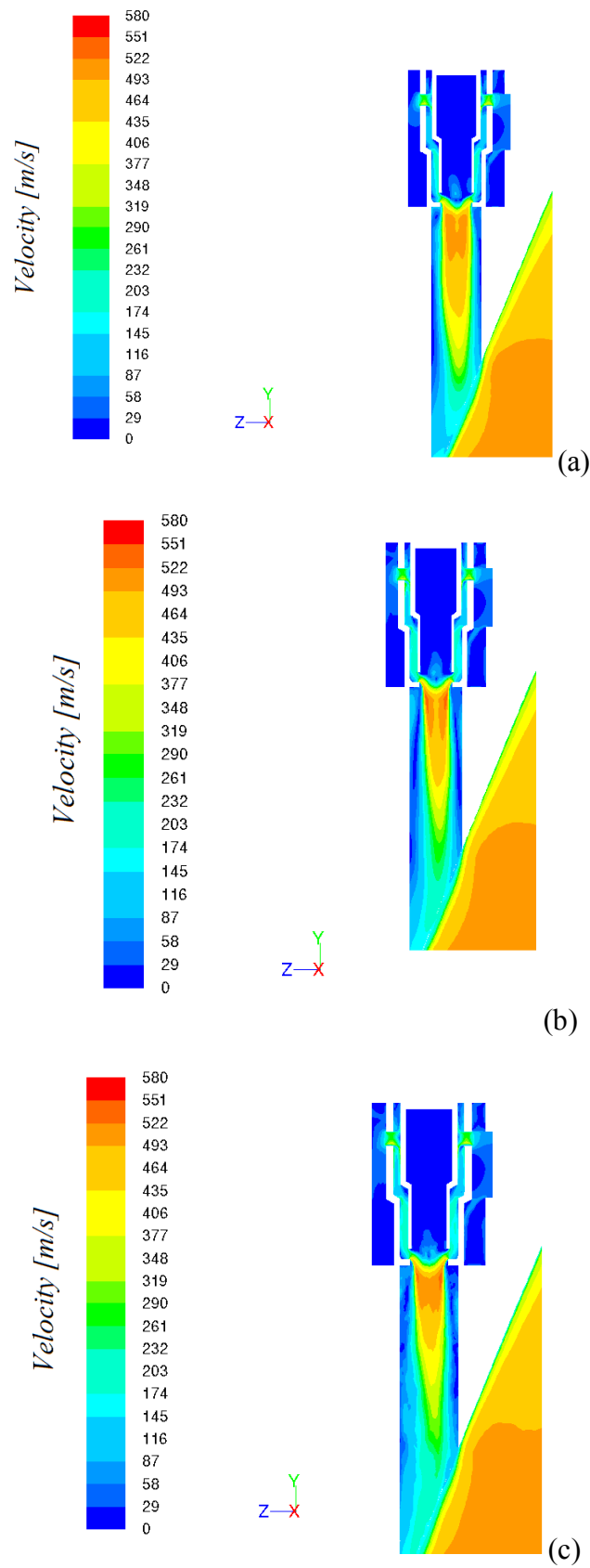
**Figure 4.6:** *Velocity field in the pyrometer/turbine interface: a) k-ε model;(b) k-ω model; (c)LES model.*
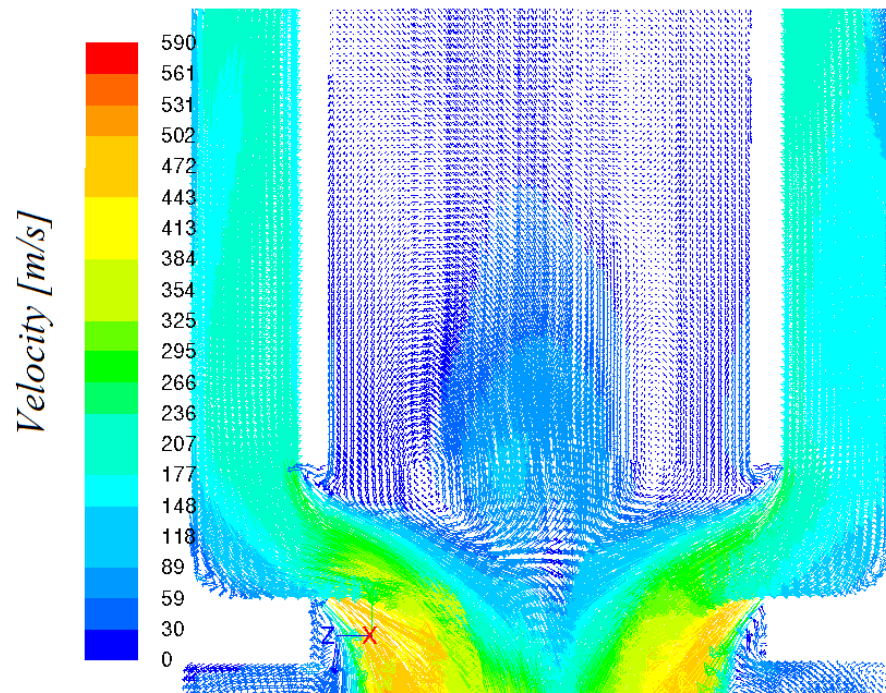
**Figure 4.7:** *Recirculation zone at the exit of the still tube (k-ω model).*
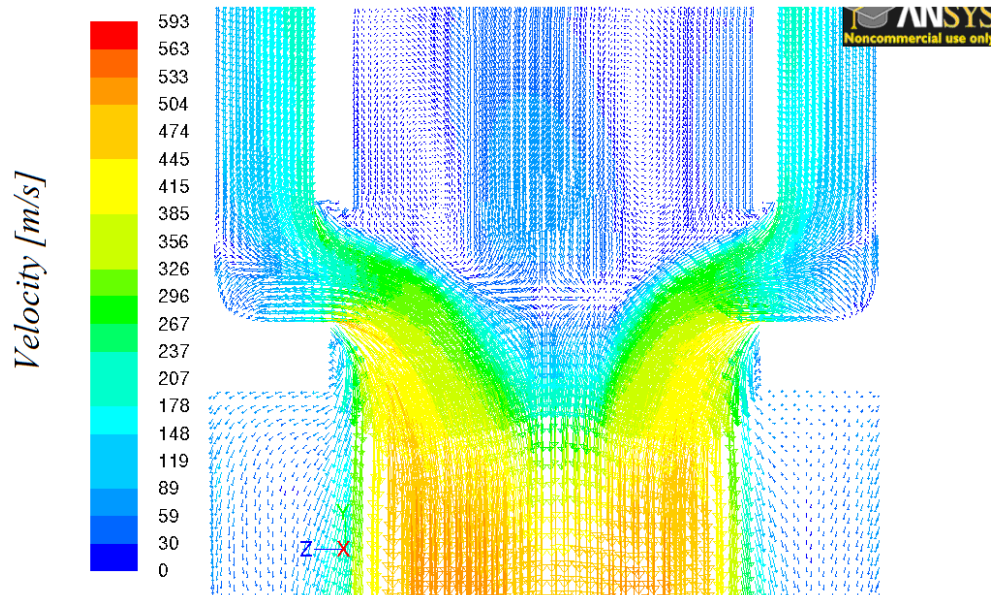


**Figure 4.8:** *Recirculation zone at the exit of the still tube (k-ε model).*
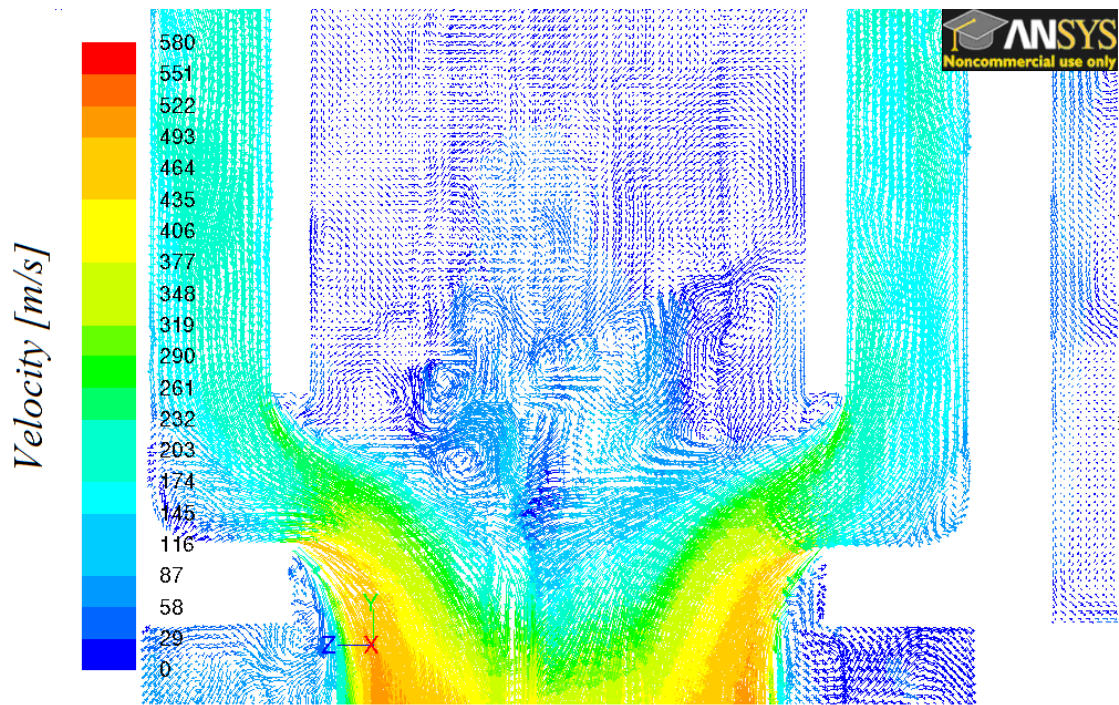
(c)

**Figure 4.9:** *Recirculation zone at the exit of the still tube (LES model).*

From Figure 4.19, it can be noted how large eddy simulation model allows capturing the transient turbulent features of the flow, although it turns out to be computationally more expensive.

In Figure 4.10-12 the three turbulence models results are compared in three different positions, which are denoted by station 1, 2 and 3, respectively. Figurq 4.10
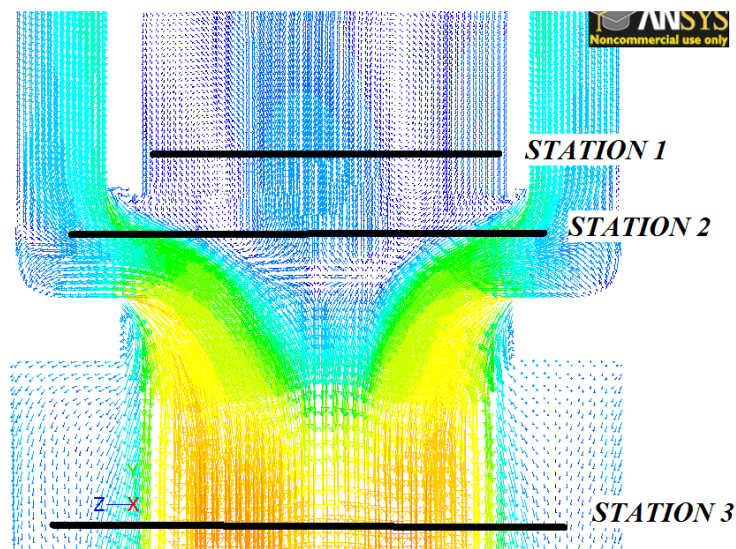


**Figure 4.10:** *Stations*

118
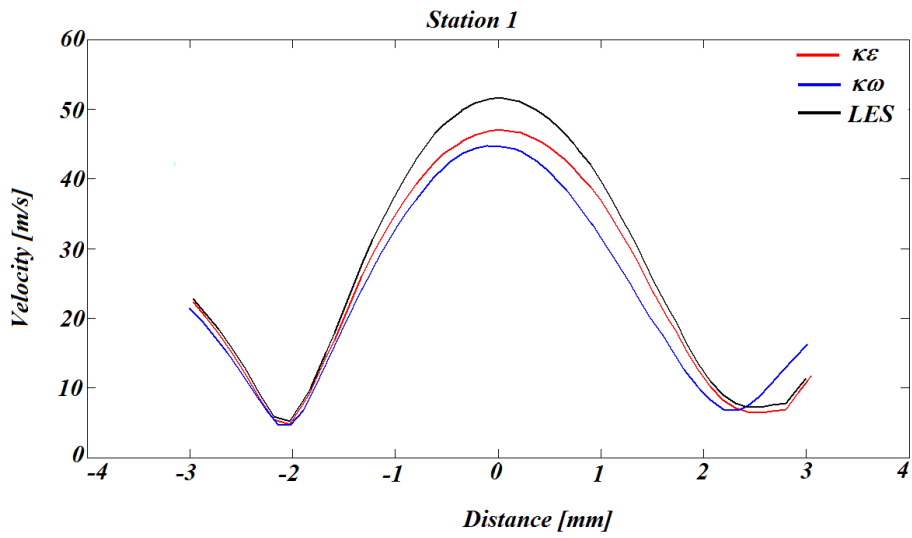
**Figure 4.11:** *Turbulence Model Comparison - Station 1.*
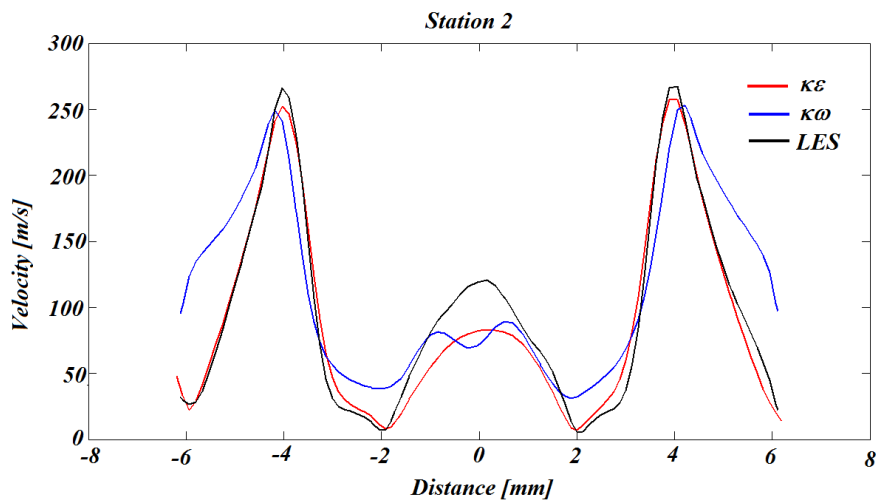


**Figure 4.12:** *Turbulence Model Comparison - Station 2.*
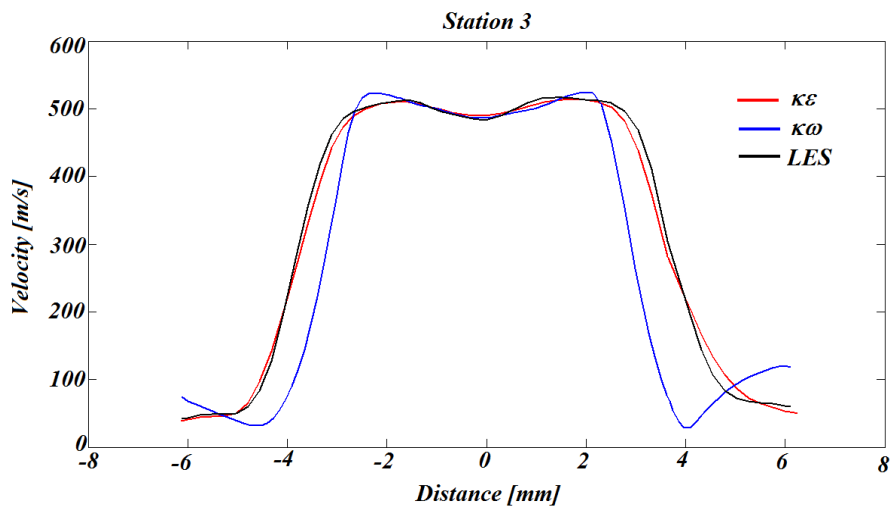


**Figure 4.13:** *Turbulence Model Comparison - Station 3.*

While the $k$-$\varepsilon$ and the LES models provide similar results, $k$-$\omega$ predicts slightly different values. It has been seen in Chapter 3, where the capabilities of the RANS model have been evaluated by means of a large scale model, that the $k$-$\omega$ model results are less correlated with the experimental results. From the experimental results the $k$-$\omega$ SST model tends to under-predict the dissipation of energy due to turbulence phenomena. Furthermore, this RANS model had more problems in converging, and it was not possible to obtain a symmetric solution. These facts suggest that the $k$-$\varepsilon$ results are more likely to be representative of the reality than the $k$-$\omega$ SST model prediction. The LES results are here reported for completeness, nevertheless, as already stated the mesh was not optimised for the LES analysis.

## 4.5 Contaminants Deposition

Once the main flow field has been resolved, it was then possible to model the second phase behaviour in a posteriori approach that it is going to be discussed in the next sections.

### 4.5.1 Contaminants Categories

Many different types of contaminants can be ingested by the engine during its operation. Nevertheless, most of them belong to only two different groups.

The first category is mainly made by sands. Terrain particles can be ingested by the engine during ground operations or in missions in which the aircraft has to overfly desert zones.

Sand is a granular material composed of finely divided rocks and particles. Its main constituents are:

- Silicon Dioxide ($SiO_2$) usually in the form of quartz;
- Eroded limestone;
- Coral;
- Gypsum;

- Shell Fragments;
- Feldspar;
- Iron.

The second contaminants group is represented by metal particles that can be easily produced through erosion and corrosion phenomena of both compressor and turbine. All these particles density is considerably higher of that of the main phase and consequently in this work particular attention is dedicated to the physics of the dispersion phenomenon of heavy particles.

### 4.5.2   Forces Acting on the Contaminants

As stated in Section 4.2, the particles transport will be described through the Lagrangian approach. The Newton's second law, written for a single particle, is expressed by (Maxey et Riley (1983)):

$$m_p \frac{dv}{dt} = F_{body} + F_{surf} + F_{coll} \quad (4.12)$$

Where with $F_{body}$, $F_{surf}$, and $F_{coll}$ are the body, surface and collision forces respectively. The body forces arise from the resulting action of the gravitational and the electromagnetic fields eventually present in the domain while the surface forces are the product of the mutual interaction particle/fluid.

In order to calculate the surface forces two main methodologies can be applied. The former, known as the resolved volume-particle approach, integrates along the surface the pressure and the shear stresses acting upon the particle. The main advantage of this method is in avoiding the evaluation of the single components of the surface forces (i.e. lift and drag). Nevertheless, this approach is sufficiently accurate only if the spatial resolution of the computational grid is in the order of the particle diameter. As the purge pyrometer contaminants size is usually in the order of few microns (see SEM images in Chapter 5) this approach implies a prohibitive computational cost. An alternative method, in which the particle is represented as a point, involves the

decompositions of the total surface force in several components. Loth (2000) states that the applicability of this approach, known as point-volume particle method, is limited to that cases for which the evaluation of the instantaneous fluctuations of the main phase around the particle is possible. As described in Section 4.4.3.2, this contrasts with the averaging procedure typical of the RANS method. Consequently, if the Reynolds averaging methodology is used to analyze the main phase, then further modelling aimed at simulating the turbulent velocity fluctuations needs to be addressed. In Figure 4.14 these two different approaches are sketched:
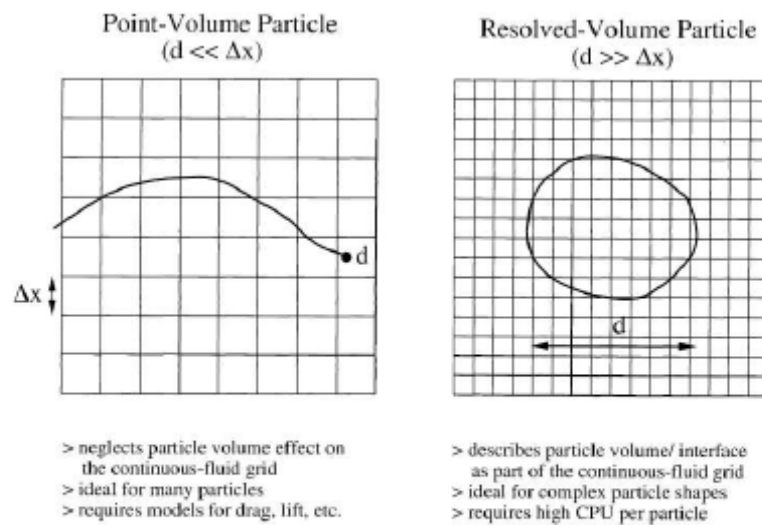


**Figure 4.14:** *Point-Volume Particle Approach, Resolved Volume Particle Approach (Loth (2000)).*

The surface forces is expressed by the composition of drag, lift, virtual mass, history, fluid stress, Brownian motion and thermophoresis contributions (Loth (2010)):

$$F_{surf} = F_{drag} + F_{lift} + F_{VirtualMass} + F_{History} + F_{BrownianMotion} + F_{thermophoresis} + F_{StressFkuid} \quad (4.13)$$

The thermophoresis components arise if the temperature gradients are important, while the Brownian force is generated from the interaction of the particle with the main phase molecules. Furthermore, the lift force is due either to the fluid shear or the particle spin. The continuous phase pressures and shear stress that would exist if the particle was not present are the source of the fluid stress force, which is related to the convective and gravitational accelerations. It is expressed as:

$$F_{StressFluid} = \rho_f \forall_p \left( \frac{Du_{@\,p}}{Dt} - g \right) \qquad (4.14)$$

Where $\rho_f$ is the density of the fluid, $\forall_p$ is the volume occupied by the particle, $u_{@p}$ is the velocity of the fluid extrapolated at the particle centre mass and g is the gravitational acceleration.

The virtual mass force is present only if the relative acceleration between the particle and the fluid is not negligible. This is often true in the case of the interaction contaminants/purge flow. When the particle relative velocity is significant, the particle transports along its path portion of fluid present in its proximity (known as virtual mass), which therefore will have the same acceleration of the particle. The virtual mass force is expressed by (Loth (2010)):

$$F_{VirtualMass} = c_\forall \rho_f \forall_p \left( \frac{Du_{@\,p}}{Dt} - \frac{dv}{dt} \right) \qquad (4.15)$$

Where $c_\forall$ is the virtual mass coefficient and $v_p$ the velocity of the particle. It is important to notice that in the expression 4.15, $\rho_f \forall_p$ is the mass of fluid that has been displaced by the particle. Nonetheless, the virtual mass contribution is directly proportional to the main phase density and therefore its value is negligible for $\rho_p >> \rho_f$. Consequently, this force will not affect considerably the motion of the purge flow contaminants.

The history force is due to an eventual unsteadiness of the viscous stresses acting upon the particle.
Basset (1888) gave the first analytical expression for this force (valid only for small particle relative velocity):

$$F_{history} = -\frac{3}{2} d^2 \sqrt{\pi \rho_f \mu_f \left[ \int_0^t \left( \frac{dw}{d\tau} \frac{1}{\sqrt{t-\tau}} \right) d\tau + \frac{w_{t=0}}{\sqrt{t}} \right]} \qquad (4.16)$$

Where $d$ is the particle diameter, $w$ the particle relative velocity and $\rho_f$ the fluid density. From this formula it is possible to observe that the history force decays with

$t^{-\frac{1}{2}}$. Unfortunately, analytical expressions do not exist for higher particle Reynolds numbers. Nevertheless, it has been demonstrated that the history force can be neglected both when high Reynolds particle numbers and/or heavy particles are involved (Loth (2010)).

In the present study, the contaminants of interest are all characterized by a particle density $\rho_p \gg \rho_f$ (Section 4.5.1) and it can be found in Wang et Stock (1983) that for scenarios characterized by the presence of heavy particles the main surface force contribution is the one generated by the drag that, therefore, will be discussed separately in the next section.

### 4.5.2.1  Drag Force

When the relative particle velocity is significant then drag is the main force component controlling the secondary phase motion. In order to understand the role played by this force, it is useful to consider the simplified case where a single particle is surrounded by an incompressible flow. Eventual rotation of the particle is here neglected.

Figure 4.15 summarizes the different status depending upon the particle Reynolds number, based on the particle relative velocity and expressed by:

$$Re_p = \frac{d_p \rho_f \left| v_p - v_f \right|}{\mu_f} \qquad (4.17)$$

Where $\rho_f$ is the density of the flow, $v_p$ and $v_f$ the particle and the flow velocity respectively, $d_p$ the particle diameter and $\mu_f$ the fluid viscosity.

For matter of simplicity a spherical particle is here taken in consideration.
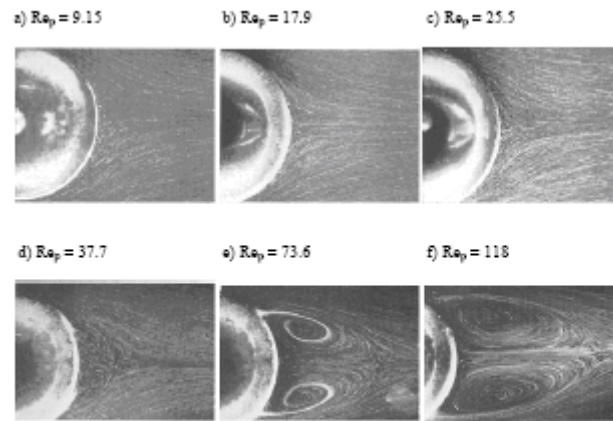
**Figure 4.15:** *Development of the flow behind a sphere vs the particle Reynolds number (Batchelor (1967)).*

At very low relative velocity the fluid is fully attached at the sphere, and it is steady and laminar. As the particle Reynolds number increases, the flow remains laminar but it is detached and as a consequence laminar wakes appear. These will pass from steady to unsteady state at higher Reynolds numbers.

As the relative particle velocity increases the flow will become transitional and then fully turbulent. The main feature of these regimes is the vortex shedding phenomenon with wakes fully turbulent.

The boundary condition given by the Stokes flow is taken as a reference, and for higher $Re_p$ this value is appropriately modified with the introduction of a Stokesian drag correction $f$.

Different Reynolds numbers are also associated with a different drag coefficient, $C_D$ through which the drag force is expressed by:

$$F_D = -3\pi d\mu_f fw = -\frac{\pi}{8}d^2\rho_f C_D w|w| \qquad (4.18)$$

In the experiment of Clift et al. (1978), the relationship between $f$, $C_D$ and $Re_p$ was examined, (Figure 4.16) thus showing how the drag force changes with increasing the

relative particle velocity. Being the flow inside the purge pyrometer system characterized by very different velocity and having a wide variety of contaminants in the work under examination the whole range of particle Reynolds number reported in figure 4.15 was investigated.
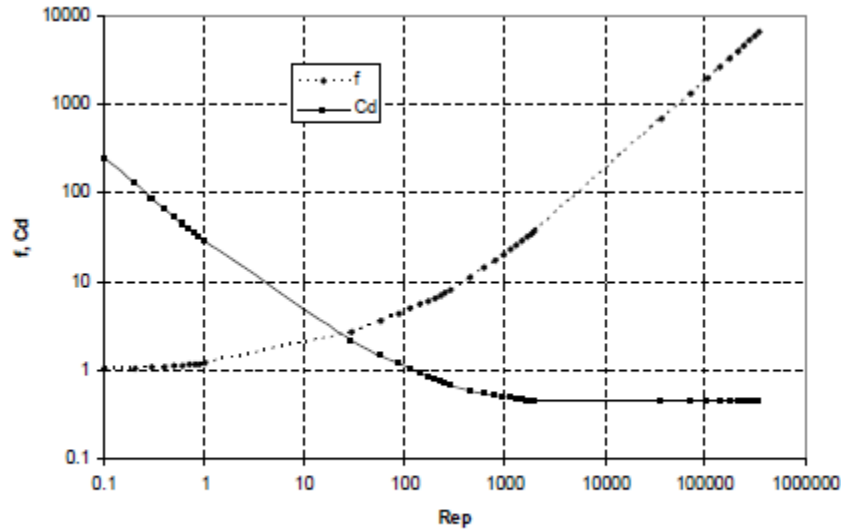


**Figure 4.16:** *f and $C_D$ trends with $Re_p$ ( Clift et al.(1978)).*

### 4.5.3 Parameterization of the Particle Tracking Problem

The behaviour of the secondary phase can be categorized by means of some important parameters that are therefore here briefly discussed.

The particle response time specifies the time required by a particle to respond to a variation in the flow velocity field. This can be either a main feature of the flow field (i.e. change in the flow direction due to the main phase adjusting to a specific geometry) or a turbulent velocity fluctuation.

It can be found in Crowe et al. (1998) that the particle response time, $\tau_p$, can be expressed by:

$$\tau_p = \frac{\left(\rho_p + c_\forall \rho_f\right)d^2}{18\mu_f f} \qquad (4.19)$$

Where $c$ is the virtual mass coefficient, $d$ is the particle diameter, $\rho_p$ and $\rho_f$ are respectively the particle and the flow density, and $f$ is the Stokes correction factor given by:

$$f = \frac{C_D}{24/\mathrm{Re}_p} \qquad (4.20)$$

With $C_D$ the drag particle coefficient and $Re_p$ the particle Reynolds number.

Consequently, the particle response time provides a first estimation on how quickly the particle will adapt to a changing surrounding flow. It is evident from Equation 4.19 that both heavy particles and contaminants that have a high relative velocity tend to be irresponsive to the actions of the main flow field.

Therefore, already from this first stage of the analysis it is possible to state that in the pyrometer case, characterised by the presence of contaminants with high density and by a geometry that forces the purge flow to quickly accelerate and to change its direction, it is expected that the contaminants path will substantially differ from that of the main phase.

The particle response time can then being conveniently expressed in a non dimensional form, known as the Stokes number.

The Stokes number, $St$, is the ratio between the particle response time and a characteristic flow time:

$$St = \frac{Particle\ Response\ Time}{Characteristic\ Flow\ Time} \qquad (4.20)$$

Once the particle properties are delineated, the particle response time is uniquely defined. On the contrary, many different characteristic flow times exist for one single scenario, depending on what it is assumed to be the dominant feature of the main phase flow field.

This problem is particularly evident if the turbulence level is significant as for each turbulent eddy a different Stokes number can be defined.

Nevertheless, once the Stokes number has been chosen, the particle behaviour is described as it follows:

- For St <<1, the particle response time is negligible; therefore the particles react immediately to any eventual modification in the fluid velocity field;
- For St~1 the particle motion is affected by the variations in the velocity fluid field, nevertheless the path-lines for the particles and the flow will substantially differ;
- For St >>1 the particle inertia does not allow for any adjustment to the variation in the continuous-phase velocity field.

In Figure 4.17 Loth (2010) described the behaviour of a single particle that it is injected in a divergent nozzle.
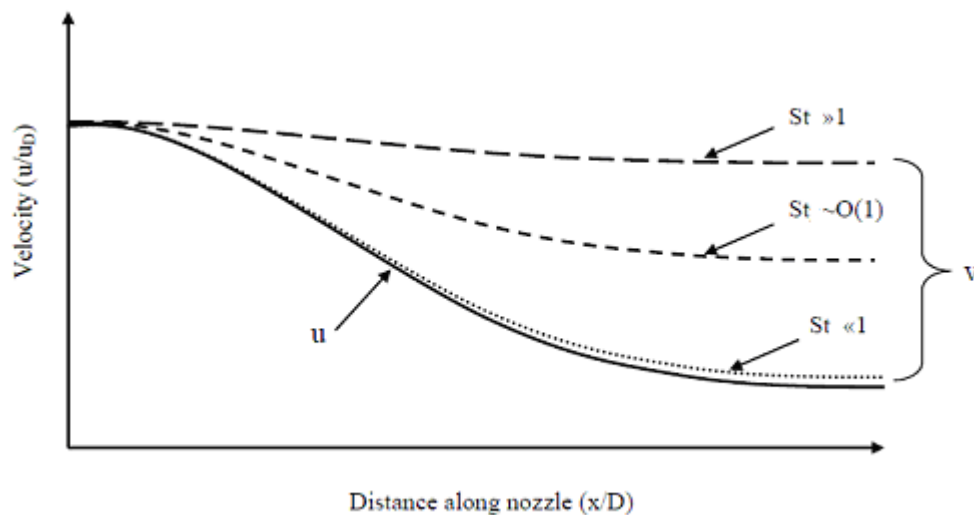


**Figure 4.17:** *Particle behaviour vs Stokes number in a divergent nozzle; dashed lines: particle velocity, continuous lines: flow velocity Loth (2010).*

## 4.5.4  Turbulence Field / Contaminants Interaction

Turbulence usually augments significantly the level of particle dispersion (Gore et Crowe (1991), Gore et Crowe (1989)). As described in Section 4.4.3.5 a turbulent flow contains vortices of different sizes, each of them described by an eddy characteristic size and an eddy lifetime. Consequently, in a turbulent flow it is possible to define several Stokes number depending upon which eddy is taken in consideration. Nevertheless, one way to tackle the problem is through the analysis of the maximum and minimum turbulent Stokes number that represent respectively the eddy of the maximum size (that have a length scale in the order of the macroscopic length of the domain and contains the most of turbulent kinetic energy) and the eddy of minimum size, that is associated with the Kolmogorov's scale at which most of the energy dissipation occurs. A specific eddy exists only for a limited period of time and therefore the outcome of the interaction particle/eddy depends upon the capability of the particle to follow the unsteady fluctuations of the flow and on the time required by the particle to cross the eddy.

The turbulence field is usually resolved simplifying the problem, considering the turbulence as homogenous, isotropic and statistically steady.

Typically, because most of the energy is contained in the integral scale these are usually firstly taken in consideration Nevertheless, either the Kolmogorov's or the integral scale are investigated, once the turbulent Stokes ($St_{turb}$) has been defined it follows:

- For $St_{turb} \ll 1$, the particle response time is negligible; therefore the particles closely follow the motion of the eddy;
- For $St_{turb} \sim 1$ the turbulent velocity fluctuations influences the motion of the particle, nonetheless the particle and the turbulent path-lines are substantially different ;
- For $St_{turb} \gg 1$ the motion of particle is independent from the presence of a turbulent field.

Furthermore, when dealing with particle/turbulence interaction it is important also to analyse the order of magnitude of the density ratio. In fact, if the particles are heavier than the main phase than they are centrifuged out from the turbulent vortices and they concentrate in areas characterised by high shear values. In an opposite scenario, when therefore the particle density is in the order of that of the main phase, the particles concentrate in the centre of the turbulent vortices, where the pressure is lower. This phenomenon has been named as preferential concentration by Eaton and Fessler who first observed it and analysed it in 1994.

Different studies can be performed depending on the level of detail that it is desired to achieve. If the second phase dispersion is analysed locally then the main interaction feature is represented by preferential concentration. Nonetheless, in average, the particles will diffuse spreading like a cloud as they are transported by the flow, Figure 4.16.

Turbulent particle dispersion was for the first time analysed in the work of Taylor (1921). This study is a simplified case in which the particles inertia is negligible and therefore the secondary phase behaves simply like a tracer. Nevertheless, more complex cases can be regarded just as scenarios in which the particle behaviour deviates of a certain degree from this ideal case. For this reason, Taylor's work is here briefly summarised.

Taylor (1921) focused the attention on a group of particles released from a single point of the domain and from which they diffuse forming a cloud. Each particle leaves the origin in a different time step and none of them follow the same path. At this point it is possible to define the main quantities able to describe the turbulent particle dispersion.

The particle average velocity $\hat{v}$ is expressed by:

$$\hat{v} \equiv \frac{1}{\tau} \int_{t_0}^{t_0+t} v(x_p, t)\,dt \qquad (4.21)$$

Where the "0" subscript indicates the initial condition.

Known the average velocity it is then possible to express the average particle position $x_p$ as:

$$x_p(\tau) = \tau\hat{v} + x_0 \qquad (4.22)$$

Given $N_p$ particles the ensemble average path is:

$$\langle q \rangle \equiv \frac{1}{N_p} \sum_{i=k}^{N_p} x_{p,k} \qquad (4.23)$$

While the deviation from the path $x_p^{'}$ is:

$$x_p^{'} = x_p - \langle x_p \rangle \qquad (4.24)$$

With a mean variation of:

$$\langle x_{p,i}^{'} x_{p,j}^{'} \rangle \equiv \frac{1}{N_p} \sum_{k=1}^{N_p} \left( x_{p,i}^{'} \right)_k \left( x_{p,j}^{'} \right)_k \qquad (4.25)$$

Finally, the particle diffusivity (spread rate) $\Theta_{p,ij}$ is:

$$\Theta_{p,ij} \equiv \frac{1}{2} \frac{d\langle x_{pi}^{'} x_{pj}^{'} \rangle}{d\tau} \equiv \frac{1}{2} \frac{d\langle x_{pi}^{'} x_{pj}^{'} \rangle}{dt} \qquad (4.26)$$

Using this notation and considering a simple tracer immersed in a homogenous, isotropic and unsteady turbulence then Taylor (1921) derived the following expression for the particle diffusivity:

$$\Theta_{turb}(\tau) = \tau_{\Lambda L} u_\Lambda^2 \left( 1 - e^{-t/\tau_{\Lambda L}} \right) \qquad (4.27)$$

$$\Theta_{turb,0}(\tau) \approx u_\Lambda^2 \tau \qquad\qquad for\ \tau \ll \tau_{\Lambda L}$$

$$\Theta_{turb,0}(\tau) \approx u_\Lambda^2 \tau_{\Lambda L} \qquad\qquad for\ \tau \gg \tau_{\Lambda L}$$

Equation 4.27 demonstrates that the cloud of particles shows a short and a long term behaviour: initially the diffusivity increases linearly with time but then it becomes proportional to the Lagrangian time scale $\tau_{\Lambda L}$ .

Remembering that one of the main Taylor's theory assumption is that the turbulence is homogenous than it is clear that the group of particles will leave the origin and then will diffuse in a sphere like shape, Figure 4.18.
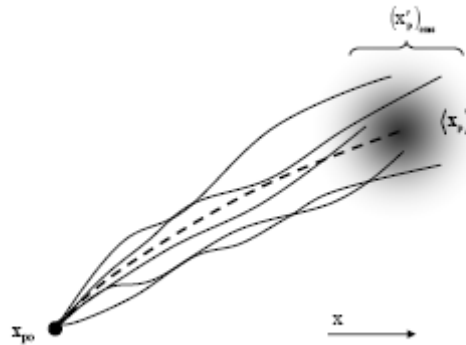


**Figure 4.18:** *In the Taylor's theory the particles are injected from a single point. The turbulent field then forces them to spread in a cloud shape.*

### 4.5.4.1 Heavy Particles and Turbulence

Taylor's theory is valid for tracers, hence for particles with a density comparable to that of the main phase. In the pyrometer case the contaminants are characterized by a density considerably larger than that of the purge flow, and therefore Taylor's work should be appropriately modified. A description of heavy particle behaviour can be obtained examining the experiment of Wang et Stock (1993), Figure 4.18 where the ratio between the response time and the Eulerian time scale is plotted against the inertia parameter (Stokes number).
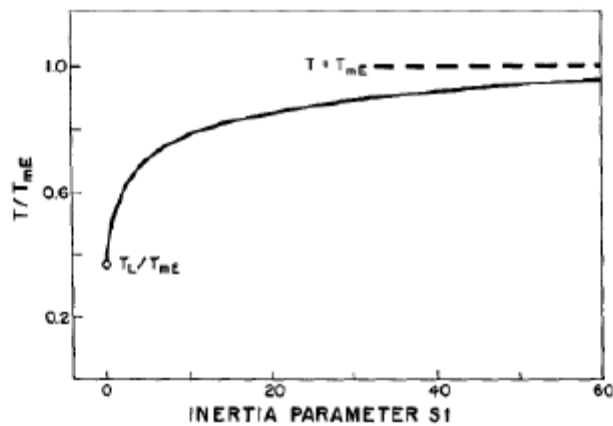


**Figure 4.19:** *Wang et Stock experiment – Turbulent dispersion of heavy particles.*

An increase in the inertia of the particle is translated in a higher Stokes number (inertia parameter in Figure 4.19) and therefore, as explained above, particles with a significant density ratio will follow a path substantially, or even totally, different from that of the main phase.

It is evident that a particle that has a negligible inertia will spend enough time trapped in an eddy to have its path substantially modified by it. Conversely, a particle with significant inertia will cut through the eddy, and therefore the turbulence field will not affect the particle trajectory.

As it possible to observe in Figure 4.19 with increasing the Stokes parameter the particle time scale pass from ($\tau_L$), the fluid Lagrangian time scale (and therefore the particle will respond to any fluid fluctuation) to asymptotically reaching ($\tau_{mE}$), the Eulerian time scale (and therefore the heavy particle will not see the main phase flow velocity variations).

### 4.5.4.2  Discrete Random Walk model (DRW)

As stated in Section 4.2, in this work the Lagrangian representation has been used to resolve the secondary phase flow field. Nevertheless, this methodology requires the turbulent velocity fluctuations to be known in each point of the domain. When the main flow field is solved using the Reynolds averaging method this information is lost.

Consequently, in order to apply the Lagrange model the effect of the instantaneous turbulent field needs to be modelled. This is usually achieved through a stochastic approach, where the flow field, that has been previously resolved exploiting one of the RANS models, is then integrated with the turbulent instantaneous fluctuations, simulated through the production of random values. Given the statistical nature of this approach, in order to achieve a general result, the path of a significant number of particles needs to be investigated

The Discrete Random Walk model, introduce by Gosman et Ioannides in 1981, is implemented in the most widespread commercial software like FLUENT or CFX. The main flow field solution quantities are used to characterize the eddies with which the particle interact along its path. In the commercial code FLUENT the eddy time scale, $\tau_\lambda$ is expressed as:

$$\tau_\lambda = c_\tau \frac{k}{\varepsilon} \qquad (4.28)$$

While the eddy length scale, $\Lambda$:

$$\Lambda = c_\mu^{3/4} \frac{k^{3/2}}{\varepsilon} \qquad (4.29)$$

Where the constant $c_\mu = 0.09$ while different values exist for the constant $c_\tau$ in literature. Nevertheless, FLUENT Software uses a value of 0.15 if the main flow field has been resolved with one of the RANS model.

The values of the turbulent fluctuating velocities component are chosen to be proportional to the turbulent kinetic energy. In the case in which the RANS model has been used the three velocity components are assumed to be the same and expressed by:

$$\overline{u'^2} = \overline{v'^2} = \overline{w'^2} = \zeta \frac{2}{3} k \qquad (4.30)$$

Where $\zeta$ is a random value generated considering a Gaussian distribution $P^*(u')$ with a variance function of k (FLUENT (2009)):

$$P^*(u') = \frac{1}{\sqrt{2\pi}\sqrt{\frac{2}{3}}} \exp\left(-\frac{(u')^2}{\frac{4}{3}k}\right) \qquad (4.31)$$

The time of interaction particle/eddy it is then the minimum between the eddy lifetime $\tau_\lambda$ and the eddy crossing time $\tau_c$, where:

$$\tau_c = \tau \ln\left(1 - \frac{\Lambda}{\tau|u_f - u_p|}\right) \qquad (4.32)$$

Where $\Lambda$ is the eddy length scale. At the end of the time of interaction another random value is calculated and a new fluctuating value is determined.

Hence, the continuous velocity fluctuations are discretized through the DRW approach, Figure 4.20.
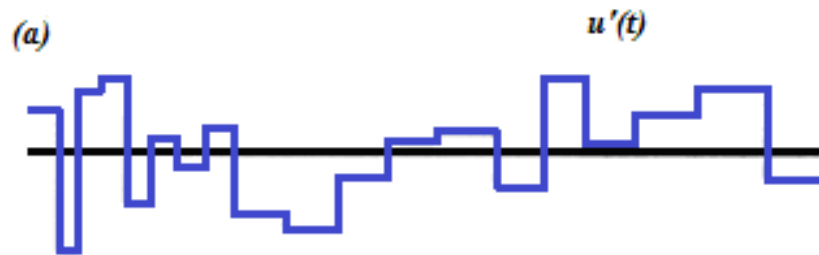


**Figure 4.20:** *In the DRW model the turbulent velocity instantaneous fluctuation are discretized.*

Nevertheless, it is important to notice that this formulation is based on the hypothesis of isotropy. Therefore, the DRW model can lead to the wrong results if the turbulent scenario under exam is highly inhomogeneous. In fact, as it is showed by different authours, i.e. Shuen et al. (1983), Strutt et Lightstone (2006), MacInnes et Bracco (1992), the DRW model tends to predict a fake migration of particles from high turbulent regions to lower turbulent intensity zones. In reality, when the main flow acceleration is zero then, even if the turbulence is inhomogeneous, assuming that the particles are injected homogenously then their concentration should remain homogenous. For how the DRW has been formulated, the particles present in a region where the turbulence is higher travel a greater distance. Consequently, they are more likely to reach regions less turbulent where they concentrate.

At the current state of art, many scientists are investigating the right expression for a correction factor to be added in the turbulent dispersion formulation in order to take in account the effects of eventual inhomogeneities. Different formulations can be found in the works of MacInnes et Bracco (1992), by Bocksell et Loth (2006), by Strutt et Lightstone (2006). Here it is important to bear in mind that FLUENT code has been used and hence eventual inhomogeneities have been neglected.

The DRW is by definition a statistical analysis. Consequently it is fundamentally important to ensure that the results have a statistically meaning. At the same time, to ensure a reasonable computational cost, the number of the particles injected has to be as lower as possible. Therefore, it is necessary to find a compromise between these two requirements. In the work here presented, the number of injected particles was increased until the number of deposited particles become independent from the number of injected particles. The final number of particles injected was 400.000.

### 4.5.5  Modelling Scenario

Summarising the assumptions described in the previous sections, it follows that:

- The secondary phase has been considered dispersed and therefore the one way coupling modelling has been considered accurate enough to correctly predict the contaminants dispersion. Consequently, the present analysis has been carried out in two steps: in the former the main flow field has been resolved and in the latter the contaminants have been injected. It has to be taken in account that, given this assumption, the study here described is valid only for a volume load up to $10^5$ (Elghobashi et Truesdell (1994));

- To resolve the secondary phase flow field the Lagrangian formulation of the problem has been applied. As a result, the Newton's second law has been employed, before evaluating and then summing up the effects of all the different forces acting upon the particles;

- The contaminants have been separated in two main categories: sand and metal fragments respectively. Both of them are characterized by $\rho_p \gg \rho_f$. As a result, from the previous studies discussed in the preceding sections, drag is expected to be the dominant force influencing the particles path, while turbulence action should be relevant only for that contaminants with negligible inertia;

- In order to predict the outcome of the particle/turbulent field interaction a statistical approach has been used. By definition, the RANS models do not provide information on the instantaneous turbulent velocity field. As a consequence, further modelling is necessary by means of the discrete random walk model. The actual turbulent quantities, estimated by one of the RANS models, are used to produce a random value representative of the fluctuating velocity components of the turbulent field. This number is then updated at the end of each eddy lifetime. It is important to keep in mind that when the turbulence is strongly inhomogeneous the DRW can give unrealistic results;

- Both particle depositions of contaminants entrapped by the purge or by the turbine flow need to be addressed. As a consequence, two main groups of injections have been investigated. The former involved introducing contaminants at the purge inlet and the latter at the turbine/pyrometer interface. They are both discussed in the next sections.

### 4.5.6 Purge Flow Contaminants

The air curtain configuration has been designed considering the possibility of using a purge air that does not carry contaminants itself and, as a consequence, it is used to keep the pyrometer lens clean. In reality, the purge air is drawn from the compressor and therefore it can be rich of contaminants produced by the eventual erosion and corrosion of the engine components or due to sand particles that have been directly ingested by the engine.

Gypsum ($\rho_p$ =2230) and Nickel ($\rho_p$ =8760) particles have been separately injected at the inlet of the purge pyrometer casing. They are representative of the behaviour of

sand and metal particles respectively. Both the flow fields resolved with the k-ε and the k-ω have been used as a baseline for the particle dispersion analysis. The particles were injected at the pyrometer inlet with zero velocity. They were allowed to stick on the lens while a perfect elastic bouncing mechanism was considered on all the other walls.

The resultant graphs of the levels of deposition versus the particle diameter are reported in Figure 4.21.
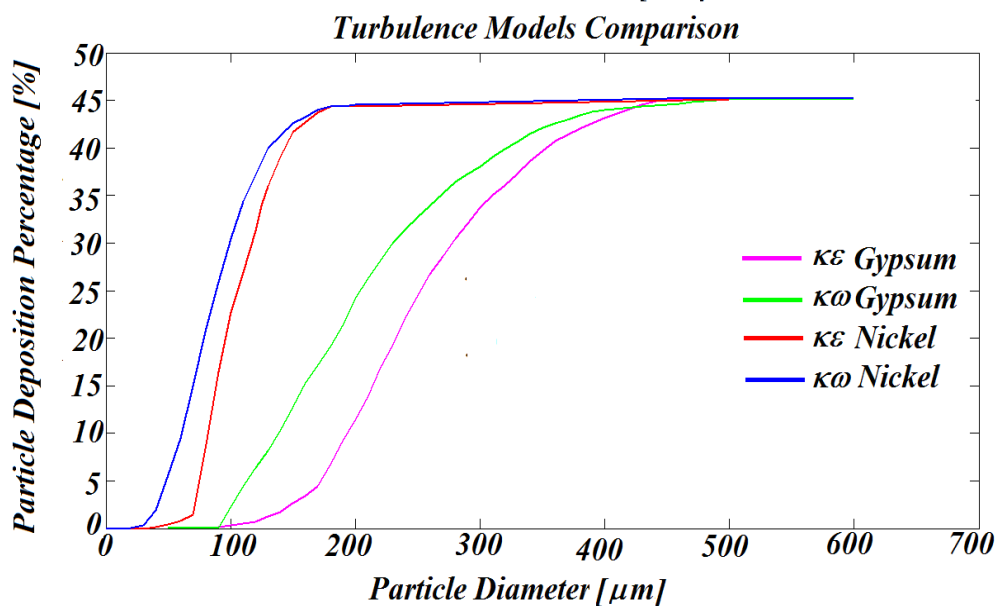


**Figure 4.21:** *Comparison between the k-ε and the k-ω results for nickel and gypsum contaminants.*

Both turbulence models under investigation predicted a similar curve shape. Nevertheless, comparing the two turbulence formulations, the k- ε model tends to estimate a lower level of deposition for the same particle diameter. This discrepancy is here considered arising from the macroscopic differences in the flow velocity fields, resolved by the two different RANS models, instead of being due to the different turbulent velocity fluctuations predicted by the two models. The justification of this statement can be found in the following analysis of the phenomena involved in the particle deposition and by relating them to the different curve sections.

_____

In Figure 4.22 the particle injection is displayed to be inside the purge tube only for illustrative purposes. In reality the graphs just described have been obtained injecting the contaminants at the inlet of the purge housing tube.

Different mechanisms have been individuated as it follows.
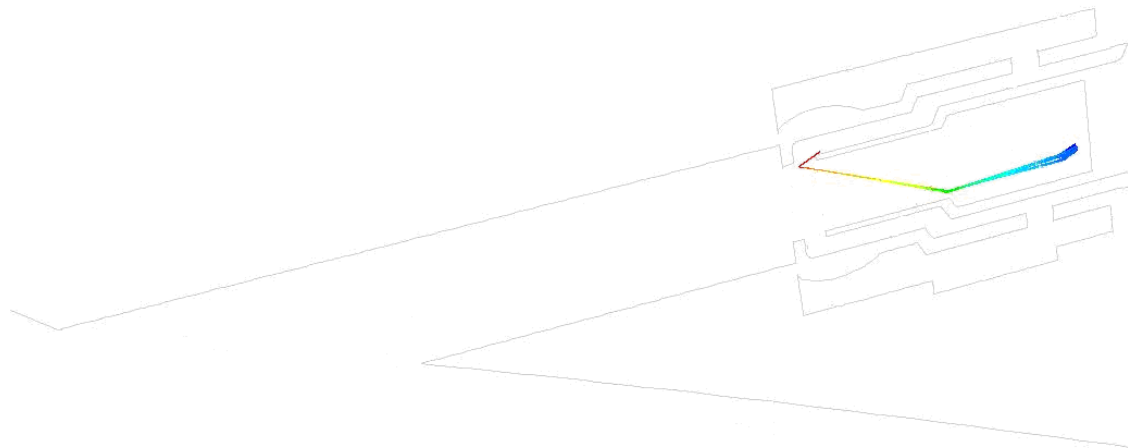


**Figure 4.22:** *Particles with high inertia are not capable of following the main phase flow trajectory. These contaminants can hit the purge wall thus being directed towards the lens (Nickel 150μm)*

In Figure 4.23 it is illustrated the mechanism connected with the constant part of the curve of the level of deposition (of about 45% in Figure 4.21). These particles have sufficient inertia not to be influenced by the turbulent field and to not be capable to respond to the main variations in direction and in velocity of the flow field. Therefore, in correspondence of the areas characterized by variable geometry the particles will hit the walls of the purge tube. While this phenomenon, generally, is not of interest, it plays a fundamental role at the edge of the purge tube, where the flow accelerates by means of the convergent zone while moving at high speed towards the turbine. As it

possible to see in Figure 4.21, as a result of this impact the particles will be then directed toward the lens. The inclination of this collision is the results of several previous impacts with the purge tube walls and therefore it is almost completely random. Furthermore, if the particles path is sufficiently inclined before reaching the purge tube wall, the contaminants can escape directly from the pyrometer without hitting the wall. As a result, the particles are equivalently likely to escape from the pyrometer purge tube or to be directed towards the pyrometer lens. This explains why the maximum level of deposition is about 45%.

It will be shown in Chapter 5 that high speed impacts are one of the main mechanisms controlling the contaminants deposition on the lens. Furthermore, it is evident that the purge flow geometry at the convergent zone and the elevated speeds involved are the factors ruling the deposition of particles with high inertia.

Hence, this first category of impacts allows the identification of one of the Stokes number related to purge flow contaminants deposition. In fact, the particle response time $\tau_p$ is expressed by equation 4.14 while the fluid time scale can be defined as the ratio between the length scale $L$, characterizing the convergent zone, and the corresponding velocity $u_D$.

The velocity $u_D$ may be chosen as the velocity at the inlet of the convergent area while L as the length of the convergent weighted by the cosine of the inclination of the line connecting the diameter at the inlet and outlet of the convergent zone. The introduction of the cosine function allows obtaining a better estimation of the fluid time scale depending on the steepness of the convergent zone. Moreover, it is also clear that, while turbulence will enhance the particle spreading, it is actually the drag force controlling the contaminants deposition.

As the particle diameter decreases its inertia diminishes with it and the drag action starts to actively stop some of the contaminants from depositing on the lens. In fact, while the particle is moving towards the still tube, its relative velocity is high. Consequently, during this interaction main phase/contaminant, the particle relative velocity decreases by means of the drag force. If, before reaching the still tube, the particle absolute velocity is negligible then the contaminant will reverse its direction

and will be transported by the purge flow towards the turbine. On the contrary, particles which absolute velocity is zero only after having entered the still tube are likely to be deposited. In fact in this case, the particle will be trapped by the vortices inside the still tube that consequently are likely to bring them towards the lens, Figure 4.23. Nonetheless, these particles impact the lens at very low speed and hence they can be easily removed by standard cleaning procedures.

This second category of particle deposition mechanism highlights the second important role played by the length of the convergent zone.

The distance between the end of the still tube and the purge tube is the space where high values of drag force act on the particle. Considering the angle formed between the trajectory of the particle that it is bouncing towards the still tube inlet and the pyrometer axes, it is clear that higher values of this angle means that the particle travels more before reaching the still tube. Consequently, being for more time under the influence of the elevated drag force it is more likely that the particle will stop and then escape from the pyrometer.
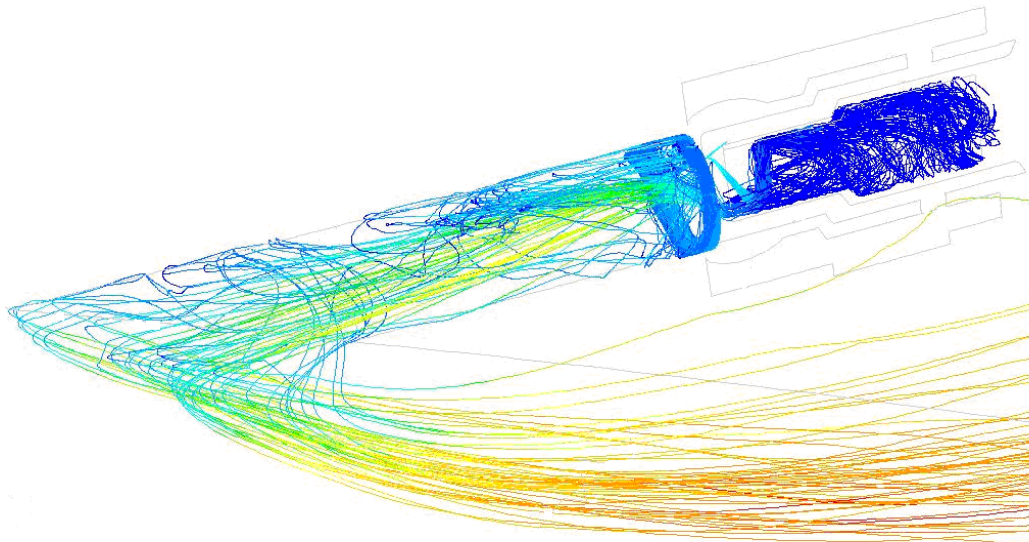


**Figure 4.23:** *As the particle inertia decreases the drag starts actively stopping the contaminants. Nevertheless, if the particle velocity is zero only after having entered the still tube they are likely to be deposited on the lens by the quasi-still flow that is spiralling towards the lens . (Nickel  50μm).*

141

A further reduction in the particle diameter is translated in a lower Stokes number. Therefore, as the ratio between the drag force and the particle inertia increases fewer particles are deposited. This corresponds to the slope in Figure 4.23.

When the Stokes number is in the order of one then the particle is capable to respond to the fluid velocity variations. The contaminant path significantly differs from that of the main phase, nonetheless there are not collisions between the wall and the contaminants, Figure 4.24. As a consequence, no particle with this Stokes number is deposited on the lens.
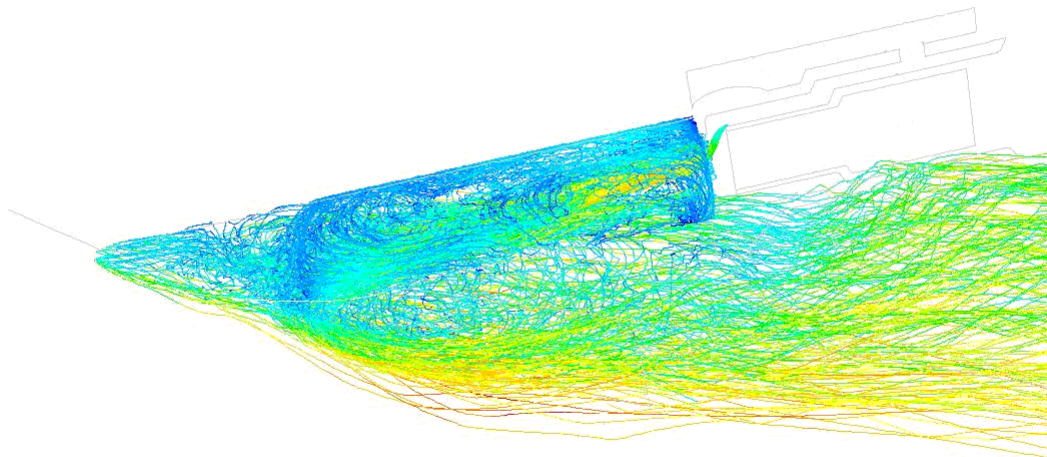


**Figure 4.24:** *If the Stokes number is about 1 the contaminants start responding to the main phase flow changes. Their path still differs from that of the flow, nevertheless these particle are capable to deviate their direction enough to not hit the purge wall . (Nickel 5μm)*

.

From the analysis of the phenomena involved in the particle deposition it is clear that the particle inertia and the drag force control the fouling of the lens. From Figure 4.25

it is possible to see that the gradient of the slopes predicted by the two different RANS model are similar, even if the k-ε estimates a lower level of deposition compared with that of the k-ω case. On the other hand, the curve gradient changes considerably whit the material under consideration. This phenomenon can be explained through the action of the drag force.

Neglecting all the forces apart from drag, by successive integrations of Newton's second law, it is possible to express the space travelled by the particle as a function of time:

$$x(t) = \frac{1}{k}\ln(w_0 kxt + 1) - v_f t + x_0 \quad (4.33)$$

With

$$k^* = \left(\frac{3}{4}\right)\frac{\rho_f}{\rho_p}\frac{c_D}{d} \quad (4.34)$$

It is convenient considering a simplified one-dimensional case where the flow velocity gradients are zero and the particle has been injected with a certain velocity in opposite direction to the flow. Imposing the absolute particle velocity to be equal to zero, it is possible to derive the expression of the time required by the particle to stop:

$$t_{stop} = \frac{1}{k}\left(\frac{1}{v_f} - \frac{1}{w_0}\right) \quad (4.35)$$

Simplifying further the problem, considering a constant coefficient of drag ($c_D$ will in reality vary with the particle relative velocity), it is possible to plot the particle stopping distance versus the diameter for different particle densities.

It is important to notice that with $\rho_p$ decreases the gradient of the curve describing the distance travelled by the particle in opposite direction to the flow. As it has been previously highlighted the stopping distance is directly connected with the level of

deposition, and therefore the same trend of the curve gradient is expected, Figure4.25.
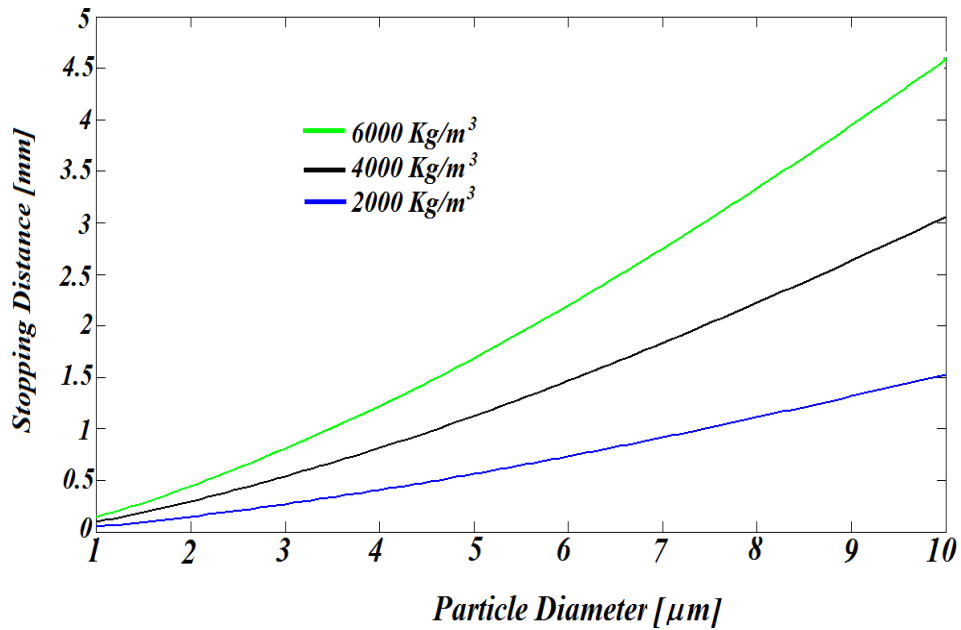


**Figure 4.25:** *Stopping distance vs diameter plotted for different particle materials.*

It is important to notice that the conclusions reached in the present study are in disagreement with Kerr's study described in Chapter 2. For clarity reasons his graph of the level of deposition on the lens of contaminants entrapped by the purge flow is reported again in Figure 4.26.
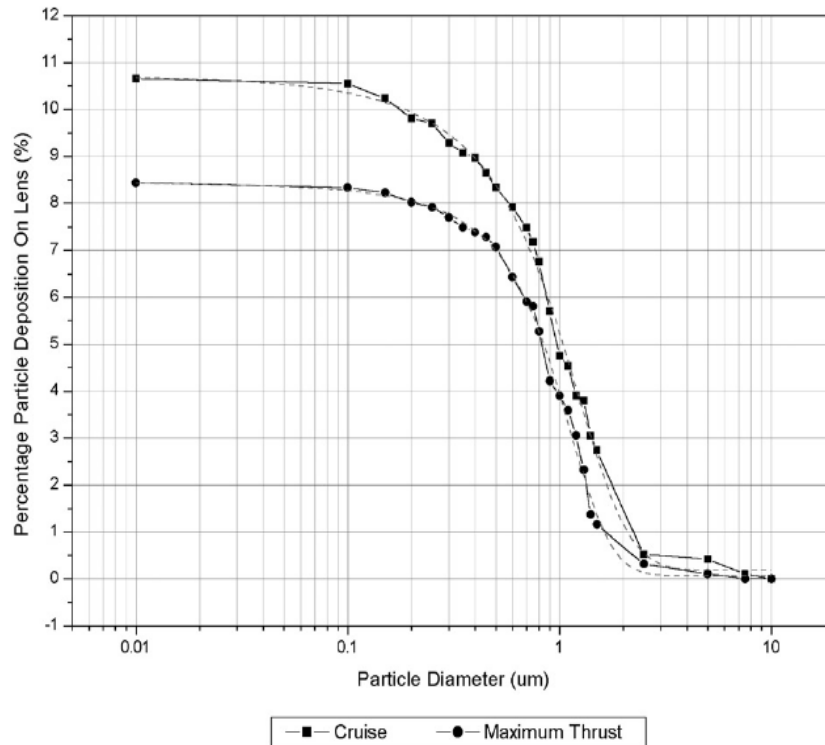
**Figure 4.26:** *Purge contaminants deposition, Kerr's results (2002a).*

Even if Kerr analysed a different pyrometer, the main geometry features and working principles are the same of the present work and consequently similar qualitative results were expected. Instead, while it is stated in Kerr's study that the level of deposition decreases as the particle diameter increases, opposite results were reached in this work.

The explanation of this discrepancy can be found by lowering the particle diameter even further. In this case another Stokes number comes into account, defined through the time flow scale associated with the recirculation zone present in front of the still tube. A particle, in order to be capable of responding to this characteristic of the flow field, should have a response time very short thus to decelerate quickly, change its direction and ultimately enter the still tube. This means that only very small particles with a response time close to zero will behave as described by Kerr's study. This has been verified by analysing the behaviour of very small particles, Figure 4.27. It has to be noted that for the pyrometer configuration under analysis the maximum percentage of particles reaching the lens is relatively small as it is the fraction of the purge flow

entering the still tube. In addition, it is possible to note from Figure 4.30 that either considering different RANS models or materials predicts very similar results. These contaminants have negligible inertia and therefore their relative velocity is not significant, hence they are in equilibrium with the surrounding flow and act as mere tracers.
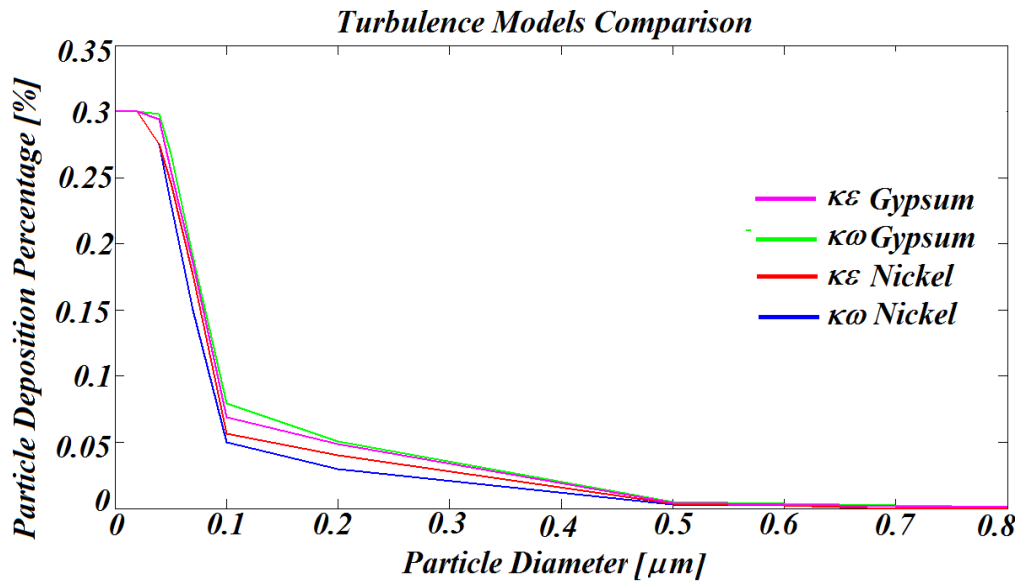


**Figure 4.27:** *Purge contaminants deposition, particles with negligible inertia.*

In addition, it is important to remember that for particles with a diameter fraction of a μm the approximation of the particle seeing the flow as a continuum is not strictly valid. A correct approach would investigate the interaction between the fluid molecules and the contaminants. Nonetheless, this can be avoided if it is noted that, as it has been showed in the present research, the bouncing mechanism is predominant. Particles with negligible inertia will always act as tracers and therefore they can always reach the lens as long as there is fluid moving towards the lens.
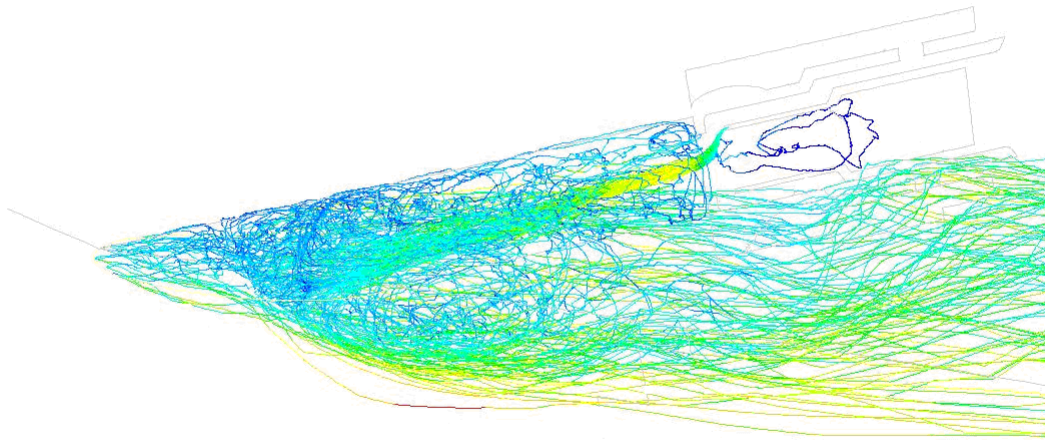
**Figure 4.28:** *Particle with negligible inertia act like fluid tracers and therefore they can reach the lens as long as the configuration makes the main phase reaching the lens.*

The idea that the purge flow can be one of the sources of contaminants was firstly hypothesized by Myhre et al. (1988). In their pyrometer design he introduced an inertial separator imposing an abrupt change on the flow direction (Figure 4.29).
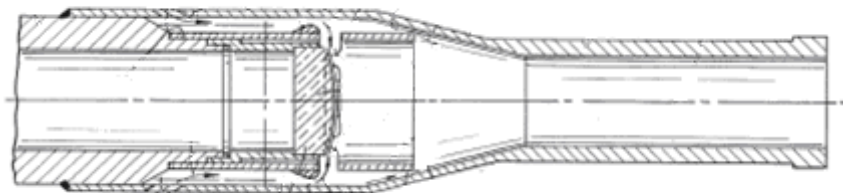


**Figure 4.29:** *Inertial separation configuration- Patent US 4836689.*

Nevertheless, Myre's work neglected the bouncing mechanism. Very small particles with negligible inertia will follow the abrupt change of direction while big particles

will hit the wall of the convergent section and then they will enter the still tube. Nonetheless, it has to been noted, as it will be explained in Chapter five, that in Myre's configuration if the velocity of the scrubbing flow is high enough very small particles will not be deposited.

### 4.5.7 Turbine Flow Contaminants

A second main category of injections analysis was carried out at the interface pyrometer/turbine. Here, only the worst case scenario has been taken in consideration for which the contaminants enter the elongated tube at maximum speed and are directed towards the lens along the pyrometer axis. The particles were injected at the pyrometer elongated tube outlet with a velocity of 500 m/s.. They were allowed to stick on the lens while a perfect elastic bouncing mechanism was considered on all the other walls.

In reality, the contaminants that have been entrapped by the turbine flow can enter the elongated tube both due to the velocity fluctuations produced by the unsteadiness of the turbine flow or due to the bouncing mechanism taking place in the turbine. This means that their direction is completely random. The results are reported in Figure 4.30
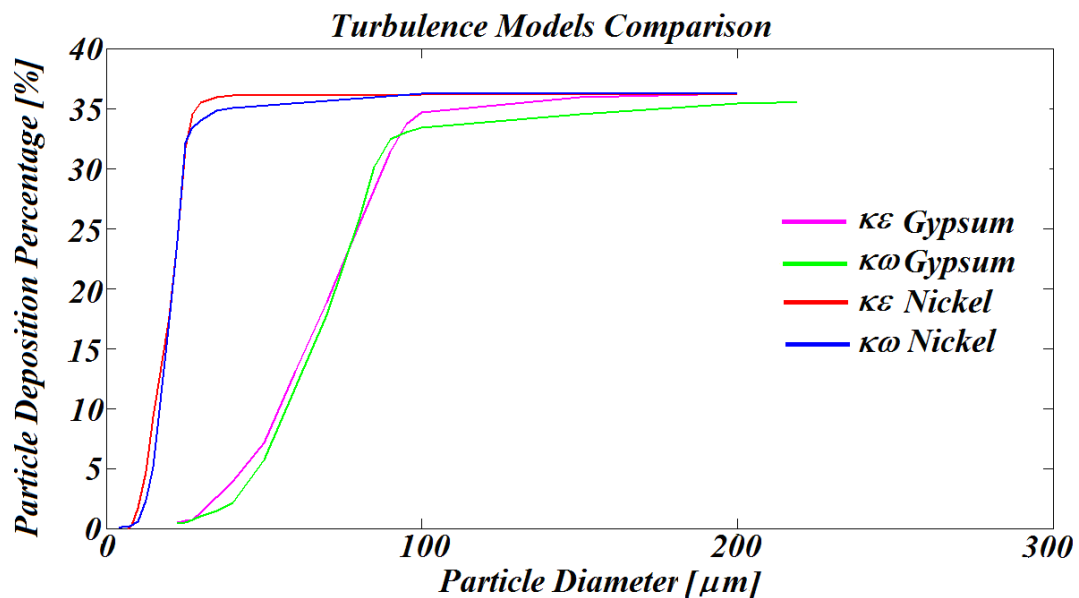


**Figure 4.30:** *Comparison between the k-ε and the k-ω results for nickel and gypsum contaminants.*

These results qualitatively agree with Kerr's study: hence the level of deposition increases with the particle diameter.

For this group of injections the role played by the drag force is very similar to that of the simplified case described in the previous Section. The particle stopping distance increases with the particle diameter until the contaminants reaches the still tube. The particle behaviour is described trough Figure 4.31-34.
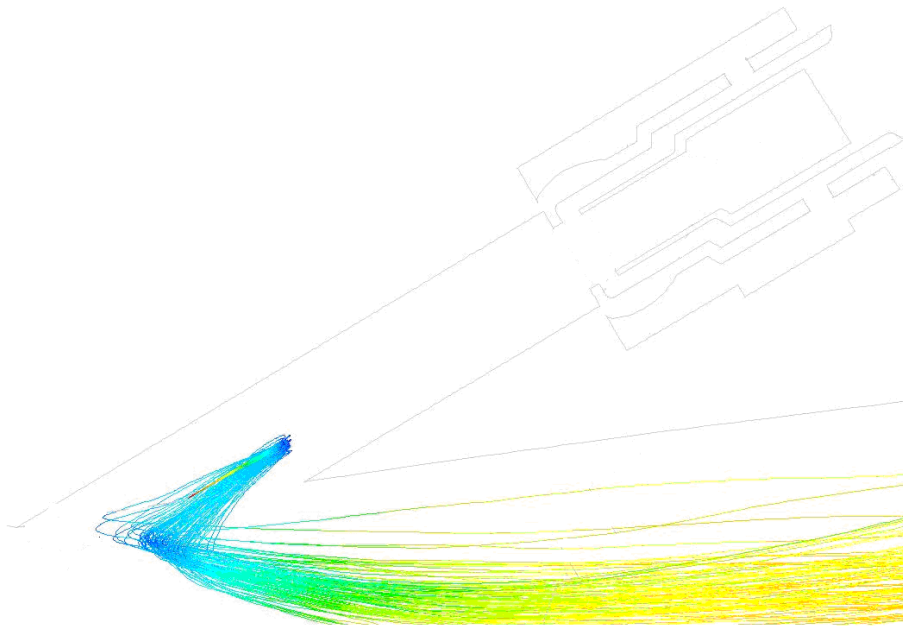


**Figure 4.31**: *A gypsum particle with a negligible diameter (5μm) is soon successfully rejected by purge flow.*
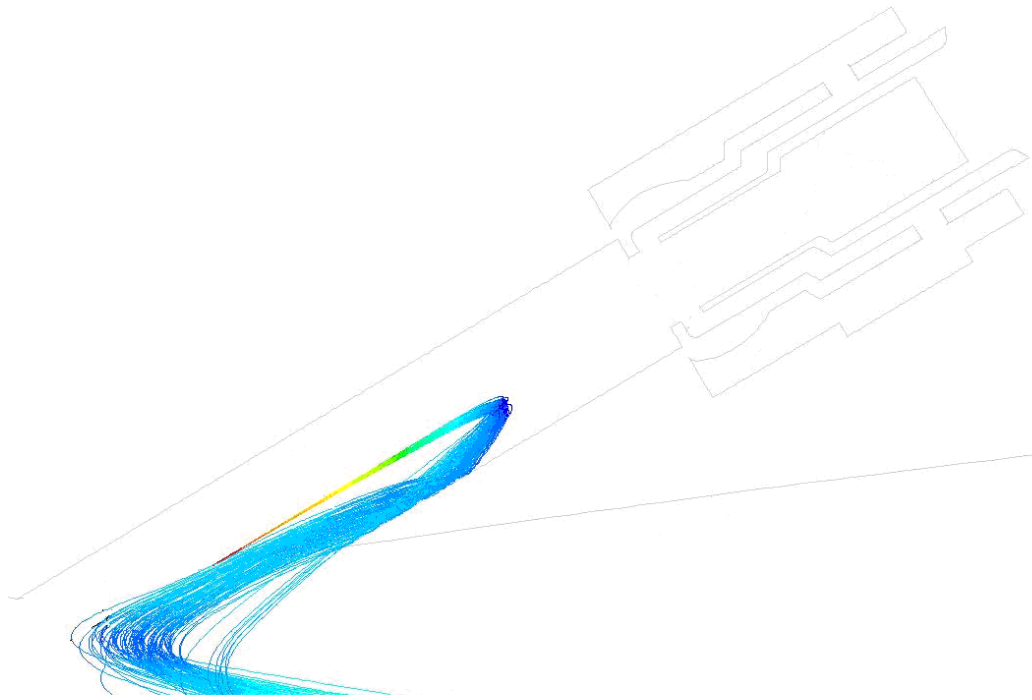
**Figure 4.32:** *A gypsum particle with a small diameter can enter more than half way through the elongated tube before being rejected by the purge flow (10μm).*
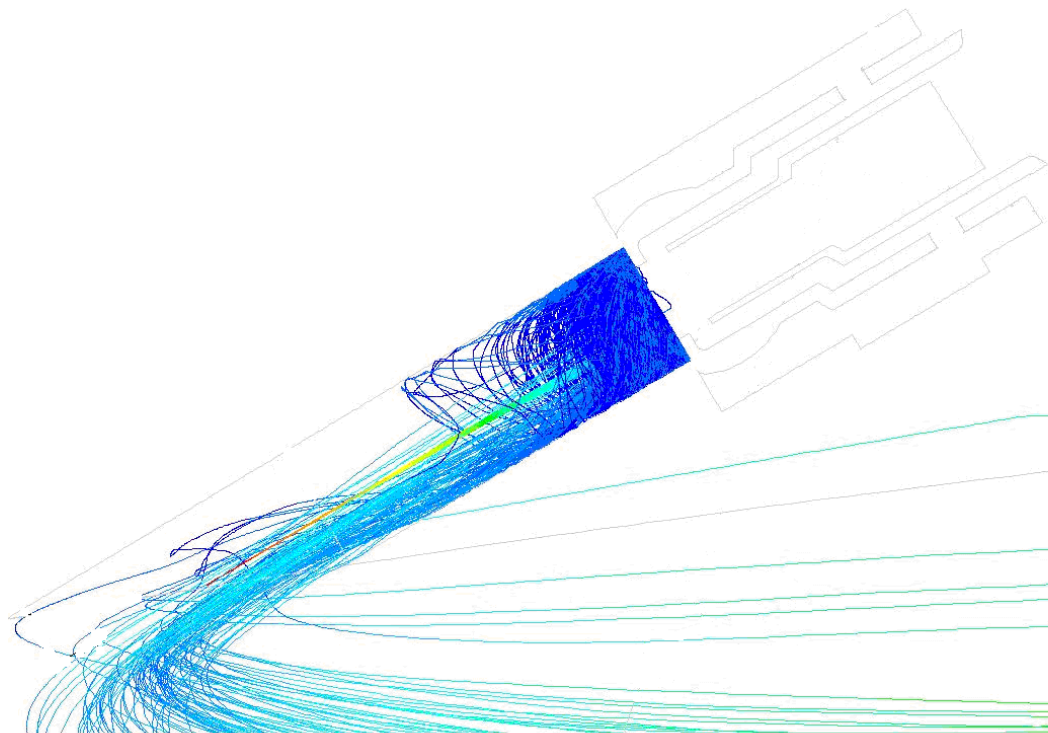


**Figure 4.33**: *Gypsum particles with a medium diameter (25μm) can be trapped by the vortices in the elongated tube being centrifuged out from the elongated tube.*
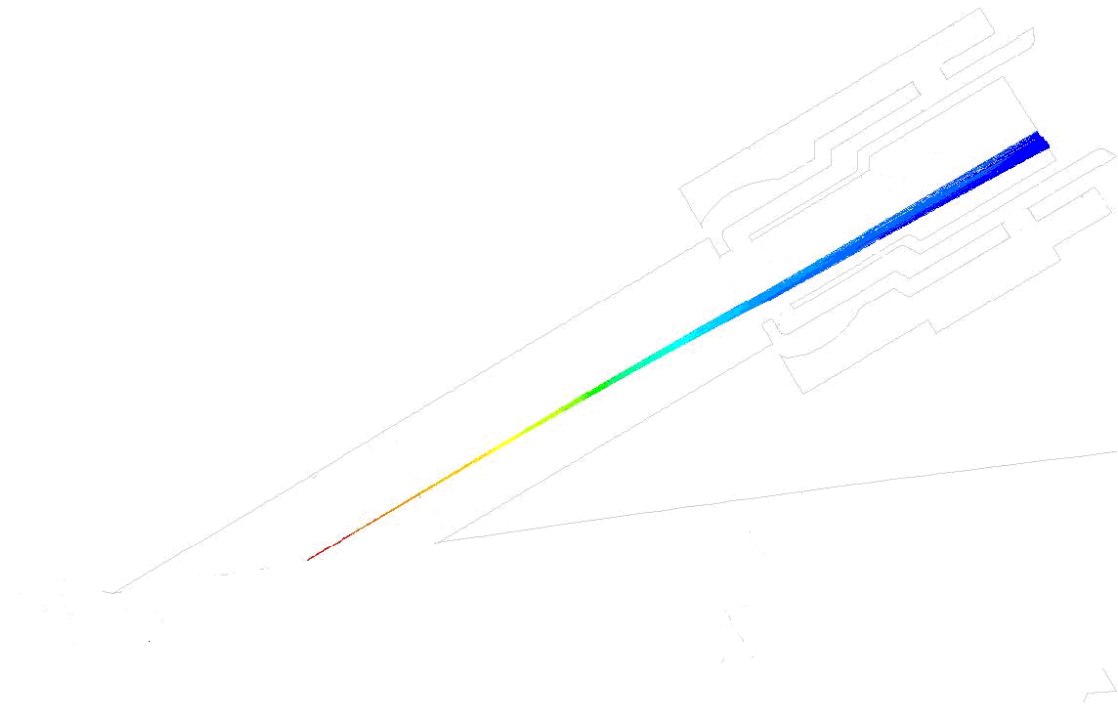
**Figure 4.34:** *A gypsum particle with a large diameter is not disturbed by the main flow field (100μm).*

The RANS models k-ε and k-ω give similar results and this can be explained noting that as for the purge contaminants scenario, the drag is controlling the particles deposition. For both RANS models the main features of the flow, controlling the turbine particle deposition, is the same and it is given by the velocity reached by the flow in the elongated tube that for both cases is almost in sonic conditions. Furthermore, it is possible to note that the curves of level of deposition have higher gradient compared with that due to the purge contaminants. This feature can again be explained through the drag force. Considering again the simplified case described in the previous paragraph, but this time keeping the density constant and changing the initial relative velocity $w_0$ it is possible to observe how the curve gradients change with increasing $w_0$ Figure 4.35.
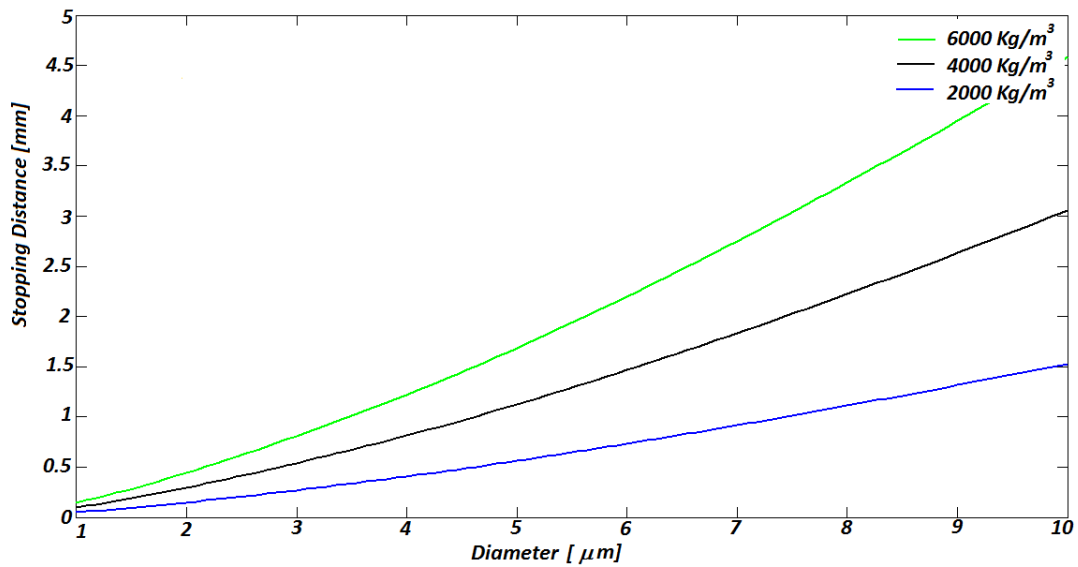
**Figure 4.35:** *Stopping distance versus particle diameter for different initial relative velocity w₀.*

Hence, the higher the component of the particle absolute velocity in the opposite direction of the flow, the higher the gradient of the stopping distance curve.

In his study, Kerr (2002a) concluded that all the particles with a diameter over a certain threshold will be deposited on the lens Figure 4.36. In this study, instead, the maximum level of deposition due the contaminants coming from the turbine environment reaches a maximum level of 36%. This discrepancy in the results is due to the fact that Kerr's did not simulate the presence of the elongated tube and he injected the contaminants directly at the purge tube outlet. Hence, very close to the still tube inlet. In reality, even if turbulence does not dominate the particle dispersion tends to scatter the particles in a cloud shape (Section 4.5.4). Therefore, even if the particles have been injected along the pyrometer axis, the final contaminants trajectory is randomly directed. This means that many particles will hit the wall of the elongated tube, thus often being redirected towards the turbine. Furthermore, it has to be noted that, neglecting the presence of the elongated tube is also synonym of not taking in account the drag force acting on the particle along the elongated tube, underestimating the particle diameter for which the particle can reach the lens.
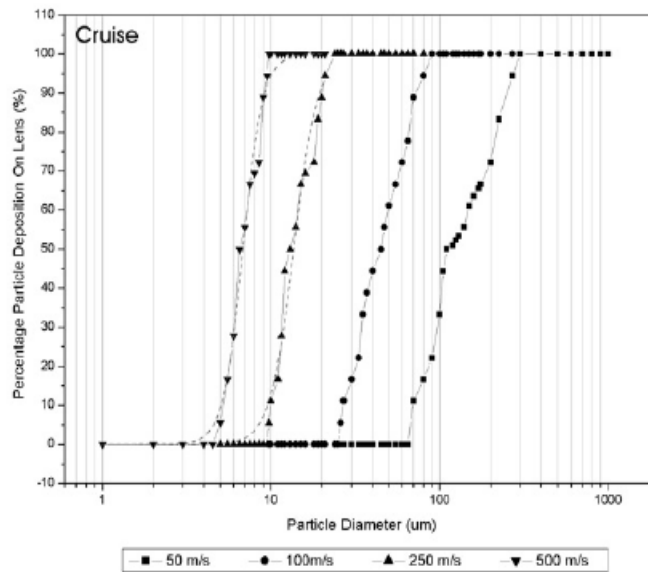
**Figure 4.36:** *Turbine contaminants deposition – Kerr's (2002a) results.*

## 4.6 Summary and Conclusions

In this Chapter the phenomena that control the particle deposition have been analysed.

For both purge flow and turbine contaminants the main force governing the particle deposition is the drag. The geometry of the air curtain configuration plays a fundamental role. The deposition of the particles entrapped in the purge flow is mainly controlled by the Stokes number that characterizes the convergent zone of the purge tube. Particles with high inertia will hit the purge tube wall and then bounce towards the pyrometer lens. Nevertheless, if the drag action is high enough then the particles will be rejected towards the turbine. The second flow feature controlling the purge contaminants deposition is represented by the recirculation zone forming in front of the still tube. If the particles are trapped by this area then they can be lead to the lens. However, it has been noted that as long as the pyrometer purge configuration involves the presence of flow in front of the lens, particles with negligible inertia can not be stopped from being deposited. The results presented in this Chapter partially disagree with the conclusions reached by the previous work of Kerr. This incongruity is mainly due to the fact that Kerr neglected the bouncing phenomenon.

The turbine contaminants deposition depends on the capability of the purge flow of rejecting these particles. For both injections categories turbulence tends to scatter the particles, nevertheless it does not significantly modify the particles path.

High inertia particles will be deposited either they are entrapped by the turbine or the purge flow. Contaminants with negligible inertia will be deposited only if they are carried towards the lens by the purge flow. Therefore, it is evident that a uniform particle distribution it is expected on the lens made of a majority of very large particles and with some very small particles.

These data were confirmed by the SEM analysis (Figure 4.37) performed by the ERA technology centre and here kindly provided by Meggitt UK. From the chemical analysis of the lens it was found that most of the contaminants deposited on the lens are sand and metal particles. The distribution was homogeneous and, as expected, only very small and big particles were found.
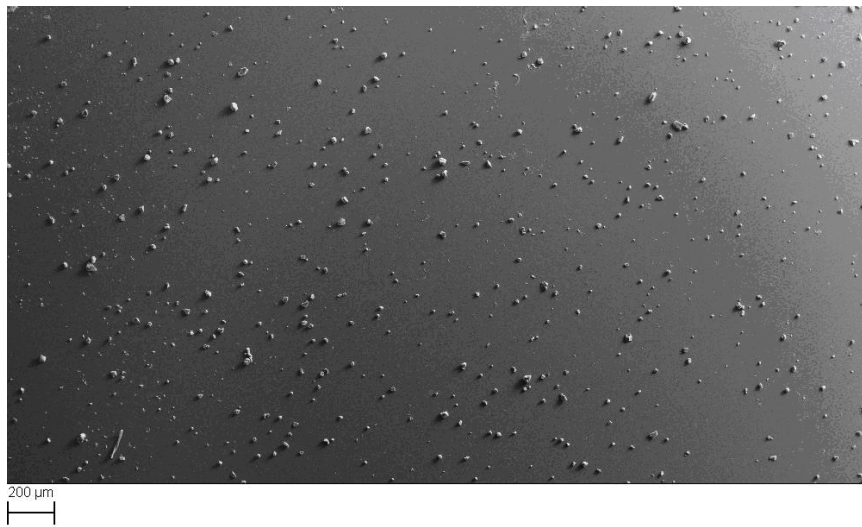


**Figure 4.37:** *SEM analysis of a fouled lens – Uniform particles distribution (kindly provided by Meggitt UK).*

The results of this Chapter will be integrated with the finite element analysis performed in Chapter 5.

# Chapter 5
# Particles Impacts Analysis

## 5.1 Introduction

A scanning electron microscope (SEM) analysis of a fouled pyrometer lens was performed in order to gain a deeper insight into the lens-fouling mechanism through the identification of different characteristics of the deposited particles by Meggitt UK. These results were here utilized to enhance the understanding of the phenomena involved in the particle deposition. A categorization of the respective physic process involved is then possible thanks to a direct comparison with data available from finite element analysis carried out in this work and from previous studies. This methodology combined with CFD results (Chapter 4) can eventually lead to the identification of the main contaminants source.

The impact of particles on flat surfaces is a phenomenon widely studied for its significant importance in very diverse engineering applications such as filter design, armour development or coating deposition. Each of these applications is characterised by a particular range of particle velocity magnitude, Klinkov et al. (2005), Figure 5.1.

At very low velocities the particles can stick onto a substrate thanks to the combined action of adhesion, Van Der Waals and electrostatic forces, as explained in section 5.2. This sticking principle is at the base of filter design.

As the particle kinetic energy increases, erosion becomes the dominant phenomenon: the particles do not stick on the surface but rebound, often after having damaged the surface.

However, at a certain point the particles velocity will be such that adiabatic shear instabilities will appear at the surface-particle interface and the consequent high values of stress produced will strongly deform the particle that will remain attached at the surface. This phenomenon was for the first time observed in the 20th century during an experiment involving the use of a shock tube: since dusty gases at high velocity were employed small particles were deposited on the test rig walls. This phenomenon is nowadays the physical principle on which a new method for coatings deposition, known as cold spray, is based (Alkhimov (1994))

A Super Deep Penetration (SDP) mechanism appears at even higher velocities when a particle can perforate the flat surface reaching a depth of penetration in the order of $10^3$-$10^4$ particle diameters.

At hypervelocities exceeding 1200 m/s (e.g. space-debris impacts), the high kinetic energy involved can destroy the flat surface.

The last impacts category comprises ballistics collisions of macro-sized particles, i.e. projectiles perforating military armours; therefore, they are not relevant to the lens fouling process.
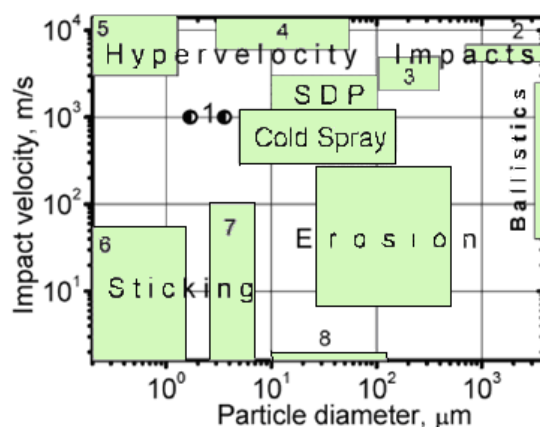


**Figure 5.1:** *Impact categories (Klinkov et al. (2005)).*

156

## 5.2 Impacts at low velocities

Impacts at low velocities between micro-particles and surfaces have been extensively investigated in many scientific and engineering applications: gas filtration and particles deposition on gas turbine blades phenomena are two examples among others.

The main aim of these studies is the identification of a criterion able to predict whether a particle impacting a particular surface at low velocity is going to stick on it or to rebound.

From these analyses, it is clear that at low velocities the outcome of the impact is controlled by several factors such as material properties, particle initial velocity, Van Der Waals and Hertzian forces. Nevertheless their interaction is not yet completely understood (Konstandopoulos (2006)).

For normal impact John (1995) ,Dahneke (1995), Wall et al. (1990), and Li et al. (1999) base their prediction criterion on the definition of a critical normal velocity: if the initial particle velocity is above this value the particle is going to rebound otherwise it is going to stick on the surface.

Oblique impacts have been studied only in the last ten years and they are not as well understood as the normal impacts because additional complexity is added to the model by strong coupling of translational and rotational motion. For this impact class a simplified prediction parameter was introduced by Konstandopoulos (2006) and it is called the critical impact angle. According to this criterion when the particle trajectory forms an angle with the surface normal higher than the critical impact angle then the particle is always going to rebound, independently of the normal velocity value.

Nevertheless, since the aim of the present research is a rough estimation of the initial velocity of the particles deposited on the lens the problem is simplified by considering only normal impacts.

### 5.2.1 Normal Impacts

Cheng et al. (2002) have developed a three dimensional model of a particle impacting on a smooth, flat surface. The dynamic physics of the phenomenon is modelled considering the combined action of all the forces acting upon the particle during the impact. The ring of forces is sketched in Figure 5.2.
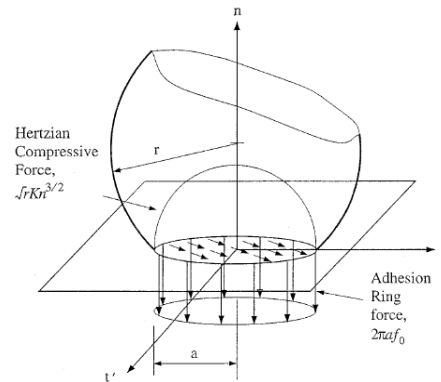


**Figure 5.2:** *Ring of forces developed at the particle-flat surface during impacts. From Cheng et al. (2002)*

Applying Newton's second law:

$$m\ddot{n} = F_H + F_{HD} + F_A + F_{AD} \qquad (5.1)$$

Where *m* is the mass, $\ddot{n}$ the acceleration, $F_H$ is the Hertzian elastic force, $F_{HD}$ is the material damping force, $F_A$ the adhesion force, $F_{AD}$ adhesion damping force and *n* the mass centre displacement.

The Hertzian elastic force can be calculated through the following formula:

$$F_H = \sqrt{r}K(-n)^{3/2} \quad n \le 0 \qquad (5.2)$$

Where *r* is the initial radius of the microsphere and *K* the effective material stiffness. *K* can be calculated through the following equation:

$$K = \frac{4}{3\pi(k_1 + k_2)} \qquad (5.3)$$

Where $k_1$ and $k_2$ are the stiffness values for the particle and the substrate respectively. $k_i$ is given by:

$$k_i = \frac{(1 - v_i^{*2})}{\pi E_i} \quad i = 1, 2 \qquad (5.4)$$

Where $v^*$ is the Poisson Ratio and $E_i$ the elastic modulus.

The adhesion force, $F_A$, in Equation (5.1) is modelled as a ring force acting on the periphery of the circular contact area. The intensity of the adhesion ring force is $f_0$:

$$F_A = -2\pi a f_0 \qquad (5.5)$$

Being $a$ the radius of the contact area.

At the static equilibrium state $\ddot{n} = \dot{n} = 0$ and therefore:

$$2\pi a_{eq} f_0 = \sqrt{r} K n^{3/2} \qquad (5.6)$$

It is possible to substitute $n$ with $n = \dfrac{a^2}{r}$ using the Hertzian theory, while the contact radius $a$ at the equilibrium state is estimated by the JKR theory as (John (1995)):

$$a_{eq}^3 = \frac{6\omega_A \pi r^2}{K} \qquad (5.7)$$

While $f_0$ is given by (Li et al. (1999)):

$$f_0 = \left(\frac{9}{2\pi} K r \omega_A^2\right)^{1/3} \qquad (5.8)$$

$\omega_A$ is the combined surface energy between the sphere and the surface materials. The value of $\omega_A$ can be obtained through Dupre's equation:

$$\omega_A = F_1 + F_2 - F_{12} \qquad (5.9)$$

Where $F_1$ and $F_2$ are surface free energies of body 1 and body 2, respectively, and $F_{12}$ is the interfacial free energy. In reality, the surface tensions of the bodies, $\gamma_1$ and $\gamma_2$, and the interfacial tension, $\gamma_{12}$ are used instead:

$$\omega_A = \gamma_1 + \gamma_2 - \gamma_{12} \qquad (5.10)$$

The interfacial tension can be estimated by:

$$\gamma_{12} = \gamma_1 + \gamma_2 - 2\phi_{12}\left(\gamma_1\gamma_2\right)^{1/2} \qquad (5.11)$$

Where $\phi_{12}$ is the interaction parameter. Considering $\phi_{12}$ equal to unity introduces an uncertainty lower than 2%.

The dynamic and adhesion damping are related to $F_A$ and $F_H$ through two coefficients $C_A$ and $C_H$ that are derivable only from experimental data.

$$F_{HD} = -F_H C_H \dot{n} \qquad (5.12)$$

$$F_{AD} = F_A C_A \dot{n} \qquad (5.13)$$

The work of adhesion can be defined either as the work done by adhesion stress to bring two surfaces together or as the work done to separate them from absolute contact. In reality, it was demonstrated experimentally that a hysteresis effect occurs, and consequently, at the equilibrium the separation work is greater than the adhesion work. Nevertheless, this effect is neglected in this work given that its physic principia still unclear. Therefore, the energy conservation requires that:

$$\frac{1}{2}mv_0^2 = \frac{1}{2}mv_r^2 + \pi a^2 \omega_a \qquad (5.14)$$

In which $\pi a^2 \omega_A$ is the expression for the adhesion work, $v_r$ is the rebound velocity and $v_0$ is the initial velocity. The critical velocity, below which the particle is captured by the flat surface can be estimated by imposing $v_r=0$, therefore requiring that all the particle kinetic energy is dissipated during the impact.

The value of this critical velocity is always very low, for example a titanium particle of 1 μm impacting on a sapphire lens has a critical velocity, calculated as explained before, of 0.7 m/s. Hence, only the particles that have entered the still tube and have lost a great part of their kinetic energy can stick on the lens.

Even if these contaminants remain attached to the lens, the bond is weak and therefore they can be easily removed from the lens surface through a normal cleaning procedure without damaging it.

Unfortunately, for these particles the identification of their source is not straightforward because they can easily come from the pyrometer purge air or from the turbine flow.

## 5.3  Impacts at High Velocities

Sapphire, commercially known as α-alumina, is a very hard material and normally shows a quasi-brittle behaviour. Interestingly, from the SEM analysis of a pyrometer fouled lens, it is clear that during the impact with contaminants the alumina behaves in a plastic way. This can happen only if the impact lens-particles occur at high velocities, as described by the finite element analysis in 5.4.

Useful information can be extracted from several studies about the cold spray deposition method in which micron-sized particles are accelerated at high velocity (usually in the supersonic range), by a gas jet and made to impact on a polished

substrate. During this process, the particles, after being highly deformed by the impact, bond with the surface.

As the name of the method suggests, a preheating of the particles is not necessary, even if, as Assadi et al. (2003) indicates, an increased temperature of the coating materials could enhance thermal softening and diffusion, two of the most important mechanisms in the bonding process.

In detail Klinkov et al. (2005) suggests that the main bonding mechanisms involved in cold spray are:

- Mechanical interlocking. During the impact the particle remains interlocked in the flat surface. This is a mechanism similar to that involved in projectiles/armours impacts. This phenomenon is not important in the coating deposition method but can be determinant in the lens fouling process;

- Repeated impacts. When a particle impacts onto a particle already deposited on the flat surface, the strength of the bond is improved. However, in the case of the lens fouling phenomenon the probability that a particle is going to impact on a particle already deposited is sufficiently low not to be considered in this work;

- Sticking. This mechanism is based on the assumption that particles stick onto the surface due to Van der Waals (sum of the attractive or repulsive forces of molecules, for a full explanation of this force please refer to Parsegian (2005)) or electrostatic forces (for electrically charged particles).

- Topochemical reactions. This kind of reaction that develops at the particle-surface interface generates strong bonds between the particle and the substrate and it is the main physical principle at the base of the thermal spray process.

The main variables involved in the cold spray process are the materials considered, temperatures, velocities, the diameter of the particles and their oxidation state.

### 5.3.1  Velocity and Oxidation State

It is widely agreed that a critical velocity exists over which particles successfully bond on the substrate. Both experimentally and numerically, many research efforts have been directed towards identifying this value for different combinations of particles-surface materials.

Experimentally it has been demonstrated that this critical velocity depends on many variables such as the materials involved in the impact, possible preheating of the particle or of the substrate, the purity of materials and its microstructure.

Initial material temperatures influence the value of the critical velocity because generally the material properties change with the temperature. Therefore, it is important always to consider the temperature of the gas stream that carries the particles.

Li et al. (2010a) suggests that in reality for each material there exists more than one critical velocity depending on its oxidation state. In detail, the critical velocity value increases with the content of the oxygen. The explanation can be found in Figure5.3
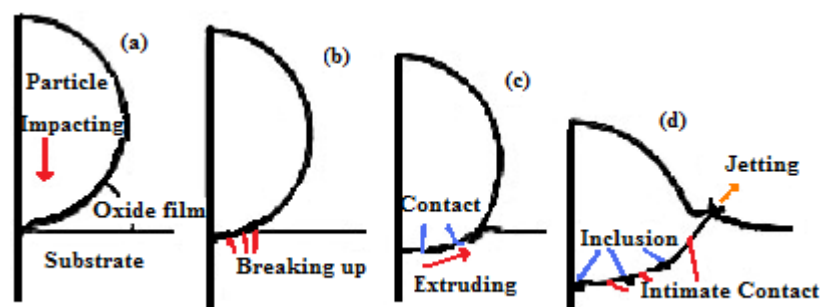


**Figure 5.3:** *Importance of the oxide film in particle/surface impacts, (Li et Gao, 2009).*

After the first contact between the particle and the substrate, the breaking up of the oxide layer follows, thus allowing the contact between the particle bulk material and the substrate. Part of the oxide layer is accelerated outwards by the developing of a jetting phenomenon while some oxide inclusions are trapped at the interface.

### 5.3.2 Particle Diameter

At the actual state of the art it is not clear if the particle diameter is an essential parameter in cold spray deposition.

Schmidt et al. (2006) state that because in cold spray deposition a particle can bond on the surface only if shear instabilities stresses develop at the interface, the thermal diffusion has to be slow enough and the velocity has to be greater than the critical velocity. Therefore, there is a limit to the value of the particle diameter under which the bonding process on a surface is not possible. Schmidt et al. calculated this critical value through the following formulas:

$$x = \sqrt{k \Delta t_p} \qquad (5.15)$$

$$k = \frac{k_t}{c_p \rho_p} \qquad (5.16)$$

$$\Delta t_p = \frac{d_p}{v_p} \qquad (5.17)$$

$$x_p = \frac{d_p}{6} \qquad (5.18)$$

$$d_{crit} = 36 \frac{k_t}{c_p \rho_p v_p} \qquad (5.19)$$

Where $x$ is the particle characteristic length and it was taken arbitrarily as a fraction of the diameter, $\rho_p$ is the particle density, $\Delta t$ is the characteristic time scale calculated from the particle diameter $d_p$ and its given impact velocity $v_p$, $k_t$ is the thermal conductivity, $c_p$ the specific heat and $d_{crit}$ the particle critical diameter.

The results are sketched in Figure5.4 for different materials.
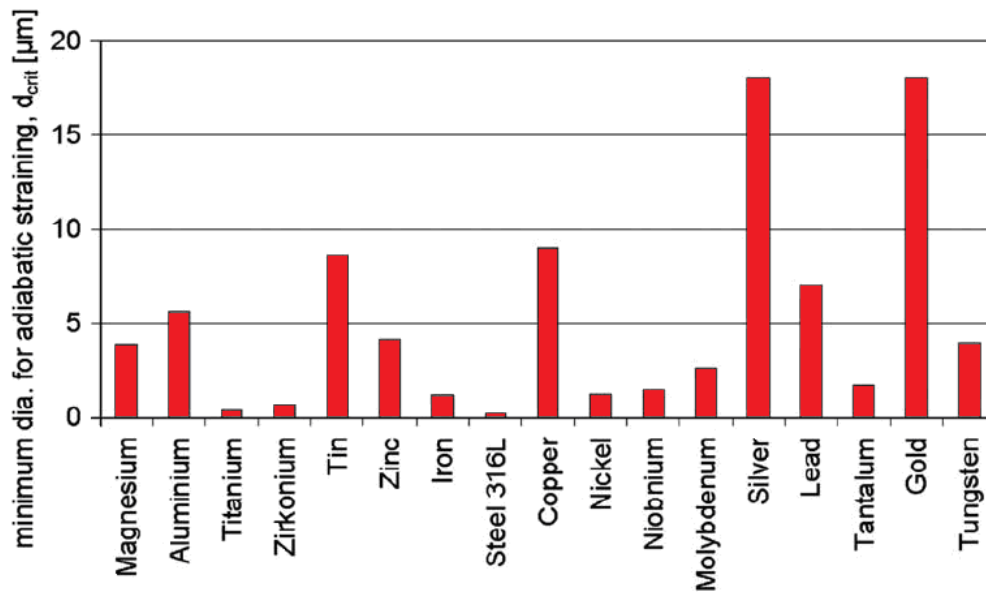
**Figure 5.4:** *Limit diameter in cold spray deposition (Schmidt et al. (2006)).*

A dissimilar conclusion was reached by Li et al. (2006) who, through experimental and numerical studies, found that the particle diameter influences negligibly the critical velocity. In a successive deeper analysis Li et al. (2010b) suggest that the oxidation state of the particles can erroneously indicate the particle size as a crucial parameter that strongly influences the value of the critical velocity. In fact, if two different powders with identical oxidation level are examined, then the finer dust contains more oxygen due to the larger specific area. Therefore, thanks to the role played by the oxide layer during the impact, the critical velocity appears to increase as the particles size becomes smaller, as reported by Schmidt et al. (2006).

### 5.3.3   Bonding Characteristic

The impact time, defined as the time interval that goes from the first particle-substrate contact until the complete conversion of kinetic energy into internal energy, is usually in the order of few nanoseconds (King (2010)). For this reason, it is impossible to experimentally observe the bonding process. The only information available is obtained via finite element analysis and from direct observation of the particles/substrate system after the impact. When the particle impacts the substrate, high-pressure levels arise from the contact point and then spread spherically through the particle and the surface (Schimdt 2006, Figure5.5). At the interface, the

temperature of the material increases considerably, adiabatic shear instabilities appear and the materials start behaving in a viscous way moving laterally and creating the so-called "jetting" phenomenon.
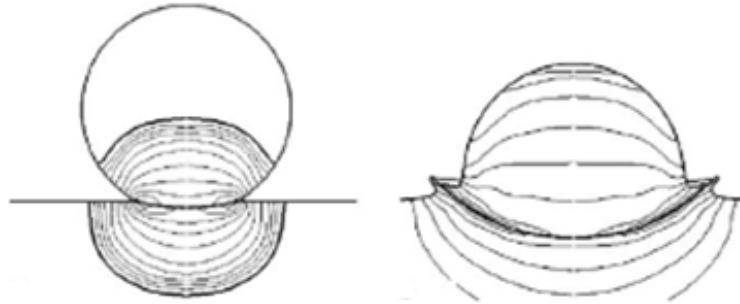


**Figure 5.5:** *High pressure levels during particle/surface impact (Schmidt et al.(2006)).*

Because this process is not directly observable, it is still not clear if during the impact melting occurs at the interface and if this mechanism is fundamental for bonding.

Frequently, cold spray is compared with explosive welding in which the development of a jet allows the bonding by removing possible contaminants present on the substrate. Remarkably, the bonding takes place with or without the melting of the particles or of the substrate (Cowan et Holtzman (1963)).

The latest studies seem to confirm that this behaviour is shared with cold spray deposition: melting is possible but not necessary. Nevertheless, different authors reached different conclusions.

For example Bae et al. (2008) carried out several finite element analyses in order to investigate the behaviour of different material combinations of the system particle/substrate. While the resulting deformed shapes were found to be quite different (Figure5.6), the temperatures involved always reached or were very close to the melting point. In detail, if two different materials were used then the transition solid-liquid occurred for the softer material.
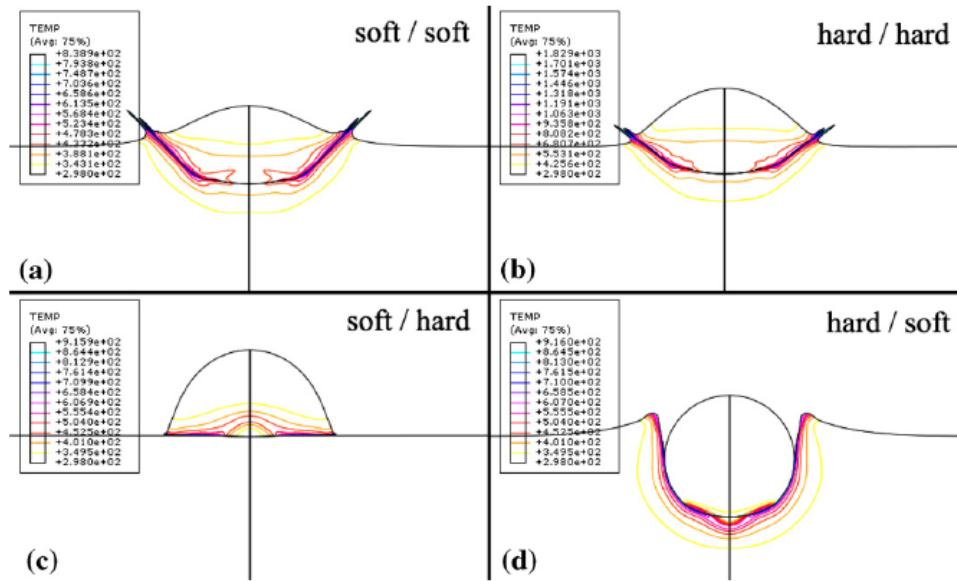
**Figure 5.6:** *Behaviour of different material combinations of the system particle/substrate (Bae et al., 2008).*

On the other hand, the experimental and the numerical analysis conducted by Dykhuizen et al. (1999) showed no melting evidence and the author reached the same conclusion as Grujicic et al. (2003): the necessary condition for bonding is the appearance of jetting and not of melting.

Nevertheless, several experimental studies, like that of Li et al. (2005,2007) found evidence of melting; an exhaustive summary of these works is analysed by King (2010) in Table 5.1-2.It is notable that in this table the value of the stagnation temperature of the jet flow carrying the particles is also reported because this can pre-heat the substrate influencing the critical velocity value (King (2010)).

In detail, King sprayed copper particles on two different aluminium substrates using different carrying flow temperatures. The author noticed that evidence of melting became clearer as the flow temperature increased. In detail, ejecta, made of melted substrate, were found spreading radially around the particle on the substrate (Figure5.7). The other significant outcome of this work is that comparing the two cases under study the crater depth was found to be shallower and the jetting more evident in the case of the copper particle hitting the hardest of the two aluminium substrates. The analytical model confirmed that higher temperatures are reached in correspondence with the harder substrate. Another important evidence of the presence

of a liquid layer during the impact is the occurrence of an interphase Cu-Al at the system interface. Its presence is justified only if melting occurs. In fact, the diffusion of the solid system Cu-Al is negligible while it is important in the system solid copper and liquid aluminium. The same conclusions were reached in Barradas et al. (2007) where intermetallics eutectic phases were found: from the calculation of the diffusion, melting was the only process justifying their presence.
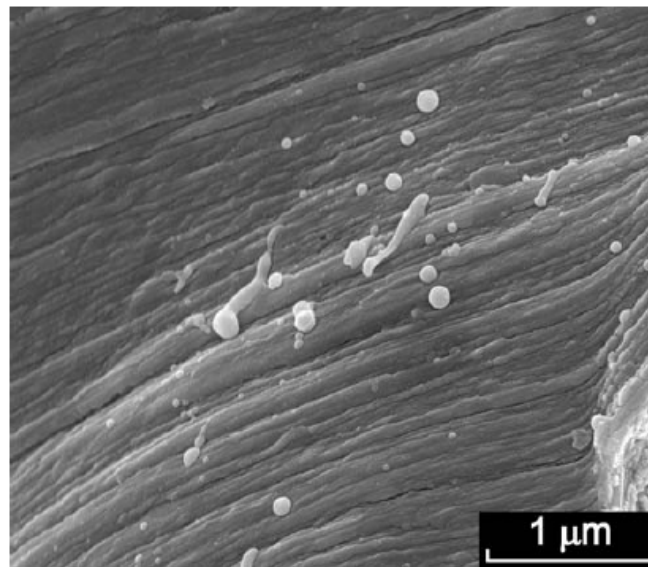


**Figure 5.7:** *Ejecta (King (2010)).*

| Reference | Material of the system | Stagnation temperature °C | Type of investigation | Evidence of melting |
|---|---|---|---|---|
| Barradas et al. (2007) | Cu onto Al | 550 | TEM of coating-substrate interface | $\alpha_2$-AlCu$_6$,$\eta_2$-AlCu, and $\theta$-CuAl$_2$ phases found, in some places layers were 20nm thick in others CuAl$_2$ grains were 400 nm in size |
| Bolesta et al. (2001) | Al Onto Ni | Not given | Grazing incidence XRD analysis of coating-substrate interface | Detection of Ni$_3$Al. Estimated interface layer thickness 20-50 nm |

| | | | FIB/TEM study | > 500 nm-thick |
| Guetta et al. (2008,2009) | Cu onto Al | 600 | of single particle interface with substrate | diffusion layer containing intermetallic phase $\theta$-CuAl$_2$ and Cu$_9$Al$_6$. Also, Al-CuAl$_2$ eutectic region |
| King et al. (2008) | Al onto PZT | 350 | Splat Studies | Spheroidized particulate ejecta and sign of adhesive interaction |
| King et al. (2008) | Cu onto Al | 600 | Splat Studies | Spheroidized Al particulate ejecta |
| Li et al. (2005) | Zn | 320,410 | TEM of deposit cross section, SEM of deposit surface | Spheroidized particulate, recrystallized grains, amorphous region |
| Li et al. (2007) | Various; Al2319,Al12Si,Ti,Ti- | 520,620 | SEM observation of deposite fracture surface | Ductile failure, dimples |

**Table 5.1:** *Summary of the latest experimental works in cold spray deposition (King (2010)).*

| Reference | Material of the system | Stagnation temperature °C | Type of investigation | Evidence of melting |
|---|---|---|---|---|
| Ning et al. (2008) | Al-10%Sn onto 304 stainless steel | ≈300 | Splat studies | Ejecta |
| Vlcek et al. (2005) | Ti-6Al-4V | Not given | SEM,TEM | Spheroidized particulates |
| Wank et al. (2006) | Zn and Zn5Al onto Al 7022 and Mg AZ91 | 250 | TEM studies of coating/substrate interface | Submicron and nanosized precipitates at interface: MgZn$_2$, and Mg$_5$Zn$_2$Al$_2$ and Mg$_{11}$Zn$_{11}$Al$_6$ |

| Xiong et al. (2008) | Al onto Al/Ni onto Al6061-T6 | 300,400 | TEM studies of interface | Formation of amorphous layer 3nm thick |
|---|---|---|---|---|
| Zhang et al. (2005) | Al onto Sn | Room Temperature | SEM | Melting of substrate-details not given |

**Table 5.2:** *Summary of the latest experimental works in cold spray deposition (King (2010)).*

In the case of the pyrometer lens/contaminants system, the particles interact with a very hard substrate. Similarities can be found in the work of Wu et al. (2006) in which Si and Al particles were sprayed on a mild steel substrate. Compared to Al–Si powder, the mild steel is a rigid material. During the spray process some of the particles bonded with the substrate (Figure 5.8a) while others bounced back leaving a small crater on the surface. In any case, evidence of melting was not found. Relevant information can be extracted by analysing the aspects of the craters (Figure 5.8b) where very small particles, smaller than the sprayed powder, are bonded onto the substrate.

It is suggested that particles asperities sliding on the surface cause stress concentration; SEM analysis showed that these small particles are crushed Al-Si powder. Also in the work of King (2010), asperities cause local melting while particle debris remain attached to the molten substrate.



(a)                                                    (b)
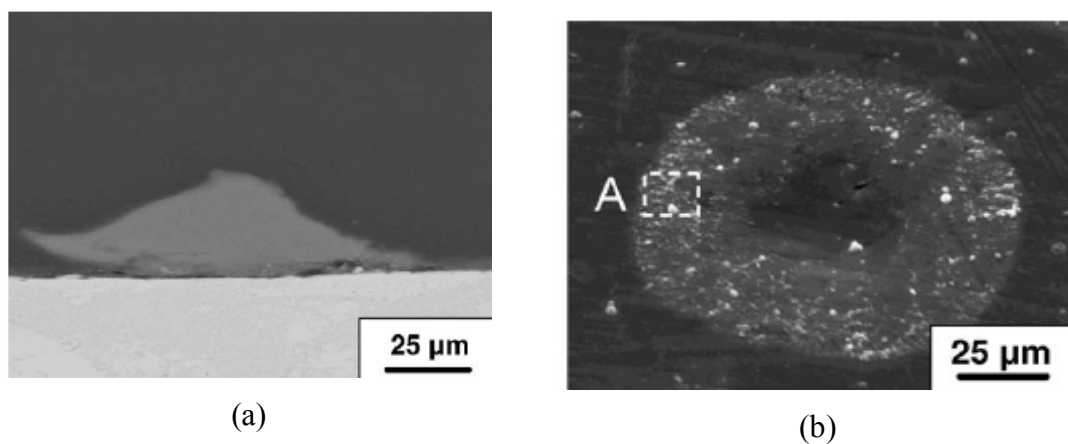
**Figure 5.8:** *(a) Bonded particle (b) Debris left by a particle that rebounded on the surface. The debris are significantly smaller than the sprayed powder, Wu et al. (2006).*

Similar results were achieved by Kim (2009a) who focused the study on jet formation in the warm spray deposition method. In this case, titanium particles were heated and sprayed onto a steel substrate. The deformed particles bonded with the substrate after the development of the jetting phenomenon (Figure 5.9)
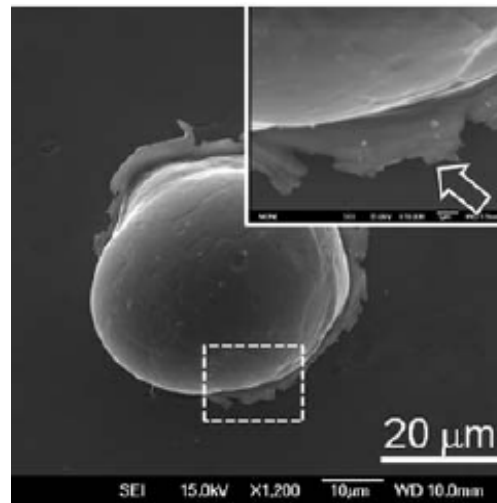


**Figure 5.9:** *A titanium particle bonded on a steel substrate after the appearance of the jetting phenomenon, Kim's experiment (2009a).*

In order to clarify some aspects of the jetting phenomenon Kim coated the substrate with a thin layer of gold. During the spraying process, some of the particles stuck to the substrate while others bounced back leaving a crater as an effect of the impact. As it is possible to see in Figure 5.10 the gold layer was removed only in the outer region of the crater suggesting that this is the zone were the highest temperatures and stresses were reached. Furthermore, the gold layer did not melt, therefore the jetting occurred in a solid state.
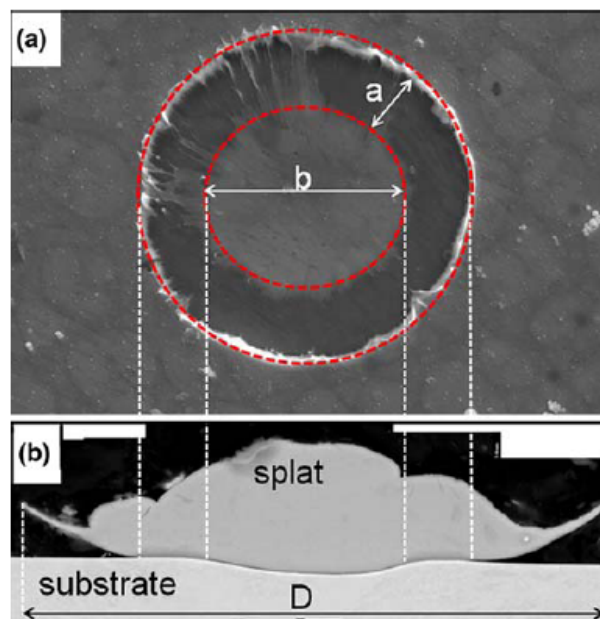
**Figure 5.10:** *(a) The gold layer was removed only in the outer region of the crater suggesting that this is the zone were the highest temperatures and stresses are reached (b) The interaction particle/substrate area can be divided in three main zones (Kim ( 2009a)).*

Thanks to the direct comparison of a deposited particle with a crater left by another particle it is possible to divide the interaction particle/substrate area into three zones (Figure 5.10b).

- An internal zone, where the particle creates a crater in the substrate but where the surface is not scratched;
- An intermediate zone, where the jet phenomenon occurs;
- A third zone, where the particle is not in contact with the surface.

Remarkably, this crater shape is able to explain why after a cleaning procedure it was possible to find on the pyrometer lens craters smaller than the relative particles attached.

A similar shape of the bonded particles can be found in the work of Kim et al. (2009b). Also in this case the zone where the highest temperatures and the strongest bond were reached was on the outer zone of the interface substrate/particle. This

outcome is additionally confirmed by the fact that a high-resolution microscope analysis of a bonded particle showed a detachment zone localised at the central part of the interface, Figure 5.11.
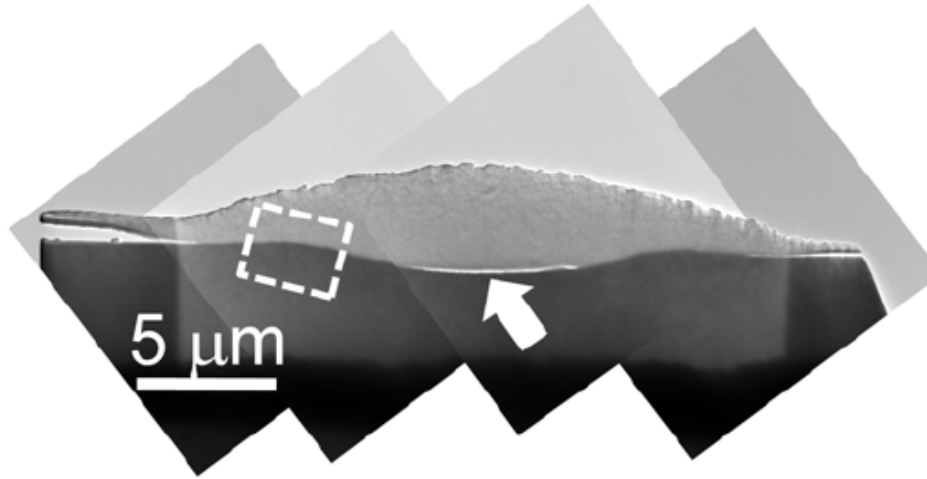


**Figure 5.11:** *A high-resolution microscope analysis of a bonded particle showed a detachment zone localised at the inner part of the interface, highlighted by the arrow (Kim ( 2009b)).*

Few works investigated the possible use of the cold spray process on a ceramic substrate. One exception is the work of King (2008) where aluminium powder was sprayed on piezoelectric ceramic (PZT). In this case, only a low percentage of particles remained deposited on the ceramic while in no case did the ceramic show a plastic behaviour (differently from what is shown by SEM results on the pyrometer lens). Nevertheless, it is important to examine the debris left by some of the particles that rebounded (Figure 5.12) because they show similarities with the pyrometer lens case.  In agreement with Kim's work, when the particle hit the surface, at the interface, the temperature rose to the point where the outer layers of the particles melted then remained bonded onto the substrate and detached from the particle.
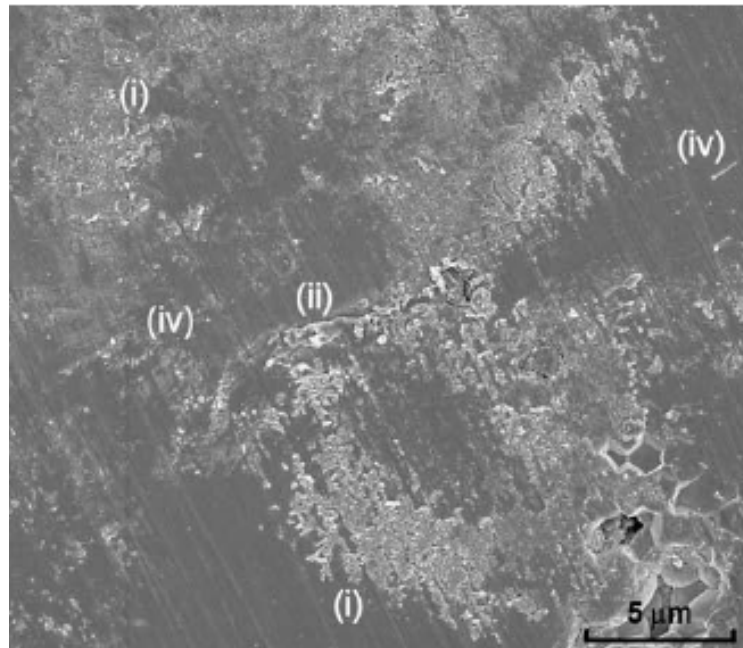
**Figure 5.12:** *Groups of submicron spherical particles that seem to have been originated from the impact point. These particles are noticeably smaller than the powder sprayed and their source can be recognised as the ejecta formed by molten layers of the impacting particle. (i) Discontinuous flakes (ii) Larger globular pieces (iii) Sheared off pieces (iv) Group of submicron particles (King (2008)).*

Another remarkable feature of the debris is the presence of groups of submicron spherical particles that seem to have been originated from the impact point. These particles are noticeably smaller than the powder sprayed and their source can be recognised as the ejecta formed by molten layers of the impacting particle. For this reason, frequently, these particles seem to be organized into ring-shapes structures. Once more, this morphology suggests that the zone of main stress is localised at the particles periphery.

The fact that the smallest particles shape is spherical is clearly due to surface tension action on the molten ejecta. It is also important to stress the fact that surface roughness and the eventual presence of grooves can greatly influence the behaviour of the molten droplets.

Furthermore, it has to be added that, as King suggests, for velocities significantly over the critical velocity, particles can penetrate deeply inside the substrate making the mechanical interlocking the main mechanism of bonding.

## 5.4 Finite Element Analysis of Particles Impacts at High Velocities.

The main aim of the finite element analysis (FEA) presented in this work is the estimation of the velocity of those particles that during the impact with the lens are able to deform it. This information can be of fundamental importance to the identification of the main source of these contaminants.

Generally, the shape of the contaminants is completely random; therefore, in order to highlight eventual differences in the impact behaviour, two main particles shapes, spherical (Figure 5.13) and square (Figure 5.14) are simulated. For both cases the substrate is considered to be a cylinder. For simplicity reasons, in this study only normal impacts are taken into consideration, and therefore the impacts where simulated through a 2D axisymmetric model.

An extensive investigation regarding setting adequately the ABAQUS solver to simulate impacts at high velocity can be found in Li's et Gao's work (2009). These guidelines are followed in the present study and their work was reproduced in the first phase of the present research to validate the approach used to simulate high speed impacts.
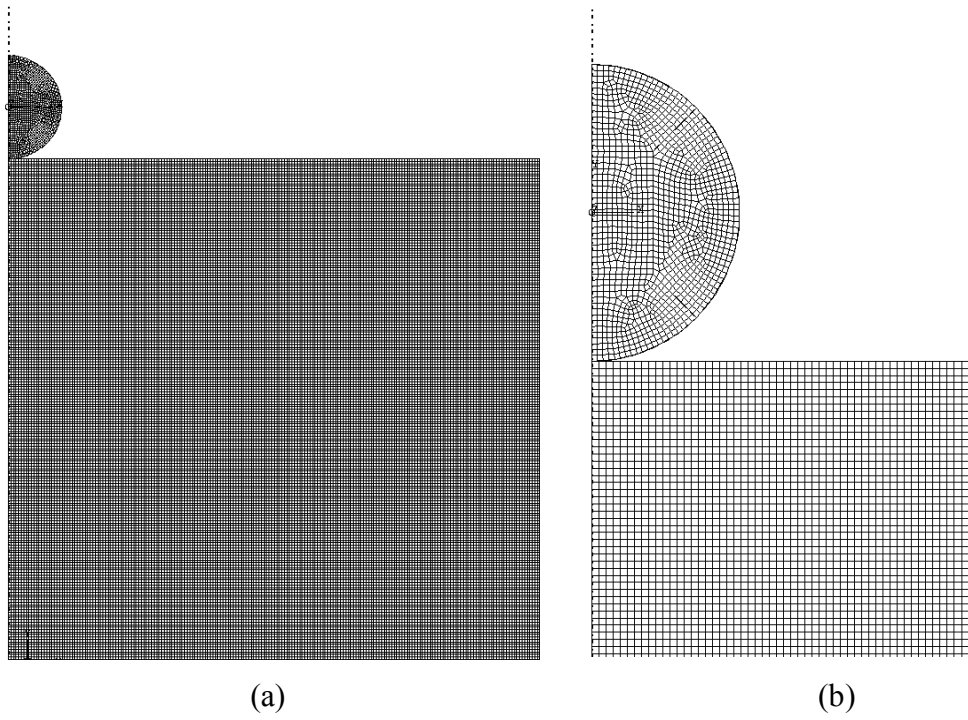
**Figure 5.13:** *(a) Mesh model of the spherical particle/base system (b) Mesh detail.*
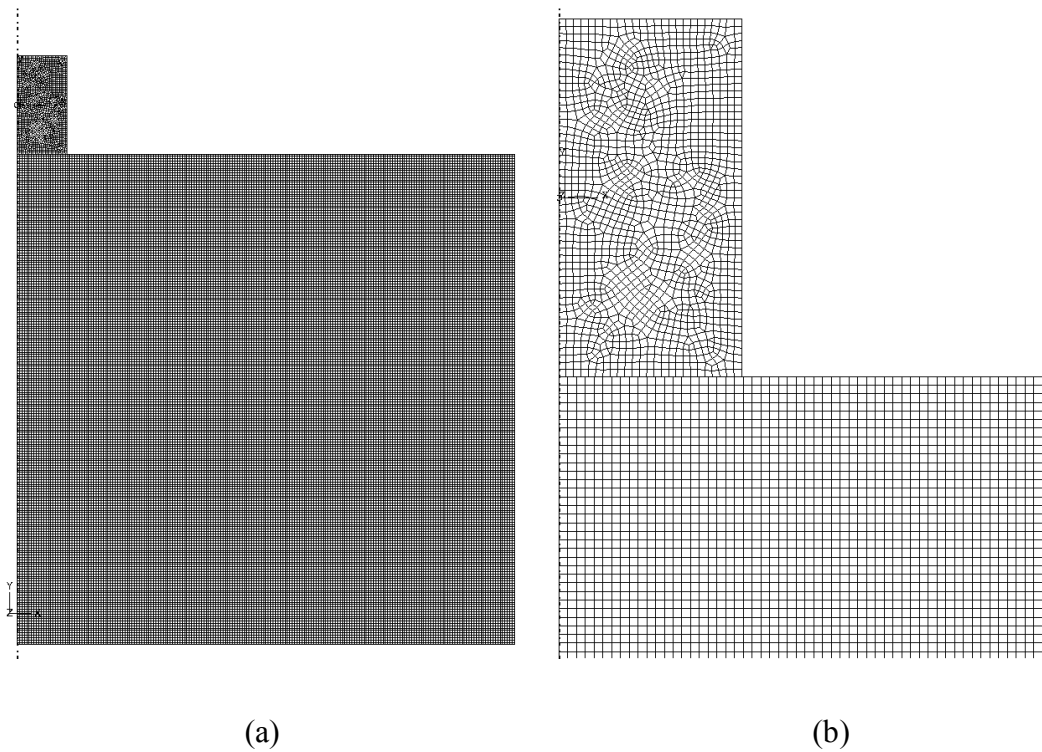


**Figure 5.14:** *(a) Mesh model of the square particle/base system (b) Mesh detail.*

### 5.4.1 Modelling of Sapphire

The properties of the sapphire lens considered in this study are those of sintered α-alumina at 99,9% reported in Munro's work (1997), Table 5.3 Exploiting the results of independent experimental studies, the author presents different criteria to predict the value of sapphire parameters at high temperature. Munro's work has the advantage of being a definitive, comprehensive set of data for one particular material specification. The formulas used to calculate the properties of the material are the following (the temperature T is expressed in °C) :

$$Elastic\ Modulus\ E^*(GPa) = 417 - 0.0525T \pm 7\% \qquad (5.20)$$

$$For\ 20°C{\leq}T{\leq}1200°C$$

$$Shear\ Modulus\ G^*(GPa) = 169 - 0.0229T \pm 6\% \qquad (5.21)$$

$$For\ 20°C{\leq}T{\leq}1200°C$$

$$Poisson's\ ratio = \frac{E}{2G} - 1 \qquad (5.22)$$

$$Compressive\ Strength = 3.1 - 0.0035T + 1.1 \times 10^{-6} \pm 15\% \qquad (5.23)$$

$$For\ 20°C{\leq}T{\leq}1500°C$$

$$Tensile\ Strength(MPa) = 267 - 256\left[1 + 5.8 \times 10^9 \exp(-0.018T)\right]^{-\frac{1}{2}} \pm 10\% \qquad (5.24)$$

$$For\ 20°C{\leq}T{\leq}1500°C$$

$$Hardness(GPa)\ H_V = 15.5\exp(-0.0012T) \pm 15\% \qquad (5.25)$$

$$For\ 20°C{\leq}T{\leq}1000°C$$

$$Thermal\ Conductivity\ k(Wm^{-1}K^{-1}) = 5.85 + \frac{15360\exp(-0.002T)}{T + 516} \pm 6\% \qquad (5.26)$$

$$For\ 20°C{\leq}T{\leq}1800°C$$

$$Specific\ heat\ C_p(Jkg^{-1}K^{-1}) = 1117 + 0.14T - 411\exp(-0.0067) \pm 2\% \qquad (5.27)$$

For 20°C≤T≤1800°C

Unfortunately, in modern FEA solvers, like ABAQUS, a designed model to describe ceramic behaviour does not exist. Therefore, following the indications given by Roeder et Sun (2001) alumina is modelled to fail at a tensile stress of 360 MPa; at this value of stress the material undergoes brittle failure. ABAQUS/Explicit models brittle tensile failure by setting the deviatoric stress components to zero while the pressure stress is required to be compressive. Elastic perfectly plastic behaviour is assumed for the compressive behaviour of the alumina. The Von Mises yield criterion and the Rankine failure criterion are used in the ABAQUS models. This material modelling for α-alumina is chosen in order to reproduce its plastic behaviour, evident from the pyrometer lens SEM analysis.

| | Temperature (K) | | | | | |
|---|---|---|---|---|---|---|
| | **293** | **773** | **1273** | **1473** | **1673** | **1773** |
| **Property** | | | | | | |
| **Density (g/cm$^3$)** | 3.984 | 3.943 | 3.891 | 3.868 | 3.845 | 3.834 |
| **Elastic Modulus (GPa)** | 416 | 390 | 364 | 354 | 343 | 338 |
| **Poisson's ratio** | 0.231 | 0.237 | 0.244 | 0.247 | 0.250 | 0.252 |
| **Shear modulus (GPa)** | 169 | 158 | 146 | 142 | 137 | 135 |
| **Specific Heat (J·kg$^{-1}$·K$^{-1}$)** | 755 | 1165 | 1255 | 1285 | 1315 | 1330 |
| **Thermal Conductivity (W·m$^{-1}$·K$^{-1}$)** | 33 | 11.4 | 7.22 | 6.67 | 6.34 | 6.23 |
| **Tensile Strength (MPa)** | 267 | 267 | 243 | 140 | 22 | 13 |
| **Compressive Strength (GPa)** | 3.0 | 1.6 | 0.7 | 0.4 | 0.3 | 0.28 |

**Table 5.3:** *Main α-alumina properties with temperature, Munro (1997)*

### 5.4.2 Modelling of Metals

The metals particles behaviour is simulated using the Johnson-Cook model offered by Abaqus solver. This model is a variant of Von Mises plasticity law. In the Von Mises plasticity model for isotropic and ductile materials the strength at compression and tension has the same value and the material fails when the distortion energy equals a critical value ($\sigma_{yield}$)Figure 5.15
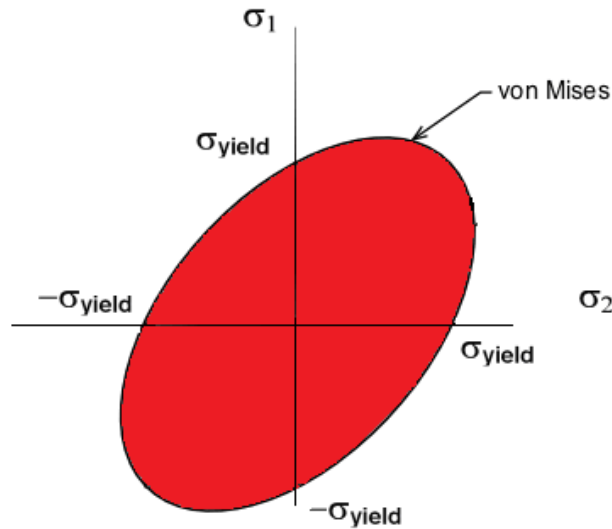


**Figure 5.15:** *Project of the von Mises criterion into the $\sigma_1/\sigma_2$ plane.*

The Johnson-Cook model with analytical forms of the hardening law and rate dependence is chosen because it is appropriate when a high-strain-rate deformation of the metals is involved and therefore it is suitable for transient dynamic analysis. An important parameter in the Johnson-Cook model is the nondimensional temperature $\hat{\theta}$ expressed by:

$$\hat{\theta} \equiv \begin{cases} 0 & \text{for} \quad \theta < \theta_{transition} \\ (\theta - \theta_{transition})/(\theta_{melt} - \theta_{transition}) & \text{for} \quad \theta_{transition} \leq \theta \leq \theta_{melt} \quad (5.28) \\ 1 & \text{for} \quad \theta > \theta_{melt} \end{cases}$$

Where $\theta$ is the actual temperature, $\theta_{melt}$ is the melting temperature, and $\theta_{transition}$ is the transition temperature defined as the one at or below which there is no temperature dependence on the expression of the yield stress.

The Johnson-Cook model expresses the isotropic hardening $\sigma^0$ as:

$$\sigma^0 = \left[A + B\left(\overline{\varepsilon}^{pl}\right)^N\right]\left(1 - \hat{\theta}^M\right) \quad (5.29)$$

where $\overline{\varepsilon}^{pl}$ is the equivalent plastic strain and $A$, $B$, $N$ and $M$ are material parameters measured below or at $\theta_{transition}$.

If $\theta > \theta_{melt}$, the metal shows a fluid like behaviour without shear resistance being $\sigma^0 = 0$. In addition, the yield stress is formulated by:

$$\overline{\sigma} = \left[A + B(\overline{\varepsilon}^{pl})^N\right]\left[1 + C^* \ln\left(\frac{\dot{\overline{\varepsilon}}^{pl}}{\dot{\varepsilon}_0}\right)\right]\left(1 - \hat{\theta}^M\right) \quad (5.30)$$

Where $\overline{\sigma}$ is the yield stress at nonzero strain rate, $\overline{\varepsilon}^{pl}$ is the effective plastic strain (PEEQ), $\dot{\overline{\varepsilon}}^{pl}$ is the effective plastic strain rate, $\dot{\varepsilon}_0$ is a reference strain rate and $C^*$ is a constant.

The value for the constants using to model Nickel in this work are taken from Bae et al. (2008) and reported in Table 5.4.

| Parameter | Nickel |
|---|---|
| Density (kg·m$^{-3}$) | 8890 |
| Young's modulus | 207 |
| Poisson's ratio | 0.31 |
| Heat Capacity (J · kg$^{-1}$K$^{-1}$) | 456 |
| Melting temperature (K) | 1726 |
| A (MPa) | 163.0 |
| B(MPa) | 648.0 |
| N | 0.330 |
| C$^*$ | 0.006 |
| M | 1.44 |
| Reference temperature (K) | 298 |
| Reference strain rate (s$^{-1}$) | 1 |

**Table 5.4:** *Nickel Johnson-Cook model main parameter*

Nickel is chosen as the particle material of the main FEA analysis because it is one of the hardest metallic materials present in the aeronautical engine. Therefore, its critical velocity value is lower than that of a softer material giving in this way an indication of the minimum velocity of the contaminants for which the lens is damaged.

### 5.4.3  Mesh Size

In many numerical papers the critical velocity is defined as the velocity for which in the trend of temperature and PEEQ, a discontinuity, representing the appearance of shear instability, is found (Assadi et al. (2003), Schmidt et al. (2006)), Figure5.16.
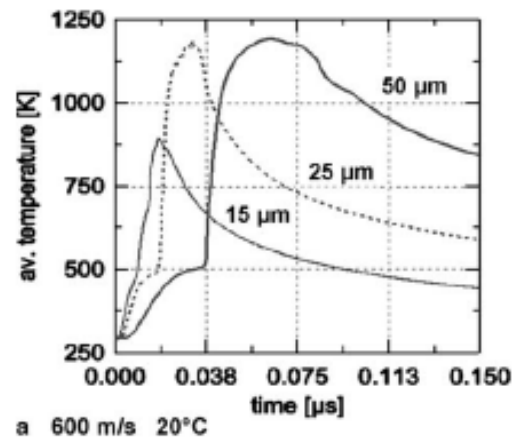


**Figure 5.16:** *The temperature discontinuity is associated with the reaching of the critical velocity (Schmidt et al. ( 2006)).*

Nonetheless, the mesh size (Assadi et al. (2003), Li et al. (2006), Li et al. (2009)) can strongly affect the results leading to erroneous conclusions. Li et al. (2009) conducted a study performing different FEA analyses with different mesh sizes going from $1/20d_p$ to $1/100d_p$. In general, it was found that if the critical velocity is defined as that for which the shear instabilities occur then this decreases with the meshing size. This can be due to a numerical problem caused by excessively distorted elements. This issue requires more numerical works, eventually validated by experimental results, to be resolved.

In Assadi et al. (2003) the possibility that the change in the critical velocity value with the mesh size can be due to a numerical instability is not taken into consideration. Therefore, the Author extrapolated the temperature reached by the interface for a hypothetical element size of 0 (copper against copper). The same procedure was followed by Li et al. (2006), Figure5.17.
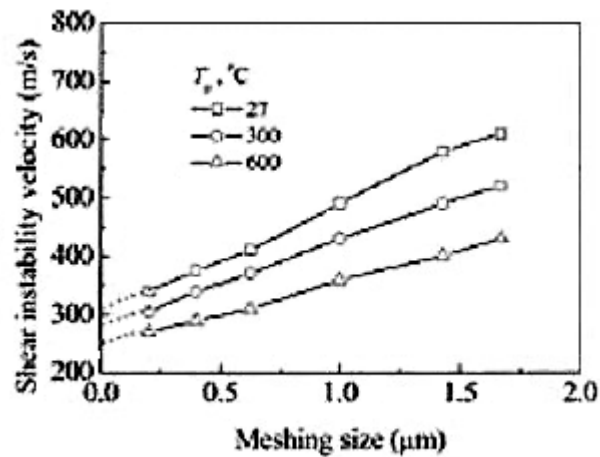
**Figure 5.17:** *Extrapolated temperature reached by the interface for an hypothetical element size of 0, Li et al. (2006).*

### 5.4.4  Mesh Control

In Li's et Gao's (2009) work high velocity impacts of a copper particle on a copper substrate are simulated. Remarkably, due to the strong mesh deformation it is not possible to obtain a convergent solution without employing a method to control the mesh distortion.

The ABAQUS solver offers two main approaches, mutually exclusive, to tackle the large deformation issue. The first technique is the implementation of an hourglass control method that enforces new mesh constraints using a penalty approach in order to control the associated distortion length ratio. Nonetheless, this method should be used cautiously because it can lead to unrealistic results.

Furthermore, distortion control cannot prevent elements from being distorted due to temporal instabilities, hourglass instabilities, or physically unrealistic deformation. When the hourglass control is used, the length ratio should be very small (e.g. 0.1) to avoid unfeasible results.

The other method offered by ABAQUS software is the ALE adaptive meshing technique that combines the features of pure Lagrangian analysis with the pure Eulerian analysis. It is a tool that, allowing the mesh to move independently of the

182

material, makes it possible to assure a high-quality mesh throughout the analysis, even when large deformation or loss of the material occurs (Abaqus, 2008). However, in some extreme cases, it does not work well, and the final shape obtained can be physically unjustified. Two main parameters control the ALE technique: the frequency that is given in increments at which the region is re-meshed and the number of remeshing sweep per increment.

In detail when Li et Gao applied the ALE adaptive method, he tried different combinations of frequency and remeshing sweeps. It has been seen that to a decrement in frequency corresponds a decrease of the maximum values of PEEQ and temperature while the jet shape appears smoother. In other words, more unrealistic deformations of the periphery were obtained.

When increasing the remeshing sweeps per increment the maximum PEEQ and temperature contours seem to undergo small changes while often the computational process was aborted due to the excessive distortion of some elements. In these cases, ALE adaptive meshing may be combined with other techniques, such as material damage, to make it work. Nevertheless, ALE adaptive meshing is not strongly recommended for use in modelling cold spray particles impacts owing to the unrealistic jet, as suggested by Assadi et al. (2003).

## 5.4.5  Failure

The material failure was included in the model of cold spray deposition for the first time by Li et Gao and it seems that, while it does not influence particularly the PEEQ and the temperature values, it leads to a more realistic deformation shape. Nonetheless, the exact shape is not of particular interest in this work, therefore the material failure is not included in the model, lowering in this way the computational cost of the simulation.

### 5.4.6  Thermal Consideration

In cold spray deposition simulations the thermal field is mainly governed by the empirical assumption that 90% of plastic work and 100% of friction work are dissipated as heat.

Different opinions exist about the validity of the assumption of the adiabaticity of the process. Based on the fact that the impact duration is in the order of a few nanoseconds then the process should be considered adiabatic (Li et al. (2006), Assadi et al.(2003). This conclusion contrasts with the recent studies of Schmidt et al. (2006) and Li et al. (2009) where interface conduction is included in the model.

In Guetta et al. (2009) only the adiabatic analysis is able to justify the experimental results that highlighted the presence of phenomena related to the development of high temperatures as melting, diffusion and nano-crystallization.

In detail, the jetting was found to be both solid and liquid, the former locking the particle in the substrate and the latter partially overlying the particle guaranteeing adhesion (Figure5.18).



(a)                                                           (b)
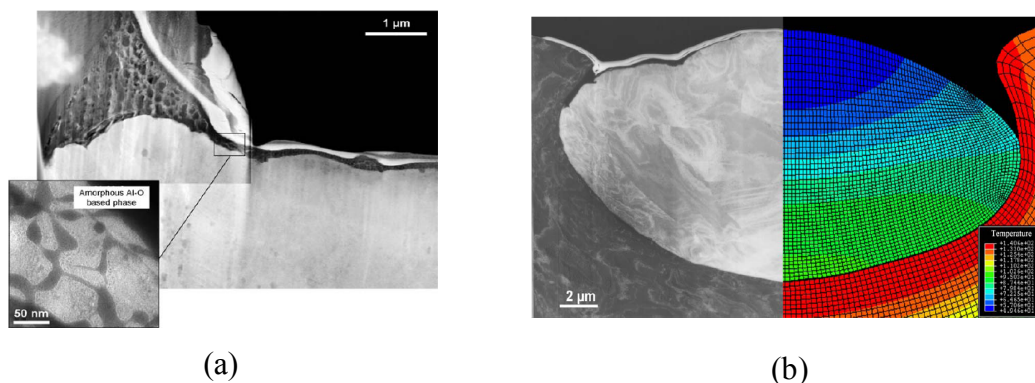
**Figure 5.18:** *(a) The experimental result highlighted the jet overlying the particle (b) Comparison of experimental and analytical results (Guetta et al. ( 2009)).*

Referring to the ABAQUS manual about this subject, it is explained that the main advantage of the Dynamic-Explicit (including adiabatic effects) formulation over the Dynamic-Temperature-Displacement-Explicit is the computational expense. Furthermore the adiabatic approach can be the more appropriate when the response times describing the process are short. Nevertheless, if the temperature and the stress field are strongly coupled then the fully coupled thermal-stress analysis is necessary. Li et al. (2009) in his work has seen that both approaches give a very similar shape but the values of PEEQ and temperature are substantially different. Due to this

incongruity and to the scientific debate still open about this subject, in the present work both adiabatic and non-adiabatic cases are examined and compared.

### 5.4.7  Friction

In the majority of recent studies, the contact between the particle and the substrate is considered frictionless. Li et al. (2009) performed different simulations using different Coulomb's friction coefficients and he found out that including the friction action in the model lowers the PEEQ and the temperature values at the interface. Nevertheless, this effect is not strong, especially in the friction factor range between 0.2 and 0.4, and, therefore, for simplicity it is not considered in the present work.

### 5.4.8  Results

Following the meshing guidelines given by Li et al. (2009), the substrate diameter is five times the particle diameter or the cube-side. The meshing resolution is $1/50d_p$ while the substrate meshing is 1.2 times that of the particle.

The mesh element is the 4-node quad element with coupled displacement and temperature, reduced integration and hourglass control.

#### 5.4.8.1  Particle Velocity, Shape and Adiabaticity

The FEA simulation results of impacts at different velocities of a spherical Nickel particle with a diameter of 20 μm on a α-alumina substrate at the instant of 60ns from initial contact are reported in Figure5.19-5.23. The initial temperature of both particle and lens is set to be 400K. For each velocity, two cases are analysed, adiabatic and non-adiabatic respectively.

In Figure5.24-5.27 the particle shape considered is square with a side length of 20 μm.
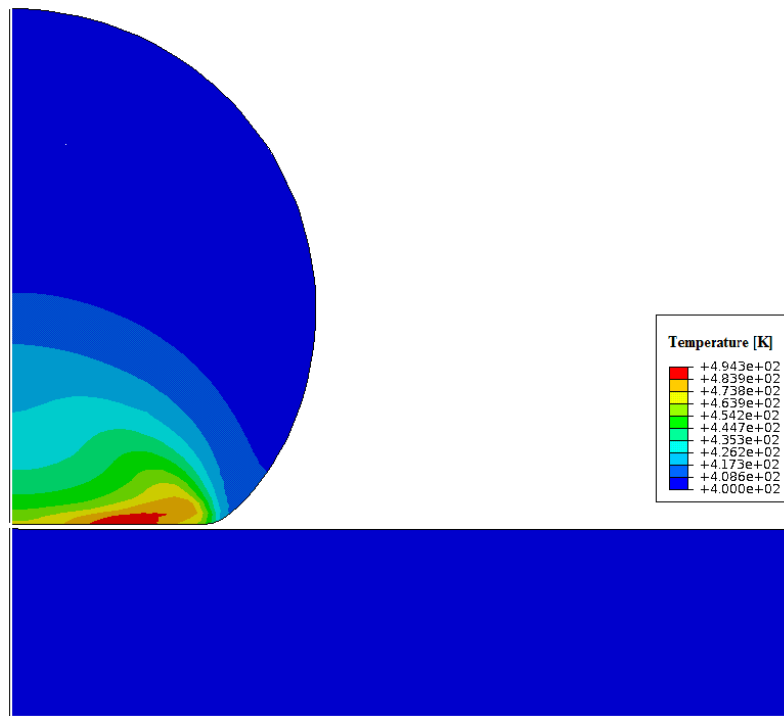
(a)
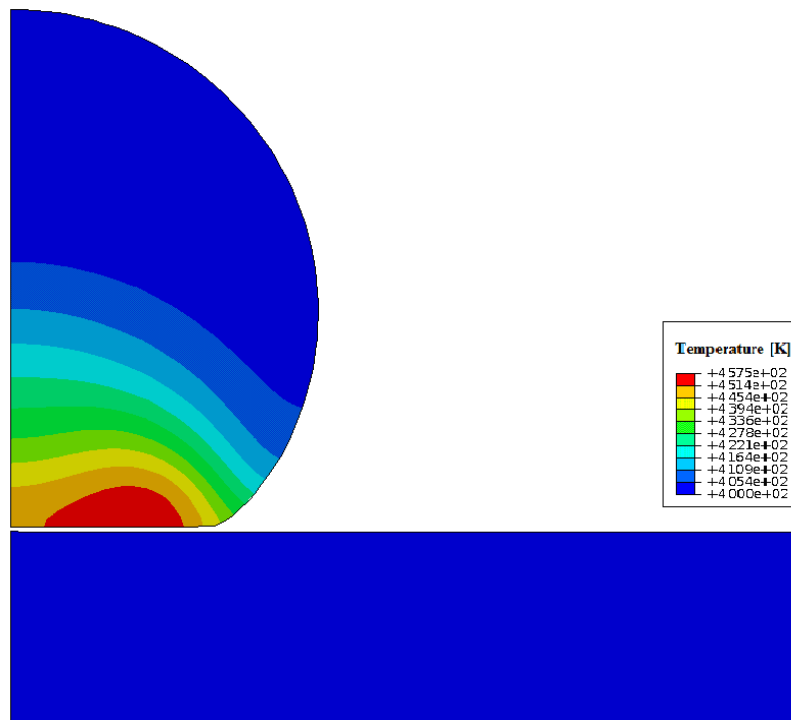


(b)

**Figure 5.19:** *Spherical Nickel particle against α-alumina substrate at 100 m/s. (a) Adiabatic case (b) Non-adiabatic case.*

(a)



(b)

**Figure 5.20:** *Spherical Nickel particle against α-alumina substrate at 200 m/s. (a) Adiabatic case (b) Non-adiabatic case.*

(a)



(b)

**Figure 5.21:** *Spherical Nickel particle against α-alumina substrate at 300 m/s. (a) Adiabatic case (b) Non-adiabatic case.*

(a)



(b)

**Figure 5.22:** *Spherical Nickel particle against α-alumina substrate at 400 m/s. (a) Adiabatic case (b) Non-adiabatic case.*

**(a)**



**(b)**

**Figure 5.23:** *Spherical Nickel particle against α-alumina substrate at 500 m/s. (a) Adiabatic case (b) Non-adiabatic case.*
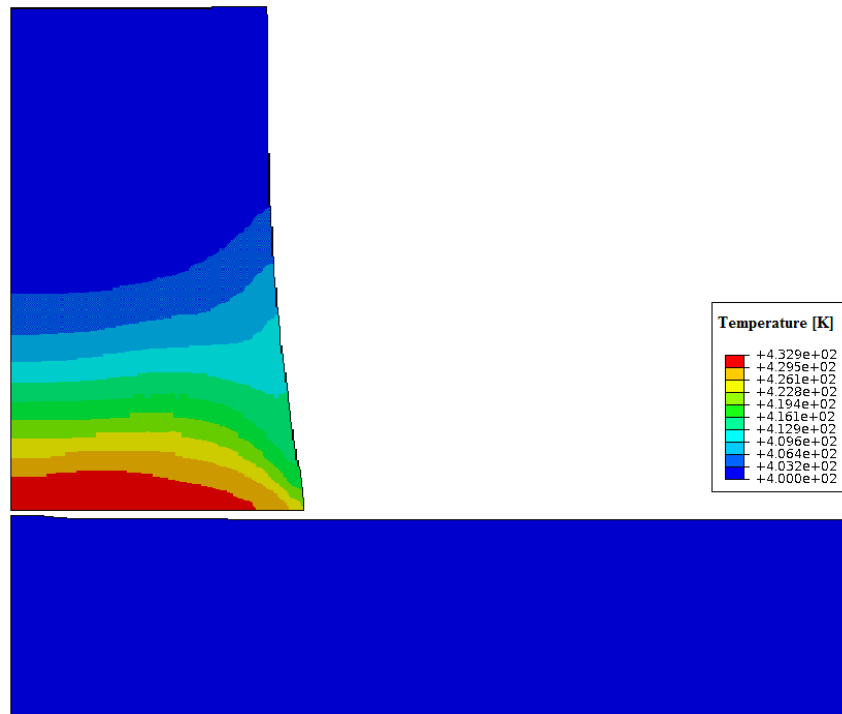
(a)
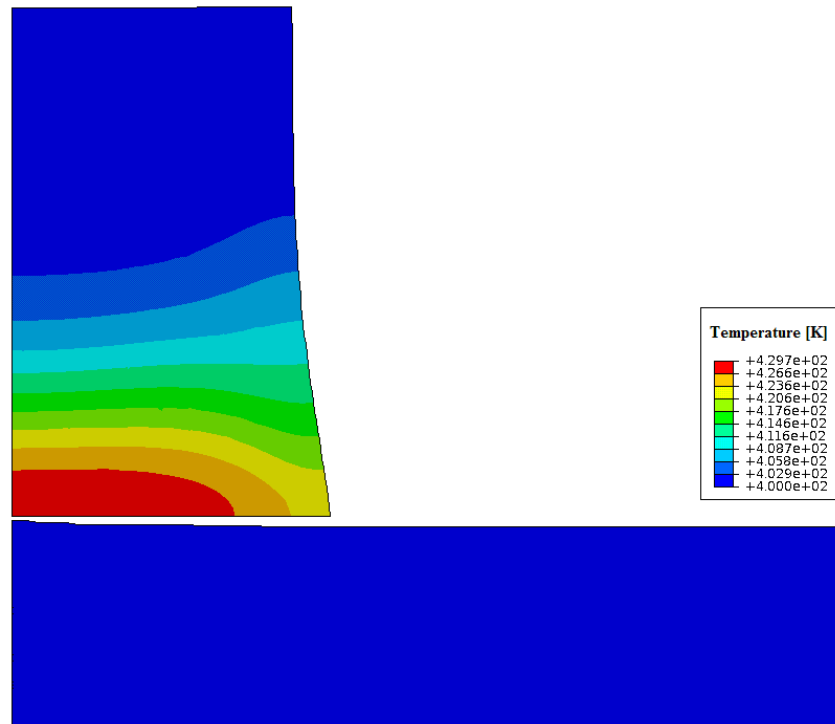


(b)

**Figure 5.24:** *Square Nickel particle against α-alumina substrate at 100 m/s. (a) Adiabatic case (b) Non-adiabatic case*

.
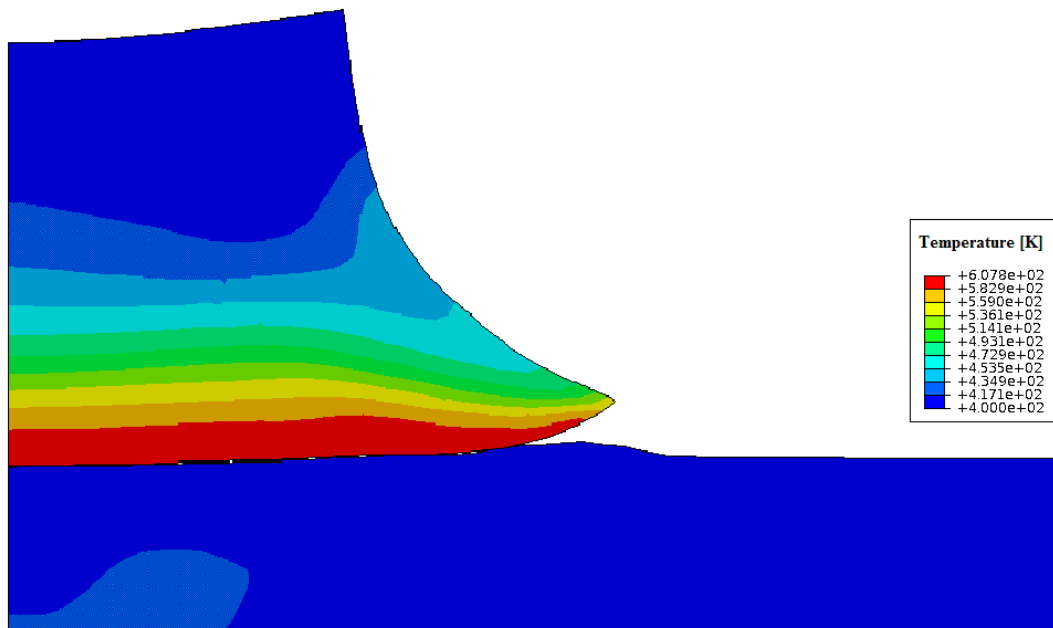
(a)
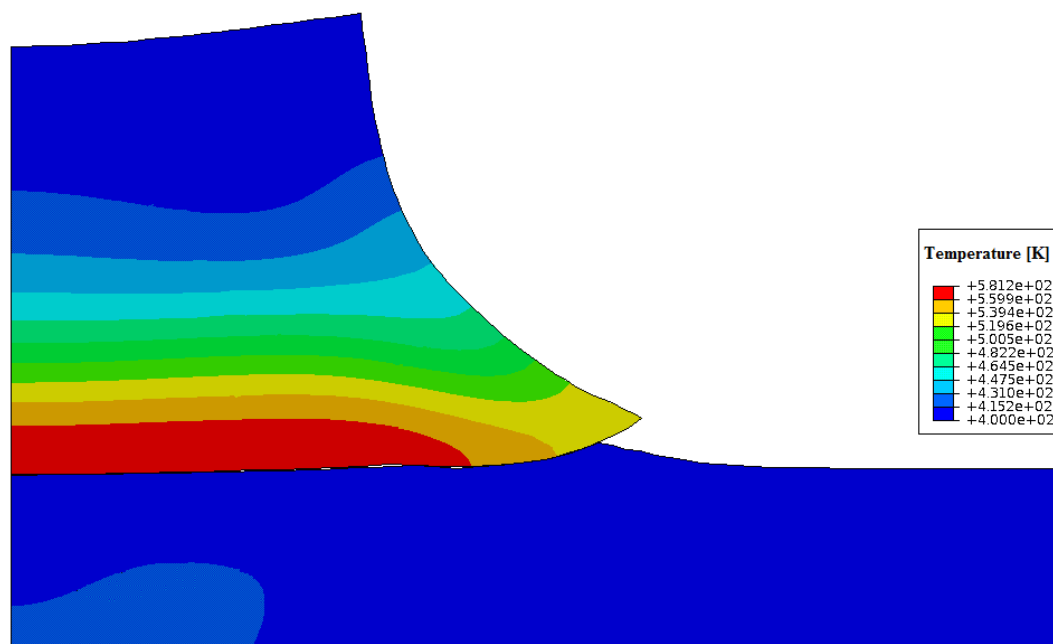


(b)

**Figure 5.25:** *Square Nickel particle against α-alumina substrate at 300 m/s. (a) Adiabatic case (b) Non-adiabatic case.*
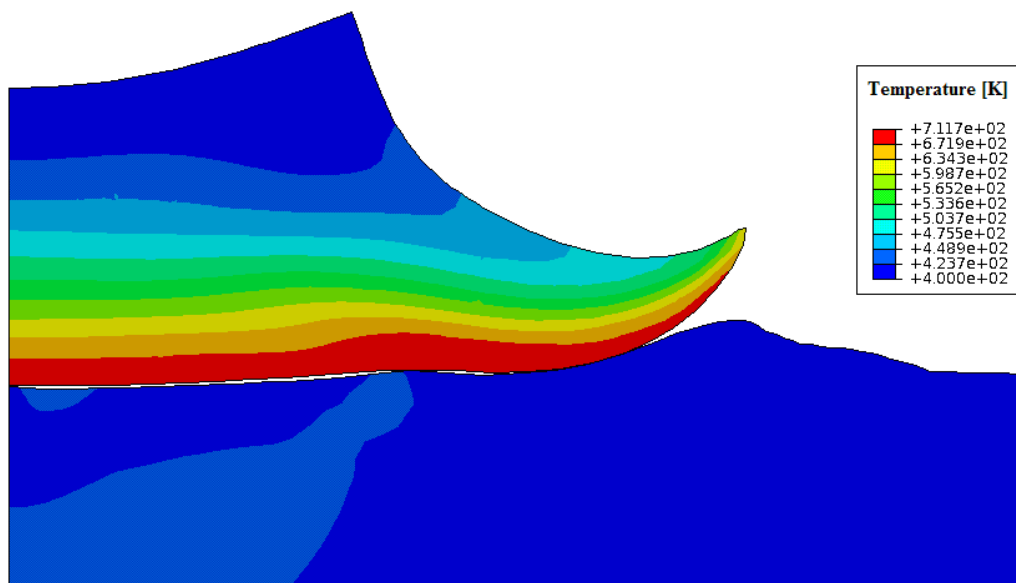
(a)
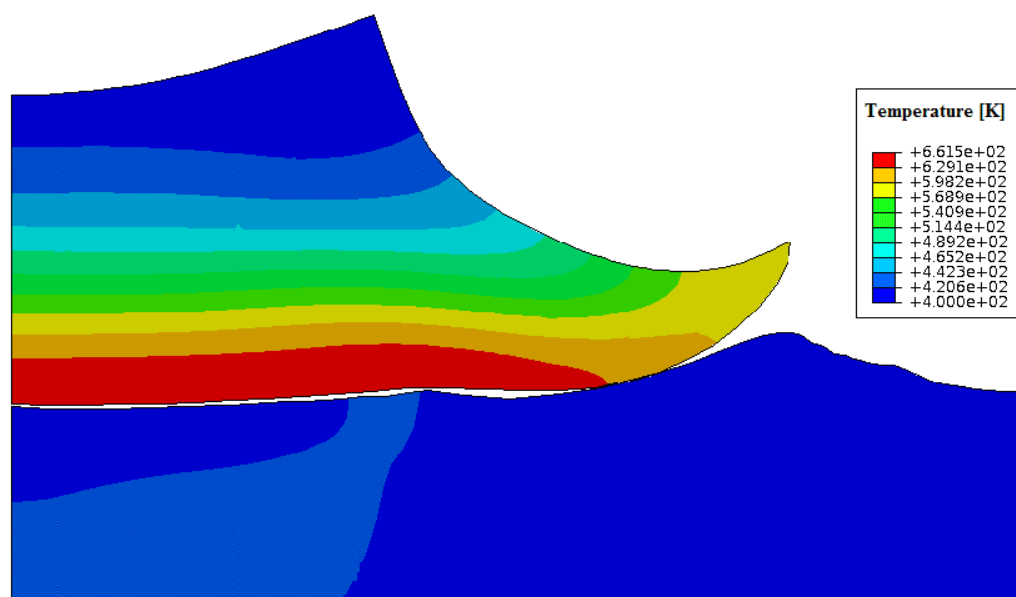


(b)

**Figure 5.26:** *Square Nickel particle against α-alumina substrate at 400 m/s. (a) Adiabatic case (b) Non-adiabatic case.*
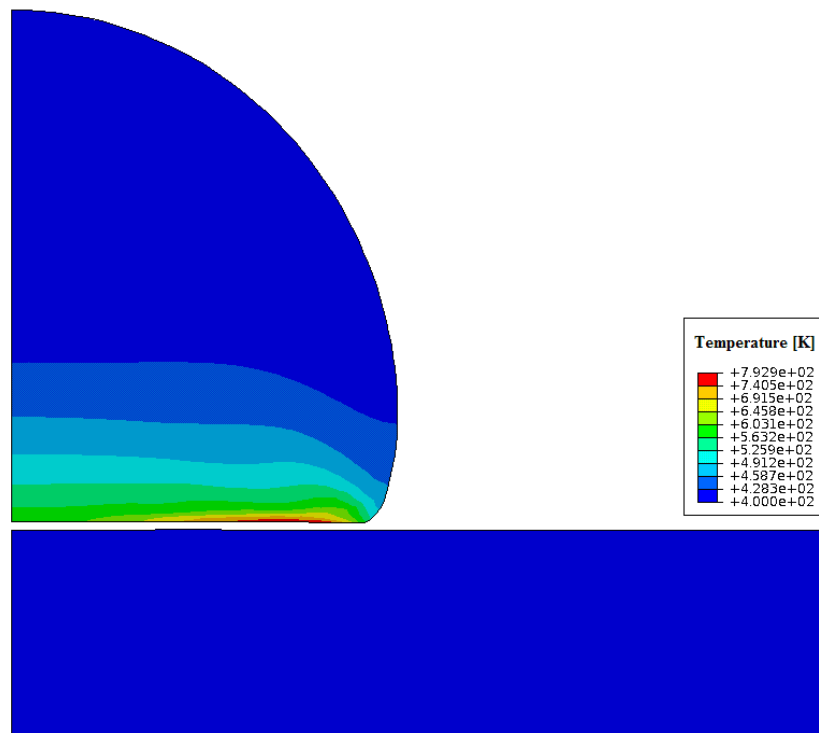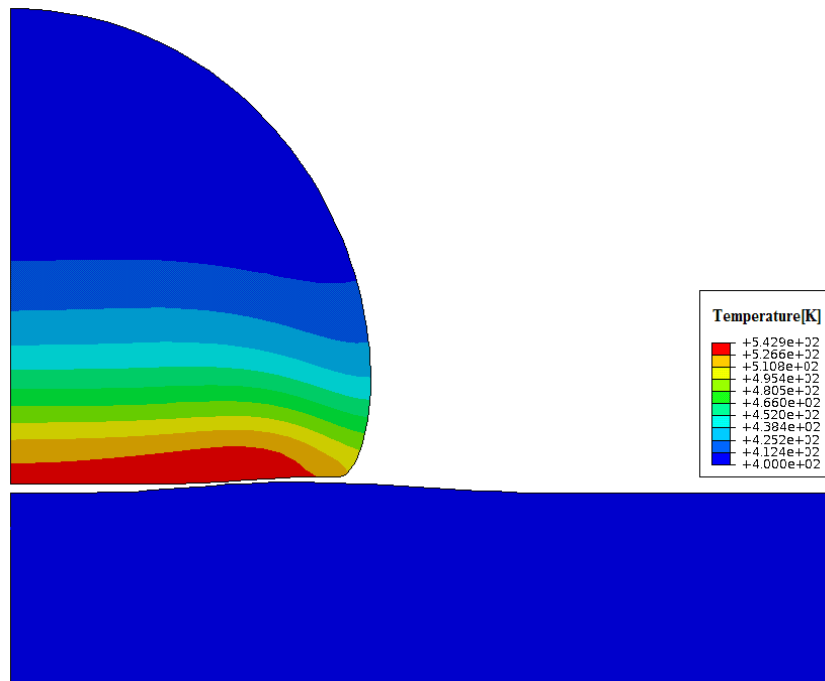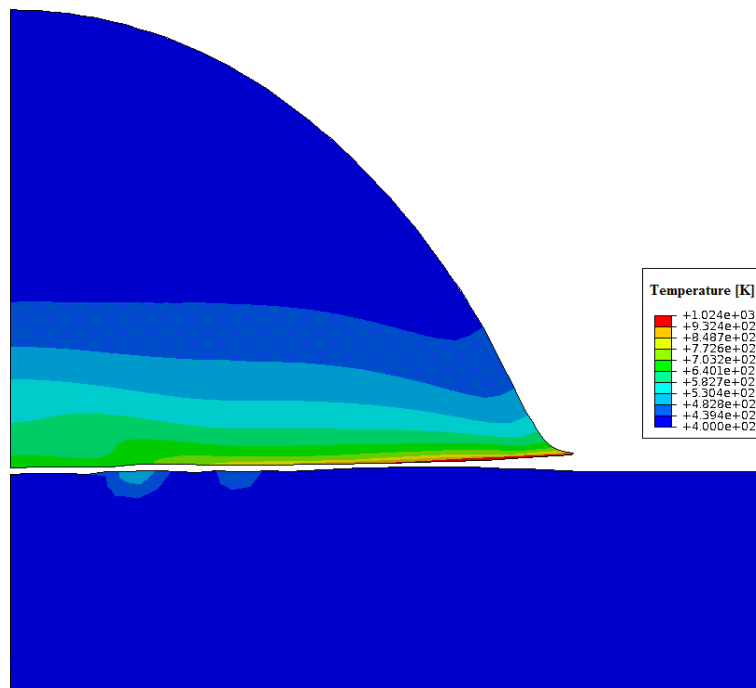
(a)



(b)
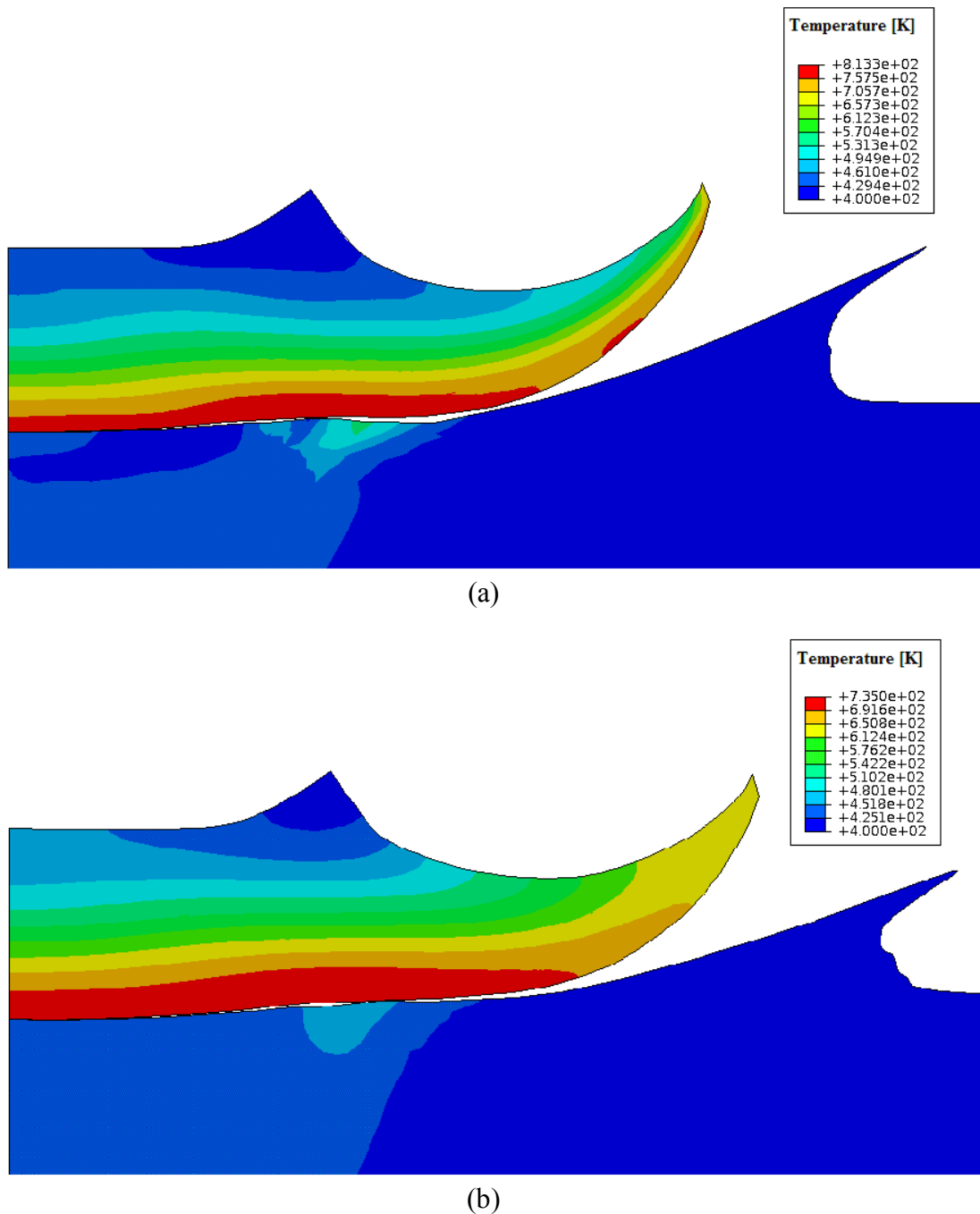
**Figure 5.27:** *Square Nickel particle against α-alumina substrate at 500 m/s. (a) Adiabatic case (b) Non-adiabatic case.*

The FEA analysis highlights the following main features of the lens/contaminants impacts simulations:

- In all the considered cases the deformation of the base is always limited while the final particle shape is realistic, therefore it is not necessary to resort to the ALE adaptive method;

194

- The adiabatic and non-adiabatic cases always produce similar deformed shapes of the particle/lens system;
- The maximum base temperature reached is very similar for the adiabatic and non-adiabatic cases. Nevertheless, in the non-adiabatic case the temperature decreases quicker due to conduction at the interface, i.e. Figure5.28-5.31.
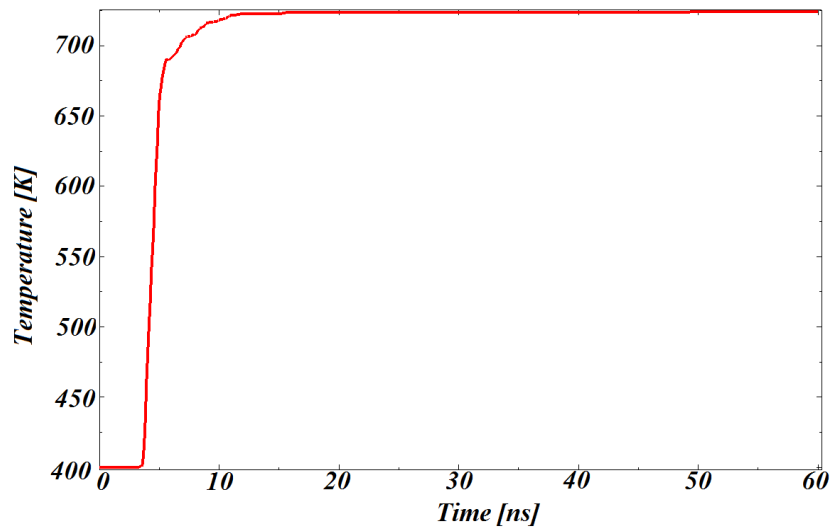


(a)
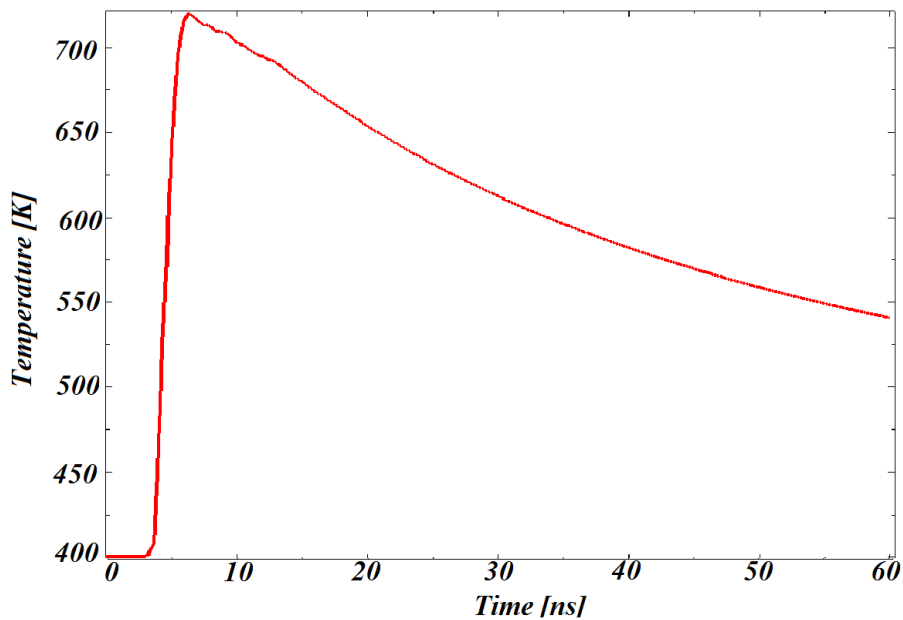


(b)

**Figure 5.28:** *Temperature trend of a base element for a spherical Nickel particle against α-alumina substrate at 400 m/s. (a) Adiabatic case (b) Non-adiabatic case.*
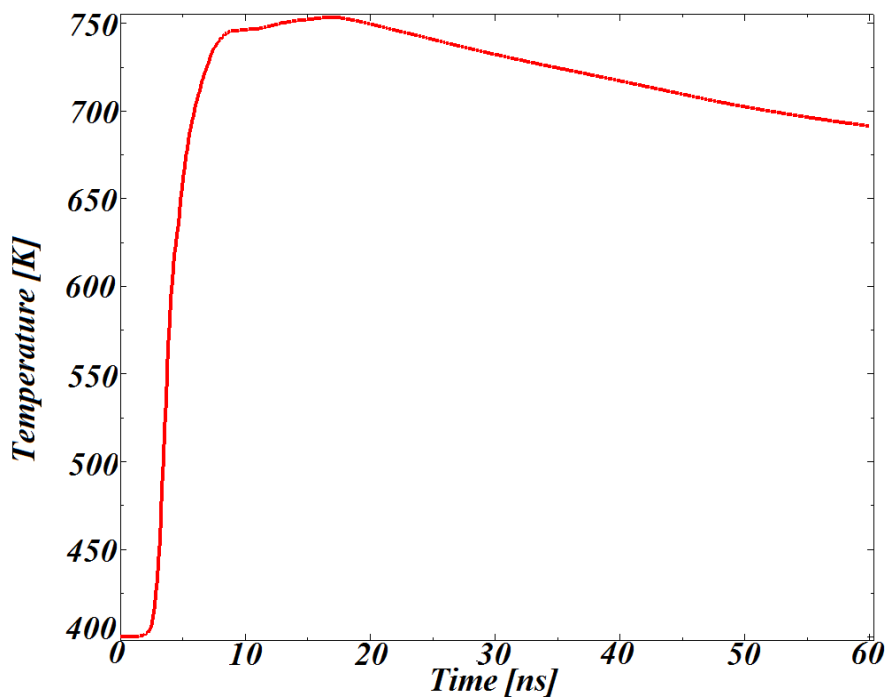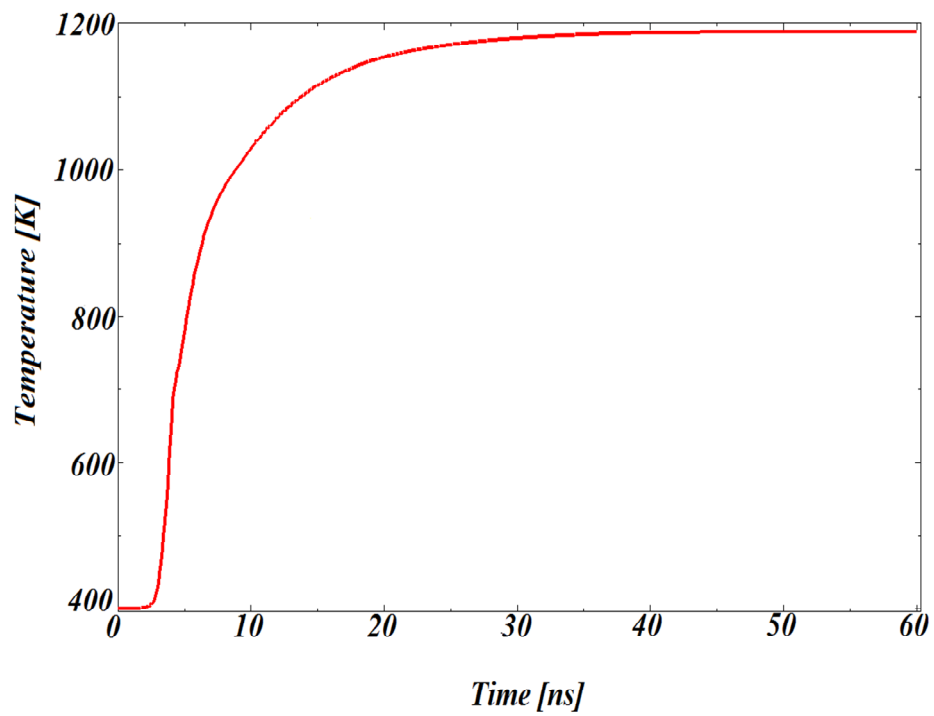
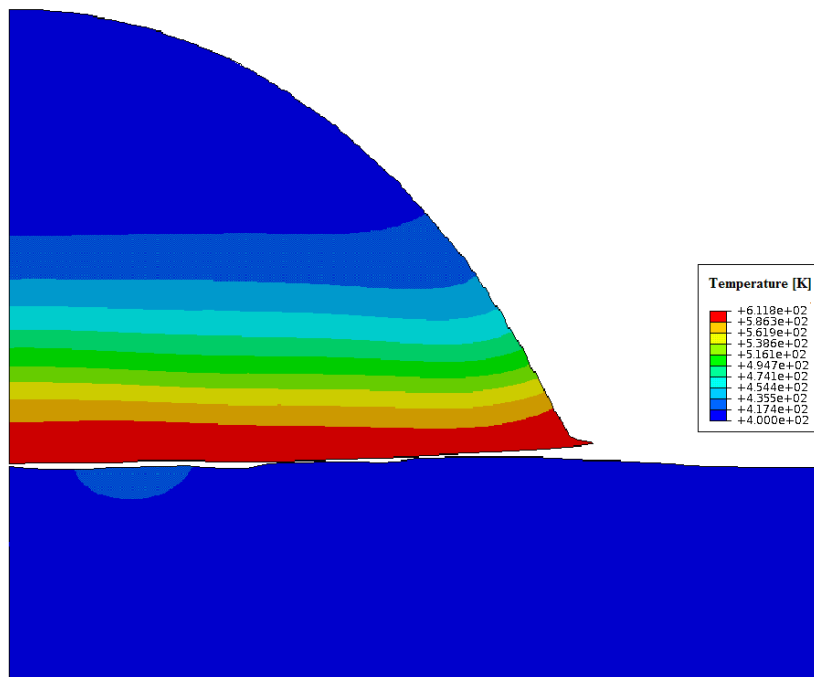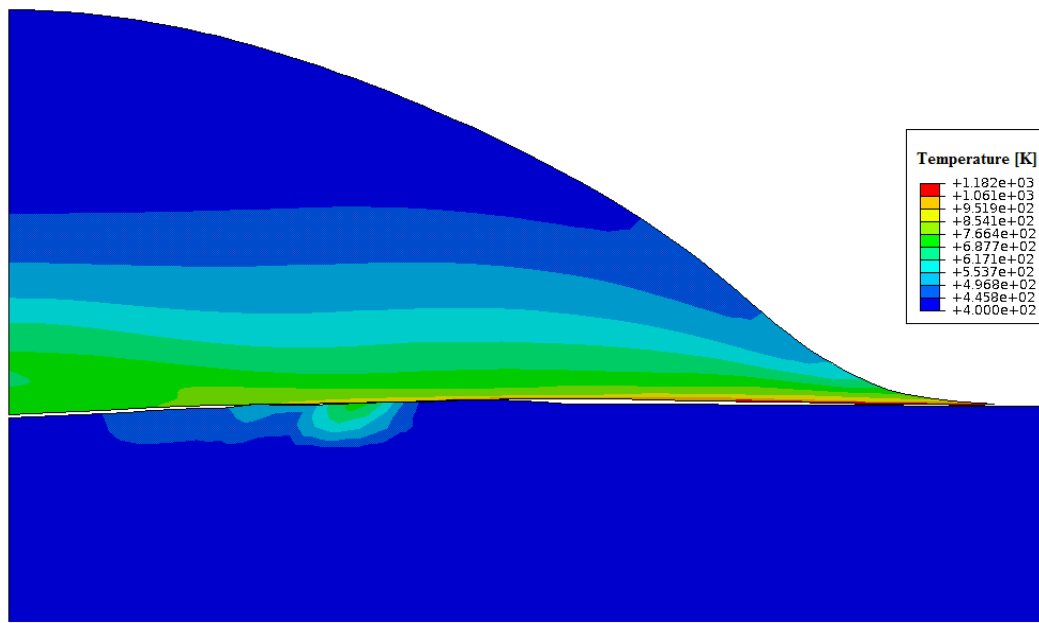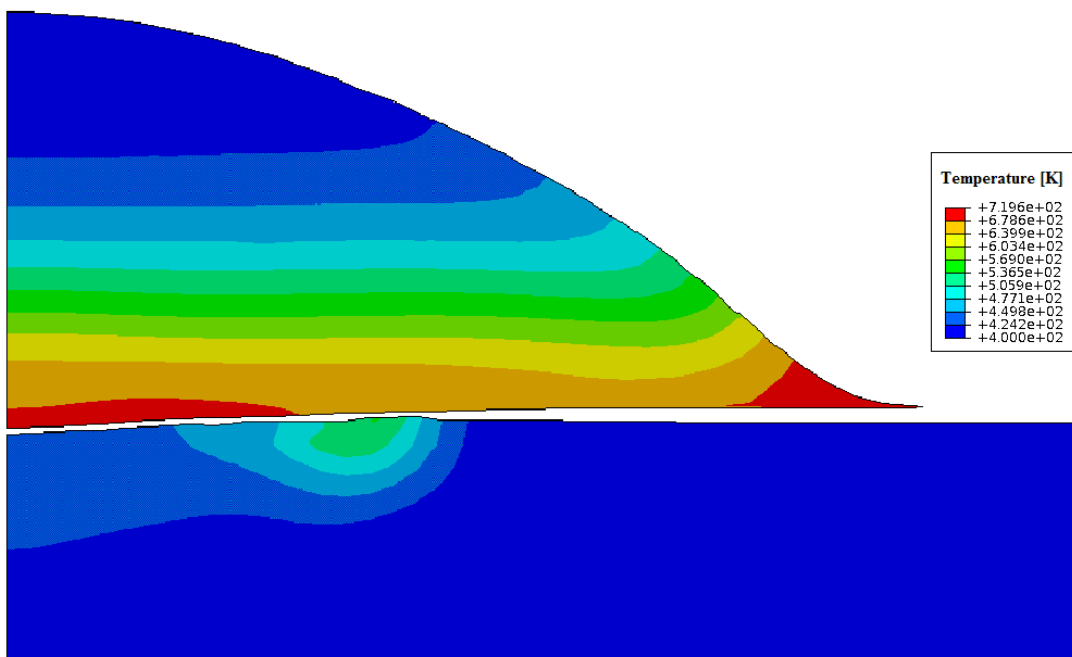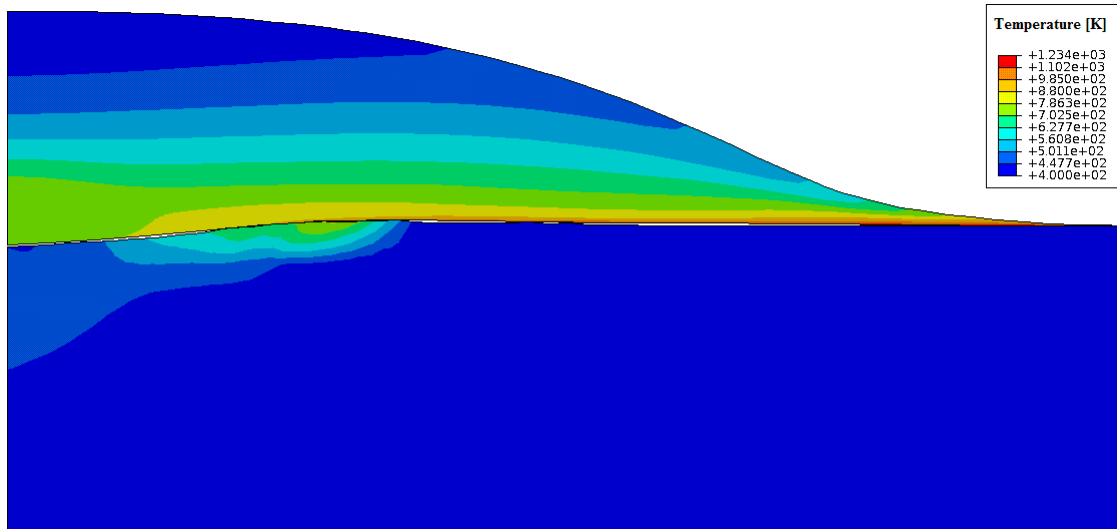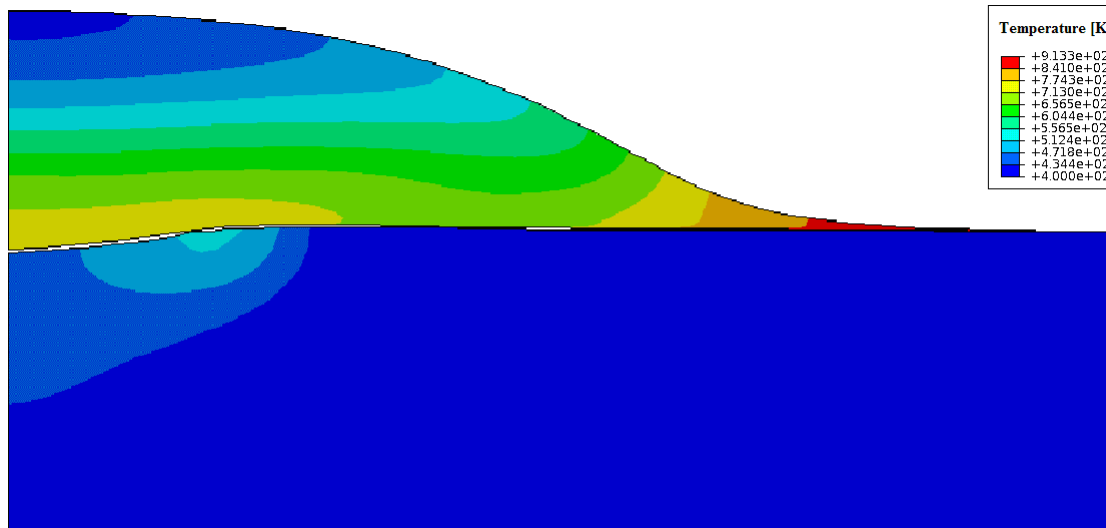**Figure 5.29:** *Temperature trend of a particle element for a spherical Nickel particle against α-alumina substrate at 400 m/s. (a) Adiabatic case (b) Non-adiabatic case.*
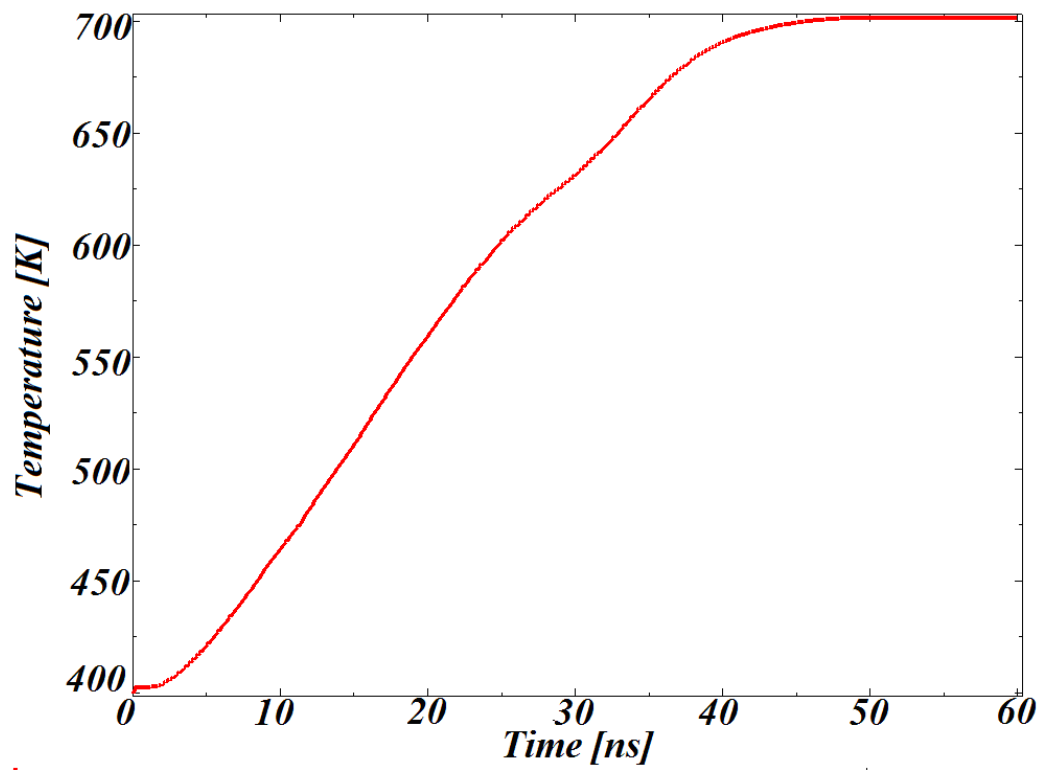
(a)
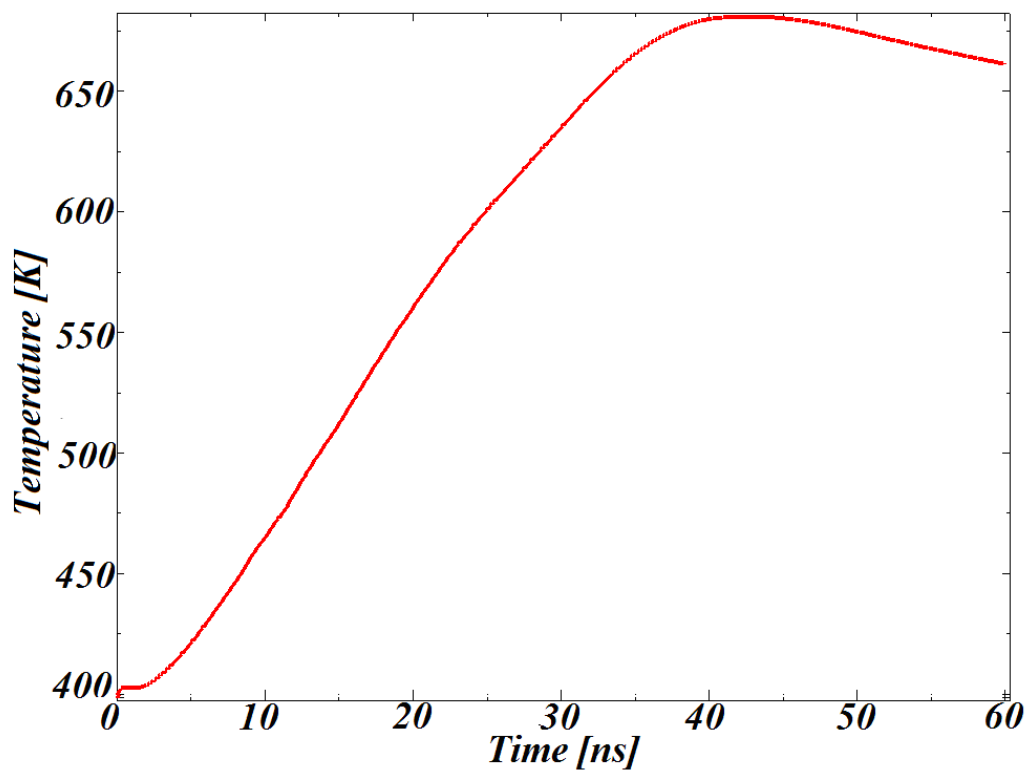


(b)

**Figure 5.30:** *Temperature trend of a particle element for a square Nickel particle against α-alumina substrate at 400 m/s. (a) Adiabatic case (b) Non-adiabatic case.*
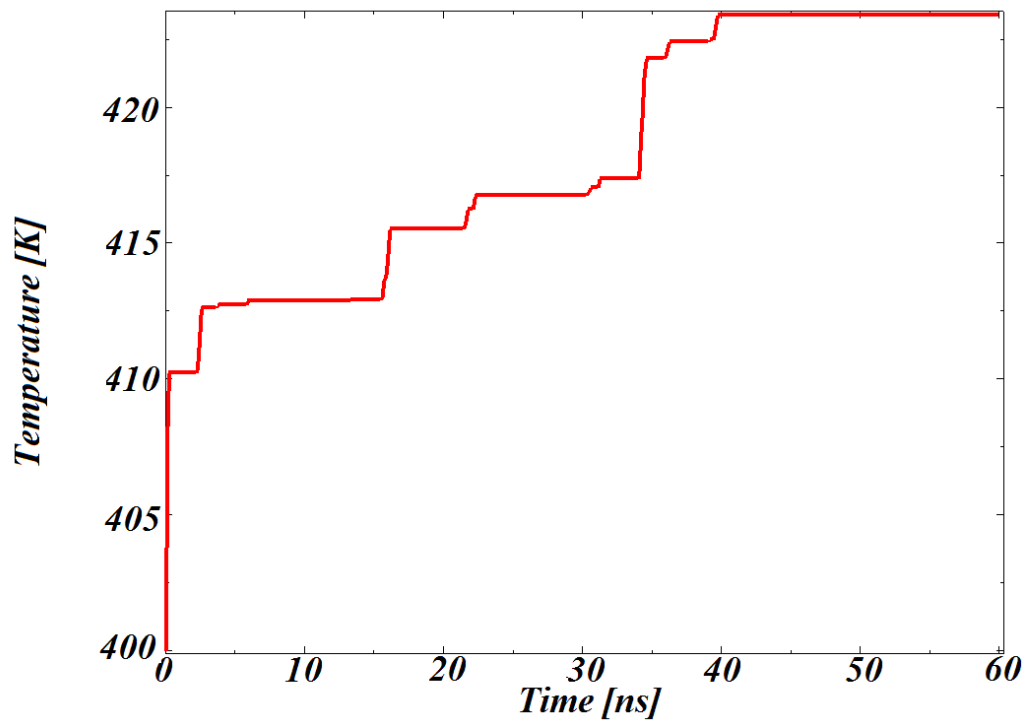
(a)
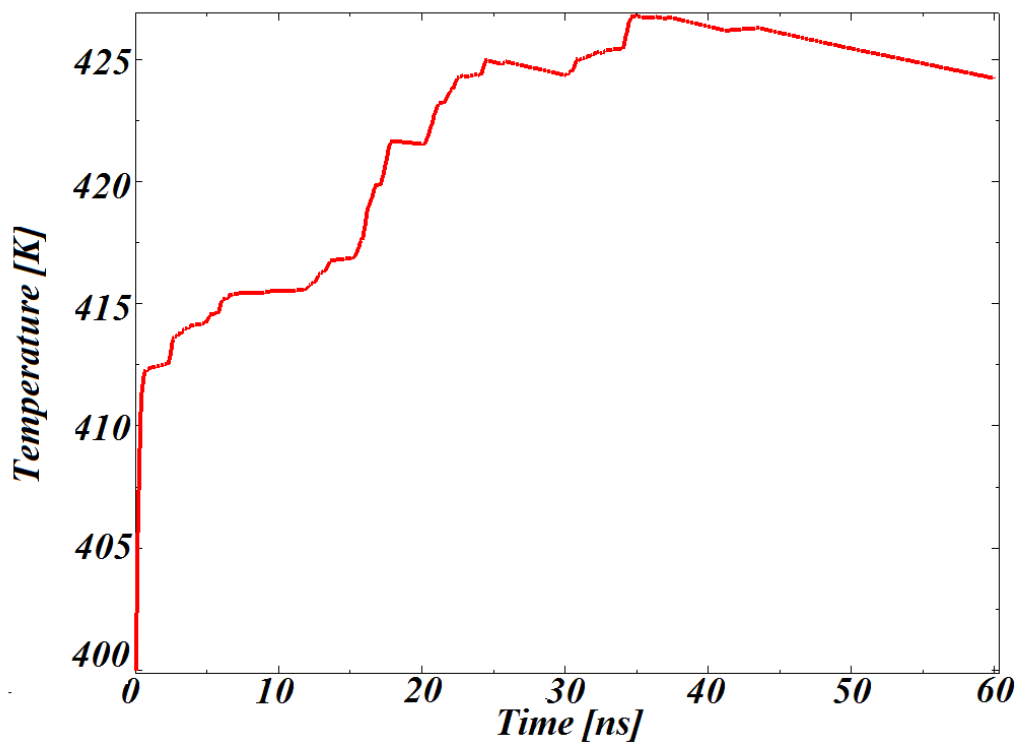


(b)

**Figure 5.31:** *Temperature trend of a base element for a square Nickel particle against α-alumina substrate at 400 m/s. (a) Adiabatic case (b) Non-adiabatic case.*

198

- The maximum particle temperatures for the adiabatic and non-adiabatic cases are substantially different even if in both cases the maximum temperatures reached are far from the materials melting points.;

- If the presence of a discontinuity is considered as an indication that the critical velocity is reached then in all the cases examined this is over 200 m/s (sudden temperature increase in a fraction of a nanosecond);

- In both the adiabatic and non-adiabatic cases the temperature discontinuity, therefore the shear instability, is reached at similar time instants;

- In no case does the field temperature suggest the melting of the lens;

- In agreement with Kim's (2009a,2009b) and King's (2010) results the maximum temperature at the base is reached corresponding to an intermediate zone, Figure 5.32
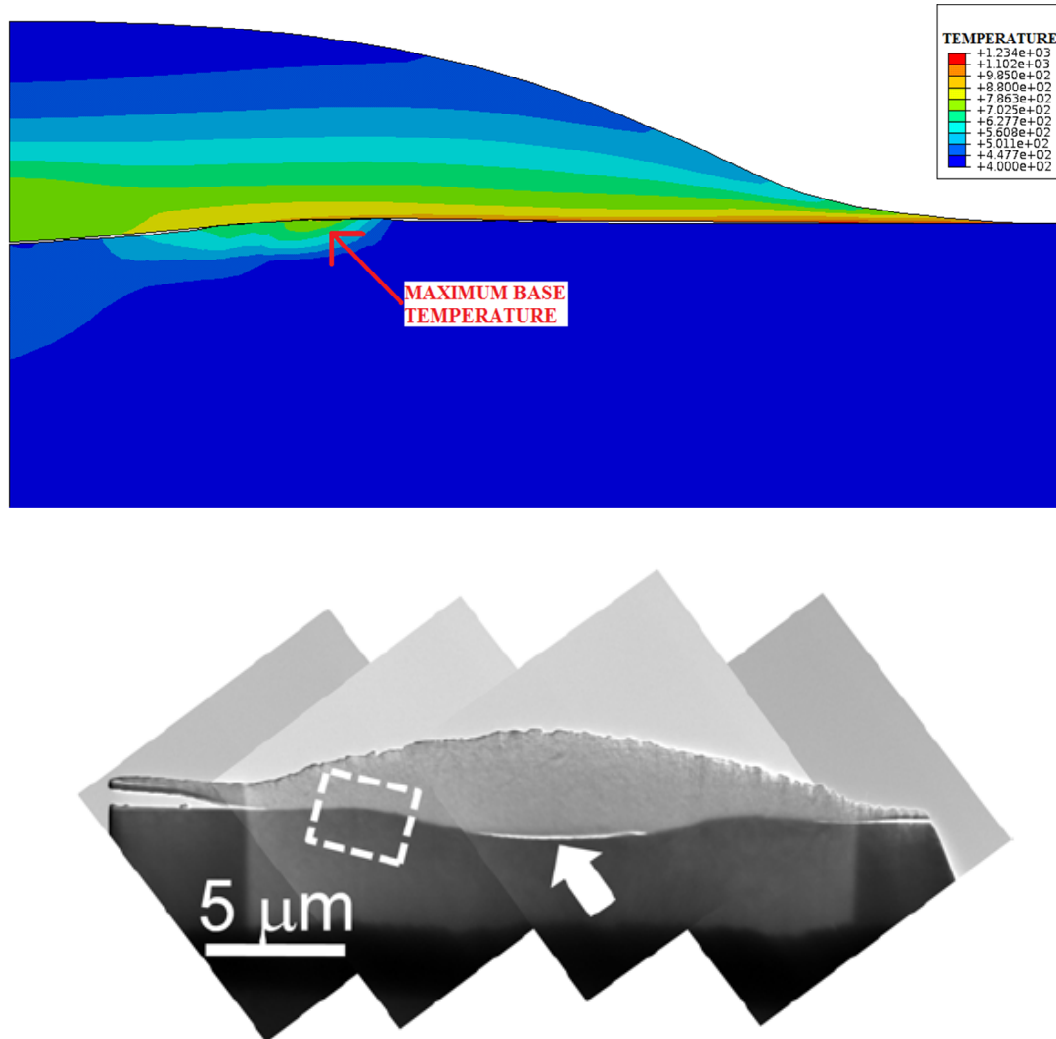
**Figure 5.32:** *The maximum temperature is reached corresponding to an intermediate interface region (a) Adiabatic FEA results for a Nickel particle impacting the sapphire lens at 500 m/s (b)Kim's experimental results (2009b), the square highlights the region where the maximum temperatures are reached where the arrow highlights the detachment area..*

- Due to the particular shape of the deformed system contaminant/lens, the size of the spherical particle that remains attached on the lens is bigger than the crater it creates, Figure5.32;

- If the particle shape is square then the stress applied on the base is more evenly distributed than the stress applied by a spherical particle. Therefore in this case, even if there is an intermediate base zone where the lens temperature is higher, this is not much higher than the base initial temperature;

- Due to the particular shape of the deformed system contaminant/lens, the square particle is interlocked in the lens surface. Therefore, in this case the crater diameter is slightly higher than the particle size. This result is confirmed by the SEM analysis performed on a pyrometer fouled lens.

- 

### 5.4.8.2  Materials

Additional simulations were performed in order to analyse the impacts of contaminants made of hard non-metallic materials. The main aim of these studies is the detection of a possible lower critical velocity. In detail, $\alpha$-alumina/$\alpha$-alumina impacts were simulated and reported in Figure 5.33.
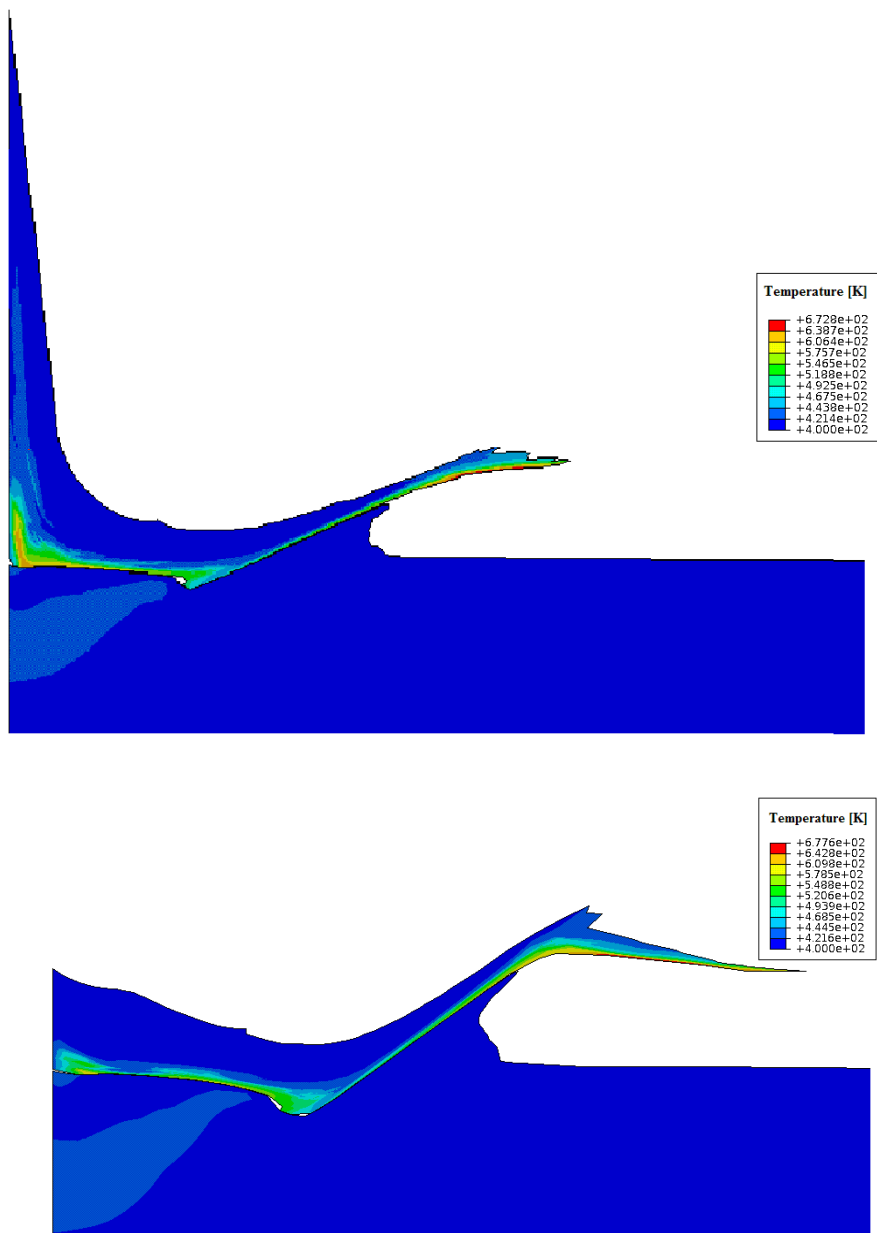
**Figure 5.33:** *Square α-alumina particle against a α-alumina lens at 500 m/s*
*(a) Without ALE adaptive meshing (b) with ALE adaptive meshing.*

The main results are:

- For velocities less than 200 m/s the lens is not damaged;
- The use of ALE adaptive mesh is necessary in order to obtain a more realistic deformation of the particle (Figure1.34).

### 5.4.8.3 Particle Diameter

Other simulations investigated the role played by the particle diameter in the determination of the critical velocity value. The results agree with Li et al. (2010a): if the oxide layer is not considered then the critical velocity does not depend on the particle diameter. In fact, as shown by Figure5.34, a square sapphire particle with a diameter of 200 μm can not damage the lens if its velocity is 200 m/s.
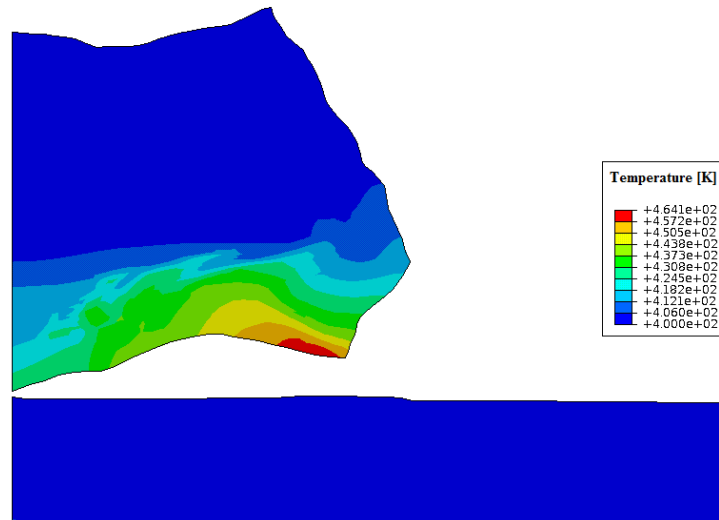


**Figure 5.34:** *Square α-alumina particle against a α-alumina lens at 500 m/s.*

### 5.4.8.4 Initial Temperature

Other simulations were performed in order to evaluate the importance of the initial temperature of both lens and contaminants. Under maximum flow conditions, the air coming from the compressor has an initial temperature over 700K, therefore this value is set as the initial condition for new simulations, whose results are reported in Figure5.35-5.37.

At higher temperatures both lens and contaminants show a softer behaviour. Despite the fact that the maximum temperatures reached are remarkably higher than the case described in Figure5.29, for which the initial temperature is 400K, the results are comparable:

- For an impact velocity of 200 m/s the lens deformation is negligible;
- The maximum temperature reached is far from the melting temperatures of both lens and contaminants.

Nevertheless, it is important to remember that higher initial temperatures can enhance thermal softening and diffusion, two of the most important mechanisms in the bonding process.
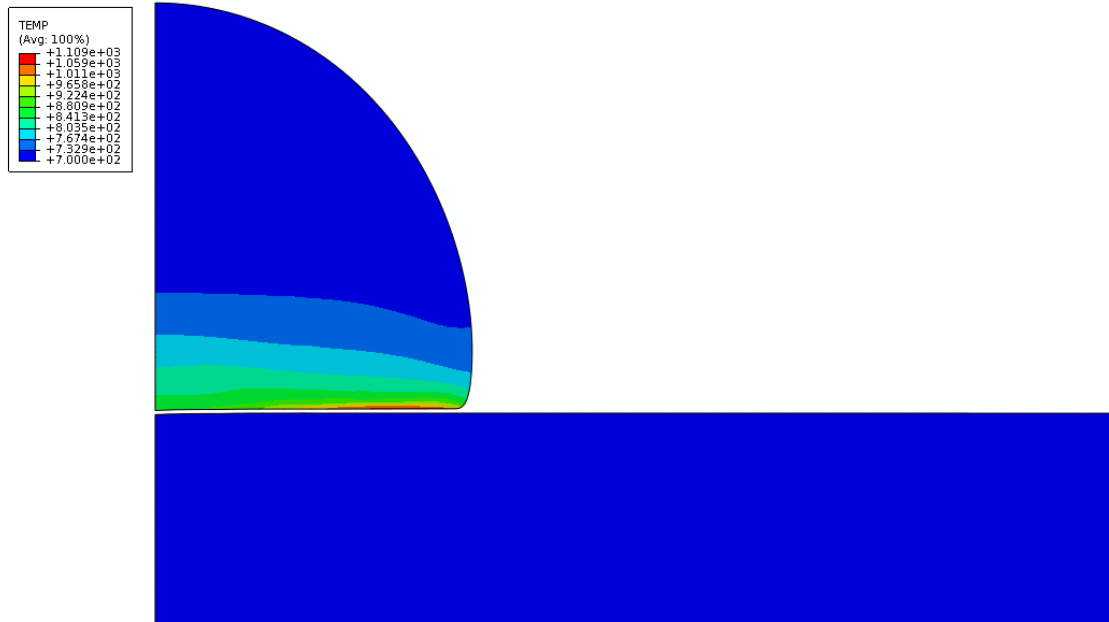


**Figure 5.35:** *Spherical Nickel particle against a α-alumina lens at 200 m/s and with the initial temperature set at 700K.*
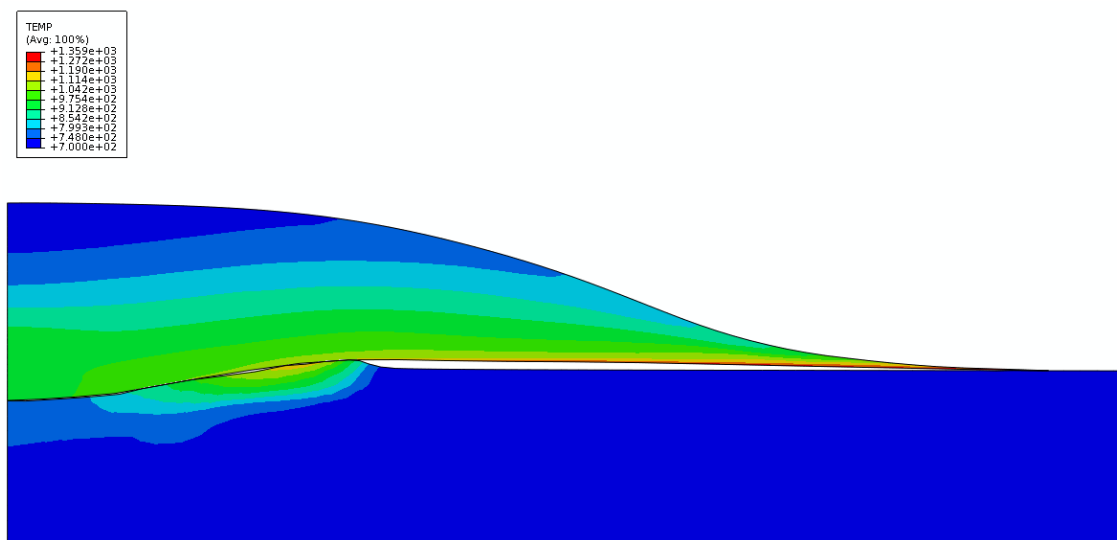


**Figure 5.36:** *Spherical Nickel particle against a α-alumina lens at 500 m/s and with the initial temperature set at 700K.*
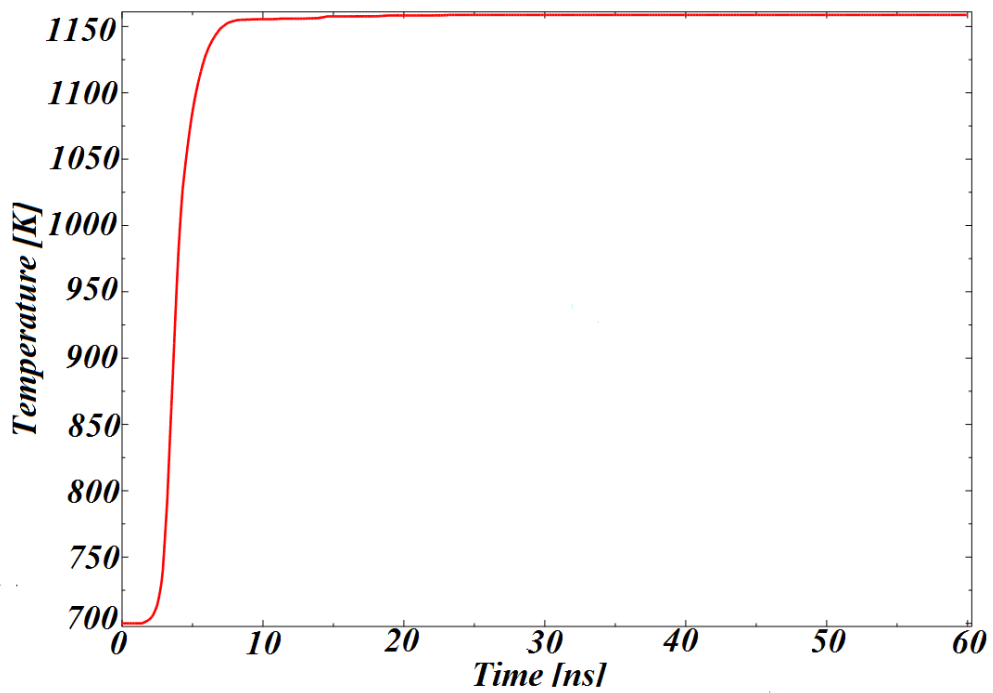
**Figure 5.37:** *Temperature trend at the interface of the flat surface when a particle impacts against a α-alumina lens at 200 m/s and with the initial temperature set at 700K.*
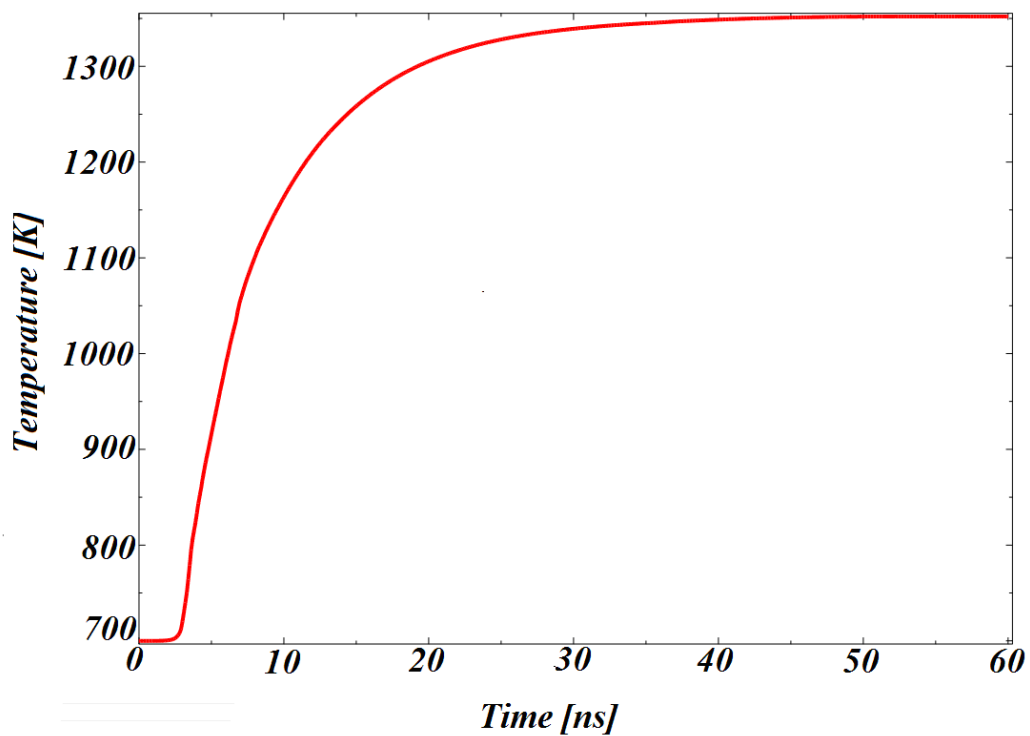


**Figure 5.38:** *Temperature trend at the interface of the contaminant when a particle impacts against a α-alumina lens at 200 m/s and with the initial temperature set at 700K.*

## 5.5 Discussion of Results

Thanks to ABAQUS analysis and state of art studies of the present work, it is now possible to take a closer look at the SEM analysis of a fouled lens and give some information about the contaminants source. These images were kindly provided by Meggitt UK.

a)  Particles in Figure5.39 are weakly bonded with the lens and can be easily removed with a normal cleaning procedure. Furthermore, these particles do not appear to be arranged in a particular way, e.g. in a circular shape like contaminants in Figure 5.42. It is very likely that their impact happened at low velocities. In the case of maximum purge air flow the source of this kind of contaminants with a diameter over 20μm can be either the turbine or the pyrometer purge air. Instead, for smaller diameters and for the pyrometer under study the particles source is the purge air. In fact, if these contaminants were coming from the turbine than they would have been discharged by the purge air.

b)
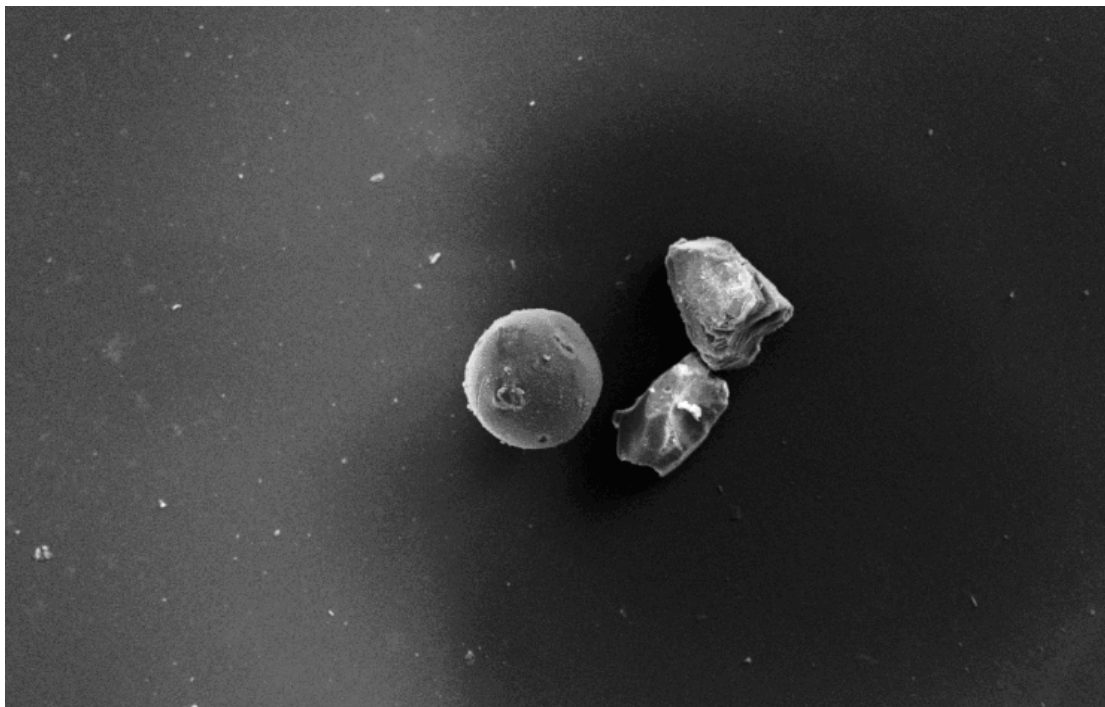


10 μm

**Figure 5.39:** *SEM picture of contaminants deposited on the lens, which do not appear to be arranged in a particular way and are easily removed with normal cleaning procedures.*

c)  Spherical particles that show signs of ejecta or of molten debris have impacted at high velocity, Figure5.40. Particles asperities, sliding on the surface, increase stress concentration causing the appearance of local melting that forces particle debris to stick on the lens.  However, if the contaminants have not damaged the lens then their velocity can be under 200 m/s and therefore their source can be either the turbine or the purge air. As in point a), if their size is under 20 μm then these contaminants are coming from the compressor airflow.



10 μm

(a)
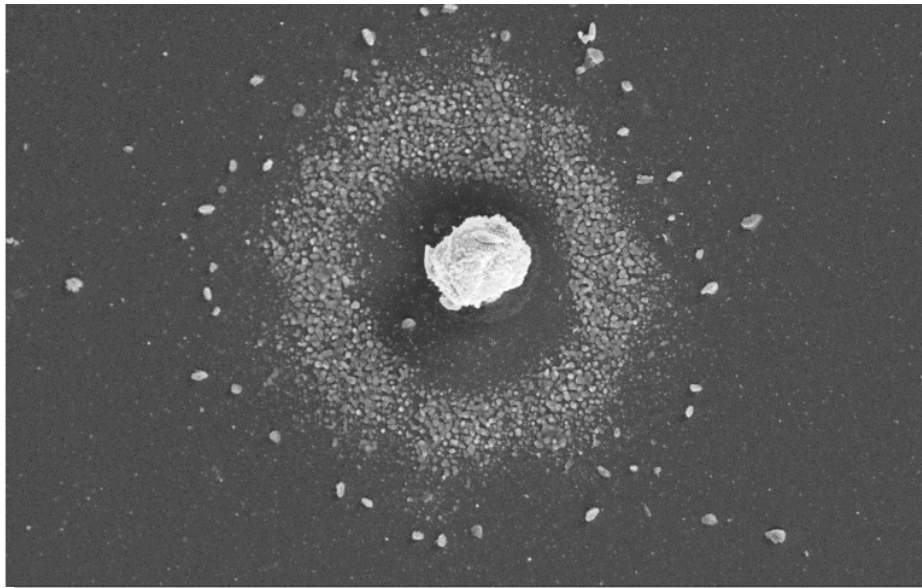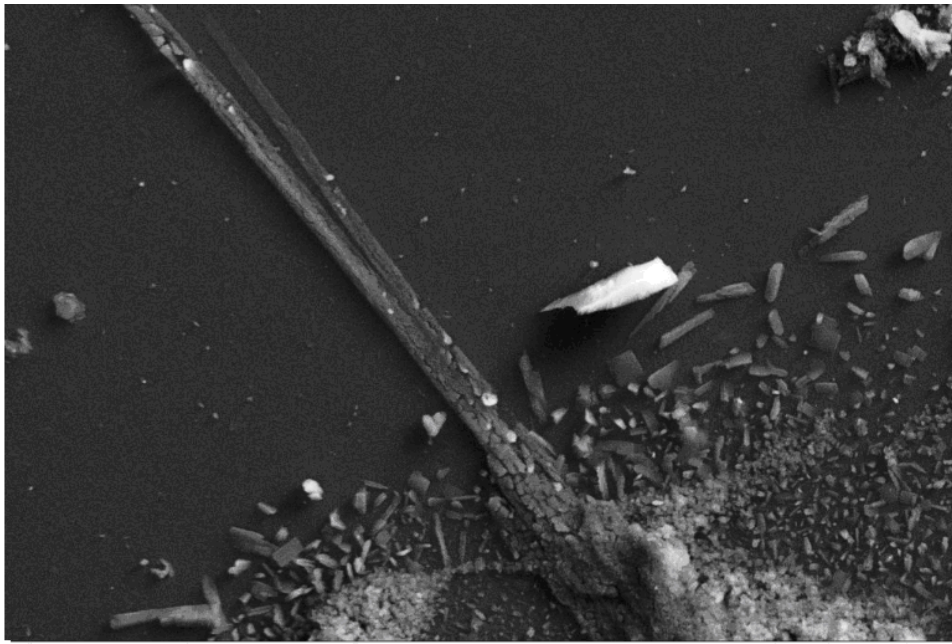
(b)

**Figure 5.40:** *Spherical particles showing signs of ejecta (b) or of molten debris (a) have impacted at high velocity.*

d)  In Figure5.41a it is possible to observe two square-shaped particles interlocked in the surface. From ABAQUS studies it is possible to conclude that these contaminants impacted at high velocities, over 200 m/s. Combining FEA results with CFD studies it is reasonable to state that these particles came from the turbine environment (Chapter 4). The sapphire lens is plastically deformed while, even after normal cleaning procedures, some residuals of the particle remain attached at the surface Figure5.41b. Asperities of the particles locally melted, thus enforcing the particle bonding with the surface.

(a)
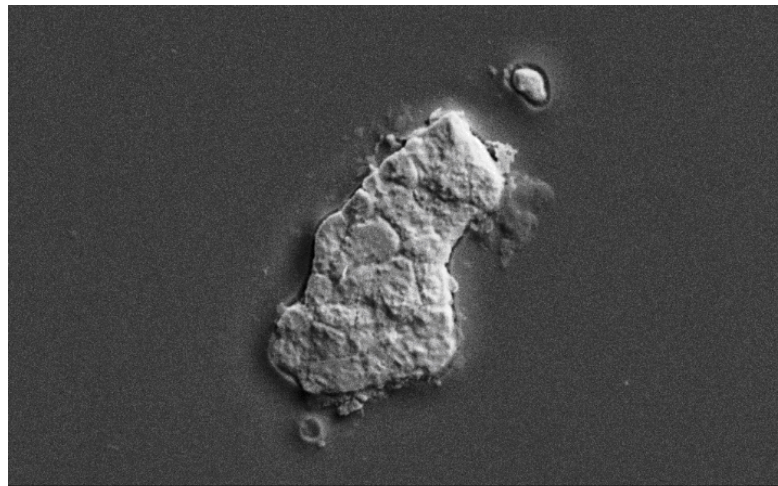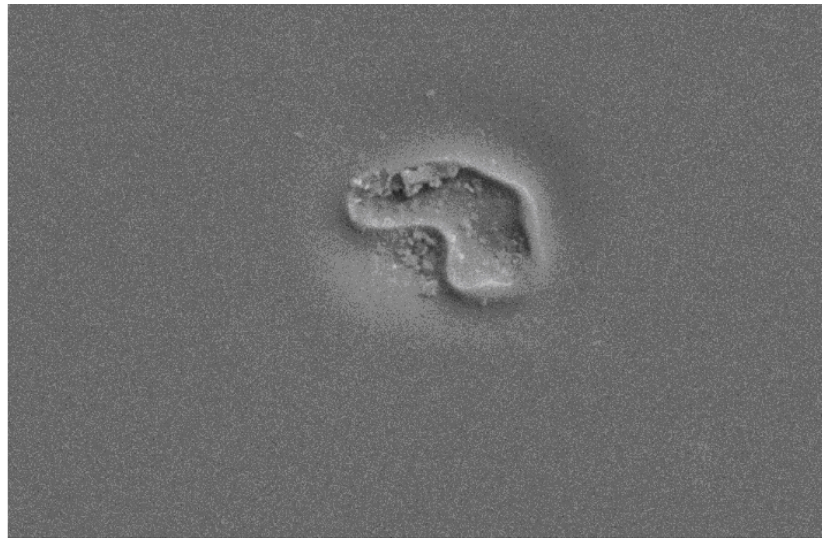


(b)

**Figure 5.41:** *(a) Square-shaped particles interlocked in the surface impacted (b) Crater left by a non-spherical particle; in this picture it is clear that some debris remained attached to the lens even after cleaning procedures.*

e) Many contaminants deposited on the lens are arranged in a circular ring, Figure5.42. Particles that impacted at high velocities, but under the critical velocity, bounced back unable to damage the lens. Nevertheless, their asperities raised the temperature locally the temperature and melted remaining attached to the lens. These particles can come either form the turbine or from the purge air.

(a)
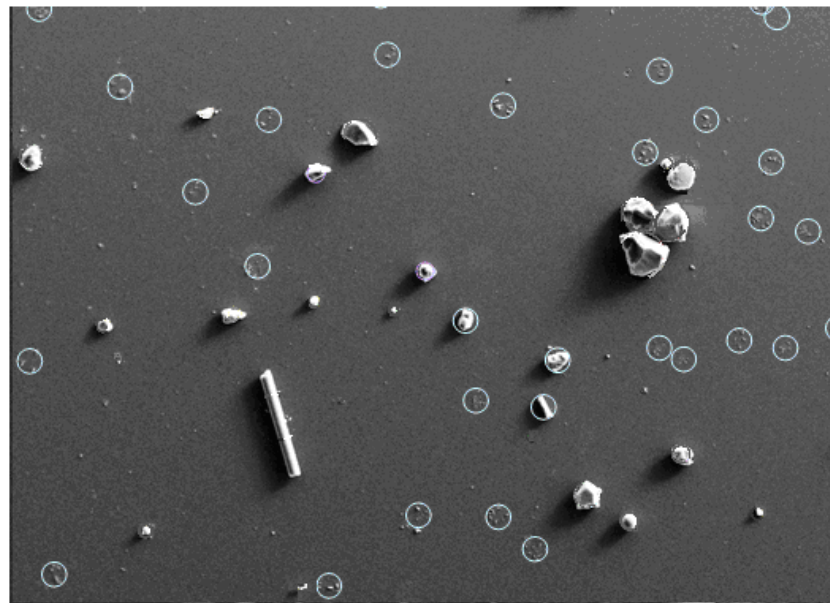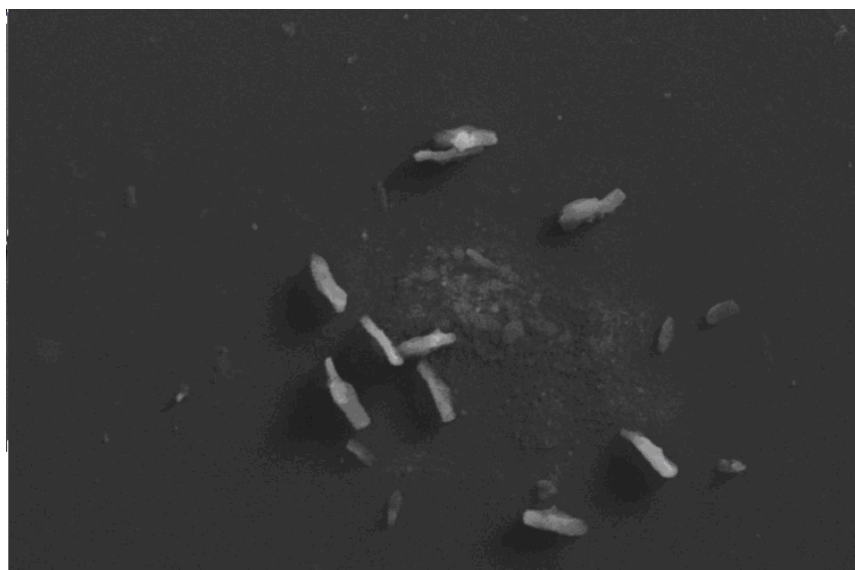


(b)

**Figure 5.42:** *(a) Small particles arranged in a circular shape (highlighted with blue circles) (b) Zoom of a single group of particles arranged in a circular shape.*

## 5.6 Summary and Conclusions

In this Chapter a FEA analysis has been used to investigate the phenomena governing the impacts between the contaminants and the lens. It has been found that for very low velocities very fine particles can reach the lens only if they have been previously trapped by the purge flow. On the contrary, larger particles, that impact on the lens with a high velocity such that they stick on the lens surface while permanently damaging it, are likely to be contaminants previously entrapped by the turbine flow. Small particles can also be debris left by the impact of larger particles which did not have enough inertia to stick on the lens and they can both be turbine or purge air contaminants. Therefore, thanks to the FEA analyses aided with the CFD results, the particles pattern on a fouled lens can be related to different classes of impacts.

# Chapter 6
# Summary and Conclusions

## 6.1 Introduction

The main results obtained through the research described in the previous Sections are critically discussed and merged together in this Chapter. This provides the guidelines for re-designing a more efficient pyrometer purge system and presents the base for future work.

## 6.2 Summary

The employment of a non contact device to measure the turbine blades temperature offers the advantage of overcoming a number of drawbacks associated with traditional devices, such as the impossibility of monitoring some critical parts of the blades surface or a slow response time, among others. Despite optical pyrometers have been improved during the years, their use has been limited mainly to the military field. In fact, in order to not jeopardize the reading accuracy, the lens has to be kept sufficiently clean during the time lapsing between maintenance tasks. This requirement derives from the fact that contaminants entrapped in the engine quickly deposit on the lens. This fouling mechanism therefore requires compulsory and frequent cleaning procedures to be performed on the pyrometer involving costs that are frequently prohibitive for civil applications.

In Chapter 2, in which a comprehensive literature review is presented, the problem area and the research motivation were delineated as follows:

- During the 80's and 90's many patents have been registered, all of them aimed at finding the optimum solution in minimizing the contaminants deposition on

- the pyrometer lens. These purge pyrometer systems differ in many geometric details; however, they are all based on the common idea of using relatively clean air, which is already available in the engine, to discourage the contaminants from being deposited on the lens. Nevertheless, none of these designs has been sufficiently successful in allowing the installations of optical pyrometers in civil engines as a common practice. The main reason can be found in an implementation of a design process without a deep understanding of the mechanisms involved in the lens fouling.

- All the different patents considered the turbine environment as one of the possible sources of contaminants. However, several of these purge systems were designed neglecting the presence of particles carried by the same air used to keep the lens free from deposits.

- The only qualitative and quantitative study available in open literature is represented by the work of Kerr (2002a) in which computational fluid dynamics has been used to predict the level of deposition on the lens. However, the mechanisms involved in the fouling process were not investigated in detail.

- The literature survey highlighted the necessity of addressing the knowledge gaps described in the previous points. This part of the research was aimed at understanding the physic mechanisms governing the fouling of the pyrometer lens.

Chapter 3 describes the study of the pyrometer purge flow by means of an experimental study. The main relevant features of the experimental study can be summarised as follows:

- The scope was to identify the main flow structure that determines the fouling process and at the same time to validate the results obtained via computational fluid dynamics (CFD) analyses conducted in a second phase of the research.

- Given the reduced dimensions of the pyrometer purge system, it was not possible to gain the appropriate optical access to take flow measurements. Consequently, a large scaled experiment was performed.

- In order to observe the flow field, the particle image velocimetry (PIV) technique was used. The distortion of the image and light reflection introduced by the presence of curved glass surfaces was investigated by means of a feasibility experiment.

- The feasibility experiments highlighted a degradation of the experimental data accuracy, nevertheless the identification of the main flow field structure was not jeopardized. Furthermore the experimental data were in a reasonable agreement with the computational studies performed by using the k-ε and the k-ω SST turbulence models.

- The large case experiment highlighted the presence of a large recirculation zone that can trap contaminants and direct them towards the pyrometer lens.

In Chapter 4 the description of the research continued by focussing on the particle deposition as seen from a fluid dynamics perspective. Main points were:

- The aim of this study was reproducing the flow field of an existing pyrometer purge system to enable the identification of those features that can significantly impact on the lens fouling process.

- It was found that the geometry of the air curtain configuration plays a fundamental role.

- Given the high speeds involved, the main force governing the contaminants deposition is the drag.

- Particles with high inertia hit the purge tube wall and then can potentially bounce towards the pyrometer lens.

- Particles with low inertia can be trapped by the recirculation zone forming at the still tube mouth and subsequently directed towards the lens.

- Contaminants entrapped by the air used to clean the lens are one of the main sources of fouling.

- The CFD analysis partially disagrees with the conclusions reached by the previous work of Kerr. This incongruity is mainly due to the fact that Kerr neglected the bouncing phenomenon.

In Chapter 5 the impacts between the contaminant particles and the lens were investigated through a finite element analysis (FEA) aimed at identifying the most important factors that contribute to the lens fouling process. Main results were:

- Particles moving at low speed can be deposited on the lens by means of electrostatic and Van der Waals forces.

- Particles with very high velocity can be deposited on the lens through the same mechanisms involved in the cold spraying process, which is a technique commonly used for coating deposition.

- Ejecta of material are formed during the impacts between the contaminants and the lens. They are usually visible on the lens as cluster of particles arranged in a circular shape.

- A local melting can occur at the interface between the lens and the contaminants due to the high stresses created by the asperities and high sliding velocity of the particles. As a result, while large particles bounce back, debris remains bonded to the lens surface.

- The sapphire lens shows a plastics behaviour when particles impact at high speed upon it.

## 6.3 Discussion of the results

The layouts of those patents based on the assumption that one of the contaminants source could be the purge air system, were aimed at avoiding the contact between the lens and the purge flow. Nevertheless, the insertion of a still tube originates a recirculation zone in front of it, which has been identified as one of the main causes of the compressor contaminants deposition. This conclusion is in agreement with Kerr (2002a) in which the deposition of compressor contaminants decreases with increasing the particle diameter, as particles with higher inertia are not able to follow the streamlines of the recirculation flow field. Although the present work confirmed

these results, it was found that such particles represent only a small fraction of all the contaminants entrapped by the purge flow and deposited on the lens. In fact, it has been shown that the time response of the particles to directional changes of the flow is directly proportional to their inertia. The flow trajectory and the high-inertia contaminants pathlines substantially differ in the convergent zone of the purge tube where, therefore, these particles impact on the walls and could be directed towards the lens through a series of bounces. It has to be noted that in the present research, only the worst case scenario has been taken in consideration, assuming that the particles/wall collisions are perfectly elastic.

Nonetheless, even if the particles entrapped in the purge flow play a significant role in the lens fouling process, the turbine contaminants are still one of the main issues to be addressed. In fact, the particle deposition study has proved that only the turbine contaminants with a small inertia are successfully discharged by the purge flow.

The impact analysis has shown that particles reaching the lens with low velocities are deposited by means of Van der Waals and Hertzian forces. These contaminants do not damage the lens, although they can filter the radiation emitted by the turbine blades surface. Particles with intermediate inertia generally do not remain deposited and they tend to bounce back. However, during these collisions, particles asperities, sliding on the lens surface, can locally melt thus remaining attached on the lens. Particles at very high speed, coming from the turbine environment, can deform the lens while remaining attached on the surface. Interlocking mechanism and local melting cause the bonding.

From these conclusions the guidelines for designing a new purge pyrometer system can be summarised in:

- The pyrometer should be installed in the upper quadrant of the engine. Conversely, every time the engine is being turned off, the positioning of the pyrometer in the lower quadrant could allow the deposition of contaminants on the lens by means of gravity.

- The likelihood of particles coming from the turbine environment reaching the lens should be minimized. Unfortunately, the field of view of the pyrometer should focus on the blades and therefore a direct connection between the turbine environment and the lens can not be avoided. The discharging action of the purge flow needs therefore to be maximized. This means that the ratio between the total pressure at the pyrometer inlet and the static pressure at the turbine interface should be such as to ensure the highest Mach number achievable. This can be estimated by means of the isentropic gas laws.

- To decrease the turbine contaminants deposition, the pyrometer should be installed as far as possible from the turbine environment. In this way the particles are more likely to lose their kinetic energy before impacting the lens.

- The recirculation zone forming in front of the still tube has been always considered the only factor causing the deposition of the contaminants entrapped by the purge tube. Conversely, this work highlighted that the particle bouncing on the pyrometer walls can be predominant. Therefore, the geometry of the purge tube has to be modified to minimize this mechanism. The actual still tube pyrometer configuration can not be significantly improved without considerably changing some geometric features. In fact, as seen in Chapter 4, particles with high inertia show a time response delay for adapting to any directional flow change and therefore they will tend to impact on the purge tube walls, thus being eventually directed towards the lens. Small changes in the geometry would see the graphs of the level of deposition shift toward higher or lower diameters but not substantially change.

- In the present work, the worst case scenario has been taken in consideration where the collisions of particles with the wall are considered to be perfectly elastic. In reality, during each impact the contaminants will lose part of their kinetic energy. Furthermore, the relative velocity of the particles decreases with increasing space travelled. Therefore, one solution for reducing the deposition of high-inertia particles on the lens could be by adopting a geometry of the pyrometer that maximizes their number of impacts and space travelled before reaching the lens.

- The analysis of the impacts lens/particles has illustrated that particle with high inertia are capable of deforming the lens and they, or their asperities, are likely

to remain attached on the lens by interlocking or local melting. These particles can not be removed by standard cleaning procedures on the lens. Particles with intermediate velocity will not be deposited even if they can reach the lens. Particles at very low velocity are deposited through Hertzian Van der Waals forces and they will tend to bounce back (again this supposes that the pyrometer is installed in the upper quadrant of the engine, otherwise these particles could be deposited on the lens thanks to the action of gravity). Therefore, the idea of using a partially clean flow to scrub the lens, thus removing part of the particles that have been deposited while avoiding the deposition of very small particles, should be re-considered. The use of an inertial separator, like the one reported in Patent US 4836689 (Figure 6.1), should be investigated. The gap in front of the lens should be kept as small as possible in order to lower the likelihood that big particles, by eventual bouncing on the wall, could pass through the gap and hit the lens. Furthermore, an asymmetric scrubbing flow should be ensured in order to avoid any dead flow zone in front of the lens.
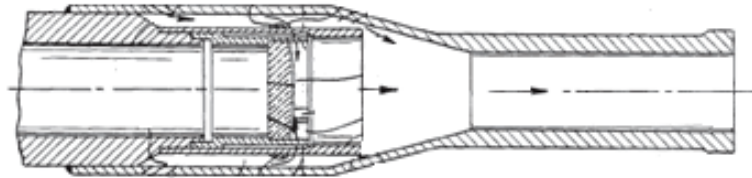


**Figure 6.1:** *Inertial separation configuration- Patent US 4836689.*

- The likelihood that particles could hit the wall and be redirected towards the lens should be minimized. Two different philosophies could be followed and an eventual trade-off between them should at the end be reached:

    I. The Stokes number in proximity of the exit of the still tube should be decreased; in this way the particles with high inertia have more time to respond to the directional changes of the flow. This can be achieved by

increasing the space between the end of the still tube and the wall of the purge tube (length A in Figure 6.2)
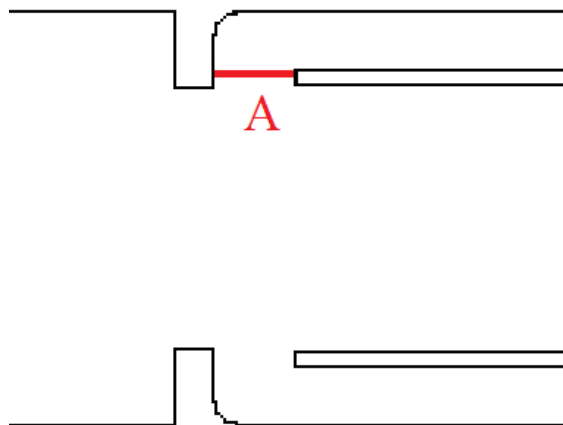


**Figure 6.2:** *Increasing the space between the end of the still tube and the purge pyrometer wall decreases locally the Stokes number. This means that particles have more time to adapt to the flow directional changes.*

II. The second approach addresses those scenarios where the impacts between the wall of the purge tube and the contaminants can not be avoided. This method is aimed at minimizing the likelihood that particles could bounce back towards the lens. This involves a substantial modification of the pyrometer geometry. A first attempt is conceptually depicted in Figure 6.3, where the particles that eventually hit the purge wall are likely to be directed towards the turbine or to bounce back on the external wall of the still tube. In the latter case, it has to be noted that containing the particles bounces out of the still tube will determine a reduction of their kinetic energy until they are carried out by the high speed flow. A comprehensive study of the geometry to achieve this has to be conducted, also by taking in consideration its effects on the dynamics of the flow (e.g., by assuring a given pressure ratio). Furthermore, further technical solutions can be taken into consideration for improving particular aspects of the flow. For example, a rounded still tube edge would be helpful in reducing flow vortexes which could capture and direct small particles towards the lens.
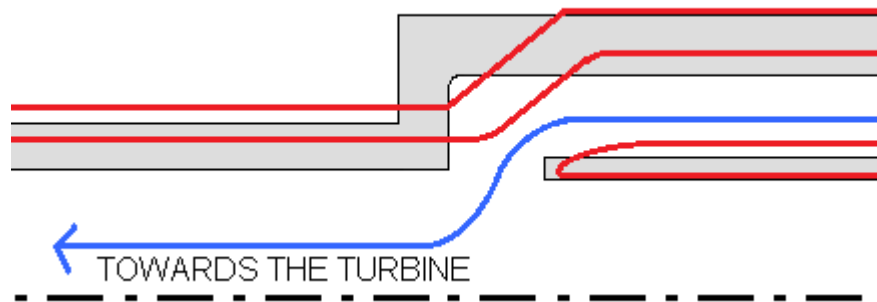
**Figure 6.3:** *The pyrometer should be designed by aiming at lowering the likelihood that the particles could bounce inside the still tube.*

## 6.4 Recommendations for Future Work

The clarification of the fouling mechanisms presented in this work and the guidelines listed in the previous section should be used to design more efficient pyrometer purge systems. The future research should take the following steps:

- The geometric changes described in the previous paragraph should be investigated in detail by means of experimental and numerical analyses. It is important in this first stage to analyze the effect of each modification separately. A trade-off between the different solutions should be achieved as the last phase of the conceptual design process.

- The CFD analysis has highlighted that neither temperature, pressure, or turbulence level is playing a fundamental role in the particle deposition. Therefore, an expensive computational 3D simulation is not justified at a conceptual design stage. Instead, a less expensive 2D model with a coarse mesh can be utilized for identifying the pyrometer configurations that would represent the optimal trade-offs between different design criteria (e.g., inertial separator, local reduction of the Stokes number, containing the particles bounces out of the still tube, minimizing flow vortexes, etc).

- In a second phase of the design, when a high-fidelity model of a new pyrometer design is required, a more detailed turbulence model should be used in the CFD modeling. The Reynolds Stress (RSM) or a LES turbulence model should be used. In this case a very fine mesh should be created and a mesh sensitivity analysis should be performed.

- An experimental analysis should be performed to validate the CFD predictions and to evaluate those mechanisms that can not be easily modeled via numerical methods (e.g evaluation of the scrubbing action). This, again, can be achieved without reproducing the engine conditions that otherwise would result in high operational costs of the test rig. In fact, it should be noted that to evaluate the quality of a new pyrometer purge system design it is sufficient that the action of drag force on the particles of a certain diameter and the bouncing mechanisms are as expected. Nonetheless, it has to be noted that, due to the impossibility of experimentally reproducing the entire spectrum of lens/particles collision velocities that is representative of the real case, only the case where the contaminants are deposited should be considered. Adequate technical solutions (e.g., sticky lens surface) need to be investigated to achieve this, which is equivalent to analyzing the worst case scenario (no particles bounce back on the lens).

# References

Alkhimov A.P., Papyrin A.N, Kosarev V.F., Nesterovich N.I.,Sushapanov M.M. (1994) *"Gas dynamic spraying method for applying a coating"* United States Patent, 5302414.

Assadi H., Gärtner F., Stoltenhoff T., Kreye H. (2003) *"Bonding mechanism in cold gas spraying"* Acta Materialia Volume 51, Issue 15, Pages 4379-4394.

Atkinson W.H, Cyr M.A., Strange R.R. (1988) *"Final report: Survey and evaluation of measurements, strain and heat flux for ceramic components in advanced propulsion systems"* NASA-CR-182111 techniques for temperature.

Atkinson W.H., Strange, R.R. (1987) *"Turbine pyrometry for advanced engines"* AIAA/SAE/ASME/ASEE 23rd Joint Propulsion Conference, San Diego, USA, June 29-July 2. AIAA-87-2011.

Bae G., Xiong Y., Kumar S., Kang K., Lee C. (2008) **"General aspects of interface bonding in kinetic sprayed coatings"** Acta Materialia Volume 56, Issue 17, , Pages 4858-4868.

Barradas S., Guipont V., Molins R., Jeandin M., Arrigoni M., Boustie M., Bolis C., Berthe L., Ducos M., (2007) *"Laser shock flier impact simulation of particle-substrate interactions in cold spray"* J. Therm. Spray Technol., 16(4), p 475-479.

References

_____

Basset A.B. (1888)  *"On the motion of a sphere in a viscous liquid"* Phil .Trans. R. Soc. London, Vol. 179A, pp. 43-63.

Batchelor G.K. (1967) *"An introduction to Fluid Dynamics"* Cambridge University Press Cambridge, England.

Baxter L. L. (1989) *"Turbulent transport of particles"* Ph.D. Dissertation, Brigham Young University, Provo, Utah

Berenblut B.J., Masom R.A., (1982) *"Radiation pyrometry for gas turbine engines- An introduction"* The British Journal of Non-destructive Testing, 24 (5), pp 268-269.

Betten J, (2005) *"Creep Mechanic"* Springer

Beynon T.G.R. (1981) *"Turbine Pyrometry – An equipment manufacturer's view"* ASME, Gas Turbine Conference and Products Show, Houston,Tex.,Mar. 9-12.

Bocksell T. and Loth E. (2006) *"Stochastic modeling of particle diffusion in a turbulent boundary layer"* Intl. J. of Multiphase Flow, Vol. 32, pp. 1234-1253.

Bolesta A.V., Fomin V.M., Sharafutdinov M.R., Tolochko B.P., (2001) *"Investigation of interface boundary occurring during cold gas- dynamic spraying of metallic particles"* Nucl. Instrum. Meth. A, 470(1-2), p 249-252.

Cheng W., Brach R.M., Dunn P.F. (2002) *"Three Dimensional Modeling of Microsphere Contacts/Impacts with Smooth Flat Surfaces"* Aerosol Science and Technology, 36:14045-1060.

Clift R, Grace JR, Weber ME. (1978) *"Bubbles, drops and particles"* New York: Academic Press.

Cowan G.R. ,Holtzman A.H.,(1963) *"Flow configurations in colliding plates: explosive bonding"* J. Appl. Phys.,  34(4), p 928-939.

References

Craft D. W. (1988) *"Pyrometer vortex air cleaning system with center masked pyrometer lens"* General Electric Company, United States Patent US 4,738,528.

Crowe C.T., Sommerfeld M., Tsuji, Y. (1998) *"Multiphase Flows with Droplets and Particles"* CRC Press, Boca Raton, FL.

Dahneke, B. (1995) *"Particle bounce or Capture-Search for an adequate theory: I.Conservation of Energy Model for a Simple Collision Process"* Aerosol Science and Technology 23(1), 25-39.

DaVis 7.2 (2009a) *"Software Manual"* LaVision GmBH, Anna-Vandenhoeek-Ring 19, D-37081 Gottingen Produced by LaVision GmbH, Gottingen.

DaVis 7.2 (2009b) *"FlowMaster Hardware"* LaVision GmBH, Anna-Vandenhoeek-Ring 19, D-37081 Gottingen Produced by LaVision GmbH, Gottingen.

De Lucia M., Lanfranchi C. (1994) *"An infrared pyrometry system for monitoring gas turbine blades: Development of a computer model and experimental results"* Transaction of the ASME Journal of Engineering for Gas Turbines and Power, 116(1), pp 172-177.

Dehbi A. (2008) *"Turbulent particle dispersion in arbitrary wall-bounded geometries: A coupled CFD-Langevin-equation based approach"* International Journal of Multiphase Flow 34 819–828.

Doorne C.W.H., Westerweel J., (2006) *"Measurements of laminar, transitional and turbulent pipe flow using stereoscopic-PIV"* Exp Fluids 42:259-279.

Douglas, J. (1980) *"High speed turbine blade pyrometry in extreme environments"* Measurements methods in rotating components of turbomachinery-Proceedings of the Joint Fluid Engineering Gas Turbine Conference and Products Show, New Orleans, USA, March 10-13.

References

Drew D.A. (1983) *"Mathematical modeling of two-phase flow"* Annu. Rev. Fluid Mech. 15, 261–291.

Dykhuizen R.C., Smith M.F., Gilmore D.L., Neiser R.A., Jiang X., Sampath S., (1999) *"Impact of High Velocity Cold Spray Particles"* J. Therm. Spray Technol., 8(4), p 559-564.

Eaton J. K., Fessler J.R. (1994) *"Preferential concentration of particles by turbulence"* Int. J. Multiphase Flow, 20, 169–209.

Elghobashi S. E. (1994) *"On Predicting Particle-Laden Turbulent Flows"* J. Applied Scientific Research, Vol. 52, 4, pp. 309-329.

Elghobashi S. E., Truesdell G. C. (1993) *"On the two-way interaction between homogeneous turbulence and dispersed solid particles; Part 1: turbulence modification"* Physics of Fluids, Vol. A5, pp. 1790-1801.

Faeth G. M., (1983*) "Recent Advances in Modeling. Particle Transport Properties and Dispersion in Turbulent Flow"* Proc. ASME-*JSME* Therm. Engng. Conf. 2: 517-34.

FLUENT (2009) *"Ansys Fluent 12.0 in Workbench User's Guide"* Ansys Inc.

Gore R.A. and Crowe C.T. (1989) *"Effect of particle size on modulating turbulent intensity"* International Journal of Multiphase Flow, Vol. 15, pp. 279.

Gore R. A., Crowe C. T. (1991) *"Modulation of turbulence by a dispersed phase"* Journal of Fluids Engineering, Vol. 113, No 2, pp. 304-307, American Society of Mechanical Engineers NY.

Gosman A.D., Ioannides E. (1981) *"Aspects of computer simulation of liquid fueled Combustors"* 19th Aerospace Science Meeting, St Louis, MO, AIAA Paper 81-0323.

# References

Grujicic M., Saylor J.R., Beasley D.E., DeRosset W.S., Helfritch D., (2003) *"Computational Analysis of the Interfacial Bonding Between Feed-Powder Particles and the Substrate in the Cold-Gas Dynamic-Spray Process"* Appl. Surf. Sci., 219(3-4), p 211-227.

Guetta S., Berger M., Borit F., Guipont V., Jeandin M., Boustie M., Ichikawa Y., Sakaguchi K., Ogawa K., (2009) *"Influence of particle velocity on adhesion of cold-Sprayed Splats,* J. Therm. Spray Technol.,18(3), p 331–342.

Guetta S., Berger M.H., Borit F., Guipont V., Jeandin M., Boustie M., Poitiers F., Ichikawa Y., Ogawa K., (2008) *"Influence of particle velocity on adhesion of cold-sprayed splats"* Thermal Spray, Crossing Borders, E. Lugscheider, Ed., ASM International, Materials Park, OH.

Harrison T.R. (1960) *"Radiation pyrometry and its underlying principles of radiant heat transfer"* John Wiley et Sons, Inc.

Hayden T, Myhre D., Pui D.Y.H., Kuehn T.H., Tsai C.J. (1988) *"Evaluating lens purge systems for optical sensors on turbine engines"* AIAA/ASME/SAE/ASEE 24th Joint Propulsion Conference, Boston, USA, AIAA-88-3037.

Hurley J.F. (1981) *"Air purging for an optical pyrometer of a gas turbine"* Avcu Corporation, United States Patent US 4,306,835.

Jane's Information Group (2003) *"Jane's aero-engines"* Jane's Information Group

John W. (1995) *"Particle-surface interaction: charge transfer, energy loss, resuspension and deagglomeration"* Aerosol Science and Technology 9 582-591.

Kast H.B., Prasad M.E. (1995) *"Pyrometer adapter"* General Electric Company, United States Patent US 5,421,652.

References

---

Kerr C.I.V. (2002a) *Purge system design for the applications of optical pyrometry in earoengines"* P.h.D. dissertion, Cranfield Univeristy

Kerr C.I.V., Ivey P.C. (2002b) *"An overview of the measurement errors associated with gas turbine aeroengine pyrometer systems"* Measurement Science and Technology, Volume 13, Number 6, pp 873-881.

Kerr C.I.V., Ivey P.C. (2002c) *"A review of purge air designs for aeroengine based optical pyrometers"* Transactions of the ASME Journal of Turbomachinery, Volume 124, Number 2, pp 227-234.

Kerr C.I.V., Ivey, P.C. (2002d) *"Particle deposition on optical pyrometer lenses: An illustrative case study"* Journal of Aerosol Science, Volume 33, number 11, pp 1577-1588.

Kerr C.I.V. , Ivey P.C. (2003) *"Optical fouling of the RB199 pyrometer"* AIAA Journal of Propulsion and Power, Volume 19, number 1.

Kerr C.I.V. , Ivey  P.C. (2004a) *"An Evaluation of Air-Purging Configurations for Optical Pyrometers in Gas Turbines"* Turbines, Aerosol Science and Technology, 38:2, 91-99

Kerr C.I.V. , Ivey  P.C. (2004b) *"Particle deposition in the GE90 pyrometer purge air system"* Particulate Science and Technology: Taylor and Francis Ltd,volume 22, Number 1, pp 51-64.

Kim, K. (2009a) *"Jetting-Out Phenomenon Associated with Bonding of Warm-Sprayed Titanium Particles onto Steel Substrate"*. Journal of Thermal Spray Technology

Kim K., Watanabe M. Mitsuishi K., Iakaoubovskii K., Kuroda S., (2009b) *"Impact bonding and rebounding between kinetically sprayed titanium particle and steel substrate revealed by high resolution electron microscopy"* J.Phys. D: Appl. Phys. 42.

# References

King P.C., Zahiri S.H., Jahedi M.H.,(2008) *"Focussed ion beam micro-dissection of cold sprayed particles"* Acta Mater., 56(19), p 5617-5626.

King P., Bae G., Zahiri S.H., Jahedi M., Lee C. (2010) *"An experimental and finite element study of cold spray copper impact onto two aluminum substrates"* Volume 19(3) , Journal of Thermal Spray Technology.

Kirby P.J. (1986) *"Some considerations relating to aero engine pyrometry"* Advance Instrumentation for Aero Engine Components, The propulsion and Energetics Panel 67th Symposium, Philadelphia, May 19-23,  AGARD-CP-399.

Klinkov S.V.M Kosarev V.F., Rein M.  (2005) *"Cold spray deposition: Significance of Particle Impact Phenomena"* Aerospace Science and Technology 582-591.

Koeschel W., Salden D., Hoch T  (1986) *"Turbine rotor blade measurements using infrared pyrometry"* Advance Instrumentation for Aero Engine Components, The Propulsion and Energetic Panel 67th Symposium, Philadelphia, USA,May 19-23, AGARD-CP-399.

Konstandopoulos A.G. (2006) *"Particle sticking/rebound criteria at oblique impact"* Aerosol Science 37 (292-305).

Li X., Dunn P.F., Brach R.M. (1999) *"Experimental and numerical studies of the normal impact of microspheres with surfaces"* Journal of Aerosol Science Vol. 30,No4,pp 439-449.

Li C.-J., Li W.-Y., Wang Y.-Y, (2005) *"Formation of metastable phases in cold-sprayed soft metallic deposit "* Surf. Coat. Technol., 198(1-3), p 469-473.

Li C.J, Li W.Y.,Liao H (2006) *"Examination of the critical velocity for deposition of particles in cold spraying"* Journal of Thermal Spray Technology Volume 15(2).

# References

---

Li W.-Y., Zhang C., Guo X., Li C.-J., Liao H., Coddet C., (2007) *"Study on impact fusion at particle interfaces and its effect on coating microstructure in cold Spraying"* Appl. Surf. Sci., 254(2), p 517-526.

Li W.Y., Gao W. (2009) *"Some aspects on 3D numerical modeling on high velocity impact of particles in cold spraying by explicit finite element analysis"* Applied Surface Science 255 7878-7892.

Li W.Y, Zhang C., Li C.-J.,Liao H. (2009) *"Modeling aspects of high velocity impact of particles in cold spraying by explicit finite element"* Analysis Journal of Thermal Spray Technology Volume 18, Numbers 5-6, 921-933, DOI: 10.1007/s11666-009-9325-2.

Li W.Y., Li C.J., Liao H. (2010a**) "***Significant influence of particle surface oxidation on deposition efficiency, interface microstructure and adhesive strength of cold-sprayed copper coatings"* Applied Surface Science Volume 256, Issue 16, Pages 4953-4958.

Li C-J., Wang H.-T., Zhang Q., Yang V, Li W.-Y. Liao H. L. (2010b) "Influence of spray materials and their surface oxidation on the critical velocity in cold spraying" Journal of Thermal Spray Technology Volume 19, Numbers 1-2, 95-101, DOI: 10.1007/s11666-009-9427-x.

Loth E. (2000) *"Numerical approach for motion of dispersed particles, droplets and Bubbles"* Progress in Energy and Combustion Science 26 161-223.

Loth E. (2010) *"Particles, drops and bubbles: fluid dynamics and numerical methods"* Cambridge University Press, Cambridge.

MacInnes J.M., Bracco F.V., (1992) *"Stochastic particle dispersion modelling and the tracer-particle limit"* Physics of Fluids A 4, 2809 2824.

References

———————————————————————————————————————————

MacKay C.G. (1990) *"Temperature measurement in turbine engines"* Allied-Signal Inc, United States Patent US 4,934,137.

Magand C.(2009) *"Joint stereo-PIV and NO-LIF in turbulent premixed hydrogen-air flames"* PhD Thesis, Cranfield University.

Maxey M.R. (1987) *"The motion of small spherical particles in a cellular flow field"* Physics of Fluids 30, pp. 1915–1928.

Maxey M. R., Riley J. J. (1983) *"Equation of motion of a small rigid sphere in a non-uniform flow"* Phys. Fluids 26, 833-889.

Menter F. R. (1993) *"Zonal Two Equation k-ω Turbulence Models for Aerodynamic Flows "* AIAA Paper 93-2906.

Mostafa A., Elghobashi. S.E. (1985) *"A two-equation turbulence model for JET flows laden with vaporising droplets"* Int. J. Multiphase Flow 11 , pp. 515–533.

Munro R.G. (1997) *"Evaluated material properties for a sintered α-alumina"* Journal of the American Ceramic Society.

Myhre D.C., O'Brien R.J., Pui D.Y.H., Tsai C.J. (1992) *"Window purging system for a combustion instrument"* Rosemount, United States Patent US 5,146,244.

Myhre D.C., Pui D.Y.H., Miller L.V. (1988) *"Purge air system for a combustion instrument"* Rosemout, United States Patent US 4,786,188.

Ning X.-J., Jang J.-H., Kim H.-J., Li C.-J., Lee C., (2008) *"Cold spraying of Al-Sn binary alloy: coating characteristics and particle bonding features"* Surf. Coat. Technol., 1681-1687.

Ntantis E. (2008) *"Capability Expansion of Non-Linear Gas Path Analysis"* P.h.D dissertation, Cranfield University

References

O'Brien R.J. ,Myhre D.C. (1989) *"Asymmetric purge air system for cleaning a lens"* Rosemount, United States Patent US 4,836,689.

Parsegian V.A. (2005) *"Van der Waals forces: A Handbook for Biologists, Chemists, Engineers and Physicists"* Cambridge University Press.

Penney C.M., Lund R.M. (1988) *"System to protect optics against dirty environment"* General Electric Company, United States Patent US 4,784,491.

Piomelli U. (1997) *"Introduction to the modeling of turbulence: large eddy and direct simulation of turbulent flows"* von Karman Institute for Fluid Dynamics, Lecture Series 1997-03.

Poelma C., (2004) *"Experiments in particle-laden turbulence"* PhD thesis, Delft University of Technology.

Pointer J., Masom R.A. (1987a) *"Pyrometer apparatus"* Smiths Industries Public Limited Company, United States Patent US 4,657,385.

Pointer J., Masom, R.A. (1987b) *"Radiation pyrometer with gas purge"* Smiths Industries Public Limited Company, United States Patent US 4,650,318.

Pope S. B. (2000) *"Turbulent Flow"* Cambridge University Press.

Prasad A (2000) *"Stereoscopic particle image velocimetry"* Exp Fluids 29:103–116.

Raffel M., Willert C.E., Kompenhans J. (2007) *"Particle Image Velocimetry: a practical guide"* Heidelberg ; New York : Springer.

Ridley I.H., Fearnehough P. (1997) *"Purge assembly"* Land Instrument International limited, United States Patent US 5,599,105.

References

_____

Roeder B.A., Sun C.T. (2001) *"Dynamic penetration of alumina/aluminium laminates: experiments and modelling"* International Journal of Impact Engineering 25 169-185.

Rohy D.A., Compton W.A. (1973) *"Radiation pyrometer for gas turbine blades"* Final Report Solar Division International Co. for National Aeronautics and Space Administration, G.C. Marhall Space Flight Center

Schmidt T., Gartner F., Assadi H., Kreye H. (2006) *"Development of a generalized parameter window for cold spray deposition"* Acta Materialai 54 729-742.

Sellers R.R., Przirembel H.R., Clevenger D.H. ,Lang J.L. (1989) *"The use of optical pyrometer in axial flow turbines"* AIAA/ASME/SAE/ASEE 25th Joint Propulsion Conference, Monterey, USA, July 10-12, AIAA-89-2692.

Shuen J.S., L.-D. Chen, G.M. Faeth (1983) *"Evaluation of a stochastic model of particle dispersion in a turbulent round jet"* AIChE Journal 29.

Sommerfeld M. (1987) *"Numerical simulation of supersonic two-phase gas-particle Flows"* Proceedings of the 16th International Symposium on Shock Tubes and Waves, pp. 235-241.

Soo S.L. (1965) *"Dynamics of multiphase flow systems"* IetEC Fund., 4, 426.

Soo S.L. (1990) *"Multiphase Fluid Dynamics"* , Science Press, Beijing, Gower Technical, Brookfield

Strutt H.C., Lightstone M.F. (2006) *"Analysis of tracer particle migration in inhomogeneous turbulence"* International Journal of Heat and Mass Transfer 49 2557–2566.

Suarez-Gonzalez, E. (1987) *"Reflection corrected radiosity optical pyrometer"* United Technologies Corporation, United States Patents, US 4,708,474

References

───────────────────────────────────────────────

Suarez E., Przirembel H.R. (1990) *"Pyrometry for turbine blade development"* Journal of Propulsion and Power, 6(5), pp. 584-589.

Swithenbank J. (1986) *"Technical evaluation report session III – Pyrometry"* AGARD, Papers presented at the Propulsion and Energetics Panel 67th symposium Pennsylvania USA 19-23 May.

Tavoularis S. (2005) *"Measurements in Fluid Mechanics"* Cambridge; New York: Cambridge University Press.

Taylor G. I. (1921) *"Diffusion by continuous movements"* Proceedings of the London Mathematical Society 20, 196.

Trenkmann I., Bok S., Korampally V.R., Gangopadhyay S., Graaf H., Von Borczyskowski C., (2012) *"Counting single Rhodamine 6G dye molecules in organosilicate nanoparticles"* Chemical Physics, Available online 2 March 2012, ISSN 0301-0104, 10.1016/j.chemphys.2012.02.014.

Vandromme D. (1997) *"Introduction to the modeling of turbulence: turbulence modeling for compressible flows and acoustics"* von Karman Institute for Fluid Dynamics, Lecture Series 1997-03.

Vlcek J., Gimeno L., Huber H., Lugscheider E., (2005*) "A systematic approach to material eligibility for the cold-spray process"* J. Therm. Spray Technol., 14(1), p 125-133.

Wall S., John W., Wang H.C., Goren S.L.(1990) *"Measurements of kinetic energy loss for particles impacting surfaces"* Aerosol Science and Technology 12, 926-946.

Wank A., Wielage B., Podlesak H., Grund T., (2006) *"High resolution microstructural investigations of interfaces between light metal alloy substrates and cold gas-sprayed coatings"* J. Therm. Spray Technol., 15(2), p 280-283

References

Wang L.P., Stock D.E. (1993) *"Dispersion of heavy particles by turbulent motion"* American Meteorological Society , 1897.

Wieneke B. (2005) *"Stereo PIV using self-calibration on particle images"* Exp Fluids 39:267–280.

Wilcox D.C. (1993) *"Turbulence modeling for CFD"* La Canada, CA: DCW Industries, Inc.

Wu J., Fang H., Kim H., Lee C., (2006) *"High speed impact behaviors of Al alloy particle onto mild steel substrate during kinetic deposition"* Mater. Sci. Eng. A, 417(1-2), p 114-119.

Xiong Y., Kang K., Bae G., Yoon S., Lee C., (2008) *"Dynamic amorphization and recrystallization of metals in kinetic spray process"* Appl. Phys. Lett., 92, p 194101.

Zhang D.Z., Prosperetti A. (1994) *"Averaged equations for inviscid dispersed twophase flow"* Journal of Fluid Mechanics Vol. 267, pp. 185-219.

Zhang D., Shipway P.H., McCartney D.G.,(2005) *"Cold gas dynamic spraying of aluminium: the role of substrate characteristics in deposit formation"* J. Therm. Spray Technol., 14(1), p 109-116.

Zilli A. (2004) *"Computational investigation of the performance of a military HP axial turbine subjected to realistic inlet temperature profiles"* MSc thesis, Cranfield University.

.